



HAL
open science

Conducting triarylamine supramolecular polymers : from electronics to plasmonics

Joseph John Armao

► **To cite this version:**

Joseph John Armao. Conducting triarylamine supramolecular polymers : from electronics to plasmonics. Other. Université de Strasbourg, 2015. English. NNT : 2015STRAF042 . tel-01674186

HAL Id: tel-01674186

<https://theses.hal.science/tel-01674186v1>

Submitted on 2 Jan 2018

HAL is a multi-disciplinary open access archive for the deposit and dissemination of scientific research documents, whether they are published or not. The documents may come from teaching and research institutions in France or abroad, or from public or private research centers.

L'archive ouverte pluridisciplinaire **HAL**, est destinée au dépôt et à la diffusion de documents scientifiques de niveau recherche, publiés ou non, émanant des établissements d'enseignement et de recherche français ou étrangers, des laboratoires publics ou privés.



UNIVERSITÉ DE STRASBOURG

ÉCOLE DOCTORALE SCIENCES CHIMIQUES

Institut Charles Sadron UPR-22

THÈSE

présentée par :

Joseph John ARMAO IV

soutenue le : **23 septembre 2015**

pour obtenir le grade de : **Docteur de l'université de Strasbourg**

Discipline/ Spécialité : Chimie

Conducting Triarylamine Supramolecular Polymers : From Electronics To Plasmonics

THÈSE dirigée par :

Mr. Giuseppone Nicolas

Professeur, Université de Strasbourg

RAPPORTEURS :

Mr. Bassani Dario

Docteur, Université de Bordeaux

Mr. Fichou Denis

Docteur, UPMC-Paris

AUTRES MEMBRES DU JURY :

Mr. Woisel Patrice

Professeur, Université de Lille

Mr. Genêt Cyriaque

Docteur, Université de Strasbourg

Joseph ARMAO

Conducting Triarylamine Supramolecular Polymers : From Electronics To Plasmonics

Resumé en Français

Dans ce travail, la chimie supramoléculaire est utilisée pour créer des polymères triarylamine auto-assemblés affichant l'auto-assemblage, la conduction, et les propriétés plasmoniques. Deux classes de polymères triarylamine auto-assemblés sont décrits en détail, y compris leurs propriétés d'auto-assemblage, structure à empiler, ainsi que le comportement électrochimique. En outre, l'application de ces matériaux à l'égard des cellules solaires organiques et spintronique moléculaire est examinée. Enfin, la capacité de ces fibres pour être utilisées dans des applications plasmoniques est détaillée, dans lequel les assemblages supramoléculaires sont présentés à quelques résonances plasmoniques de nanoparticules, agissent comme guides plasmoniques, et induisent l'ordre des nanoparticules plasmoniques à une interface liquide-liquide. Ces propriétés émergentes sont intimement liées aux interactions supramoléculaires démontrant ainsi de nouvelles applications de polymères supramoléculaires.

Resumé en Anglais

In this work, supramolecular chemistry is used to create self-assembled triarylamine polymers displaying novel self-assembly, conduction, and plasmonic properties. Two classes of self-assembled triarylamine polymers are described in detail, including their self-assembly properties, stacking structure, as well as electrochemical behavior. Additionally, the application of these materials towards organic solar cells and molecular spintronics is examined. Finally, the ability of these fibers to be used in plasmonic applications is detailed, wherein the supramolecular assemblies are shown to couple plasmonic nanoparticle resonances, act as plasmonic waveguides, and induce the ordering of plasmonic nanoparticles at a liquid-liquid interface. These emergent properties are intimately linked to the supramolecular interactions thereby demonstrating novel applications of supramolecular polymers.

Table of Contents

ABSTRACT	11
ABSTRACT EN FRANÇAIS	18
ACKNOWLEDGEMENTS	26
ABBREVIATIONS AND SYMBOLS	29
OBJECTIVES	33
CHAPTER I: BACKGROUND - FROM SUPRAMOLECULAR CHEMISTRY TO PLASMONICS	35
1. SUPRAMOLECULAR POLYMERS	35
A) SUPRAMOLECULAR CHEMISTRY AND SELF-ASSEMBLY	35
B) SUPRAMOLECULAR POLYMERS	40
I) SUPRAMOLECULAR POLYMERS FORMED FROM HYDROGEN BOND ARRAYS	41
II) SUPRAMOLECULAR POLYMERS FORMED FROM METAL-COORDINATION BONDS	45
III) SUPRAMOLECULAR POLYMERS FORMED FROM HOST-GUEST INTERACTIONS	47
IV) SUPRAMOLECULAR POLYMERS OF STACKED AROMATIC COMPOUNDS	51
V) MECHANISMS OF SUPRAMOLECULAR POLYMERIZATION	53
2. PHOTONICS AND PLASMONICS	58
A) INTRODUCTION	58
B) WAVEGUIDES	58
I) PLASMONIC WAVEGUIDES	59
II) ORGANIC WAVEGUIDES	64
C) PLASMONIC NANOPARTICLES	66
I) ORIGIN OF THE PLASMONIC RESPONSE	66
II) PLASMONIC COUPLING	68
CHAPTER II: SUPRAMOLECULAR SELF-ASSEMBLY AND RADICAL KINETICS IN CONDUCTING SELF-REPLICATING NANOWIRES	75
1. INTRODUCTION	75
2. SYNTHESIS AND SELF-ASSEMBLY OF MONO-AMIDE TRIARYLAMINES	75
3. AUTOCATALYTIC SELF-REPLICATION	77
4. DERIVATION OF THE MASTER EQUATION	80
5. LIGHT-INDUCED MECHANISM AND SELF-ASSEMBLED STRUCTURE	81
6. FIBRIL GROWTH AND RELAXATION IN THE DARK	84
5. CONCLUSIONS	88
CHAPTER III TRIARYLAMINE SELF-ASSEMBLY AT ELECTRODE SURFACES	91
1. INTRODUCTION	91
2. ELECTROCHEMICALLY TRIGGERED SELF-ASSEMBLY OF MONO-AMIDE TRIARYLAMINE NANOWIRES	92
3. ELECTROCHEMICAL BEHAVIOR OF TRIS-AMIDE TRIARYLAMINE NANOWIRES	97
4. ELECTRODE FUNCTIONALIZATION AND ATTACHMENT OF TRIARYLAMINE NANOWIRES	101
5. CONCLUSIONS	105
CHAPTER IV SELF-ASSEMBLING TRIARYLAMINES AS THE HOLE-TRANSPORT LAYER IN PEROVSKITE SOLAR CELLS	107
1. INTRODUCTION	107
2. SYNTHESIS AND CHARACTERIZATION OF SELF-ASSEMBLING TRIARYLAMINES WITH 2 AND 3 REDOX CENTERS	108
3. SOLAR CELL PERFORMANCE	112
4. ONGOING WORK	115
CHAPTER V TRIARYLAMINE-NITRONYL NITROXIDE DERIVATIVES AS STABLE DIRADICALS WITH APPLICATIONS TOWARDS MOLECULAR SPINTRONICS	117

1. INTRODUCTION	117
2. DENSITY FUNCTIONAL THEORY CALCULATIONS ON VARIOUS TRIARYLAMINE-NITRONYL NITROXIDE DERIVATIVES 118	
3. SYNTHESIS OF TRIARYLAMINE-NITRONYL NITROXIDE DERIVATIVES	120
4. CRYSTAL STRUCTURE	122
5. CHARACTERIZATION	125
6. CONCLUSIONS	126
CHAPTER VI: HEALABLE SUPRAMOLECULAR POLYMERS AS ORGANIC METALS	129
1. INTRODUCTION	129
2. PHYSICAL CHARACTERIZATION OF TRIS-AMIDE TRIARYLAMINE SELF-ASSEMBLIES	130
3. INTERMOLECULAR CHARGE-TRANSFER INDUCED ERROR CORRECTION AND SELF-HEALING	134
4. TATA AS AN ORGANIC METAL	143
5. CONCLUSIONS	149
CHAPTER VII: SUPRAMOLECULAR PLASMONIC INTERCONNECTS AND THEIR DIRECTED SELF-ASSEMBLY INTO OPTICAL NANOCIRCUITS	151
1. INTRODUCTION	151
2. HIERARCHICAL CONSTRUCTION OF NANOPARTICLE ARRAYS CONNECTED VIA TRIS-AMIDE TRIARYLAMINE NANOWIRES	151
3. OPTICAL PROPERTIES OF CONNECTED NANOCUSTER ARRAYS	159
4. OPTICAL NANOCIRCUIT THEORY	163
5. CONCLUSIONS	166
CHAPTER VIII: A TRIARYLAMINE SUPRAMOLECULAR ORGANIC FRAMEWORK AS PLASMONIC WAVEGUIDE	167
1. INTRODUCTION	167
2. A TRIARYLAMINE SUPRAMOLECULAR ORGANIC FRAMEWORK (TSOF)	168
3. PROPERTIES OF DOPED TSOF	172
4. PLASMONIC WAVEGUIDING FROM A SUPRAMOLECULAR ORGANIC FRAMEWORK	174
5. CONCLUSIONS	177
CHAPTER IX ORDERED PLASMONIC ASSEMBLIES AT A LIQUID-LIQUID INTERFACE	179
1. INTRODUCTION	179
2. FORMATION OF TRIARYLAMINE/GOLD NANOPARTICLE FILM AT A LIQUID-LIQUID INTERFACE	180
3. FORMATION OF ORDERED NANOPARTICLE/NANOFIBER ASSEMBLIES AT A LIQUID-LIQUID INTERFACE	182
A) FILM FORMATION THROUGH STIRRING LEADING TO ALIGNED NANOPARTICLE FILMS	182
B) CENTRIFUGATION AS AN EXTERNAL ORDERING FORCE	184
C) QUANTITATION OF ALIGNMENT	188
4. FUTURE DIRECTIONS	192
CONCLUSIONS	193
APPENDIX	197
PROCEDURES	199
1. GENERAL PROCEDURES	199
2. ORGANIC SYNTHESIS PROCEDURES	203
A. MONO-AMIDE TRIARYLAMINE SYNTHESIS	203
B. TRIS-AMIDE TRIARYLAMINE SYNTHESIS	207
C. PHOSPHONIC ACID TRIS-AMIDE TRIARYLAMINE	211
E. TWO-CENTER AND THREE-CENTER TRIARYLAMINE SYNTHESIS	217
F. TRIARYLAMINE NITRONYL NITROXIDE SYNTHESIS	228
G. THIOLATED TRIS-AMIDE TRIARYLAMINE SYNTHESIS	234
3. PROCEDURES SPECIFIC TO CHAPTER 2	238
4. PROCEDURES SPECIFIC TO CHAPTER 6	240

Table of Contents

5.	GOLD NANOPARTICLE SYNTHESIS AND FUNCTIONALIZATION PROCEDURES	240
6.	DENSITY FUNCTIONAL THEORY CALCULATIONS	242
	A. DFT CALCULATIONS FROM CHAPTER 5	242
	B. DFT CALCULATIONS FROM CHAPTER 6	242
	C. TATA OPTIMIZED GEOMETRY COORDINATES	244

ABSTRACT

Self-assembly is one of the critical chemical phenomena leading to the emergence of life. Increasingly, these concepts are being applied to design synthetic chemical systems programmed for a variety of applications. Towards this end, the work I have undertaken during my PhD has led to the understanding of a novel self-assembling system composed of organic triarylamine molecules which, upon assembly, display metallic properties suitable for applications ranging from organic electronics to organic plasmonics.

Triarylamines are a class of organic compounds that have been studied for decades as hole transport materials. Recently, it had been discovered by our group that appropriately substituted triarylamines undergo a self-assembly process resulting in stacking of the core units upon light-induced oxidation giving highly conductive one-dimensional self-assembled stacks. In chapter 2, we elucidate the mechanism and kinetics of this process through a combined experimental and theoretical examination of the self-assembly process. Specifically, we followed the self-assembly process by NMR, UV/Vis absorption spectroscopy, and Electron Paramagnetic Resonance (EPR) spectroscopy, which were combined with quantum mechanical simulations to derive a theoretical model of triarylamine self-assembly. Oxidation of the monomeric species in solution either by chemical methods or by light-triggered oxidation in chlorinated solvents gives rise to a sigmoidal assembly curve indicative of an autocatalytic process. By altering the variables in the process, such as concentration, level of oxidation, and the presence of a small amount of previously self-assembled material, we were able to derive a general equation describing the self-assembly process:

$$\omega(t) = \frac{M(t)}{c_A} = 1 - \left(\cosh\left(\frac{t}{t^*}\right)\right)^{-2/n^*}$$

where $M(t)$ is the number of aggregates per unit time, c_A is the total concentration, n^* is the critical aggregation number, and t^* contains factors for the nucleation rate, rate of association of free TAA, light intensity, and concentration.

The mechanism of this unique process can be described as a nucleation and growth mechanism. Briefly, the triarylamines undergo a light-induced oxidation in chlorinated solvents giving rise to the radical cation species. This radical species forms transiently stable charge transfer complexes with a chloride counterion, which associates into loose chains. These chains then associate through hydrogen bonding interactions to form a nucleus, onto which neutral molecules may then attach. In this way, we are able to trigger the oxidation and

subsequent growth of the self-assembled structures through only a catalytic quantity of the oxidized species. Additionally, the structure of the self-assembly, confirmed by X-ray diffraction, displays a double columnar stacking held together by hydrogen bonding between the two columns of molecules. This represents a truly unique self-assembly mechanism where we can have the molecules in the monomer or self-assembled form regardless of the concentration but only dependent on the presence or absence of oxidized species.

In chapter 3 we demonstrate the ability to electrochemically trigger the self-assembly. We demonstrate that the process takes place through a several step sequence: (1) diffusion of the neutral species into the electrochemical double layer, (2) oxidation at the electrode surface forming the radical cation species, (3) diffusion out of the double layer, (4) nucleation, and (5) subsequent growth in the bulk solution. Additionally, we demonstrate that the self-assembly process may be arrested in the presence of excess decamethylferrocene (DmFc). Due to the lower oxidation potential of DmFc, it can effectively reduce the oxidized triarylamine species before nucleation begins, thereby shunting the self-assembly pathway. Additionally, we examine the electrochemical behavior of the tris-amide triarylamine (TATA) self-assembly, whose full properties are detailed in chapter 6. This species is already present in the self-assembled form in solution and the efficient through-space charge-transfer properties of stacked molecules leads to quasireversible electrochemical behavior. Finally, we synthesize a triarylamine with pendant phosphonate groups for stable attachment to electrode surfaces. We show that upon functionalize, we are able to attach triarylamine through supramolecular interactions to the surface. We see this as an important step towards the implementation of these molecules in organic devices where interaction and orientation at the electrode interface plays a big role.

Chapter 4 details a collaborative effort towards making self-assembling triarylamine as hole transport layers in perovskite solar cells. We synthesized two-center and three-center triarylamine that have been designed to have appropriate energy levels for application in perovskite solar cells. We demonstrate the self-assembly of these molecules and application in solar cells. Results so far have demonstrated enhanced solar cell performance with photooxidation induced assembly. We have recorded up to 10% power conversion efficiencies with efforts still ongoing.

Chapter 5 concerns the design of diradical triarylamine species through the covalent attachment with nitronyl nitroxide units. Through extensive density functional theory calculations as well as the synthesis of a prototype functionalized molecule, we demonstrate the feasibility of this class of compound as stable diradicals with strong ferromagnetic

coupling tunable by the molecular spacer between the triarylamine and the nitronyl nitroxide unit. The application of this research is ongoing and is aimed towards the design of either bulk ferromagnets or as conductive self-assemblies displaying magnetoresistance.

Chapter 6 examines in detail the self-assembling nature and physical properties of tris-amide triarylaminines (TATA). The TATA compound self-assembles in a variety of organic solvents without the need for oxidation forming long fibers that give organogels at high enough concentrations. Additionally, the self-assembly forms longer fibers leading to gelation at appropriate concentrations. Structural studies of the self-assembly using a combination of X-ray scattering, high resolution AFM, and DFT calculations showed that the triarylamine core units stack on top of each other driven by intracolumnar hydrogen bonding of the amide groups, resulting in a helical self-assembled nanofiber. Upon oxidative doping, the fibers display through-space charge transfer within the self-assembled structures as observed by near-infrared absorption and EPR measurements. Fascinatingly, we observed error correction of the supramolecular stacking due to the migration of charges through the fibers. The improvement in stacking was followed both electronically by absorbance, fluorescence, and EPR as well as structurally by high resolution AFM and X-ray scattering. Additionally, the fibers displayed signatures of delocalized electrons with metallic characteristics when analyzed by variable temperature EPR and optical reflectance measurements. This indicates the formation of a band-like structure of the energy levels within the fibers. Taken together, the general picture of these supramolecular fibers is that the photoinduced through-space charge transfer complexes are essentially “supramolecular polarons” which diffuse through the fibers and fix defects in the stacking structure, thereby leading to coherent adiabatic domains with a metallic band-like electronic structure. We were also able to demonstrate the formation of light-responsive conducting gels, whereby remote, light-triggered doping induced up to 4 orders of magnitude increase in the conductivity. Additionally, we showed that we have an increase in the conductivity due to the self-healing error correction mechanism.

Building on this work in chapter 7, we were able to demonstrate that the metallic electrons within these nanofibers are able to couple to the plasmonic modes of gold nanoparticles effectively forming an interconnect between plasmonic nanoclusters. In order to demonstrate this, a hierarchical self-assembly strategy was used. First, hexagonal patterning of hydrophilic and hydrophobic domains on either glass or silicon was formed by spin coating reverse micelles of the block copolymer polystyrene-poly-2-vinylpyridine. Then, 13 nm gold nanoparticles were selectively adsorbed onto hydrophilic polymer domains producing gold

nanoclusters. Subsequent plasma treatment removed exposed polymer to leave gold nanoclusters with an average height of 48.9 ± 4.3 nm and an edge-to-edge distance of 94.5 ± 15.5 nm. Next, a monolayer of thiol-modified TATA was formed on the surface of the gold nanoparticles. Critically, the parallel orientation of the TATA core to the gold surface was controlled by using a multivalent thiol-gold interaction at low concentrations. This is critical because in order to attach the TATA fibers, the triarylamine core and amide bonds need to be readily accessible. An interwoven network of organic nanowires connecting the plasmonic gold nanoclusters was formed in the final step by incubating the non-thiolated TATA fibers for 24 hrs. with the thiolated gold nanocluster substrate. The far-field scattering spectrum exhibited a red shift of the nanoparticle plasmonic peak upon addition of the nanowires. In addition, the optical constants of the plasmonic nanoclusters were determined. The nanoclusters attached with the undoped wires gave an optical conductivity of $259 \Omega^{-1}\text{cm}^{-1}$. This value dramatically increased to $3193 \Omega^{-1}\text{cm}^{-1}$ for the doped unattached (no thio functionalization) nanowires and $4271 \Omega^{-1}\text{cm}^{-1}$ for the doped attached (with thiol functionalization) wires demonstrating coupling of the metallic electrons inside the TATA nanowires with the plasmonic oscillations of the gold nanoparticles. Additionally, the far-field scattering spectra were fit using optical nanocircuit theory. These experiments are critical as a proof-of-principle that organic nanowires may be used as plasmonic interconnects, an important step towards realizing organic plasmonic devices.

In chapter 8, we expand on the waveguide concept by demonstrating waveguiding in a supramolecular organic framework composed of triarylamines. While organic materials have increasingly become investigated as photonic materials, the dominant waveguiding mechanism remains the photoluminescence mechanism, whereby an incident laser induces an excited state in the molecules which then, due to the close packing of the chromophoric part of the molecule, leads to energy transfer in the form of exciton polaritons along the coherently stacked structures. Through a series of confocal microscopy experiments we demonstrate waveguiding with doped crystals, which is not a result of the photoluminescence mechanism. Instead, waveguiding appears to be plasmonic, originating from the delocalized band structure of the crystal. This demonstrates a novel mechanism of waveguiding for organic materials.

Finally, in chapter 9 we demonstrate the ability to form organized plasmonic arrays at a liquid-liquid interface. This originates from film formation at the interface of a biphasic system of triarylamine wires and plasmonic gold nanoparticles. The film can be formed simply upon shaking, though what we observe is largely an unorganized mixture of fibers and nanoparticles. However, upon application of a force perpendicular to the film interface, we

observe a drastic increase in the ordering. We are able to demonstrate the change from an unorganized film to a film displaying an ordering value of 0.96 for a domain size of $25 \mu\text{m}^2$. Additionally, the application of a strong enough force results in liquid crystal domains observable under an optical microscope. This is important as it is the first demonstration, through the manipulation of fundamental self-assembly concepts, of long-range stable ordering of NPs at a liquid-liquid interface.

Overall, I feel that I have successfully contributed to furthering the mechanistic and structural insights of the original self-assembly process. Additionally, I have discovered several new self-assembled derivatives that give novel properties not observed with the initial molecule. Finally, I have succeeded in demonstrating the potential plasmonic applications of these molecules, which should provide lasting returns into the future. From that sense, this work is really about bridging the gap between organic self-assembly and plasmonic materials.

ABSTRACT en Français

Auto-assemblage est l'un des phénomènes chimiques critique conduisant à l'émergence de la vie. De plus en plus, ces notions sont appliquées à concevoir des systèmes chimiques de synthèse programmés pour une variété d'applications. À cette fin, le travail que je suis engagé pendant ma thèse a conduit à la compréhension d'un nouveau système d'auto-assemblage composé de molécules de triarylamine organiques qui, lors de l'assemblage, les propriétés d'affichage métalliques appropriés pour des applications allant de l'électronique organique à la plasmonique organiques.

Triarylamines sont une classe de composés organiques qui ont été étudiés depuis des décennies en tant que matériaux de transport de trous. Récemment, il avait été découvert par notre groupe que triarylamines convenablement substitués subissent un processus d'auto-assemblage résultant à empiler des unités de base lors de l'oxydation induite par la lumière donnant piles auto-assemblées à une dimension hautement conducteurs. Dans le chapitre 2, nous élucider le mécanisme et la cinétique de ce processus par un examen théorique et expérimentale combinée du processus d'auto-assemblage. Plus précisément, nous avons suivi le processus d'auto-assemblage par RMN, spectroscopie d'absorption UV / VIS et résonance paramagnétique électronique (RPE), qui ont été combinés avec des simulations de mécanique quantique pour dériver un modèle théorique de triarylamine auto-assemblage. L'oxydation des espèces monomères en solution, soit par des procédés chimiques ou par oxydation déclenché par la lumière dans des solvants chlorés donne lieu à une courbe sigmoïdale de montage indicateur d'un processus auto-catalytique. En modifiant les variables dans le processus, comme la concentration, niveau d'oxydation, et la présence d'une petite quantité de matériel déjà auto-assemblée, nous étions en mesure de tirer une équation générale décrivant le processus d'auto-assemblage:

$$\omega(t) = \frac{M(t)}{c_A} = 1 - \left(\cosh\left(\frac{t}{t^*}\right)\right)^{-2/n^*}$$

où $M(t)$ est le nombre d'agrégats par unité de temps, c_A est la concentration totale, n^* est le nombre critique d'agrégation, et t^* contient des facteurs pour le taux de nucléation, le taux d'association des monomères, l'intensité de la lumière, et la concentration .

Le mécanisme de ce processus unique peut être décrit comme un mécanisme de nucléation et de croissance. En bref, les triarylamines subissent une oxydation induite par la lumière dans les solvants chlorés donnant lieu à des espèces de cations radicalaires. Ce radical formes d'espèces transitoirement des complexes de transfert de charge stables avec un contre-ion chlorure, qui associe dans les chaînes lâches. Ces chaînes ensuite associer par des interactions de liaison hydrogène pour former un noyau, sur lequel des molécules neutres peuvent alors fixer. De cette façon, nous sommes en mesure de déclencher l'oxydation et la croissance ultérieure de structures auto-assemblées uniquement par une quantité catalytique des espèces oxydées. En outre, la structure de l'auto-assemblage, confirmée par diffraction des rayons X, présente un empilement à double colonne maintenus ensemble par des liaisons hydrogène entre les deux colonnes de molécules. Cela

représente un mécanisme unique d'auto-assemblage où l'on peut avoir dans les molécules du monomère ou de la forme auto-assemblée indépendamment de la concentration mais uniquement dépendante de la présence ou l'absence d'espèces oxydées.

Des conclusions importantes sont que le mécanisme de base est un mécanisme de nucléation-croissance où le processus de nucléation est déclenchée par la formation du radical complexe cation-anion triarylamine qui associe pour former des piles courtes. Le noyau essentiel est prévu pour être un minimum de 6 radicaux dans un ensemble à double colonne. Intercolumnar liaison hydrogène entre deux de ces piles conduit à un auto-assemblage à double colonne, sur laquelle des molécules neutres suivantes peuvent se fixer. Il est important, en sautant entre les unités de base pour permettre la diffusion des radicaux à travers les fibres, et poursuivi l'oxydation des fibrilles formées peut être affectée à partir des extrémités. De même, la réduction des radicaux qui se passe dans l'obscurité à partir des extrémités de fibrilles et espèces "piégées" radicaux peuvent diffuser vers les extrémités et être réduit. Ces résultats sont d'intérêt pour d'autres systèmes d'auto-réplication basées sur les processus de nucléation croissance fibres

Dans le chapitre 3, nous démontrons la capacité de déclencher électrochimique l'auto-assemblage. Nous démontrons que le processus se déroule à travers une séquence de pas plusieurs: (1) la diffusion des espèces neutres dans la double couche électrochimique, (2) l'oxydation à la surface de l'électrode formant les espèces de cation radicalaire, (3) la diffusion de la double couche, (4) la nucléation, et (5) la croissance ultérieure dans la solution en vrac. En outre, nous démontrons que le processus d'auto-assemblage peut être arrêté à la présence d'un excès décaméthylferrocène (DMFC). En raison du potentiel d'oxydation inférieur de DMFC, il peut réduire efficacement les espèces triarylamine oxydés avant nucléation commence, shuntant ainsi la voie auto-assemblage. En outre, nous examinons le comportement électrochimique de l'triarylamine de tris-amide (TATA) auto-assemblage, dont les propriétés plein sont détaillées au chapitre 6. Cette espèce est déjà présente sous la forme d'auto-assemblé en solution et l'efficacité charge- travers l'espace propriétés de transfert de molécules empilées conduit à quasireversible comportement électrochimique. Enfin, nous synthétisons une triarylamine pendentif avec des groupes phosphonates pour la fixation stable à l'électrode surfaces. Nous montrons que, lors de fonctionnaliser, nous sommes en mesure de joindre triarylamine par des interactions supramoléculaires à la surface. Nous voyons cela comme une étape importante vers la mise en œuvre de ces molécules dans les dispositifs organiques où l'interaction et de l'orientation à l'interface de l'électrode joue un grand rôle.

Chapitre 4 détaille un effort de collaboration pour faire de triarylamine d'auto-assemblage de couches de transport de trous dans les cellules solaires perovskite. Cellules solaires pérovskites sont actuellement l'architecture de cellule solaire organique la plus prometteuse à l'étude, avec des rendements aussi élevés que 15%. La configuration de l'appareil contient une couche semi-conductrice de perovskite ($\text{CH}_3\text{NH}_3\text{PbX}_3$; X = Cl, Br, ou I), que le matériau absorbant la lumière. Après l'irradiation, une séparation de charge induit dans la couche de perovskite tandis que une

couche de transport de trous adjacente transporte la charge positive à une électrode en or et la couche de perovskite transporte les électrons vers l'électrode opposée. Nous avons testé la capacité de remplacer le matériau de transport de trous (HTM) avec triarylamines qui ont été soigneusement conçus pour produire des auto-assemblages conducteurs avec les décalages de niveau d'énergie appropriées pour correspondre à la conception de cellules solaires perovskite. Idéalement, l'incorporation d'auto-assemblages conductrices à l'intérieur de la couche de transport de trous mènera à la séparation de charge plus efficace avec moins de recombinaison et la fonction solaire plus efficace de la cellule globale. Nous avons synthétisé deux centres et trois centres triarylamines qui ont été conçus pour avoir des niveaux d'énergie appropriées pour l'application dans les cellules solaires perovskite. Nous démontrons l'auto-assemblage de ces molécules et l'application dans les cellules solaires. Les résultats obtenus jusqu'ici ont démontré de meilleures performances de la cellule solaire avec photooxydation induite assemblage. Nous avons enregistré jusqu'à 10% l'efficacité de conversion de puissance avec les efforts toujours en cours.

Chapitre 5 porte sur la conception d'espèces triarylamines diradical travers la liaison covalente avec des unités nitronyl nitroxydes. En raison de la capacité de l'unité centrale de triarylamine être facilement converti en son cation radical, nous avons étudié l'effet de fixation d'un groupe radical nitroxyde nitronyl. La rationalisation derrière cette stratégie est qu'en raison de la délocalisation vaste du radical parmi les unités de base aromatiques triarylamine, il devrait y avoir un fort couplage par liaison quand une espèce de radical stable est attachée. Nos objectifs de ce projet étaient de trois ordres: (1) faire preuve d'un couplage fort entre la triarylamine oxydé et le nitroxyde nitronyl, (2) pour contrôler la force et le signe de l'accouplement en changeant le modèle de substitution sur la molécule, et (3) pour vérifier si nous pouvons observer un effet de magnétorésistance avec des piles assemblées de ces molécules. Grâce à des calculs théoriques fonctionnelles de densité ainsi que la synthèse d'une molécule d'prototype fonctionnalisé, nous démontrons la faisabilité de cette classe de composés diradicaux comme stables avec une forte accordable de couplage ferromagnétique par l'espaceur moléculaire entre la triarylamine et l'unité nitronyl nitroxyde. Un prototype molécule TAA-NN a été synthétisé avec succès avec une grande stabilité dans des conditions ambiantes. En outre, la structure cristallin a été déterminée et des mesures magnétiques initial ont confirmé l'interaction entre les espèces ferromagnétique diradical. Voltamétrie cyclique affiche deux pics réversibles correspondant à l'oxydation de triarylamine suivie par le pic d'oxydation de nitroxyde nitronyl. Fait important, le fait que le pic de triarylamine vient avant le pic d'oxydation du nitroxyde nitronyl prend en charge la capacité d'oxyder le noyau de triarylamine et avoir une espèce diradical stables. Si le potentiel d'oxydation de triarylamine était plus élevé que le pic nitronyl nitroxyde, nous ne serions pas en mesure d'atteindre les espèces diradical, comme le radical nitroxyde nitronyl serait oxydé en l'espèce d'oxyde au moment où le triarylamine a été oxydée. Les expériences de RPE initiales ont été réalisées sur le TAA oxydé, qui a été oxydé par $SbCl_5$. Mesures de températures basses détecté un signal de la moitié de terrain indicative d'une espèce présentant diradical couplage d'échange. Une parcelle de la dépendance de température confirme une interaction ferromagnétique

entre les espèces radicalaires. L'application de cette recherche est en cours et est orientée vers la conception de matériaux ferromagnétiques soit en vrac ou auto-assemblages comme conducteurs affichant magnétorésistance.

Le chapitre 6 examine en détail la nature de l'auto-assemblage et les propriétés physiques de triarylamines tris-amide (TATA). Les composés TATA auto-assemble dans une variété de solvants organiques, sans le besoin d'oxydation formant des fibres longues qui donnent organogels à des concentrations suffisamment élevées. En outre, l'auto-assemblage forme des fibres plus longues conduisant à la gélification à des concentrations appropriées. Des études structurales de l'auto-assemblage en utilisant une combinaison de diffusion des rayons X, à haute résolution AFM, et calculs DFT ont montré que les unités de base de triarylamine empiler les uns sur les autres entraînée par intracolumnar liaison hydrogène des groupes amide, ce qui entraîne des hélicoïdal nanofibres. Sur dopage oxydatif, les fibres présentent transfert à travers l'espace-responsable au sein des structures auto-assemblées comme observé par l'absorption dans le proche infrarouge et des mesures RPE. Fascinante, nous avons observé une correction d'erreur de l'empilement supramoléculaire en raison de la migration des charges à travers les fibres. L'amélioration de l'empilage a été suivie à la fois par voie électronique par l'absorbance, la fluorescence, et EPR ainsi que structurellement par la résolution haute AFM et diffusion des rayons X. En outre, les fibres affichés signatures des électrons délocalisés avec des caractéristiques métalliques lorsqu'il est analysé par RPE à les bas températures et des mesures de réflectance optiques. Ceci indique la formation d'une structure en forme de bande des niveaux d'énergie à l'intérieur des fibres. Pris ensemble, le tableau général de ces fibres supramoléculaires est que les photo-induit à travers l'espace des complexes de transfert de charge sont "polarons supramoléculaires" essentiellement qui diffusent à travers les fibres et corriger les défauts dans la structure d'empilement, ce qui conduit à des domaines adiabatique cohérents avec une passante métallique comme la structure électronique. Nous avons également été en mesure de démontrer la formation de gels conducteurs sensibles à la lumière, de sorte à distance, la lumière dopage déclenchée induite jusqu'à 4 ordres de grandeur en augmentation de la conductivité. En outre, nous avons montré que nous avons une augmentation de la conductivité en raison du mécanisme de correction d'erreur d'auto-guérison. Cette première démonstration que polymères supramoléculaires peuvent présenter les signatures électroniques, magnétiques, optiques et similaires à celles mesurées par liaison dans les meilleurs polymères conjugués étend la compréhension actuelle de deux champs et les unifie. La capacité d'auto-assemblages supramoléculaires douces pour auto-optimiser leurs propriétés de conduction fournit des alternatives à métaux organiques classiques en termes de réactivité, la guérison et la transformation, qui est d'intérêt pour des applications dans l'électronique organique et l'électronique de spin.

Construire sur ce travail dans le chapitre 7, nous avons pu démontrer que les électrons métalliques au sein de ces nanofibres sont en mesure de couple pour les modes plasmoniques de nanoparticules d'or formant une interconnexion efficace entre nanoclusters plasmoniques. Pour

démontrer cela, une stratégie d'auto-assemblage hiérarchique a été utilisée. Tout d'abord, un motif hexagonal des domaines hydrophiles et hydrophobes sur verre ou du silicium a été formé par dépôt à la tournette reverse micelles de copolymère séquence polystyrène-poly-2-vinylpyridine. Puis, 13 nm nanoparticules d'or ont été sélectivement adsorbées sur des domaines de polymères hydrophiles produisant nanoclusters d'or. Après traitement par plasma retiré polymère exposée à quitter nanoclusters or avec une hauteur moyenne de $48,9 \pm 4.3\text{nm}$ et une distance bord à bord de $94,5 \pm 15,5\text{ nm}$. Ensuite, une monocouche de thiol-TATA a été modifiée formée sur la surface des nanoparticules d'or. Critique, l'orientation parallèle du noyau TATA à la surface de l'or a été contrôlée en utilisant une interaction thiol-or multivalent à de faibles concentrations. Ceci est important car pour fixer les fibres TATA, les obligations triarylamine de base et amide doivent être facilement accessibles. Un réseau de nanofils organiques entrelacées reliant les nanoclusters plasmoniques d'or a été formé dans l'étape finale en incubant les fibres non-TATA thiolés pendant 24 heures avec le substrat de nano-grappe d'or thiolé. Le spectre de diffusion en champ lointain présentait un décalage vers le rouge de la nanoparticule pic plasmonique lors de l'addition des nanofils. En outre, les constantes optiques des nanoclusters plasmoniques ont été déterminées. Les nanoclusters attachés avec des fils non dopés ont une conductivité optique de $259\ \Omega^{-1}\text{ cm}^{-1}$. Cette valeur considérablement augmenté à $3193\ \Omega^{-1}\text{ cm}^{-1}$ pour les (pas thiol fonctionnalisation) nanofils seules dopées et $4271\ \Omega^{-1}\text{ cm}^{-1}$ pour le dopée joint (avec une fonctionnalisation thiol) des fils démontrant couplage des électrons métalliques à l'intérieur des nanofils TATA avec le plasmoniques oscillations des nanoparticules d'or. En outre, les spectres de champ lointain de diffusion ont été ajustées en utilisant la théorie de nanocircuit optique. Ces expériences sont essentiels comme une preuve de principe que nanofils organiques peuvent être utilisés comme des interconnexions plasmoniques, une étape importante vers la réalisation de dispositifs plasmoniques organiques. Les données présentées dans ce chapitre démontre le couplage des modes plasmoniques entre nanoparticules métalliques à travers les modes de nanofils TATA d'oscillation, démontrant la capacité d'agir comme les interconnexions optiques Subwavelength. Cette preuve de principe est important car les interconnexions plasmoniques sont prévus comme des outils clés pour atteindre les topologies de nanocircuit complexes, et parce qu'ils doivent résoudre le problème du déplacement indésirable courant «fuite» qui se produit lorsque les nanoparticules sont mis en contact direct. En outre, les caractères organiques et auto-assemblées de STANWs ouvrent un tout nouveau domaine de recherche vers la plasmonique "supramoléculaires" "plastique" et, en fournissant un grand nombre de possibilités de mettre en œuvre 2D doux et traitable et dispositifs et métamatériaux de nanophotonique 3D.

Dans le chapitre 8, nous étendons sur le concept de guide d'ondes en démontrant de guidage d'onde dans un cadre organique supramoléculaire composé de triarylamines. Bien que les matières organiques sont de plus en plus étudiés comme matériaux photoniques, le mécanisme de guidage d'onde dominante reste du mécanisme de photoluminescence, grâce à quoi un laser incidente induit un état excité dans les molécules qui ensuite, en raison de l'emballage à proximité de la partie

chromophore de la molécule, conduit à l'énergie transférer sous forme de polaritons excitons le long des structures empilées de manière cohérente. Ici, nous vous proposons l'avancée conceptuelle de l'utilisation de métaux organiques, matières organiques avec la structure électronique de type bande avec des électrons délocalisés, comme des guides d'ondes de lumière et de transport d'énergie. En outre, nous montrons le transport de l'énergie claire sur l'échelle du micron en raison de ce mécanisme. Cette preuve-de-principe devrait être facilement étendue à d'autres métaux organiques permettant la formation de guides d'ondes plasmoniques organiques comme matériau photonique roman. Grâce à une série d'expériences de microscopie confocale, nous démontrons guidage d'ondes dopées avec des cristaux, ce qui est un résultat non du mécanisme de photoluminescence. Au lieu de cela, waveguiding semble y avoir plasmonique, provenant de la structure de bande délocalisée du cristal. Ceci démontre un mécanisme de guidage d'ondes nouveau pour des matériaux organiques.

Enfin, dans le chapitre 9, nous démontrons la capacité de former des réseaux organisés plasmoniques à une interface liquide-liquide (ILL). Ici, nous démontrons le premier exemple de commander des nanoparticules plasmoniques anisotropes dans des assemblages à une interface liquide-liquide. En outre, ceci est réalisé sans qu'il soit nécessaire de fonctionnalisation de surface des nanoparticules, mais est induit par structurant lyotrope avec des nanofils dopés supramoléculaires. Cela permet aux nanoparticules, une fois assemblés, de conserver leur capacité à former des guides plasmoniques à l'ILL. Nous prévoyons que les principes généraux définis ici peuvent être appliqués à une variété de systèmes d'ouverture à l'avenir la possibilité de nouveaux modèles de dispositifs à surfaces interfaciales. Ceci provient de la formation de film à l'interface entre un système biphasique de fils de triarylamine et des nanoparticules d'or plasmoniques. Le film peut être formé tout simplement lors de l'agitation, mais ce que nous observons est en grande partie un mélange non organisé de fibres et de nanoparticules. Cependant, lors de l'application d'une force perpendiculaire à l'interface du film, on observe une augmentation drastique de la commande. Nous sommes en mesure de démontrer le changement partir d'un film à un film non organisé l'affichage d'une valeur de commande de 0,96 pour une taille de domaine de 25 μm^2 . En outre, l'application d'une forte résultats suffisamment de force dans les domaines de cristaux liquides observables au microscope optique. Ceci est important car il est la première démonstration, à travers la manipulation des concepts d'auto-assemblage fondamentaux, de longue portée commande stable des IP à une interface liquide-liquide.

Dans l'ensemble, je pense que je l'ai contribué avec succès à faire avancer les connaissances mécanistes et structurales du processus d'auto-assemblage d'origine. En outre, je ai découvert plusieurs nouveaux dérivés auto-assemblés qui confèrent de nouvelles propriétés non observés avec la molécule initiale. Enfin, je l'ai réussi à démontrer les applications plasmoniques potentiels de ces molécules, qui devraient fournir des rendements durables dans l'avenir. De ce sens, ce travail est vraiment de combler le fossé entre l'auto-assemblage et des matériaux plasmoniques organique.

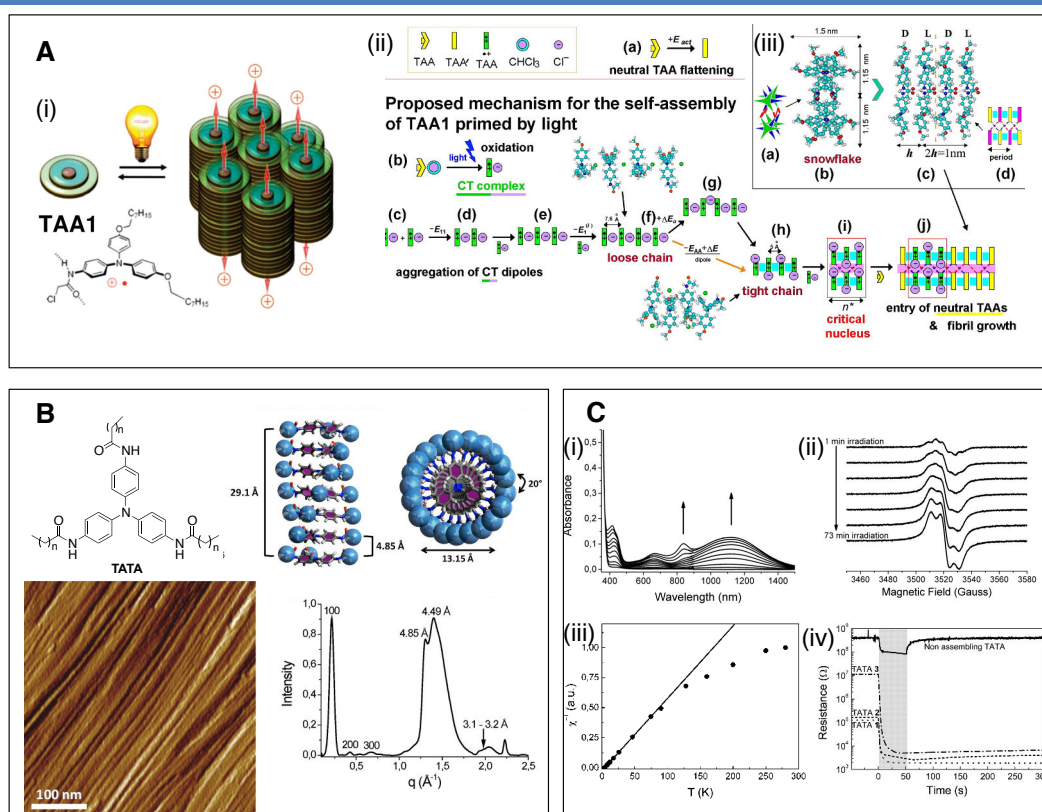


Figure A | Les deux systèmes d'autoassemblage (A;i) Représentation schématique de l'auto-assemblage supramoléculaire obtenu à partir d'une triarylamine amide modifié lors de l'irradiation de lumière. (ii) Cinétique d'agrégation dans les solutions de TAA. (a) Aplatissement spontanée hautement improbable de isolé molécule TAA neutre (transition TAA → TAA'). (b) Lumière induit l'oxydation d'une molécule d'TAA neutre production TAA et Cl^- radical. (c,d) Deux radicaux libres TAA • + complexé avec le contre-ions Cl^- attirent chaque queue-à-tête des autres. (e,f) Une pile croissante des dipôles radicales. (f,g,h) Le serrage de la pile: ions chlorure se déplacent latéralement (g); cycles aromatiques du molécules TAA bénéficient de contacts plus étroits, tout en anions chlorure sont finalement logés dans les interstices entre les queues éther de molécules de TAA (h). (i) La formation de noyaux à double colonne stabilisées par des liaisons hydrogène entre les colonnes. (j) La croissance de la structure par fixation de molécules neutres du TAA. (iii) Arrangements moléculaires dans bicolumnar piles «flocon de neige» de TAA3 neutre: (a) Une caricature montrant alternance orientation moléculaire dans les colonnes. (b) La vue de dessus (le long de l'axe principal), et (c) la vue de côté de la structure. (d) Une bande dessinée avec la chaîne en zigzag des liaisons H reliant les colonnes. (B) Les caractéristiques structurales de la TATA auto-ensembles présentant la formation de nanofibres de longues entraînés par intracolumnar liaison hrydrogen des trois groupes amides pendants résultant d'une périodicité longitudinal de 29.1 Å, une distance azote-azote de 4,85 Å entre des molécules adjacentes, et un angle dièdre de 20 ° entre chaque plateau. Imagerie AFM des fibres et le X-ray profil de diffusion sont indiqués sur la droite en bas à gauche et en bas, respectivement. (C) Propriétés électroniques des assemblées TATA. (i) Spectres d'absorption séquentielle prise lors de l'irradiation de lumière (10 W cm^{-2}) d'une solution à 0,1 mM de TATA 1 dans $CHCl_3$ pendant les 6 premières minutes de l'irradiation de lumière. (ii) Chambre spectres EPR de température pris tout en irradiant (avec une lampe à halogène; 10 W cm^{-2}) une solution à 1 mM dans du $CHCl_3$ TATA 1 1-73 min. (iii) RPE mesure dépendant de la température de 1 TATA afficher une région à basse température entièrement composé de localisée Curie tourne (voir comportement linéaire) et une région de température supérieure affichant un mélange de Curie et délocalisée Pauli tourne. (iv) la résistance en fonction du temps pour des échantillons de 17 mM TATA dans le tétrachloroéthane et un tri (bromophényl) amine nonassembling en tant que molécule de commande. L'arrière-plan gris correspond à la durée d'irradiation de lumière (lampe halogène, 10 W cm^{-2}).

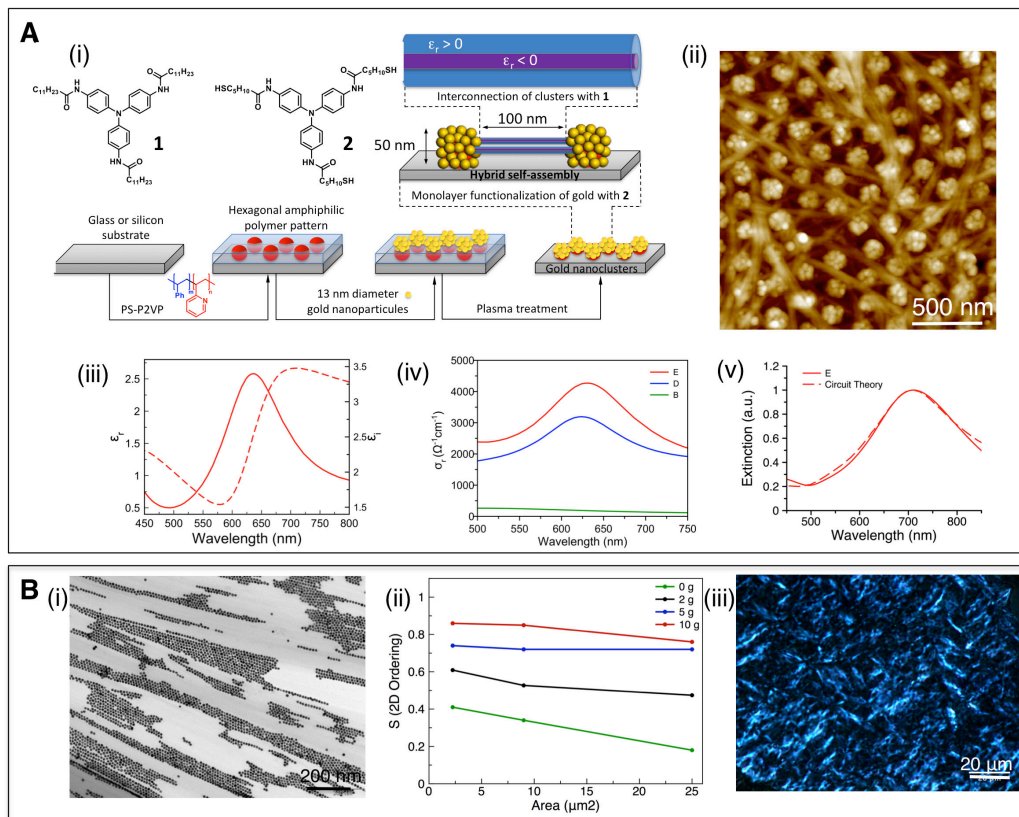


Figure B | Triarylamine matériaux plasmoniques (A; i) les structures chimiques des composés 1 et 2 qui sont utilisés pour former des nanofils et de fonctionnaliser la surface de l'or comme indiqué dans la schématic. En bref, la construction de la matrice de nano-amas d'or suivi d'un processus séquentiel: (1) en utilisant le motif amphiphile du substrat par séparation en microphases d'un copolymère séquencé, (2) le dépôt sélectif de nanoparticules, et le traitement au plasma, coulé par (3) fonctionnalisation de la surface d'or par deux (voir les détails dans la figure 2), et enfin (4) la matrice de nano-amas d'or est mis à incuber avec STANWs et conduit à un réseau totalement interconnecté avec les nanofils STANS afficher un profil coaxial diélectrique. (ii) l'image de la hauteur de l'AFM du tableau hybride de fibres organiques avec nanoclusters d'or, obtenue après le processus de construction représenté dans la figure 1f, qui est y compris STANWs que les interconnexions. (iii) réelles (en pointillés) et imaginaires (nature) parties de la constante diélectrique, tel que déterminé par ellipsométrie, pour les fibres dopées ci-jointe. (iv) Superposition des véritables conductivités optiques, dérivées de mesures d'ellipsométrie, en fonction du traitement de surface des nanoparticules d'or et du dopage de fibres. (v) mesurées et prévues spectres d'extinction pour les nanoparticules dopées attachés. (B; i) Alignement des nanoparticules d'or et de fibres de triarylamine à une interface liquide-liquide. (ii) la commande à deux dimensions en fonction de la zone démontre l'augmentation commande dans le film en fonction de la force centrifuge appliquée. (iii) optique de l'image des films plasmoniques sous polariseurs croisés affichant domaines cristallins liquides.

ACKNOWLEDGEMENTS

First, I would like to acknowledge my parents for their support through my life, especially with my decision to move 5873 miles from ‘home’. This may have seemed like a crazy decision because (1) I had been gainfully employed in the biotechnology industry for more than 5 years already, thereby putting my ‘career’ on hold so to speak (not to mention a rather significant reduction in wages) and (2) moving to a country I’d never been to before when there are plenty of educational opportunities in the United States.

...

Two roads diverged in a wood, and I —
I took the one less traveled by,
And that has made all the difference.
- Robert Frost

Secondly, I’d like to thank Professor Nicolas Giuseppone, who offered me a PhD position and has allowed me rather free rein during the past four years to develop my scientific intuition (even if sometimes my methods and thinking are a bit idiosyncratic). Additionally, I’d like to acknowledge Gad Fuks and Emilie Moulin for their support in the lab over the past 4 years. There have been many collaborators who have brought their expertise to the many projects I’ve worked on who I’d like to acknowledge, especially Mounir Maaloum, Tom Ellis, Artem Osypenko, Michel Rawiso, Irina Nyrkova, Alexander Seminov, and Raul Arenal.

I’d like to acknowledge my labmates who I’ve shared a lot of time together with, especially...
Quan Li, together we started our PhDs together and shared a lab for 4 years
Justin Foy and Simon Mckie, who are always around to talk (in ‘proper’ english)
e soprattutto a Vale (tvbgb)

Finally, I’d like to acknowledge the writings of the Swiss psychologist Carl Jung.

“All the works of man have their origin in creative fantasy. What right have we then to depreciate imagination? In the ordinary course of things, fantasy does not easily go astray; it is too deep for that, and too closely bound up with the tap-root of human and animal instinct. In surprising ways it always rights itself again. The creative activity of the imagination frees man from his bondage to the “nothing but” and liberates him in the spirit of play.”

- C.G. Jung

“Imagination is more important than knowledge. For knowledge is limited to all we now know and understand, while imagination embraces the entire world, and all there ever will be to know and understand.”

– Albert Einstein

ABBREVIATIONS AND SYMBOLS

Å	ångström
Ac	acetyl
AFM	atomic force microscopy
°C	celsius degree
δ	chemical shift
CT	charge-transfer
CV	cyclic voltammetry
DCM	dichloromethane
DFT	density functional theory
DMSO	dimethylsulfoxide
DNA	deoxyribonucleic acid
DLS	dynamic light scattering
DSC	dynamic light scattering
EM	electromagnetic
EPR	electron paramagnetic resonance
eq	equivalent
ESI-MS	mass spectrometry with electrospray ionization
ET	electron transfer
EtOAc	ethyl acetate
FFTEM	freeze-fracture TEM
h	hour
HOMO	highest occupied molecular orbital
HPLC	high performance liquid chromatography
HRMS	high resolution mass spectrometry
IR	infrared
ITC	isothermal titration calorimetry
ITO	Indium tin oxide
J	coupling constant
K	kelvin
K_d	dissociation constant
L	liter
LED	light-emitting diode
LLI	liquid-liquid interface
LC/MS	liquid chromatography coupled to mass spectrometry
LUMO	lowest unoccupied molecular orbital
λ_{\max}	maximum of emission/absorption wavelength
μL	microliter
μm	micrometer

mL	milliliter
μmol	micromole
mmol	millimole
MCPBA	<i>meta</i> -Chloroperoxybenzoic acid
MS	mass spectrometry
MTAA	mono-amide triarylamine
nm	nanometer
NMR	nuclear magnetic resonance
NMP	<i>N</i> -methylpyrrolidinone
NN	nitronyl Nitroxide
NP	nanoparticle
NIR	near infrared
r.t.	room temperature
RPM	revolutions per minute
SAXS	small angle X-ray scattering
SEM	scanning electron microscopy
SERS	surface-enhanced raman scattering
SOF	supramolecular organic framework
SOMO	singly occupied molecular orbital
STANW	self-assembled triarylamine nanowires
T	temperature
TAA	triarylamine
TAA-NN	triarylamine nitronyl nitroxide
TATA	tris-amide triarylamine
TBQ	tetrabromoquinone
TCE	tetrachloroethane
TCNQ	tetracyanoquinodimethane
TEA	triethylamine
TEM	transmission electronic microscopy
TLC	thin layer chromatography
TSOF	triarylamine supramolecular organic framework
TTF	tetrathiafulvalene
QCM	quartz crystal microbalance
UPLC	ultra performance liquid chromatography
UV	ultra-violet
Vis	visible
WAXS	wide-angle X-ray scattering

Objectives

Upon entering the laboratories in the fall of 2011 I was assigned to work on the self-assembling triarylamine project in our lab. Just several years prior, our group had discovered the ability of appropriately substituted, mono-amide triarylamine molecules to undergo light-induced self-assembly process (Figure 1a).¹ Interestingly, it was observed that in chlorinated solvents an excited state photo-catalyzed reaction occurs between the triarylamine molecules and the chloroform solvent leading to the formation of self-assemblies. From electron paramagnetic resonance (EPR) studies it was determined that only a catalytic amount of radical molecules was necessary to induce the self-assembly process. This was the first observation of a triarylamine self-assembly reported in the literature, even though triarylamine are a fairly widely studied group of compounds as hole transport layers. Additionally, from the self-assembly point of view, the initial results pointed to a novel self-assembly mechanism quite different than what had been previously reported in the literature. Furthermore, our group had demonstrated the ability to self-assemble these molecules between lithographically defined electrodes of 80 nm (Figure 1b).² These results showed outstanding conductivity through the nanowires on the order of $5 \times 10^3 \text{ S m}^{-1}$. Additionally, temperature-dependent measurements displayed metallic behavior in the doped nanowires.

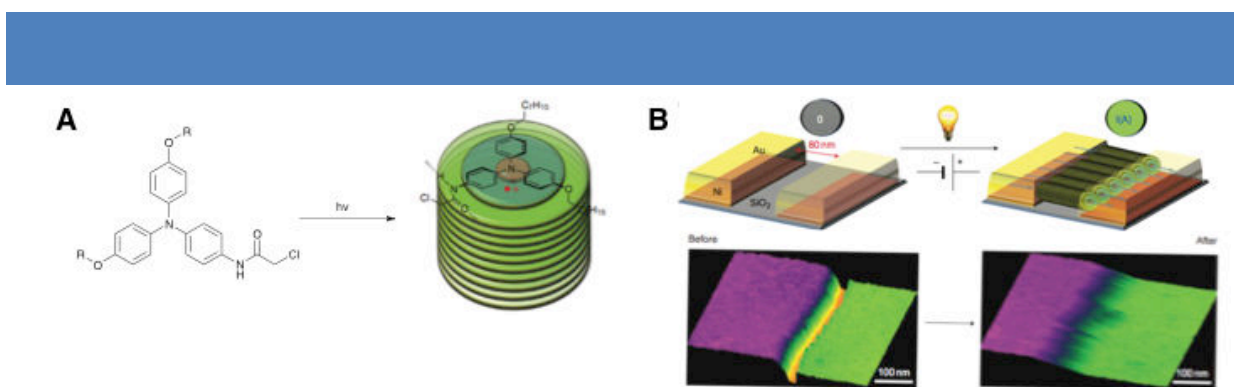


Figure 1 | Self-assembling triarylamine molecules reported by our group in 2010¹ (a). Assembly of the triarylamine between two lithographically defined electrodes² (b).

My goal was two-fold upon initially entering the lab. First, was to help to further

¹ Moulin, E.; Niess, F.; Maaloum, M.; Buhler, E.; Nyrkova, I.; Giuseppone, N., *Angew. Chem. Int. Ed.* **2010**, *49*, 6974-6978.

² Faramarzi, V.; Niess, F.; Moulin, E.; Maaloum, M.; Dayen, J.-F.; Beaufrand, J.-B.; Zanettini, S.; Doudin, B.; Giuseppone, N., *Nat Chem* **2012**, *4*, 485-490.

elucidate the mechanistic aspects as well as the structural details of this unique self-assembly process. Second was to explore the possible applications of these self-assemblies given their highly conductive nature.

Chapter I: Background - From Supramolecular Chemistry to Plasmonics

1. Supramolecular Polymers

a) Supramolecular Chemistry And Self-Assembly

Supramolecular chemistry is the “chemistry beyond the molecule” in the words of Jean-Marie Lehn, Nobel Prize in chemistry in 1987.³ It is based on the ability to control interactions between molecules using weak intermolecular forces such as ionic interactions, dipole interactions, hydrogen bonding, van der Waals forces, and π - π interactions. Furthermore, these forces, while dynamic in nature, may be used to design self-organizing systems, i.e. systems that are capable of spontaneously forming well-defined supramolecular architectures from their components. In a sense, this can be thought of as a primitive version of *chemical programming*⁴ wherein the design of the constituent molecules takes into account the resultant supramolecular interactions to realize a rationally designed supramolecular structure. This type of chemical programming through supramolecular interactions is ubiquitous in nature, with the most striking examples being DNA and proteins. DNA takes advantage of the different hydrogen bonding patterns of the nucleobases to ‘write’ the genetic code. The high fidelity of the interactions ensures proper base pairing and subsequent transmission through replication. In proteins, sequences of amino acids with differing side-chains give rise to complex network of non-covalent interactions resulting in secondary, tertiary, and quaternary structures based on the molecular program written into the sequence. It is vital to understand that the supramolecular organization of these amino acid sequences in the form of proteins ensures the functionality which would not exist in the native, unfolded state. An excellent biological example of the power of supramolecular chemistry is DNA polymerase II. It is responsible for synthesizing DNA in the cell. The crystal structure in figure 2 displays a myriad of supramolecular interactions giving rise to highly specific, and vital biological function.

³ Lehn, J.-M., *Angew. Chem. Int. Ed.* **1998**, *27*, 89-112.

⁴ Lehn, J.-M., *Angew. Chem. Int. Ed.* **2013**, *52*, 2836-2850.

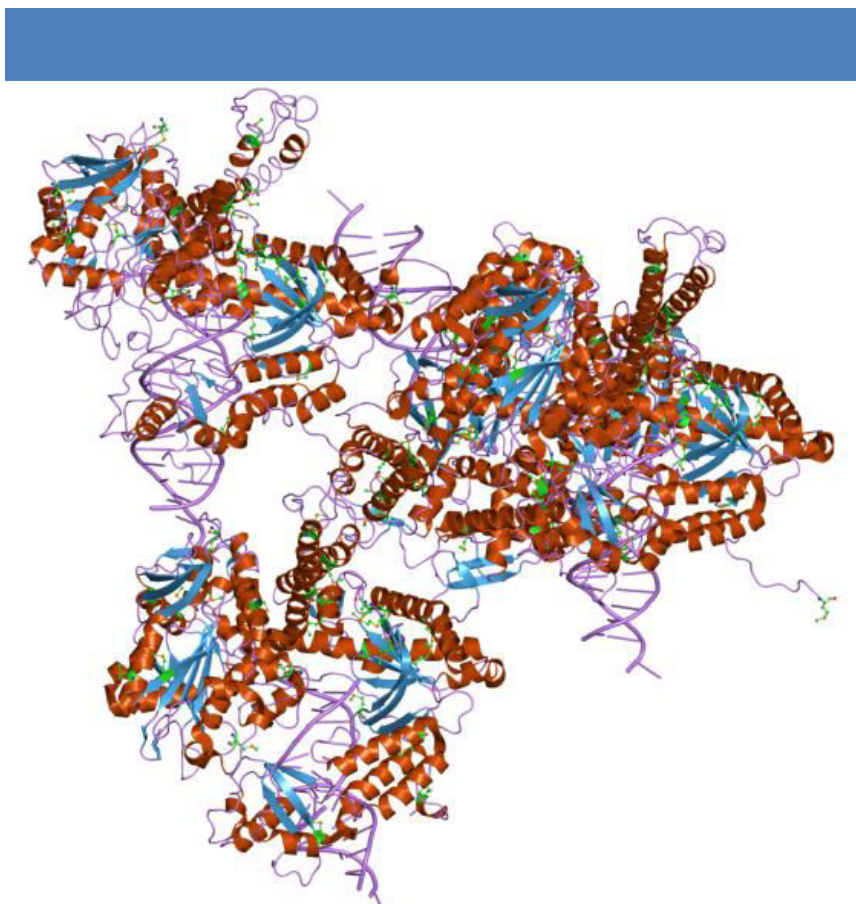


Figure 2 | DNA polymerase II demonstrates the level of complexity attainable by supramolecular interactions which are encoded for in the molecular structure.

The toolbox of non-covalent forces available to the supramolecular chemist varies widely in terms of strength, from only a few kJ mol^{-1} to 300 kJ mol^{-1} (table 1). The first group of is based on ionic and dipole interactions, which can be split into three categories: (1) *ion-ion interactions*, (2) *ion-dipole interactions*, and (3) *dipole-dipole interactions*. These forces are based on the Coulombic attraction between opposite charges, which in the case of ions are full charges, $1^+/1^-$, $2^+/2^-$, etc. and in the case of dipoles are partial charges. Accordingly, interactions between ions are stronger than interactions between dipoles, due to the higher charge on the species. The scalar form of Coulomb's law is

$$|F| = k_e \frac{|q_1 q_2|}{r^2} \quad (1)$$

where k_e is Coulomb's constant, q_1 and q_2 are the magnitude and signs of the charges and r is the distance between the charges. One can observe that the distance dependence goes as r^{-2} . Additionally, ion-ion interactions tend to be non-directional in nature, whereas ion-dipole and dipole-dipole interactions are directional in the sense that the two molecular species need to be aligned to maximize the attractive interaction.

Interaction	Strength (KJ mol ⁻¹)	Example
Ion-ion	200-300	Tetrabutylammonium chloride
Ion-dipole	50-200	Sodium-crown ether
Dipole-dipole	5-50	Acetone
Hydrogen bonding	4-120	DNA
Cation- π	5-80	K ⁺ /benzene
π - π	0-50	Benzene/graphite
Van der Waals	< 5; dependent on surface area	Crystal packing
Hydrophobic	Related to solvent-solvent interaction	Cyclodextrin inclusion complex

Table 1 | The different types of non-covalent interactions which underlie supramolecular chemistry.⁵

Hydrogen bonding interactions are among the most widely used interactions to program supramolecular architectures by chemists. This is due to the relatively high strength as well as directionality of the bonds. It can be thought of as a special kind of dipole-dipole interaction that consists of a hydrogen bond donor (D) and a hydrogen bond acceptor (A). The hydrogen bond donors are groups with a hydrogen atom attached to a strongly electronegative atom such as nitrogen or oxygen thereby giving a strong partial positive charge on the hydrogen atom. The hydrogen bond acceptor is a strongly electronegative atom with a partial negative charge. Figure 3 displays hydrogen bonding between the nucleobases guanine and cytosine. The bonding motif takes advantage of a triple hydrogen bonding pattern in order to increase the attraction between the two molecules as well as secondary interactions between adjacent motifs.

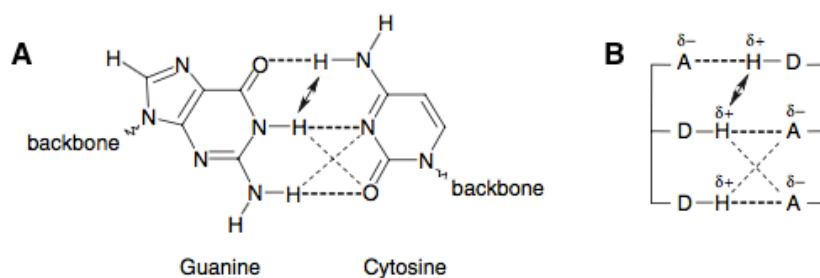


Figure 3 | Hydrogen bond interaction between guanine and cytosine basepairs: structural representation (a), abstraction (b).³

⁵ Steed, J.W.; Turner, D.R.; Wallace, K.J.; *Core Concepts in Supramolecular Chemistry*, 2007, Wiley

By altering the hydrogen bond donor and acceptor groups, hydrogen bonds displaying strong, moderate, and weak interactions can be obtained (Table 2). In general, one observes shorter bonding distances, more directional bonding, and higher bonding energies as the interaction strength increases. The ability to finely tune the strength of the interaction as well as the ability to combine multiple interactions together allows the chemist to create an almost infinite variety of motifs with varying specificity, binding strength and directionality. Also, the high degree of reversibility is key in allowing the thermodynamic product and not the kinetic product to be realized. This stands in contrast to covalent bonding, where often the kinetic path dictates bond formation and there is a decided lack of diversity in the bond characteristics (a carbon-carbon bond has little deviation in its physical characteristics in comparison to hydrogen bonds).

Interaction/ Property	Strong	Moderate	Weak
D-H --- A	Mainly Covalent	Mainly electrostatic	Electrostatic
Bond Energy (KJ mol ⁻¹)	60-120	16-60	< 12
Bond length (Å)			
H --- A	1.2-1.5	1.5-2.2	2.2-3.2
D --- A	2.2-2.5	2.5-3.2	3.2-4.0
Bond Angle (degrees)	175-180	130-180	90-150
Example	HF complexes	Acids Alcohols DNA/RNA	C-H --- A D-H --- π

Table 2 | Characteristics of strong, moderate, and weak hydrogen bonding motifs.³

Recently, halogen bonding as a supramolecular interaction has become quite *en vogue*. While similar to hydrogen bonding, the non-covalent interaction takes place between a halogen-bond donor (X) and a halogen bond acceptor (B). The internuclear distance is less than the sum of the van der Waals radius and the interaction occurs in a nearly strictly linear fashion ($> 175^\circ$), with a bonding strength upwards of 200 kJ mol⁻¹.⁶ Interestingly, the strength can be tuned by changing the substitution on the molecule with the halogen bond. While perhaps a bit counterintuitive that a strongly electronegative atom could be the source

⁶ Gilday, L. C.; Robinson, S. W.; Barendt, T. A.; Langton, M. J.; Mullaney, B. R.; Beer, P. D., *Chem. Rev.* **2015**, DOI: 10.1021/cr500674c

electrophilicity, it is best to take a simple example to understand the effect. In figure 4, the electrostatic potential is displayed for four molecules with the general formula of CF_3X . As one moves from the small fluorine and chlorine substitutions to the larger, more polarizable bromine and iodine substitutions there is a region of positive potential, termed the σ -hole which points away from the rest of the substituents. This allows the subsequent halogen bonding with a Lewis base. The density plots nicely demonstrate the high degree of directionality possible with this motif.

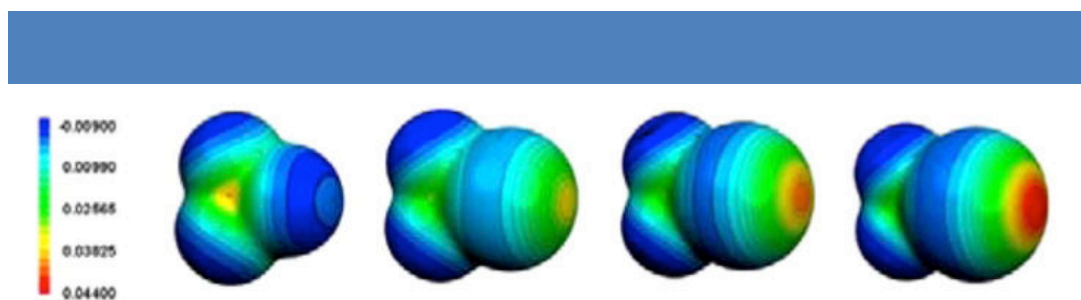


Figure 4 | Molecular electrostatic potential, of the isodensity surface of CF_3X (from left to right, X = F, Cl, Br, I).⁷

Moving from hydrogen bonding to π interactions, it is critical to distinguish two varieties: (1) π - π interactions and (2) cation/anion- π interactions.³ The first class of interaction, π - π interactions are furthermore found in two varieties, (1) *face-to-face* where the aromatic rings are parallel to one another with a slight offset and (2) *edge-to-face* where the aromatic rings are positioned perpendicularly from one another. Both of these interactions are driven by the attraction between the negatively charged π electron cloud and the positively charged σ framework on a neighboring molecule. This is likewise the driving force for cation- π interactions. Anion- π interactions, on the other hand, requires substitution of the aromatic group with strongly electron withdrawing substituents, such as hexafluorobenzene, to create an electropositive region above the aromatic ring.

Van der Waals forces are dispersion effects arising from momentary polarization in the molecule.³ Clearly, this is dependent on the polarizability of the molecule and one molecule can induce these effects in another. These forces are rather weak and not often exploited in terms of supramolecular design, as the energy decreases rapidly as a function of the distance, r^{-6} . The supramolecular interaction is the hydrophobic effect. It arises from the exclusion of non-polar groups from aqueous systems. This is commonly observed in the immiscibility of oil and water. The effect may be derived from either an enthalpic or entropic effect. Enthalpic

⁷ Clark, T.; Hennemann, M.; Murray, J.; Politzer, P. *J. Mol. Model.* **2007**, *13*, 291–296

effects occur for example when a guest replaces water inside a hydrophobic cavity. Entropic effects occur when two separated hydrophobic molecules in a aqueous solvent aggregate together, leading to less disruption in the water layer and consequently a higher degree of entropy. This effect is widely used in biology, with the most ubiquitous example being the formation of lipid membranes due to the organization of the hydrophobic lipid tails together.

b) Supramolecular Polymers

Supramolecular polymers are part of a rapidly developing research field at the interface between supramolecular chemistry and polymer science. The term supramolecular polymers may be defined as “polymeric arrays of monomeric units that are held together by highly directional and reversible noncovalent interactions, resulting in polymeric properties in solution and bulk”.^{8,9} Generally, supramolecular polymers may be classified according to three criteria: (1) the non-covalent force behind the reversible interaction between the monomer units (physical origin), (2) the type of structural monomer used (structural origin), and (3) evolution of the Gibbs free energy of the polymer as a function of the conversion (thermodynamic profile).⁷ Hydrogen bonding motifs, metal coordination, hydrophobic interactions, host-guest interactions, and aromatic stacking are among the noncovalent interactions which have been employed to form supramolecular polymers (Figure 5). By far, the most widely used interaction to form supramolecular polymers is the hydrogen bonding interaction, and thus we will start our overview of supramolecular polymers from this point.

⁸ Brunsveld, L.; Folmer, B. J. B.; Meijer, E. W.; Sijbesma, R. P. *Chem. Rev.* **2001**, *101*, 4071–4098.

⁹ De Greef, T. F. A.; Smulders, M. M. J.; Wolfs, M.; Schenning, A. P. H. J.; Sijbesma, R. P.; Meijer, E. W. *Chem. Rev.* **2009**, *109*, 5687– 5754.

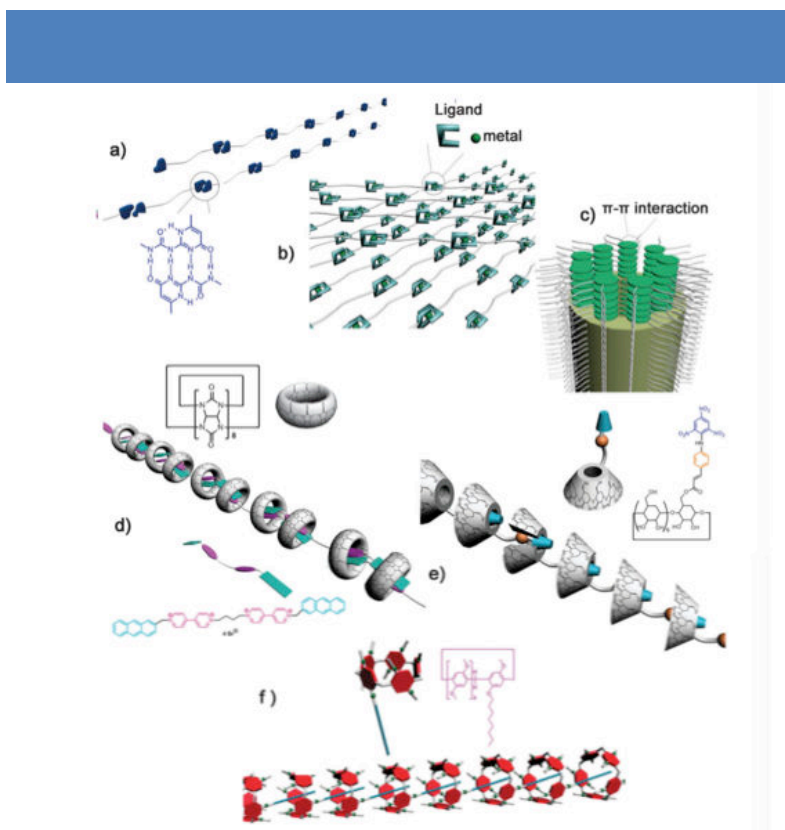


Figure 5 | Overview of the different types of interactions used to form supramolecular polymers: (a) multiple hydrogen bonding, (b) metal coordination, (c) π - π interaction, (d) cucurbit[8]uril, (e) β -cyclodextrins, and (f) pillar[5]arenes.¹⁰

i) Supramolecular Polymers Formed From Hydrogen Bond Arrays

First, we turn to an examination of the most commonly employed motif for forming supramolecular polymers, namely, hydrogen bond arrays. Typical energies of a single hydrogen bond are relatively weak (around 5 – 30 kJ/mol) and therefore are insufficient to form supramolecular polymers. However, by designing motifs containing multiple hydrogen bonding units, both the strength and directionality of the intermolecular interactions can be used to initiate supramolecular polymerization. Figure 6 demonstrates how the binding constants (the ratio of bound species to the ratio of free unbound species) of various hydrogen bond arrays may vary over many orders of magnitude by varying the number of hydrogen bonding units and their orientation. One can see the direct influence of nucleobase binding patterns on the design of these “artificial” molecules. Interestingly, aside from the number of hydrogen bond units in the motifs, we also observe a strong influence on the sequence of donors (D) and acceptors (A) in the array.

¹⁰ Guo, D.; Liu, Y. *Chem. Soc. Rev.* **2012**, *41*, 5907–5921.

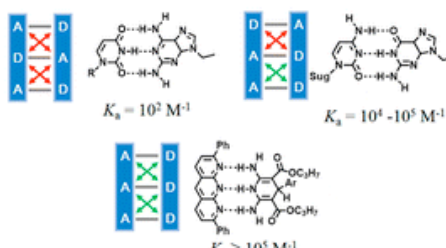
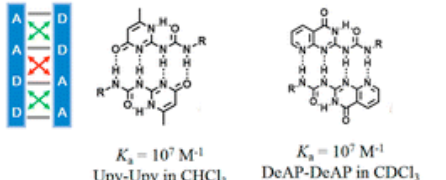
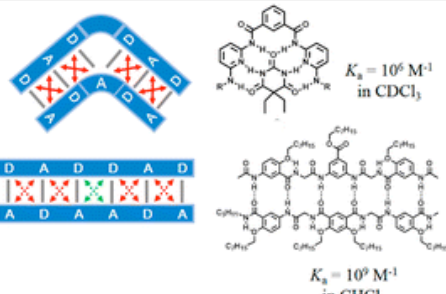
Type	Example
Triple	 <p> $K_a = 10^2 \text{ M}^{-1}$ $K_a = 10^4 - 10^5 \text{ M}^{-1}$ $K_a \geq 10^5 \text{ M}^{-1}$ </p>
Quadruple	 <p> $K_a = 10^7 \text{ M}^{-1}$ $K_a = 10^7 \text{ M}^{-1}$ Urypy-Urypy in CHCl_3 DeAP-DeAP in CDCl_3 </p>
Sextuple	 <p> $K_a = 10^6 \text{ M}^{-1}$ in CDCl_3 $K_a = 10^9 \text{ M}^{-1}$ in CHCl_3 </p>

Figure 6 | Examples of multiple hydrogen-bonding arrays and their binding constants.¹¹

For instance, the DAA-ADD and ADA-DAD binding motifs have identical hydrogen bond pairs, however, the binding constant of the DAA-ADD array is significantly higher than that of the ADA-DAD array ($K_a = 10^4$ vs. 10^2 M^{-1}). This is due to the additional attractive secondary electrostatic interactions in the DAA-ADD arrays.¹² That is to say, each hydrogen bond pair can also participate in a secondary (and tertiary if the geometry so permits) hydrogen bond interaction with adjacent hydrogen bond pairs. Computational calculations revealed that the optimal configuration for strong binding involves all of the donors and acceptors separated on two distinct molecules in order to maximize secondary interactions. Using this secondary interaction understanding, other multiple hydrogen-bonding arrays were designed with even higher binding constants. The quadruple binding motif AADD gave dimerization constants on the order of 10^7 .^{13,14} Quadruple hydrogen bonding complexes of

¹¹ Yang, L.; Tan, X.; Wang, Z.; Zhang, X., *Chemical Reviews* **2015**, DOI: 10.1021/cr500633b

¹² Jorgensen, W. L.; Pranata, J. *J. Am. Chem. Soc.* **1990**, *112*, 2008–2010.

¹³ Quinn, J. R.; Zimmerman, S. C.; Del Bene, J. E.; Shavitt, I. *J. Am. Chem. Soc.* **2007**, *129*, 934–941.

¹⁴ Sijbesma, R. P.; Beijer, F. H.; Brunsveld, L.; Folmer, B. J. B.; Hirschberg, J. H. K. K.; Lange, R. F. M.; Lowe, J. K. L.; Meijer, E. W. *Science* **1997**, *278*, 1601–1604.

AAAA-DDDD arrays, theoretically the strongest possible quadruple hydrogen bonding motif, exhibited hydrogen bonding constants as high as 10^{12} M^{-1} .¹⁵ Finally, several examples of sextuple hydrogen bonding arrays are exhibited in the figure displaying binding constants of 10^6 and 10^9 , which interestingly is significantly weaker than the quadruple motif of AAAA-DDDD, even though there are two additional hydrogen bond groups. This is a good demonstration of why secondary interactions in supramolecular cannot be discounted even though they may not be as readily apparent upon first glance.

By arranging multiple hydrogen bonding arrays on the same molecule, supramolecular polymers could be created. Initial examples were constructed from AA-type monomers. That is to say, that polymerization was effected by the placement of two self-complementary hydrogen bonding arrays on the same molecule. The first supramolecular polymer (AA-type) was reported by Lehn, *et al.* in 1990 and consists of bifunctional diamidopyridine and uracil derivatives to form linear polymeric chains via triple-hydrogen-bonding interactions (Figure 7).¹⁶ Polymerization resulted in liquid crystalline phases not observed with the unpolymerized monomer building block. In 1997, Meijer, *et al.* reported the formation of supramolecular polymers from quadruple hydrogen bonding motifs, as depicted in Figure 8.¹⁷

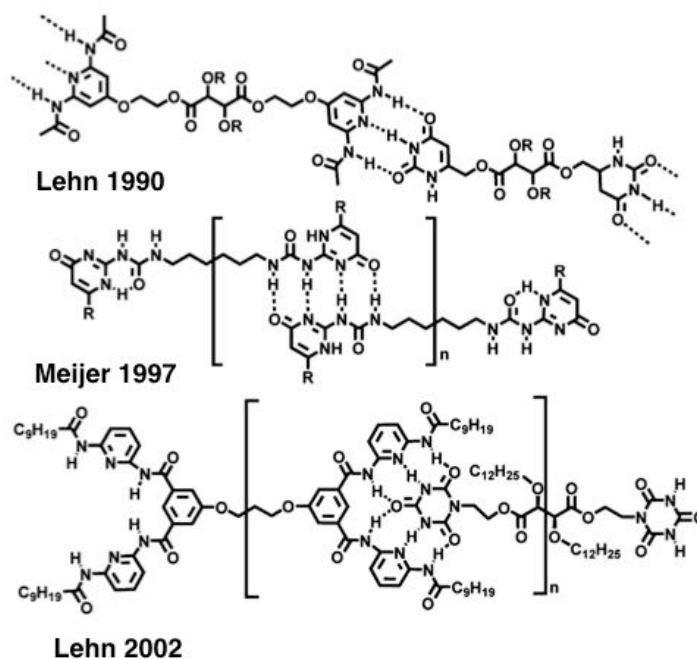


Figure 7 | Classic supramolecular polymers formed by using various multiple hydrogen-bonding motifs.

¹⁵ Velten, U.; Rehahn, M. *Chem. Commun.* **1996**, 2639–2640.

¹⁶ Fouquey, C.; Lehn, J.; Levelut, A. *Adv. Mater.* **1990**, 2, 254–257.

¹⁷ Sijbesma, R. P.; Beijer, F. H.; Brunsveld, L.; Folmer, B. J. B.; Hirschberg, J. H. K. K.; Lange, R. F. M.; Lowe, J. K. L.; Meijer, E. W., *Science* **1997**, 278, 1601-1604.

It was shown that the molecular mass of the supramolecular polymers could be tuned by varying the solvent and concentration. In another example from Lehn in 2002, a DAD-DAD (D = donor, A = acceptor) motif with binding sites for double-faced cyanuric acid wedges initiated the supramolecular polymerization of long fibers in organic solvents.¹⁸

Further development of the hydrogen bonding arrays led to the formation of the first supramolecular block copolymers. In figure 8, we see another example from Meijer wherein the first molecule will form a supramolecular polymer upon complimentary hydrogen bonding with itself.¹⁹ Upon the addition of the second molecule, there is efficient insertion into the supramolecular polymer chain due to the complementarity of the hydrogen bonding array. By altering the stoichiometric ratio, one can arrive at supramolecular block copolymers of varying block sizes.

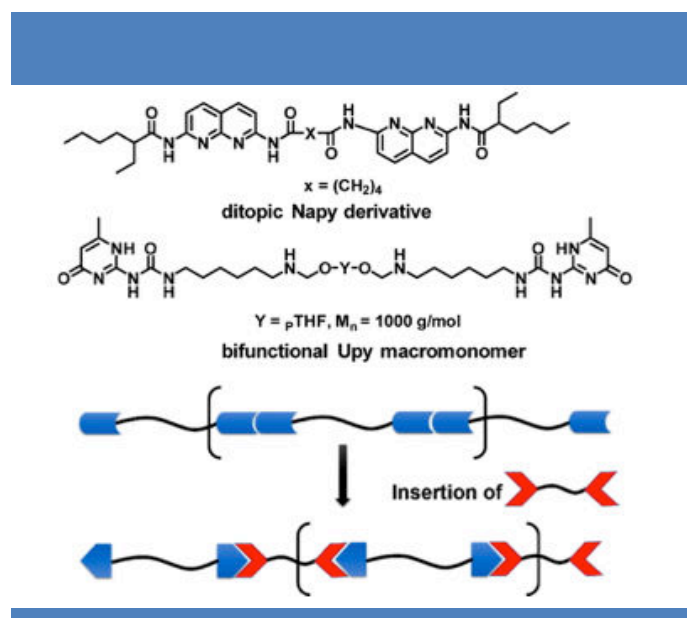


Figure 8 | Formation of a supramolecular block copolymer by controlling the ratio of two complementary monomer units.

A strict alternating supramolecular polymer was reported by Zimmerman *et al.*, wherein the two monomer building blocks exhibit strong complementary hydrogen bonding associations ($K = 10^7 \text{ M}^{-1}$) but negligible self-complementarity ($K = 230^{-1} \text{ M}^{-1}$).²⁰ The two structures are depicted in figure 9. Upon mixing, an alternating supramolecular block copolymer was formed, while no polymer was formed in the presence of just the monomers.

¹⁸ Berl, V.; Schmutz, M.; Krische, M. J.; Khoury, R. G.; Lehn, J.-M., *Chem. Eur. J.* **2002**, 8 (5), 1227-1244.

¹⁹ Ligthart, G. B. W. L.; Ohkawa, H.; Sijbesma, R. P.; Meijer, E. W. *J. Am. Chem. Soc.* **2004**, 127, 810-811.

²⁰ Murray, T. J.; Zimmerman, S. C., *J. Am. Chem. Soc.* **1992**, 114, 4010-4011

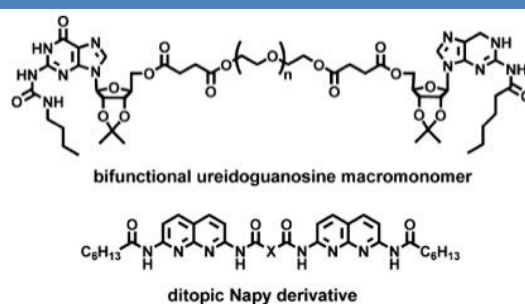


Figure 9 | Alternating supramolecular polymer from two complementary monomer units with minimal self-complementarity.

ii) Supramolecular Polymers Formed From Metal-Coordination Bonds

Metal-coordination bonds provide another framework for preparing supramolecular polymers. Metallosupramolecular polymers (MSP) are metal-containing polymers in which the metal-ligand coordination bond is dynamic and reversible. Thus, it is important to choose the right metal/ligand system in order to ensure thermodynamic reversibility. For example, Ru^{II} complexes with multidentate ligands are nondynamic on a reasonable timescale. In general, binding constants increase with (1) multidentate ligands and (2) multivalent metal ions. An example of the strategy is illustrated in figure 10.²¹ One can see an extraordinary increase in the binding constants, going from 10^3 M^{-1} for a single Zn²⁺/pyridine interaction to more than 10^{14} M^{-2} for the three-fold chelating terpyridine unit. For fully reversible coordination polymers, the degree of polymerization is proportional to square root of the binding constant.²² For a 1 mM solution with $K = 10^5 \text{ M}^{-1}$ we expect chain lengths of around 10 units. In contrast, molecules with an increased K of 10^7 M^{-1} gives chains of around 100 units. Additionally, the design and geometry of the ligands is of the utmost importance as rigid ligands with non-linear coordination configurations often lead to the formation of macrocyclic compounds such as MOFs, coordination cages, etc. Therefore, *linear configurations* and *flexible linkers* will favor polymer formation.

²¹ Dobrawa, R.; Würthner, F. J. *Polym. Sci., Part A: Polym. Chem.* **2005**, *43*, 4981–4995.

²² Ciferri, A. *Macromol. Rapid Commun.* **2002**, *23*, 511–529.

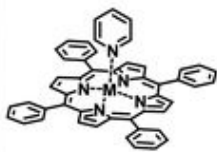



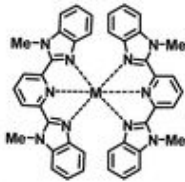
Ligand Type	Metal	K_a	Solvent/Counterion
	Zn ²⁺ Co ²⁺	$4.1 \times 10^3 \text{ M}^{-1}$ $1.0 \times 10^6 \text{ M}^{-1}$	CHCl ₃ /— Pyridine/OAc ⁻
	Zn ²⁺	$\sim 10^{13} \text{ M}^{-3}$	Aqueous KNO ₃
	Zn ²⁺	$1 \times 10^{17} \text{ M}^{-3}$	Aqueous KNO ₃
	Zn ²⁺ Fe ²⁺	$2 \times 10^{14} \text{ M}^{-2}$ $\sim 10^{21} \text{ M}^{-2}$	CH ₃ CN/ClO ₄ ⁻ /TBAPF Water
	Zn ²⁺ Fe ²⁺	$\sim >10^6 \text{ M}^{-2}$ $\sim 10^{14} \text{ M}^{-2}$	CHCl ₃ /CH ₃ CN/ClO ₄ ⁻ —

Figure 10 | Comparison of metal-coordination binding strengths.²¹

The first reported example of a soluble MSP was reported by Rehahn *et al.* and is shown in figure 11.²³ The monomer units consist of copper ions chelated by two phenanthroline ligands. The key is that each phenanthroline unit is bis functionalized with a rigid linker allowing for it to coordinate to two different copper ions.

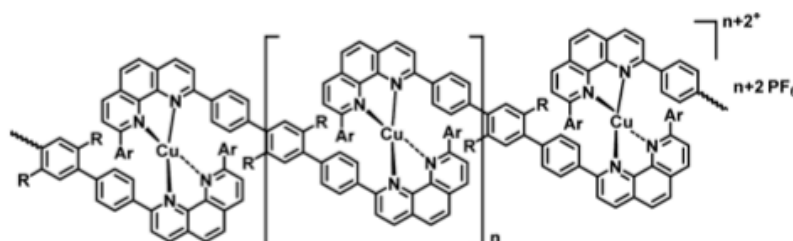


Figure 11 | The first example of a metallosupramolecular polymer formed from copper ions and phenanthroline ligands.²³

²³ Velten, U.; Rehahn, M. *Chem. Commun.* **1996**, 2639–2640.

One of the most important chelating units is the terpyridine motif, a representative example is displayed in figure 12. The chelating unit contains three nitrogen atoms allowing it to form stable complexes with a variety of transition metal ions. While early research was hampered by solubility issues, this was effectively fixed by constructing a water soluble linking chain as shown in the figure.²⁴ Simply mixing the ligands and ions together induces the formation of metallosupramolecular polymers. It is important to note several crucial experimental factors for polymerization. First, is that the stoichiometry should be carefully controlled, either by conductivity measurements or by viscosity measurements during the formation of the MSPs. Second is that the solvent can play a deciding role if it competes with the ligand in chelating the ions. Third, the concentration can play a role in whether or not cyclic by products are formed. Once formed, these cyclic products are very stable and difficult to break. Finally, temperature plays an important role in balancing the thermodynamic stability and kinetic liability of the polymers.

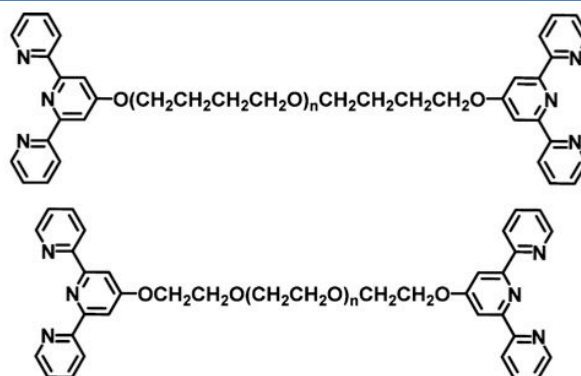


Figure 12 | Water soluble terpyridine ligands for metallosupramolecular polymers.

iii) Supramolecular Polymers Formed From Host-Guest Interactions

Host-guest complexes involve cooperative effects of various non-covalent interactions such as hydrophobic interactions, hydrogen bonding, van der Waals forces, and electrostatic interactions. The most common host-guest systems for fabricating supramolecular polymers are shown in figure 13. Cyclodextrins are the first motifs in the table and are composed of cyclic oligomers built up from six, seven, or eight glucopyranose units linked via α -(1-4)-glycosidic linkages. These molecules readily form inclusion complexes in water with

²⁴ Schmatloch, S.; van den Berg, A. M. J.; Alexeev, A. S.; Hofmeier, H.; Schubert, U. S. *Macromolecules* **2003**, *36*, 9943–9949.

a variety of organic molecules and have been widely used to construct different supramolecular architectures, for example layer-by layer assembly using cyclodextrin interactions.²⁵ For simplicity hosts are denoted “A” and guests are denoted “B”. Figure 14 depicts several strategies for forming supramolecular polymers, including the AB-type heteroditopic monomers and AA/BB types homoditopic molecules, the most common monomer types. Formation of supramolecular polymers needs to be conducted in high concentration solutions in order to avoid cyclization byproducts. The ABBA example was used to promote polymer formation in dilute solutions.

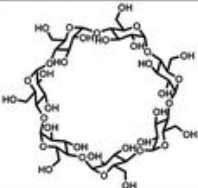
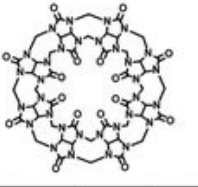
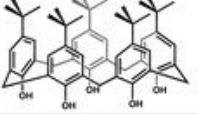

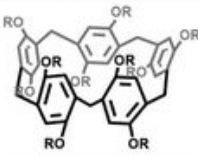
host molecules	molecular structures	typical guest molecules
β -cyclodextrin		adamantane, coumarin
cucurbit[8]uril		methyl viologen, charged naphthalene, anthracene and alkane
calixarene		charged alkane, viologen
crown ether		viologen, charged amine
pillararene		charged imidazole and DABCO

Figure 13 | Examples of host-guest systems used to create supramolecular polymers.¹⁵

Cucurbiturils (CBs) can bind a variety of neutral or positively charged guests with very high binding constants.²⁶ While supramolecular polymers are rare from CB[5], CB[6], and CB[7], CB[8] displays exceptionally high binding affinities due to its ability to bind two guests in its

²⁵ A. Pérez-Anes, M.Gargouri, W.L., H. V. D. Berghe, E. Courcot, J. Sobocinski, N. Tabary, F. Chai, J-F Blach, A. Addad, P.Woisel, D. Douroumis, B. Martel, N. Blanchemain, and J. Lyskawa *ACS Appl. Mat. & Int.*, **2015** 7, 12882-12893

²⁶ Rekharsky, M. V.; Mori, T.; Yang, C.; Ko, Y. H.; Selvapalam, N.; Kim, H.; Sobransingh, D.; Kaifer, A. E.; Liu, S.; Isaacs, L.; Chen, W.; Moghaddam, S.; Gilson, M. K.; Kim, K.; Inoue, Y. *Proc. Natl. Acad. Sci. U.S.A.* **2007**, 104, 20737–20742.

large binding cavity. However, due to aqueous solubility limitations (<1 mM), in most cases dimerization and oligomerization are more predominant than linear chain formation. Calixarenes are an important host in supramolecular chemistry, but examples have emerged recently demonstrating the ability of the compounds to participate in polymer formation.²⁷ They are easier to functionalize than cucurbiturils, allowing the ready ability to make water-soluble polymers. Similarly, pillararenes are another supramolecular host that can be easily functionalized to achieve supramolecular polymer formation.

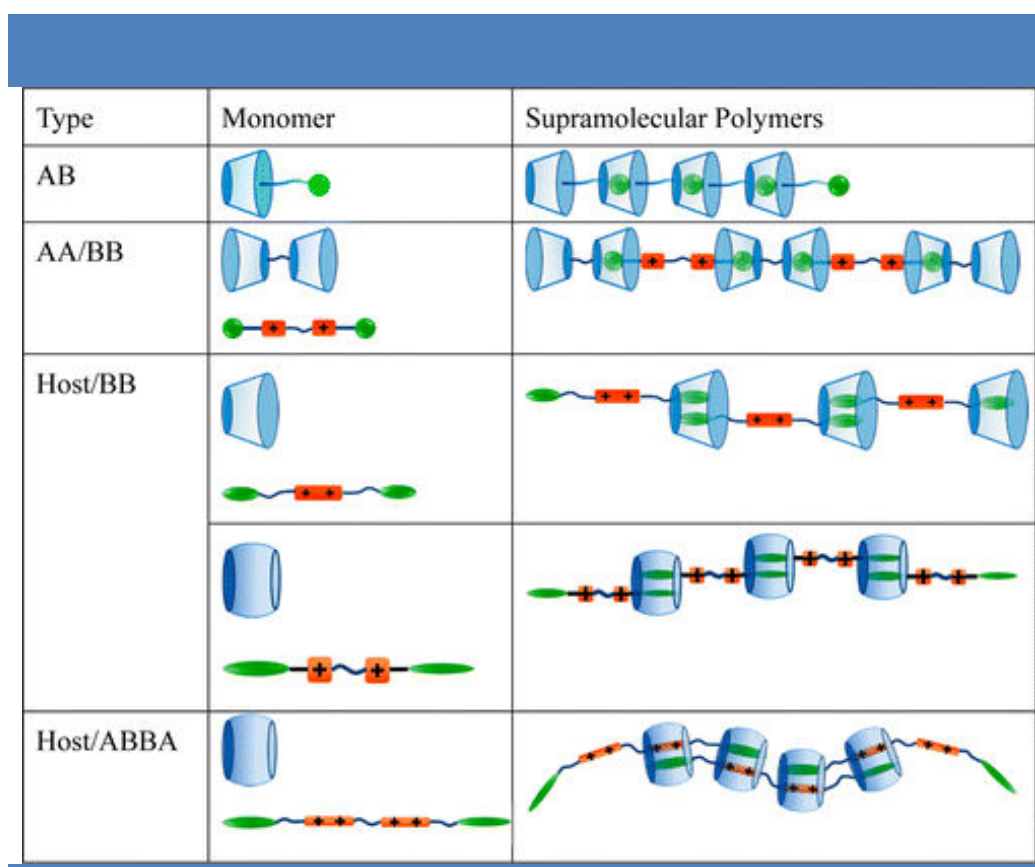


Figure 14 | Strategies for building up supramolecular polymers from cyclodextrin host-guest interactions.¹⁵

Finally, we come to the crown ether based supramolecular polymers, which are perhaps the most important class of host motifs. Crown ethers are macrocycles containing several ether groups, which bind strongly to cationic species. The central concept behind forming crown ether based supramolecular polymers is to design a bis functionalized linker with a rigid linker. Towards this end Stoddart, *et al.* designed such a supramolecular polymer based on a crown ether host complex and dibenzylammonium salt guest units (Figure 15).²⁸

²⁷ Guo, D.; Liu, Y. *Chem. Soc. Rev.* **2012**, *41*, 5907–5921.

²⁸ Ashton, P. R.; Baxter, I.; Cantrill, S. J.; Fyfe, M. C. T.; Glink, P. T.; Stoddart, J. F.; White, A. J. P.; Williams, D. J. *Angew. Chem., Int. Ed.* **1998**, *37*, 1294–1297.

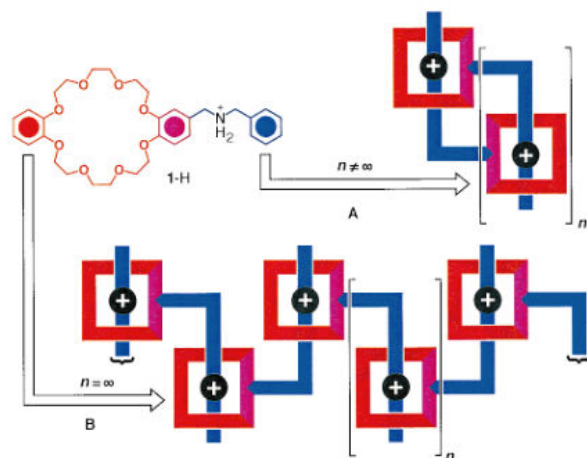


Figure 15 | Early example of a “daisy chain” supramolecular polymer from Stoddart.²⁸

This basic design was improved upon and even longer supramolecular polymers were formed from the examples shown in figure 16.^{29,30} Linear polymers could also be formed from monomer units with flexible chains, promoted by either high concentrations or by mismatching the length of the host and guest linkers.

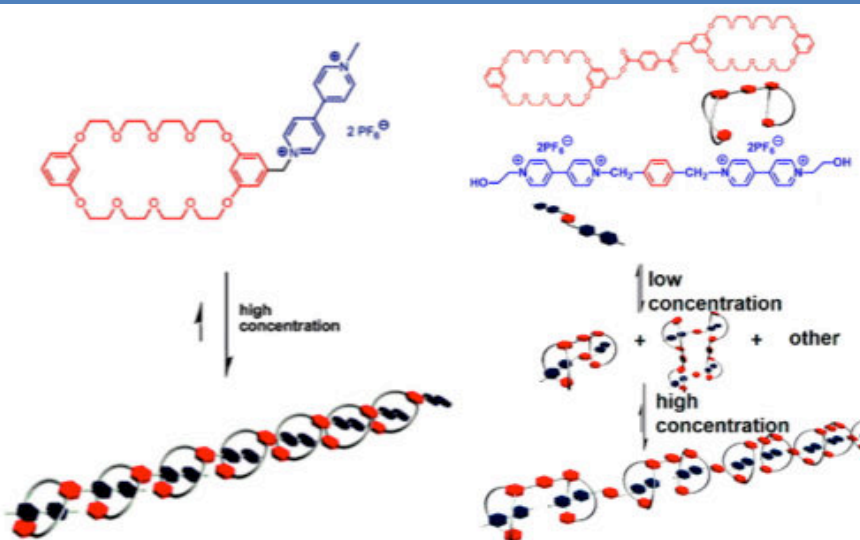


Figure 16 | Two more examples of daisy chain polymers.^{31,32}

²⁹ Yamaguchi, N.; Nagvekar, D. S.; Gibson, H. W., *Angew. Chem., Int. Ed.* **1998**, *37*, 2361–2364

³⁰ Zheng, B.; Wang, F.; Dong, S.; Huang, F., *Chem. Soc. Rev.* **2012**, *41*, 1621–1636

³¹ Yamaguchi, N.; Nagvekar, D. S.; Gibson, H. W., *Angew. Chem., Int. Ed.* **1998**, *37*, 2361–2364.

³² Zheng, B.; Wang, F.; Dong, S.; Huang, F., *Chem. Soc. Rev.* **2012**, *41*, 1621–1636.

iv) Supramolecular Polymers Of Stacked Aromatic Compounds

The last group of supramolecular polymers are formed from stacks of aromatic compounds. Unlike the previous structures, which are largely structural in function, the formation of close stacking of aromatic cores leads to supramolecular polymers displaying useful electrical and optical properties. This class of supramolecular polymer is driven by *face-to-face* π - π interactions, though often there are supplementary driving forces such as hydrogen bonding. An important example is the formation of supramolecular polymers in the form of charge transfer nanostructures (Figure 17).³³

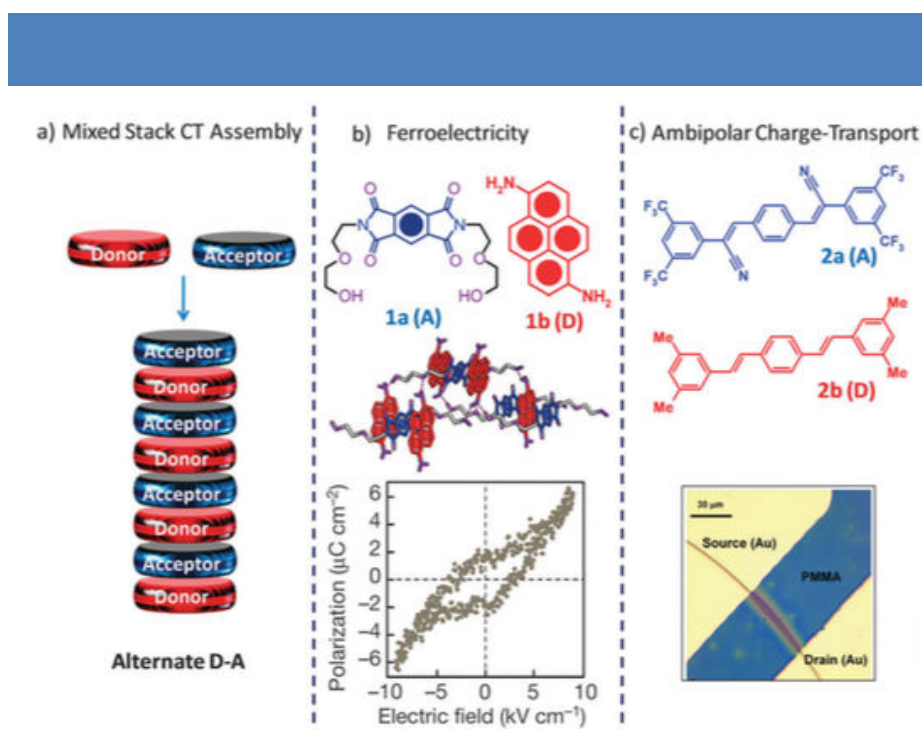


Figure 17 | Schematic representation of mixed stack charge-transfer (MS-CT) assemblies (a). An example of a room temperature organic ferroelectric assembly (b). A MS-CT assembly exhibiting ambipolar charge transport (c).

These interactions are based on aromatic donor and an aromatic acceptor molecules arranged in an alternating manner in stacks forming one-dimensional assemblies. These are the supramolecular analogues of charge transfer crystals, which have been long-studied for their conductive properties. The prime example is charge transfer crystals formed between tetrathiafulvalene (TTF) and Tetracyanoquinodimethane (TCNQ) displaying metallic properties and later superconducting properties. Recently, examples of room temperature ferroelectricity³⁴ and ambipolar charge transport³⁵ have also been demonstrated. Mixed-stack

³³ Kumar, M.K.; Rao, V.; George S.J. *Phys Chem Chem Phys*, **2014**, *16*, 1300 - 1304

³⁴ A. S. Tayi, A. K. Shveyd, A. C.-H. Sue, J. M. Szarko, B. S. Rolczynski, D. Cao, T. J. Kennedy, A. Sarjeant, C. L. Stern,

charge transfer compounds allow for the possibility of long-range ordering of electrical dipoles leading to spontaneous electrical polarization whose alignment direction can be switched by an external electric field. Meanwhile, direct overlap of frontier orbitals and high transfer integrals explain the ambipolar charge transport properties recently observed.

Another important example which has been very well studied by the group of Bert Meijer is 1,3,5 benzene tricarboxamide.³⁶ The core molecule readily undergoes intermolecular hydrogen bonding through the three pendant amide groups, giving assemblies with stacked aromatic cores at the center. An example of the wide range of applications is displayed in figure 18, which include liquid crystals, organogels, MRI contrast reagents, nucleating agents, and microcapsules.

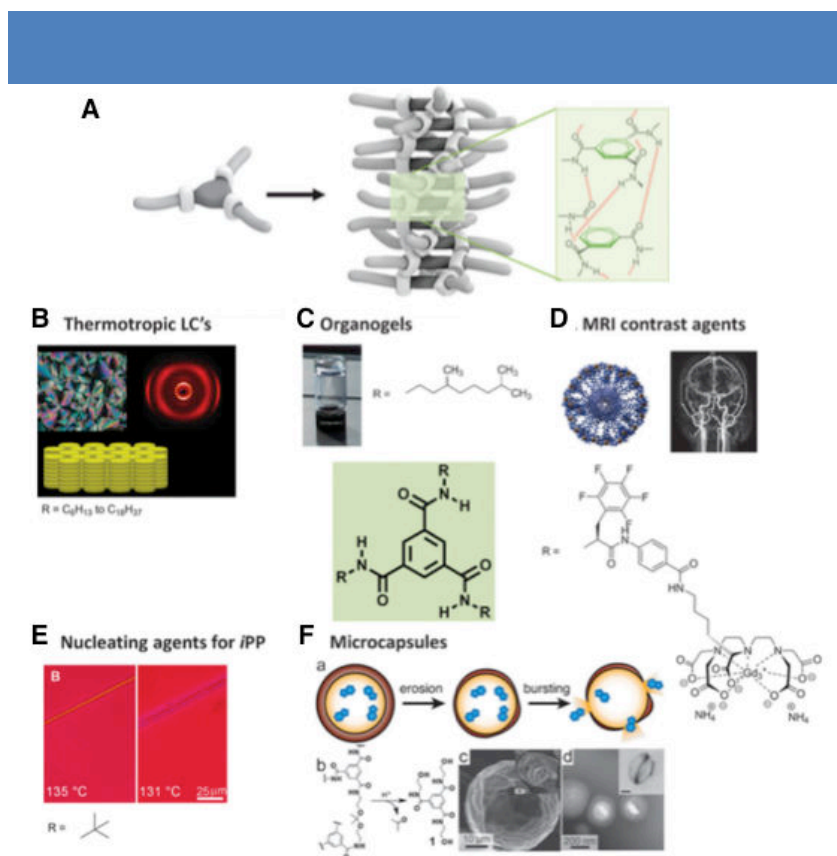


Figure 18 | Self-assembly from 1,3,5 benzene tricarboxamide derivatives (a). Examples of applications of these molecules and their self-assembly as liquid crystals (b), organogels (c), MRI contrast agents (d) nucleating agents (e), and microcapsules (f).³⁶

W. F. Paxton, W. Wu, S. K. Dey, A. C. Fahrenbach, J. R. Guest, H. Mohseni, L. X. Chen, K. L. Wang, J. F. Stoddart and S. I. Stupp, *Nature*, **2012**, *488*, 485 - 488.

³⁵ S. K. Park, S. Varghese, J. H. Kim, S. Yoon, O. K. Kwon, B. An, J. Gierschner and S. Y. Park, *J. Am. Chem. Soc.*, **2013**, *135*, 4757.

³⁶ Cantekin, S.; de Greef, T. F. A.; Palmans, A. R. A., *Chem. Soc. Rev.*, **2012**, *41*, 6125-6137.

v) Mechanisms of Supramolecular Polymerization

Polymerization involving covalent bond formation is kinetically determined due to the activation barrier of the backward depolymerization being much larger than the forward polymerization. As a result, dilution or heating will not change the degree of polymerization. Supramolecular polymerization, on the other hand, is a thermodynamically controlled process due to the reversibility of the interactions holding the polymer together, i.e. one can go ‘backwards’ and depolymerize the chain after it has been formed. Therefore, thermodynamic forces, such as the concentration, temperature, and pressure, directly control the extent of polymerization. The most general case is that of supramolecular polymerization under dilute conditions with a single ditopic monomer capable of non-covalent association. There are three major growth mechanisms: isodesmic, ring-chain, and cooperative growth which will be explained in detail (figure 19).⁹

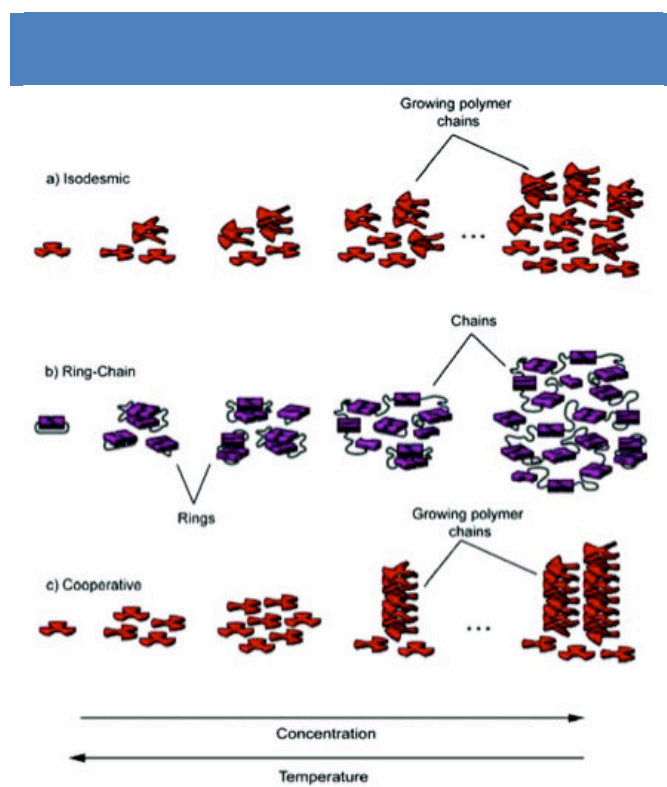


Figure 19 | The three growth mechanisms of supramolecular polymers: isodesmic (a), ring-chain (b), and cooperative (c).³⁷

The *isodesmic* assembly process is represented by the reversible formation of a single noncovalent bond, which is kinetically and thermodynamically identical at all steps in the polymerization process (Figure 20). This implies no fundamental change in the reactivity of the functional group due to incorporation within the supramolecular structure. Importantly,

there is no competing cyclization pathway either. An isodesmic polymerization pathway is characterized by a single binding constant for each step in the assembly pathway. The successive addition of monomers to the growing chain results in a continual decrease in the free energy, which implies that the affinity for a monomer attaching to the end of the chain is independent of the length of the chain. This represents the idealized case, and therefore there may exist some kinetic barriers in the free energy landscape. Additionally, the previous statements also imply the lack of a critical concentration or temperature for assembly. Several further important implications of this mechanism are also worth mentioning. The first is that only at very high equilibrium constants are large polymers obtained. For example, in dilute solutions ($c < 1 \text{ M}$) an equilibrium value on the order of 10^6 M^{-1} is needed in order to form polymers with a high degree of polymerization. Another result is that the monomer always exists in solution simultaneously with polymers of varying lengths. Finally, the polydispersity index grows steadily to a value of 2, while the size distribution in the high molecular weight limit corresponds to a broad exponential distribution.

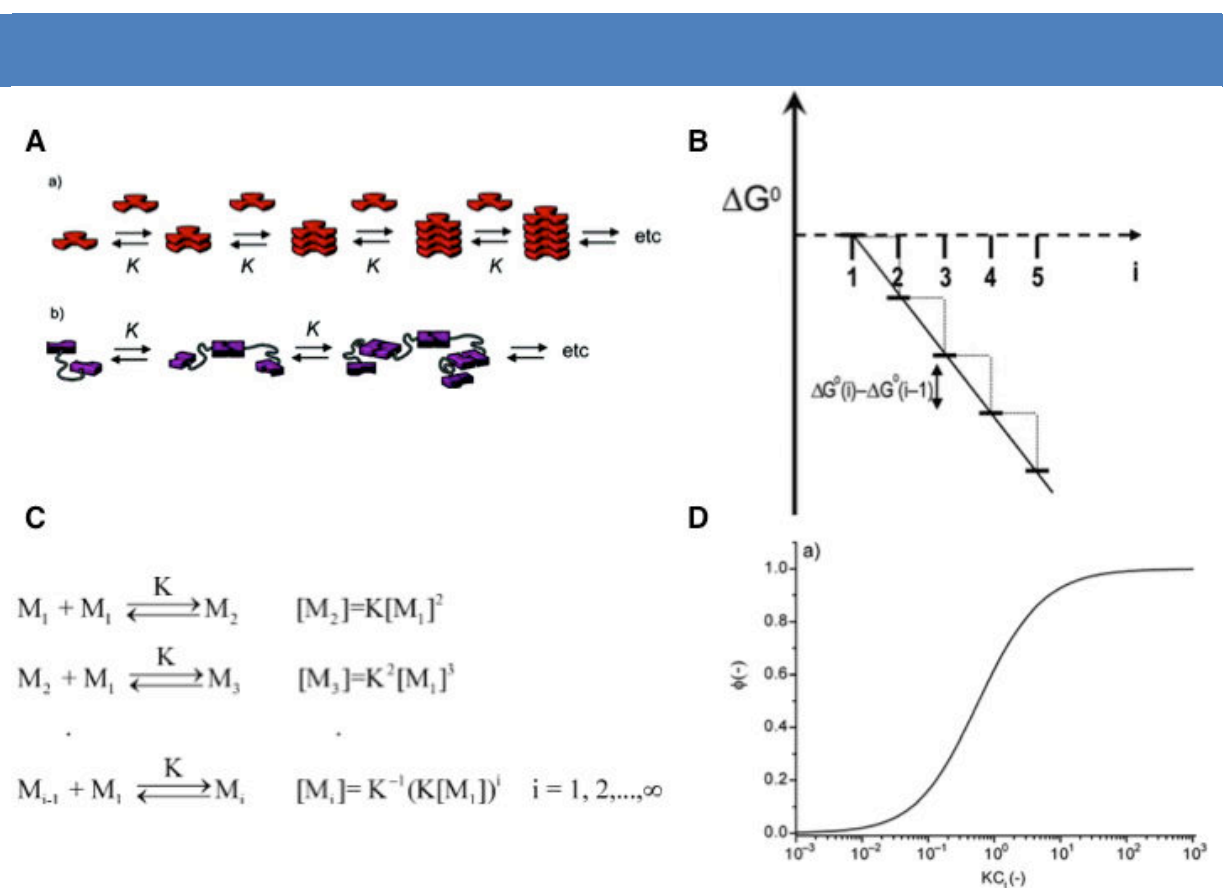


Figure 20 | Schematic representing isodesmic supramolecular polymerization (a) between a rigid discotic molecule (top) and a flexible bifunctional monomer with two binding groups (bottom). Energy diagram demonstrating the ‘downhill’ energetics of the isodesmic mechanism (b). The abscissa represents the size of the oligomer and the ordinate represents the free energy. Scheme of the equilibrium constants for each step, which should be equivalent (c). Fraction of polymerized material as a function of concentration.⁹

The second supramolecular polymerization mechanism is called the *ring-chain mechanism*. Fundamentally, this is a reversible polymerization of a ditopic monomer wherein the linear pathway and a cyclization pathway are in equilibrium with each other. In contrast to covalent polymerization, macrocyclizations occur under thermodynamic control due to the fast association/dissociation equilibrium. This is schematically represented in figure 21. An important concept in this mechanism is the idea of the effective concentration in terms of one chain end being in proximity to the other chain end. Theoretically, a Gaussian distribution of cyclized chains is predicted in relationship to the size of the macrocycle. This contribution can be quantified as the effective molarity (EM):

$$EM = \frac{K_{intra}}{K_{inter}} \quad (2)$$

in which K_{inter} (M^{-1}) is the association constant for an intermolecular reaction and K_{intra} is the dimensionless equilibrium constant for the intramolecular reaction. Furthermore, when the chain separating the two groups is strainless, the EM represents a pure entropic measurement.³⁷ In supramolecular polymerization, the EM represents the concentration below which cyclization is favored, and above which linear polymerization is favored (see Figure 21D for graphical depiction).

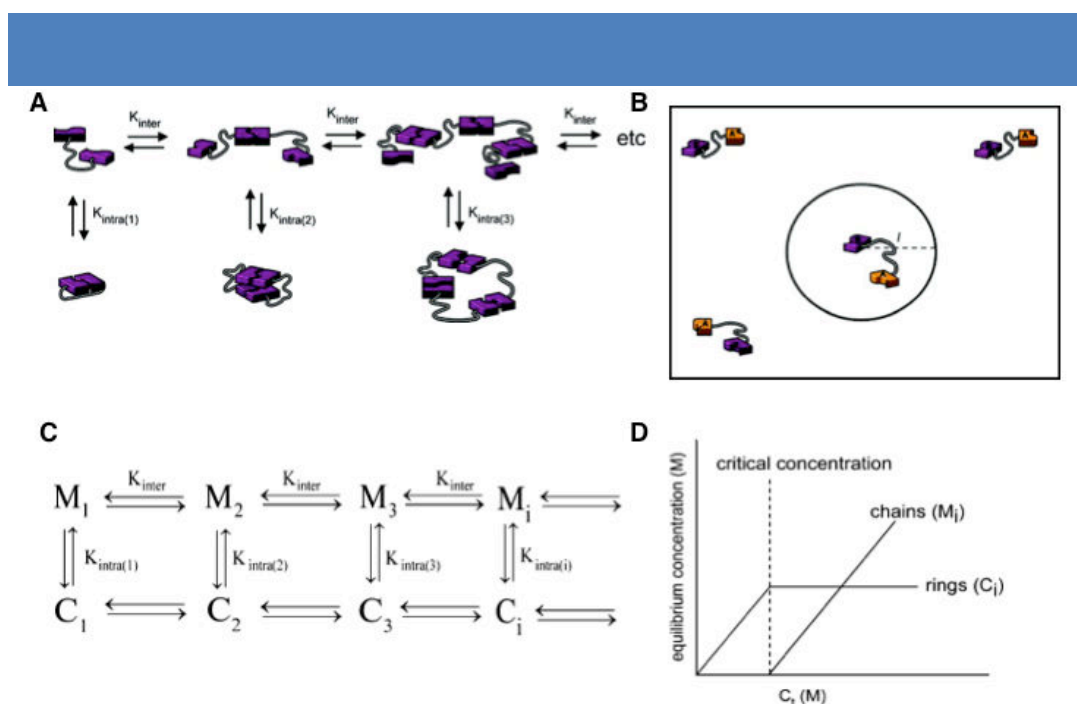


Figure 21 | Schematic of the ring-chain polymerization mechanism (a). Graphical depiction highlighting the effective molarity (EM) concept (b). State changes and the corresponding equilibrium constants (c) as well as the critical concentration concept (d).³⁷

³⁷ Hamacek, J.; Borkovec, M.; Piguet, C. *Dalton Trans.*, **2006**, 1473 -1477.

The final supramolecular polymerization measure is the *cooperative* supramolecular polymerization mechanism (Figure 22). The first variety is a *cooperative nucleated* mechanism. This occurs in two steps, the first being an ‘uphill’ nucleation phase, which is followed by a ‘downhill’ elongation phase. The nucleation phase involves the spontaneous association of monomers in solution which is an energetically unfavorable process. Indeed, during this mechanism, the nucleated proto-polymer is the least stable and least prevalent species in solution, thereby acting as the kinetic bottleneck towards polymerization. There are three criterion which distinguish nucleation-elongation from isodesmic polymerization: (1) the presence of a time-dependent lag in the formation of the supramolecular polymer, (2) the lag can be removed by seeding the monomer solution with preformed nucleus, and (3) there is a critical concentration/temperature where the monomer is in equilibrium with the polymer.³⁸

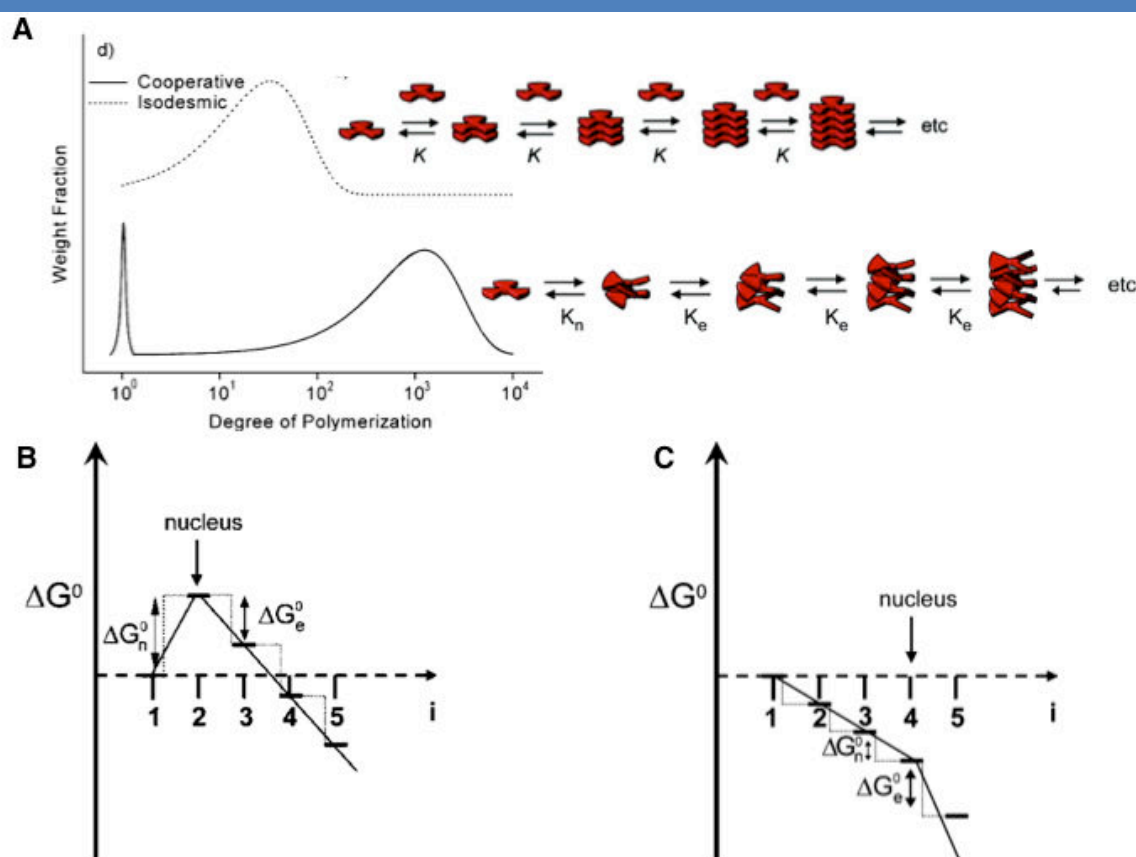


Figure 22 | Distribution of aggregate sizes as well as a general schematic comparing isodesmic and cooperative polymerization mechanisms (a). Energetic landscape of cooperative nucleated (b) and cooperative downhill supramolecular polymerizations (c).⁹

³⁸ Frieden, C. *Protein Sci.* **2007**, *16*, 2334 - 2339.

A *cooperative downhill* supramolecular polymerization does not have an initial increase in the Gibbs free energy, but instead is characterized only by a lower association constant during the initial growth phase, followed by an elongation phase with a higher association constant. Thereby, the fundamental difference with the cooperative nucleated mechanism is that the monomer is the highest energy species (as opposed to the nucleus). The two energy diagrams are depicted in figure 22. The distinction between the two mechanisms is concentration dependent and a nucleated cooperative polymerization can become a downhill polymerization at high enough monomer concentrations. Therefore, concentration dependent kinetic experiments are required in order to differentiate the mechanisms³⁹ ultimately revealing that the nucleus in the downhill mechanism is a stable species with respect to the monomer, whereas this is not the case with the nucleated mechanism. The mass distribution of cooperative polymer formation reveals a large monomer population and an exponential polymer size distribution. The isodesmic model on the other hand leads to a much smaller monomer population in solution.

³⁹ Powers, E. T.; Powers, D. L. *Biophys. J.* **2006**, *91*, 122 - 126.

2. Photonics and Plasmonics

a) Introduction

Current computer architecture relies on the use of semiconducting components to build devices that can carry out information processing through electronic signals. The current paradigm is rapidly reaching its fundamental limits, which requires the search for novel paradigms for information processing reliant upon materials used in unconventional architectures. One of the possible solutions is the replacement of electronic signals with light.⁴⁰ However, a major technological hurdle is the integration and miniaturization of photonic materials. Photonics, broadly defined, deals with the manipulation of light through the interaction with materials. Additionally, at the nanoscale, the diffraction limit of light in dielectric media does not allow for the localization of electromagnetic waves at subwavelength scales. Not all is lost, as a possible way around this seemingly insurmountable challenge involves the use of materials with negative dielectric permittivity (i.e. containing metallic electrons) in which electromagnetic energy can be confined to the nanometer scale. The field dealing with the interaction of light with metallic electrons is known as plasmonics. Metallic structures have the capability of sustaining surface plasmon-polariton modes ('plasmonic modes') at the interface due to the coherent oscillations of the electrons in the material.⁴¹ The possibility of using these modes to guide electromagnetic radiation on the nanometer scale, and the subsequent explosion of research in these materials, started in 1997 with two papers highlighting the theoretical possibility for the subdiffraction properties.^{42,43} This provides the fundamental theory for developing interconnects for highly integrated optical circuits on the subwavelength (nanometric) scale.

b) Waveguides

Photonic waveguides have been demonstrated with at least five distinct classes of materials: (1) metallic-plasmonic waveguides, (2) inorganic-semiconductor waveguide, (3) polymer-dielectric waveguides, (4) photonic crystal waveguides, and (5) organic waveguides.⁴⁴ We will limit the focus of this short background to (1) metallic-plasmonic waveguides and (5) organic waveguides as they are the most relevant to the research results

⁴⁰ Gramotnev, D. K.; Bozhevolnyi, S. I., *Nat Photon* **2010**, *4*, 83-91

⁴¹ Barnes, W. L.; Dereux, A.; Ebbesen, T. W., *Nature* **2003**, *424*, 824-830.

⁴² Takahara, J., Yamagishi, S., Taki, H., Morimoto, A. & Kobayashi, T., *Opt. Lett.*, **1997**, *22*, 475-477.

⁴³ Nerkararyan, K. V., *Phys. Lett. A*, **1997**, *237*, 103-105.

⁴⁴ Chandrasekar, R., *Phys. Chem. Chem. Phys.* **2014**, *16*, 7173-7183.

presented later in the text.

i) Plasmonic Waveguides

Extended metallic structures (as opposed to metallic nanostructures to be described in the following sections) exhibit propagating surface plasmons (movement of unbound metallic electrons) along the surface in the form of charge-density waves. The surface plasmon wavevector may be defined as

$$k_{sp} = k_0 \sqrt{\frac{\varepsilon_d \varepsilon_m}{\varepsilon_d + \varepsilon_m}} \quad (3)$$

where k_{sp} is the wavevector of the surface plasmon mode (with momentum $\hbar k_{sp}$), k_0 is the wavevector of the free space photon (with momentum $\hbar k_0$), ε_d is the permittivity of the dielectric and ε_m is the permittivity of the metal. Two important consequences of this relation are the momentum mismatch between the free-space photon and the surface plasmon as well as the necessity of having a metallic (negative permittivity).³⁷ Additionally, the propagation length of the surface plasmon mode may be determined by

$$\delta_{SP} = \frac{1}{2k_{sp}''} \quad (4)$$

where k_{sp}'' is the complex component of the surface plasmon wavevector. This is directly related to the imaginary part of the permittivity and therefore represents losses in the material due to absorption processes.³⁷ Importantly, metallic nanowires with micron length dimensions and nanoscale transverse dimensions exhibit subwavelength lateral confinement, making possible the ability to guide light at smaller than optical wavelength dimensions (Figure 23). In contrast, dielectric waveguides, once they reach the diameter of the incident light begin to increase the electromagnetic mode size resulting in deeper and deeper penetration into the surrounding medium. Subwavelength confinement is not observed in this instance. Metallic nanowires may be produced by either lithographic methods or by chemical methods. Interestingly, chemical methods have an advantage because they produce monocrystalline wires as opposed to polycrystalline wires obtained by the lithographic method. The monocrystalline wires display enhanced waveguiding properties over the crystalline ones. The most common materials used are gold and silver, with silver presenting the advantage of having lower optical losses.

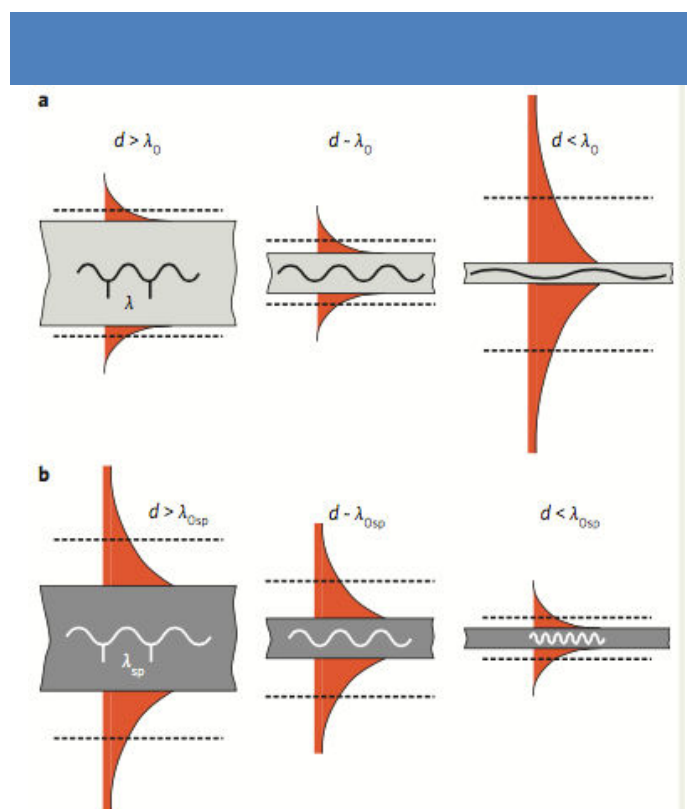


Figure 23 | Typical field structures, localization, and wavelengths of fundamental waveguiding modes in dielectric waveguides (a) and metallic waveguides (b).⁴¹

Plasmons in nanowires are launched by illuminating one end of the structure with a focused laser beam or an evanescent field (in the form of a nanoparticle, quantum dot, or excited state molecular species). Symmetry breaking at the nanowire ends allows a conversion between photons and plasmons.⁴⁵ Propagating plasmons are damped by absorption in the metal. For efficient plasmon propagation in waveguides of sufficiently short length, there is an observable output at the distal end of the nanowire. However, due to reflection at the nanowire tip, output at the end of the waveguide is not necessarily an accurate indication of plasmon propagation efficiency. The emitted intensity, I_e , should behave as follows:

$$I_e = I_0 C(d) e^{-L/r(D,d)} \quad (5)$$

where I_0 is the incident light intensity at the nanowire end, $C(d)$ is incoupling efficiency, D is the nanowire diameter, and d is the thickness of the spacer layer between the nanowire and the substrate. This allows the determination of the damping as a function of nanowire width and spacer thickness. Figure 24 demonstrates the ability to couple an incident light to the plasmons in the metal at various defects in the nanowire, including the nanowire end, a kink in the middle of the nanowire, and a metallic nanoparticle adjacent to the nanowire. This

⁴⁵ Knight, M. W.; Grady, N. K.; Bardhan, R.; Hao, F.; Nordlander, P.; Halas, N. J., *Nano Lett.* **2007**, 7, 2346–2350.

coupling leads to light propagation and output at the distal end (or defect) of the nanowire. No waveguiding effect is observed if the laser is focused directly on top of the nanowire, away from defects.

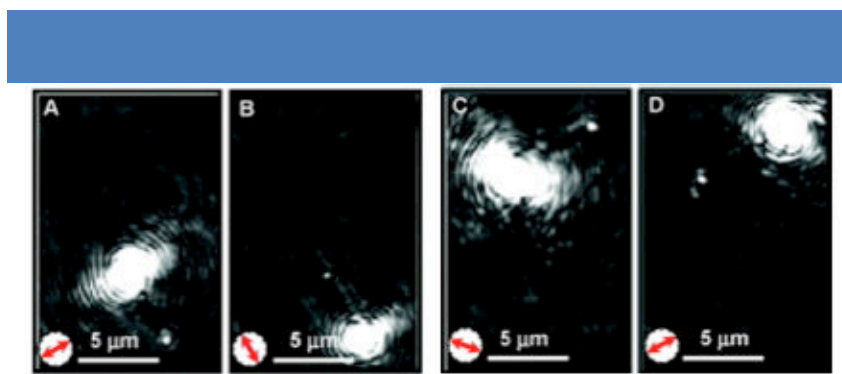


Figure 24 | Plasmon coupling in a kinked nanowire at defects along the nanowire. Coupling at a nanoparticle adjacent to the nanowire (a), at the nanowire end (b), at a kink in the nanowire (c), and at the other end of the nanowire showing an output at the nanowire kink (d).⁴⁶

Additional techniques for detecting plasmonic modes include scanning near-field optical microscopy (SNOW), photoemission electron microscopy, electron energy loss spectroscopy, and cathodoluminescence imaging. While powerful techniques, they are also intensive techniques that need to be done with specialized equipment not readily available at most research institutes. Therefore, several far-field methods have been developed which require less specialized equipment to perform. These methods involve converting the propagating plasmon modes into a readily detectable signal easily detected by far-field methods. These methods include the use of fluorescent molecules or quantum dots placed within the evanescent field of the nanowire thereby resulting in a photobleaching effect upon coupling to the plasmons. Figure 25 shows the ability of quantum dots covering a silver nanowire to allow visualization of the plasmonic near-field. Excitation is performed at one end of the nanowire which results in an output at the distal end of the wire, demonstrating the waveguiding properties. Furthermore, excitation of the quantum dots with the evanescent (near-field) of the propagating plasmons within the nanowire allows a visualization of the local electric field intensity. The fact that an output is still observed at the distal end even though the near-field appears to collapse towards the middle of the nanowire is explained by the excitation of multiple plasmonic modes within the nanowire by the incident light. This multimodal waveguiding results in a fast dissipation and quenching of the fundamental mode, while higher order modes can propagate through the wire. Additionally, there is a polarization dependence of the plasmon propagation. An incident light parallel to the nanowire length couples to the azimuthally symmetric $m = 0$ fundamental plasmonic mode, while coupling to

the $m = 1$ antisymmetric mode is expected for polarization perpendicular to the wire.⁴⁶

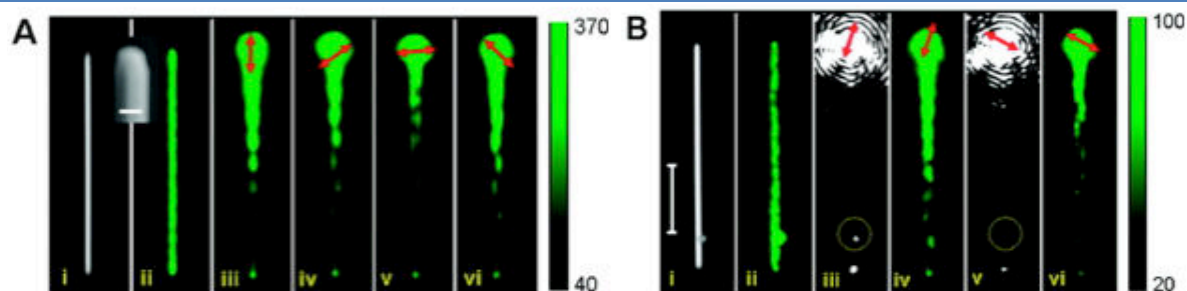


Figure 25 | Quantum dot emission due to plasmons launched at one end of a Ag nanowire with a 632.8nm laser. (A) (i) Optical image of a NW and a SEM image of a typical NW coated with 30 nm Al_2O_3 (inset). (ii) The QD emission image with wide field excitation. (iii–vi) QD emission images for different incident polarizations. (B) (i) Optical image of a NW-NP system. (ii) The QD emission image with wide field excitation. (iii) Scattering image. (iv) QD emission image corresponding to (iii). (v,vi) Scattering and QD emission images for a different polarization. The scale bar is 200 nm in Ai, and 5 μm in Bi. The red arrows indicate the laser polarization. To enhance the contrast, we use a green color scale to show the intensity distribution of the QD emission. The color scales on the right corresponds to the QD emission images with the excitation light focused on the top ends of the wires.⁴⁷

Bleach-imaged plasmon propagation (BIIPP) is a fluorescence technique that works by imaging the photobleaching of dye molecules adjacent to the plasmonic structure due to near-field coupling with the plasmonic modes (Figure 26).⁴⁷ By taking the fluorescence spectrum over the entire crystal and comparing it with the non-photobleached spectra, one can create a ‘map’ of the plasmon propagation through the nanowire. This technique is able to reveal essentially the same information as the previous technique with quantum dots.

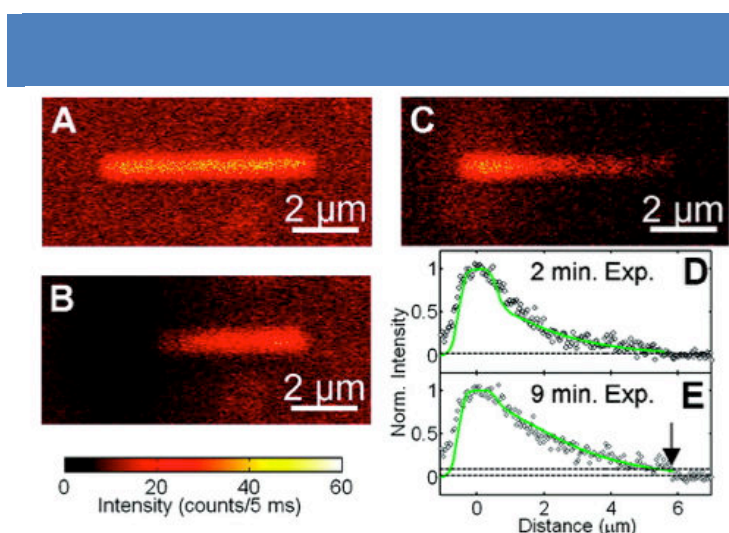


Figure 26 | Bleach-imaged Plasmon Propagation (BIIPP). Confocal fluorescence images recorded before (A) and after (B) continuous excitation of the left NW end for 9 min with a power of 40 nW. (C) Difference image generated by subtracting (B) from (A). (D) Photobleaching as a function of distance

⁴⁶ Fang, Y. R.; Li, Z. P.; Huang, Y. Z.; Zhang, S. P.; Nordlander, P.; Halas, N. J.; Xu, H. X., *Nano Lett.* **2010**, *10*, 1950–1954.

⁴⁷ Solis, D.; Chang, W.-S.; Khanal, B. P.; Bao, K.; Nordlander, P.; Zubarev, E. R.; Link, S., *Nano Lett.* **2010**, *10*, 3482–3485.

along the nanowire.⁴⁸

Beyond demonstrating plasmonic waveguiding, active nanophotonic devices have been created from plasmonic nanowires with various geometrical configurations. In a branched configuration, plasmon propagation along the various branches is controlled by the amplitude and phase at the branch point. Additionally, the plasmons may be rerouted and modulated upon the application of a second laser input. In the example in figure 27, the y-shaped design allows for the combination of two separate plasmonic modes at inputs I1 and I2 with a single output at O. Changing the relative phase of the two incident beams leads to constructive or destructive interference of plasmons as they meet at the junction point. A modulation factor of 18 could be achieved by changing the phase difference between the incident lasers while keeping the polarization and intensities equal. This allows the formation of a plasmonic modulator where the output can be carefully controlled due to the combinations of the inputs.

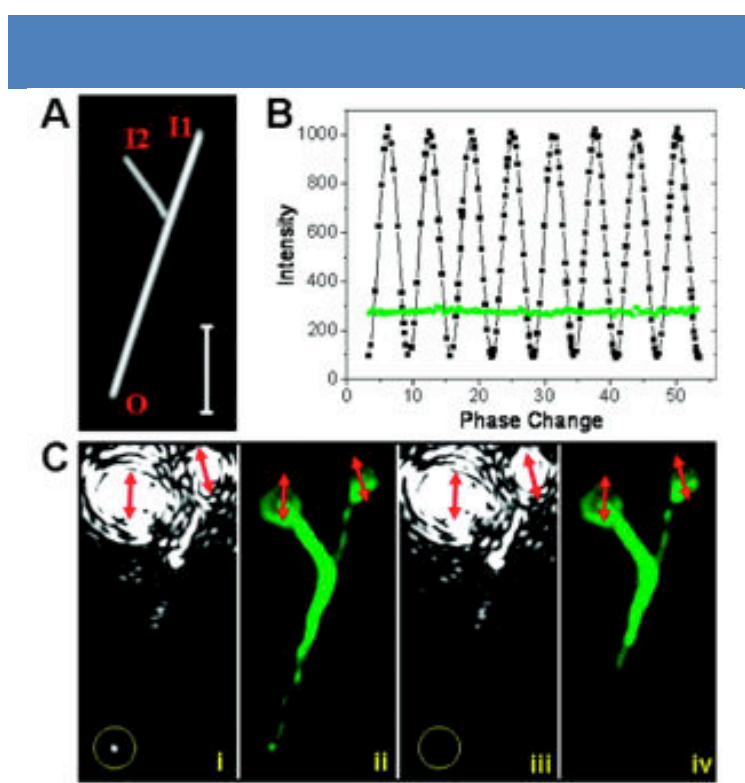


Figure 27 | (A) Optical image of a simple two-nanowire network composed of a primary nanowire and a converging secondary input nanowire. (B) Scattering intensity at output O as a function of optical phase delay when input is either I1 or I2 (green); scattering intensity at output O as a function of optical phase delay for both I1 and I2 inputs (black). (C) (i,iii) Scattering images for the case of two inputs I1 and I2, but with differing phase change. (ii,iv) QD emission images corresponding to i and iii. The red arrows indicate the polarization of the input excitation laser. The Al_2O_3 thickness is 30 nm, and the scale bar is 5 μm .⁴⁸

Additionally, the formation of plasmonic routers has been demonstrated by changing the

incident polarization on a plasmonic nanowire that has a junction and two outputs (the reverse configuration as above). By combining the router and modulator concepts, a complete set of plasmonic logic circuits can be realized, as is demonstrated in figure 28.

AND				
OR				
XOR				
NOT				
NAND				
Adder				

Figure 28 | Possible optical logic operations on nanowire networks using the router and modulator paradigm.⁴⁸

ii) Organic Waveguides

Organic waveguides function via either *passive* or *active* waveguiding mechanisms.⁴⁵ *Passive waveguiding* functions via the internal reflection mechanism at the interface between the waveguide and the environment. As such, it requires a waveguiding material with a higher refractive index than the surrounding environment. Additionally, the wavelength of the light being waveguided should be in a region where the material does not absorb, otherwise there would be large optical losses. The *active waveguiding* mechanism on the other hand functions via the photoluminescent mechanism. In this mechanism, the waveguide is composed of organic chromophores that are closely stacked together. The incident laser induces a local excited state on the wire that is then transferred along the wire due to resonance energy transfer in the form of diffusing exciton-polaritons.

An example is displayed in figure 29, where two nearly identical molecules, 2-acetyl-6-dimethylaminonaphthalene (ADN) and 2-acetyl-6-methylaminonaphthalene (AMN)

crystallize into rods or sheets with overlapping naphthalene cores.⁴⁸ The photoluminescence mechanism is responsible for waveguiding along the fiber direction. As one can see from image D, that as the incident laser is moved along the crystal (at 6, the laser is on the lefthand side of the crystal, from 5 to 1 it moves towards the right) there is output at both ends of the crystal. This behavior is in contrast with plasmonic waveguides, where the light can only couple and be guided at defects in the structure. Additionally, the formation of platelets leads to two-dimensional directional waveguiding (Figure 29h).

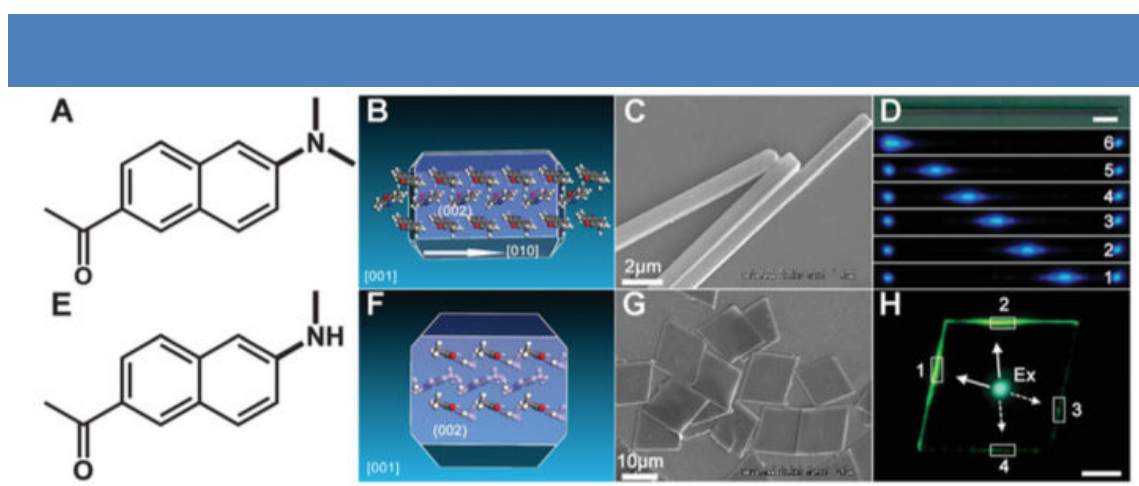


Figure 29 | Assembled materials with 1D and 2D structures obtained through molecular design. (A, E) Molecular structures of ADN and AMN, respectively. (B, F) Predicted growth morphologies based on the attachment energies of ADN and AMN molecules. (C, G) SEM images of 1D nanowires aggregated from ADN and 2D rhombic plates from AMN molecules. (D, H) Distinct waveguide behaviors of 1D and 2D structures. Scale bars in D and H are 5 nm and 10 nm, respectively.⁴⁸

Separately, Yao and coworkers demonstrated the ability to produce heterogeneous structures through a combination of competing assembly interactions.⁴⁹ First, a tubular organic crystal was grown using 2,4,5-triphenylimidazole (TPI), which can act as a host for the insertion of ‘guest’ molecules. The guest molecules, in this case the sphere-like organometallic complex Iridium(III) bis(2-phenyl benzothiazolato-N,C2’) ((BT)2Ir(acac)) and a planar π -conjugated compound 9,10-bis(phenylethynyl) anthracene (BPEA) incorporate into the structure resulting in segmented structures as demonstrated in figure 30. Due to the geometrical mismatching of the spherical iridium complex, it acts to terminate the crystal growth. Doping with coumarin 6 during crystal growth leads to a donor-acceptor interaction inside the crystal. Upon UV light excitation, both TPI and coumarin 6 could be excited, thereby emitting fluorescence with different colors. Using this structure, a photonic

⁴⁸ Yao, W.; Yan, Y.; Xue, L.; Zhang, C.; Li, G.; Zheng, Q.; Zhao, Y. S.; Jiang, H.; Yao, J., *Ang. Chemie Int. Ed.* **2013**, *52*, 8713-8717.

⁴⁹ C. Zhang, Y. Yan, Y.-Y. Jing, Q. Shi, Y. S. Zhao and J. Yao, *Adv. Mater.*, **2012**, *24*, 1703 - 1707.

triode was designed and successfully tested. Similar to an electronic triode, there exists the optical analogues of source, drain and gate components. The excitation with fixed laser intensity at the left end acts as the source, while the outcoupled light from the right tip is regarded as the drain. The gate beam with different attenuations irradiates at the middle part of the individual tube to control the conducting signal from the source to the drain. The output from the drain gradually changes from blue to red based on the intensity of the laser at the gate.

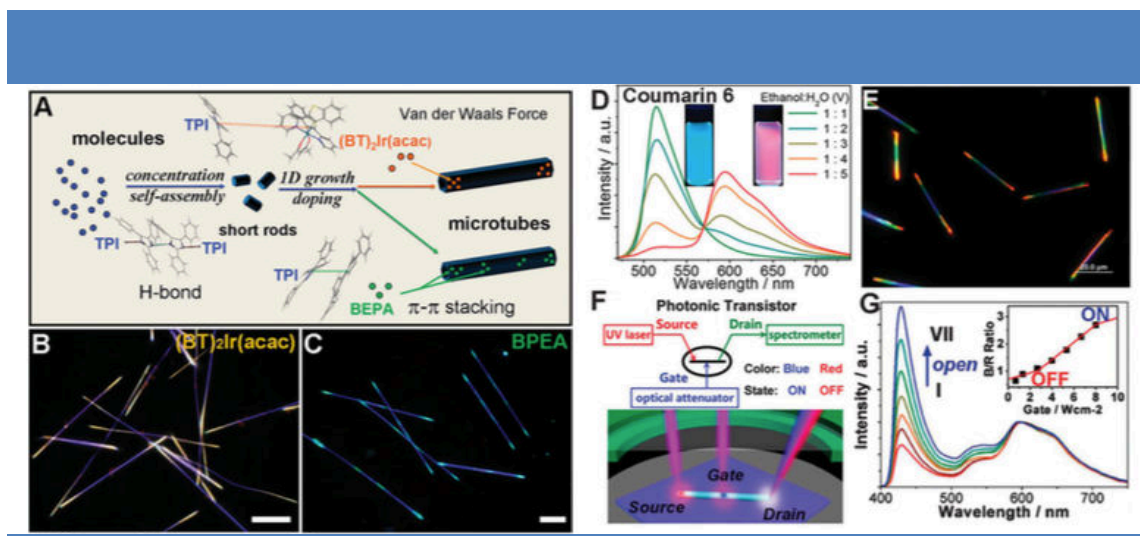


Figure 30 | Formation and optical properties of the gradiently doped 1D nanostructures. (A) Schematic illustration of the formation of doped TPI tubes with different guest molecules. (B, C) PL microscopy images of the triblock and multiblock doped TPI microtubes. (D) Fluorescence spectra of Coumarin 6 aggregates with different contents in the ethanol–water mixture. (E) PL microscopy image of Coumarin 6 doped TPI microtubes. (F) Schematic illustration of the design concept (top) and realization (down) of a photonic transistor in rainbow colored microtubes. (G) Outcoupled emission spectra from the drain port at various gate powers. The inset shows the relationship between blue to red light output ratio and the power of the gate laser. (A–C)⁵¹

c) Plasmonic Nanoparticles

i) Origin of the Plasmonic Response

Plasmonic nanoparticles, such as gold nanoparticles, demonstrate an optical absorption band due to the oscillation of the metallic electrons at a resonance frequency. Due to the size of the nanoparticle being significantly smaller than the wavelength of the incident electromagnetic radiation (more than 10-fold difference), as the electromagnetic wave passes over the nanoparticle the free metallic electrons inside the nanoparticle experience a momentary uniform force in one direction which results in a movement of the electrons along the field lines. As the wave passes over the nanoparticle in time, the electrons inside the

nanoparticle experience an oscillating force. At the appropriate wavelength (resonant wavelength), the electrons become in resonance with the oscillating field leading to coherent oscillations, also known as plasmonic resonance. The response of the material may be described using the dielectric formalism of the optical constants of the material, which allows the prediction of the resonance frequency. In the simplest model, the plasmonic response is depicted as a harmonic oscillator where the resulting dielectric response is given by the Drude formula:

$$\varepsilon(\omega) = 1 - \omega_p^2 / (\omega(\omega + i\gamma)) \quad (6)$$

where γ is the frequency dependent damping, ω_p is the bulk metal plasma frequency, which in turn can be represented by the following equation:

$$\omega_p^2 = 4\pi n e^2 / m_e \quad (7)$$

Here, n is the metal electron density, e the electron charge, and m_e the mass of an electron. For spherical plasmonic nanoparticles, the lowest mode ($l = 1$) is dipolar with energy

$$\hbar\omega = \hbar\omega_p / \sqrt{3} \quad (8)$$

This mode redshifts as particle size increases due to retardation effects of the plasmonic oscillation. Higher order, multipolar modes may also be excited, with the plasmon energy approaching that of a plain plasmonic surface:

$$\hbar\omega = \hbar\omega_p / \sqrt{2} \quad (9)$$

Figure 31 depicts the basic processes which occur when a nanoparticle is experiencing plasmonic resonance. The extinction of incident light is dominated by absorption process with small contributions from scattering events (the figure depicts the relative contribution for a 10 nm gold nanoparticle). Note that, as one would surmise, when the particle size increases, there is increasing contribution from scattering. Critical to the construction of an overall picture of plasmonic resonance is the understanding of the near-field and far-field effects. The near-field, or evanescent field, is the induced electric field around the nanoparticle due to the oscillation of the electrons. This has also been described as virtual photons that instead of propagating into space are emitted and reabsorbed by the nanoparticle. This is in contrast to free photons, which are emitted by the nanoparticle and propagate into space. Importantly, it is by taking

advantage of this near-field that we can realize novel technologies, such as surface enhance Raman scattering detection techniques⁵⁰ or create integrated photonic circuits for the next generation of computing architecture.⁵¹

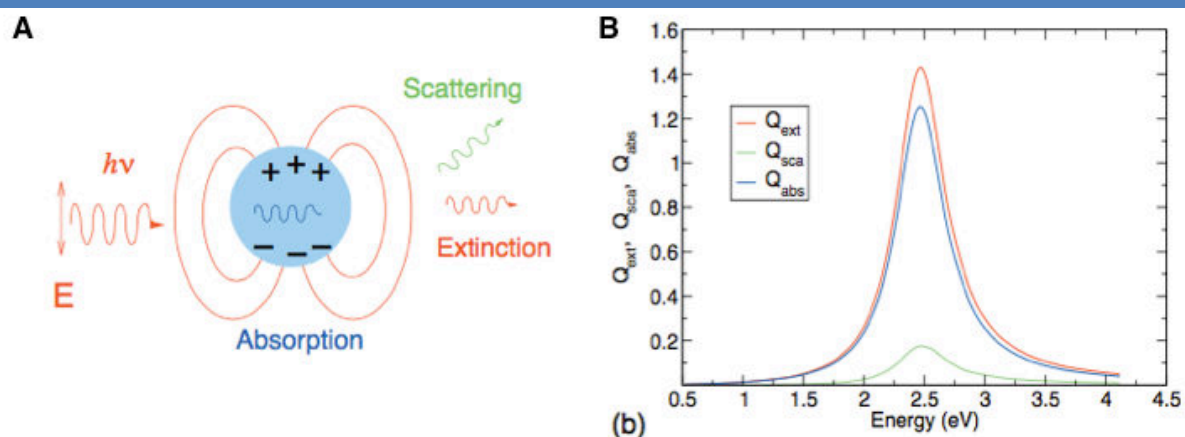


Figure 31 | Schematic of the excitation of the fundamental plasmonic mode in a plasmonic nanoparticle resulting in charge oscillation and the formation of an evanescent near-field depicted by the red circles around the nanoparticle (a). The far-field response is interpreted as extinction of the incident electromagnetic field due to absorption and scattering. Each of the cross-sectional areas is depicted the following graph for a 10nm nanoparticle (b).

ii) Plasmonic Coupling

While the plasmonic properties may be altered by changing the size and shape of the nanoparticles, even more dynamic manipulation of the plasmonic properties can be achieved by placing nanoparticles within the near-field coupling regime of adjacent nanoparticles. The simplest depiction of this effect is the coupling of two nearby oscillators. The interaction energy is given by

$$V \propto p_1 p_2 / r^3 \quad (10)$$

where p_1 and p_2 are the magnitudes of the dipole moments and r is the interparticle distance. At sufficiently close distances, on the order of the radius of the nanoparticles, the coupling energy is large enough to result in a red-shift of the plasmonic absorption band. This has been further developed into the plasmon hybridization theory, wherein constituent plasmon modes in coupled nanostructures hybridize like in molecular orbitals to form new

⁵⁰ I. Schlücker, S., *Angew. Chem. Int. Ed.*, **2014**, *53*, 4756-4795.

⁵¹ Ohtsu, M., *Progress in Nanophotonics I*, Ohtsu, M., Ed. Springer Berlin Heidelberg: 2011; pp 1-58.

hybridized plasmonic modes.⁵² The simplest case is between two adjacent nanoparticles illuminated by light polarized along the interparticle axis, resulting in the hybridization picture depicted in figure 32. This is the plasmonic equivalent of the hybridization of the atomic orbitals of a homogenous diatomic molecule. This plasmonic dimer produces a split in the dipolar plasmon mode of each of the individual nanoparticles, resulting in a lower-energy ‘bonding’ mode and a higher energy ‘antibonding’ mode. These modes display a noticeable difference in their coupling to incident light. The optical properties are dominated by the lower energy mode, which displays mutually aligned longitudinal dipoles, resulting in a large induced dipole over the entire dimer and a strong coupling to the far-field. This mode is also known as the ‘bright’ plasmon mode. In contrast, the antibonding mode displays antialigned dipoles and therefore no net dipole over the dimer system and is therefore incapable of coupling to far-field radiation. This mode is also known as a ‘dark’ or ‘cavity-like’ plasmonic mode. In the limit of small, nearly touching, nanoparticle distances and larger nanoparticles, the higher order modes, such as the $l = 2$ (or quadrupolar) mode are excited as well.

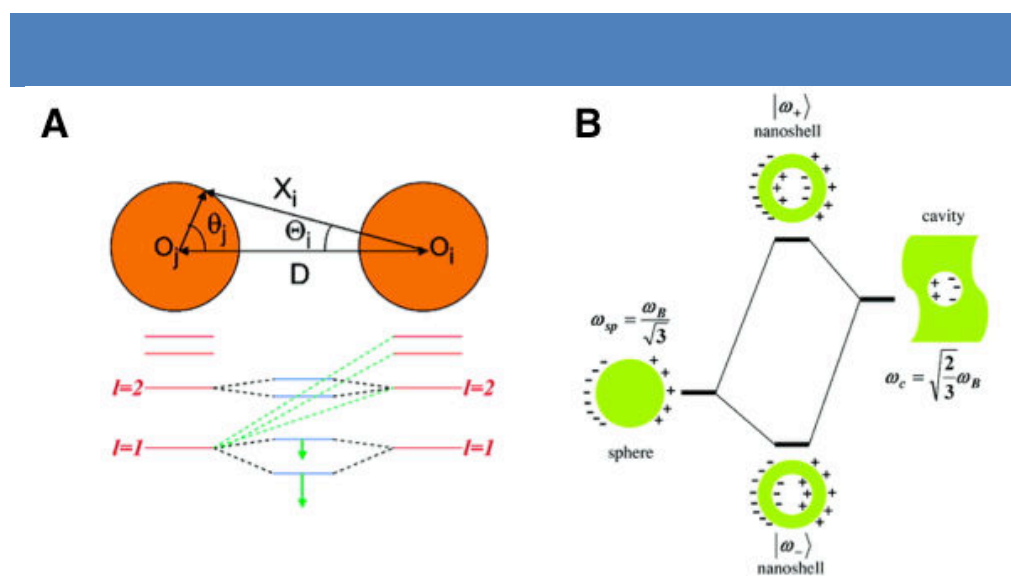


Figure 32 | Schematic of plasmon hybridization between two nanoparticles (a). An energy level diagram describing plasmon hybridization in metallic nanoshells (b).⁵⁴

Another interesting example of plasmonic coupling occurs between two plasmonic rods. Due to the anisotropic nature of the particles, there exist two fundamental plasmonic modes, the transverse mode corresponding to light polarized orthogonal to the long axis of the rod and the longitudinal mode corresponding to light polarized parallel to the long axis of the rod.

⁵² Prodan, E.; Radloff, C.; Halas, N. J.; Nordlander, P., *Science* **2003**, *302*, 419-422.

This leads to an orientational dependence on the nanorod interactions. The figure 33 displays the large change in the plasmonic bonding mode energy as a function of the geometrical arrangement of the nanorods. End-to-end coupling with incident polarization along the interparticle axis leads to a strong red-shift from the uncoupled energy (707 nm uncoupled, 797 nm, coupled). In contrast, side-to-side coupling with the incident light polarized along the long-axis of the nanorod leads to a small blue-shift of the collective plasmon mode (649 nm). In general, rod-rod couplings tend to be weaker than the spherical equivalent, requiring very small interparticle distances (1 – 2 nm) for any effect to be observed.

The case of two parallel rods has also been demonstrated to be important in the design of metamaterials.⁵³ Specifically, the case of two adjacent nanorods aligned in transverse orientation gives rise to in-phase (higher energy) and antiphase (lower energy) dipole oscillations (see figure 33). The configuration of two stacked antiphase nanorods is known to be in “magnetic resonance” because the combination of the currents in the two wires along with the displacement current between the two wires results in magnetic excitation of the magnetic dipole moment of the structure. This results in an optical frequency magnetic response critical for the development of negative refractive index metamaterials. This is one of the fundamental building blocks of metamaterials, along with U-shaped metallic structures and split-ring resonators.⁵⁰

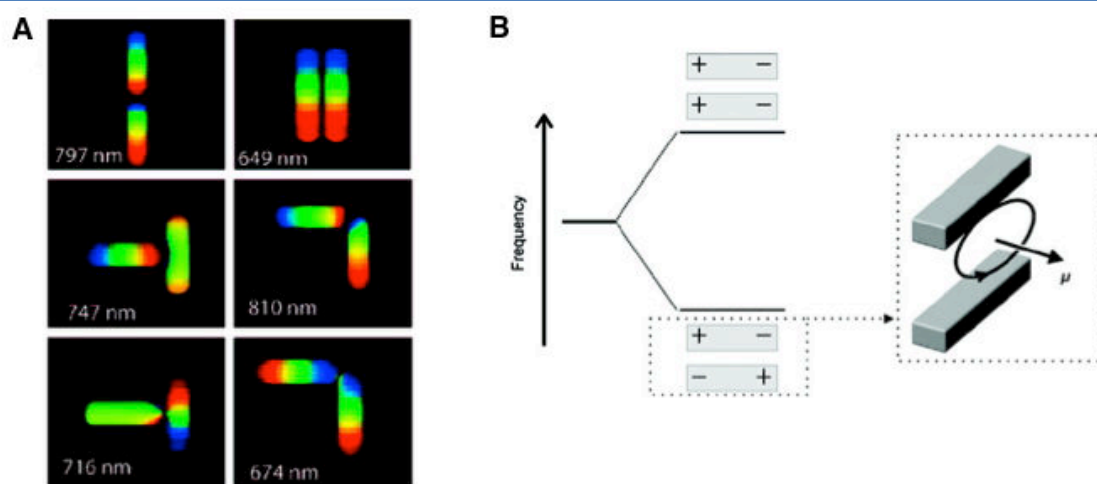


Figure 33 | Calculation of the surface charge density of two coupled nanorods (a). The wavelength shows the resonance wavelength of the coupled mode. Transverse coupling of two metallic nanorods, a fundamental building block of metamaterials (b).⁵⁵

⁵³ Liu, N., Giessen, H., *Angew. Chem. Int. Ed.*, **2010**, *49*, 9838–9852.

Coupling can also be extended to chains of nanoparticles, resulting in extended plasmonic modes, effectively forming plasmonic waveguides from individual nanoparticles.⁵⁴ It has been suggested that by analogy, one is forming plasmonic molecules from plasmonically coupled nanoparticle aggregates due to the hybridization of the plasmonic modes throughout the nanostructure. In figure 34 the plasmonic modes were imaged using the electron energy loss spectroscopy technique. Briefly, this technique is performed in a transmission electron microscope whereby the sample is bombarded with an electron beam. A detector on the other side of the sample beam detects the energy spectrum of the beam. Due to interactions with the plasmons, there is a typical loss of energy between 1 and 3 eV. Due to the extremely high spatial resolution, one can form a ‘map’ of the plasmonic modes around the structures. For the isolated nanoparticle, there is one plasmonic mode, with an even intensity around the edges. When two nanoparticles are brought into close proximity, one can observe the formation of two plasmonic modes, a longitudinal and a transverse one. These modes vary in intensity according to the spatial location on the nanoparticle dimer.

⁵⁴ Barrow, S. J.; Rossouw, D.; Funston, A. M.; Botton, G. A.; Mulvaney, P., *Nano Lett.* **2014**, *14* (7), 3799-3808.

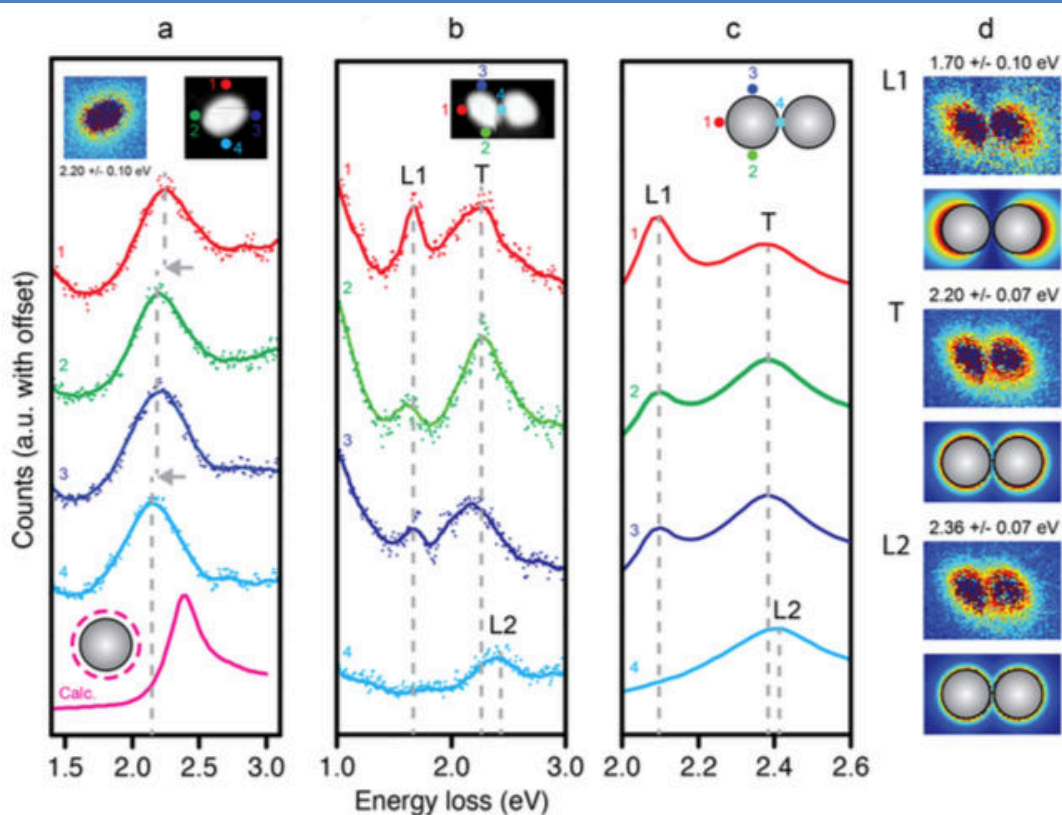


Figure 34 | Electron Energy Loss Spectroscopy (EELS) of a single nanoparticle and (a), a nanoparticle dimer (b), the calculated dimer spectrum (c), and the spatial distribution of the different modes (d).⁵⁶

While there are top-down nanofabrication technologies for creating plasmonic nanoparticle arrangements, such as e-beam lithography, we will highlight bottom-up self-assembly methods. Chemical methods to produce controlled assemblies of plasmonic nanoparticles are a daunting challenge. Homogenous surface functionalization will result in non-specific interactions between the nanoparticles leading to random aggregation. One of the few successful chemical methods so far has been DNA functionalization. This gambit has resulted in the formation of a plethora of structures with well-defined geometries. As an aside note, while one can achieve a variety of geometries with this method, there is no doubt an influence of functionalizing the nanoparticle surface with organic molecules that has scarcely been studied. Figure 35 demonstrates various nanoparticle geometries achievable by DNA-directed assembly methods. DNA directed self-assembly is affected by first functionalizing the gold nanoparticle with a thiolated DNA single-strand. By functionalizing different batches of nanoparticles with complimentary DNA strands and mixing, one can achieve controlled aggregation due to DNA hybridization.

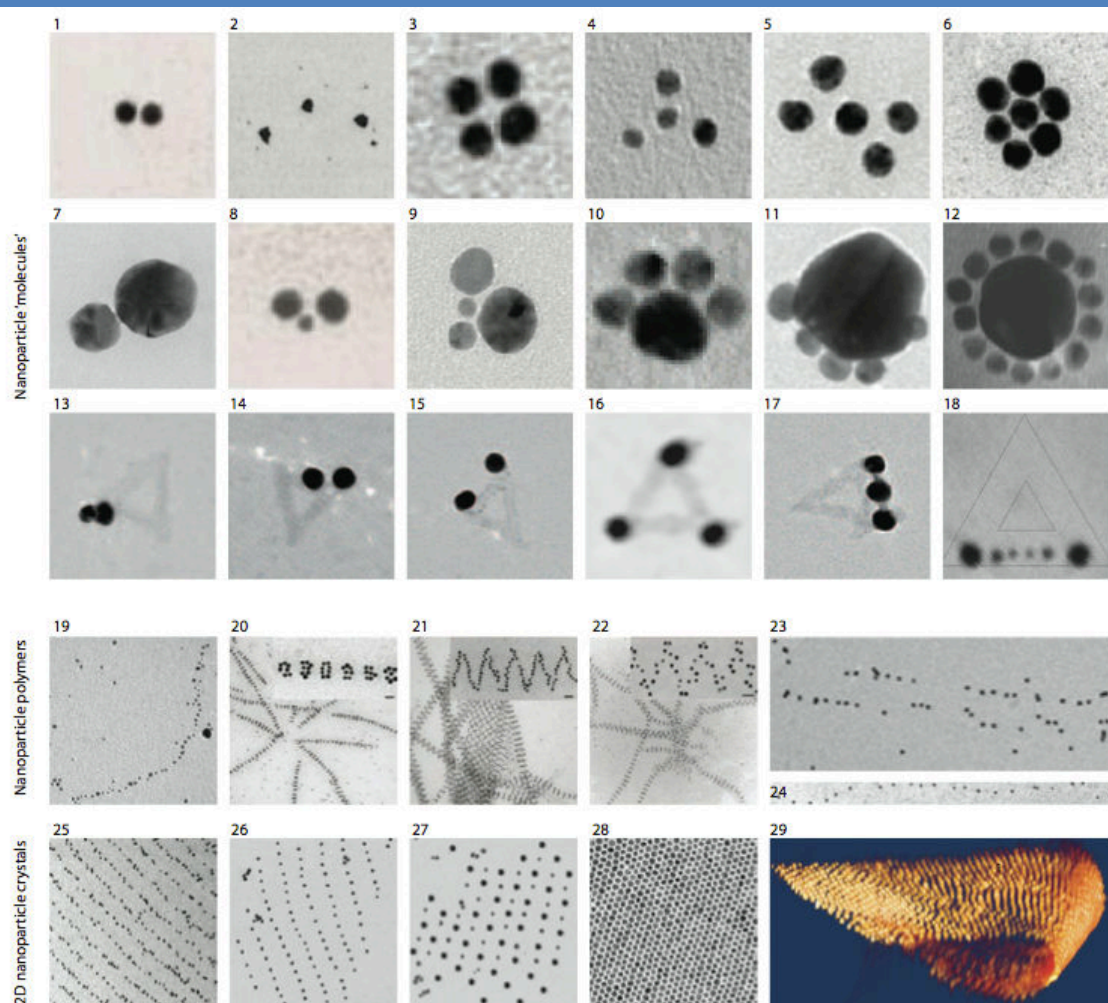


Figure 35 | Survey of the current state of the art in DNA directed self-assembly of plasmonic nanoparticles.⁵⁵

⁵⁵ Tan, S. J.; Campolongo, M. J.; Luo, D.; Cheng, W., *Nat Nano* **2011**, *6*, 268-276.

Chapter II: Supramolecular Self-Assembly And Radical Kinetics In Conducting Self-Replicating Nanowires

1. Introduction

My initial studies started with a project designed to elucidate the complex self-assembly mechanism of the self-assembling triarylamines. As outlined in the introduction, self-assembly processes can be generally broken down into either a cooperative mechanism where the association constants are equal at each step or a nucleation and growth mechanism where the initial nucleation process may be either ‘uphill’ (a net increase in Gibbs free energy) or ‘downhill’ (a net decrease in the Gibbs free energy). From a qualitative standpoint, it seemed likely that we were dealing with a nucleation process due to the light-triggered aspect. The self-assembly process was investigated experimentally through NMR, EPR, and UV/VIS absorbance experiments.

We demonstrate that the self-assembly may be triggered by chemical oxidation and through seeding with a solution of preformed fibers in addition to the light-induced process. In collaboration with two theoretical physicists (Irina Nyrokova and Alexander Semenov), we were able to perform extensive kinetic analysis on the self-assembly process thereby elucidating a unique nucleation and growth mechanism previously unlike any so far reported in the literature. We also elucidate the structure of this unique self-assembly, and demonstrate through theoretical calculations and X-ray diffraction, the formation of a double-columnar structure supported by hydrogen bonding interactions.

2. Synthesis and Self-assembly of Mono-amide Triarylamines

The synthetic route to the mono-amide triarylamine is displayed in figure 36a. Precursor **1** determines the side-chains that are on the triarylamine core. Correspondingly, this precursor may be altered in order to synthesize triarylamines with varying side-chain units. The synthesis of **1**, 1-iodo-4-octyloxybenzene was performed via a Williamson ether synthesis reaction between 4-iodophenol and 1-bromooctane mediated by potassium carbonate in acetone. The deprotonation of the phenol precursor leads to a nucleophilic aromatic substitution on the bromooctane reactant giving the ether product. A quick extraction leads to the product in 90% yield. Next, the triarylamine core was constructed using an Ullman coupling between **1** and 4-nitroaniline. Briefly, the two reactants are mixed with copper (I)

iodide, potassium carbonate, and L-proline and heated for 15 days at 115°C in DMF. Column chromatography afforded the product in 73% yield. From the nitro intermediate **2** to the product **4** we were able to affect a two-step sequence of reduction followed by amination. For the reduction step, **2** was dissolved in a mixture of acetonitrile and ethanol (1:1.2) along with an excess of tin (II) chloride. After overnight refluxing, the product was extracted and quickly worked up to provide the amino intermediate **3** (not shown in the synthetic scheme). The amino intermediate is quasi-stable in air, with oxidation byproducts observable after several days in air. Therefore it is preferable to quickly use the amino intermediate in the following reaction the same day that it is worked up. Alternatively, it may be stored under argon for limited amounts of time. The amidation to the amide product **4** was affected by dissolving the amino intermediate in dichloromethane along with triethylamine on an ice bath and adding dropwise chloroacetyl chloride. After the addition, the reaction temperature was allowed to come to room temperature and then proceed over the course of several hours. After a quick extraction, the product was purified by column chromatography to afford the final product **4** in 95% yield.

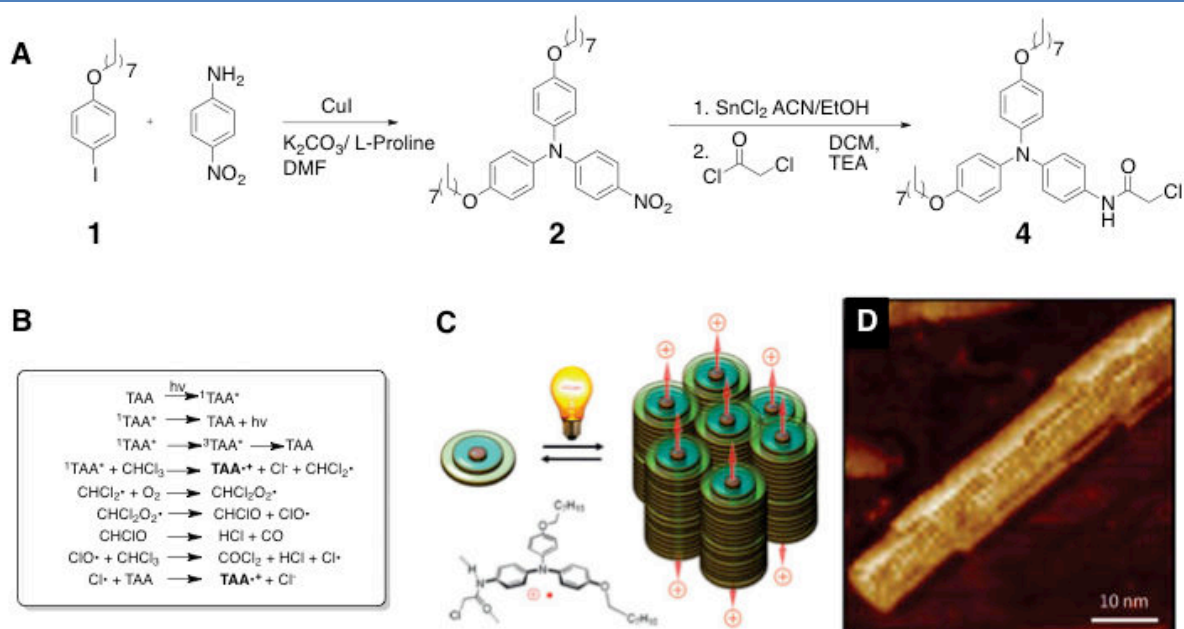


Figure 36 | Synthetic Route to Mono-amide Triaryl Amines (a). Radical cascade reaction upon UV light irradiation in chlorinated solvents leading to the radical triarylamine cation and a chloride counterion (b). Schematic of the light-induced self-assembly process (c). AFM imaging of the triarylamine fibers (d).

Upon light-irradiation in chlorinated solvents, triaryl amines undergo an excited state radical reaction, inducing the formation of the radical cation and a chloride counterion

species.⁵⁶ This process is displayed in figure 36b and is quite critical to the unique self-assembly mechanism of **4**. Upon light-induced irradiation, the molecules form stacks of self-assembled fibers as is displayed in the cartoon in figure 36c. AFM imaging of the self-assembled molecules is shown in figure 36d. Conveniently, the self-assembly process may be followed by NMR spectroscopy as well. In figure 37a we see the NMR spectrum of **4** in chloroform which has been protected from light. The peaks are well defined, as one would expect. However, upon light-induced irradiation, the solution turns a green color indicative of radical cation formation and the aromatic NMR signals disappear. This is one of the methods that we will use to elucidate the self-assembly process in this chapter. Another method that we will use is absorbance measurements. Upon oxidation there is a distinct band that appears at 800 nm, as well as some minor bands around 400 nm and 650 nm. Additionally, electron paramagnetic resonance spectroscopy (EPR) was used to follow the magnetic signal due to the radical cation.

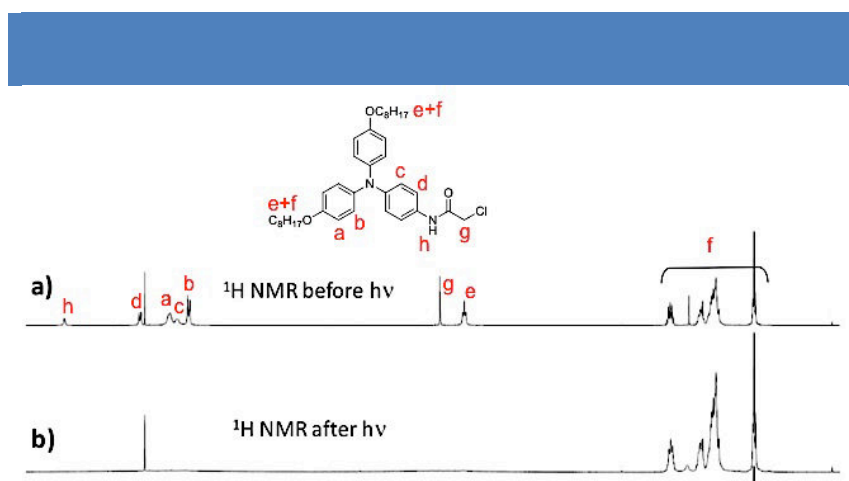


Figure 37 | Disappearance of the NMR signals of the mono-amide triarylamine due to the self-assembly process. NMR spectra before irradiation (a), after irradiation (b).

3. Autocatalytic Self-replication

A qualitative assessment of the self-assembly process displays very fast aggregation kinetics upon irradiation with a 20 watt halogen lamp placed 5 cm from the sample. Irradiation times as short as 5 seconds leads to complete disappearance of the NMR signals by the time the sample is placed in the NMR. By reducing the irradiation time down to 1s, we were able to significantly slow down the self-assembly process. The data is displayed in

⁵⁶ Fitzgerald, E. A.; Wuelfing, P.; Richtol, H. H. *J. Phys. Chem.* **1971**, *75*, 2737–2741.

figure 38a. We see a sigmoidal shaped curve depicting the self-assembly kinetics. As was outlined in the introduction, this is a typical signature of an autocatalytic self-assembly process. The initial lag time lasts for 15 – 20 minutes, during which the initial self-assembly steps occur. The solution is then transformed into the fully self-assembled state after about two hours. We observed the same sigmoidal behavior when the solution was “seeded” with an already fibrillized **4** material, figure 38b. Additionally, the same observation was made upon the addition of catalytic quantities of the chemical oxidant tetrabromoquinone, figure 38c. These observations confirm the idea that while the presence of radicals may trigger the aggregation, the fibrils in **4** solutions are absolutely stable thermodynamically even in the absence of radicals.

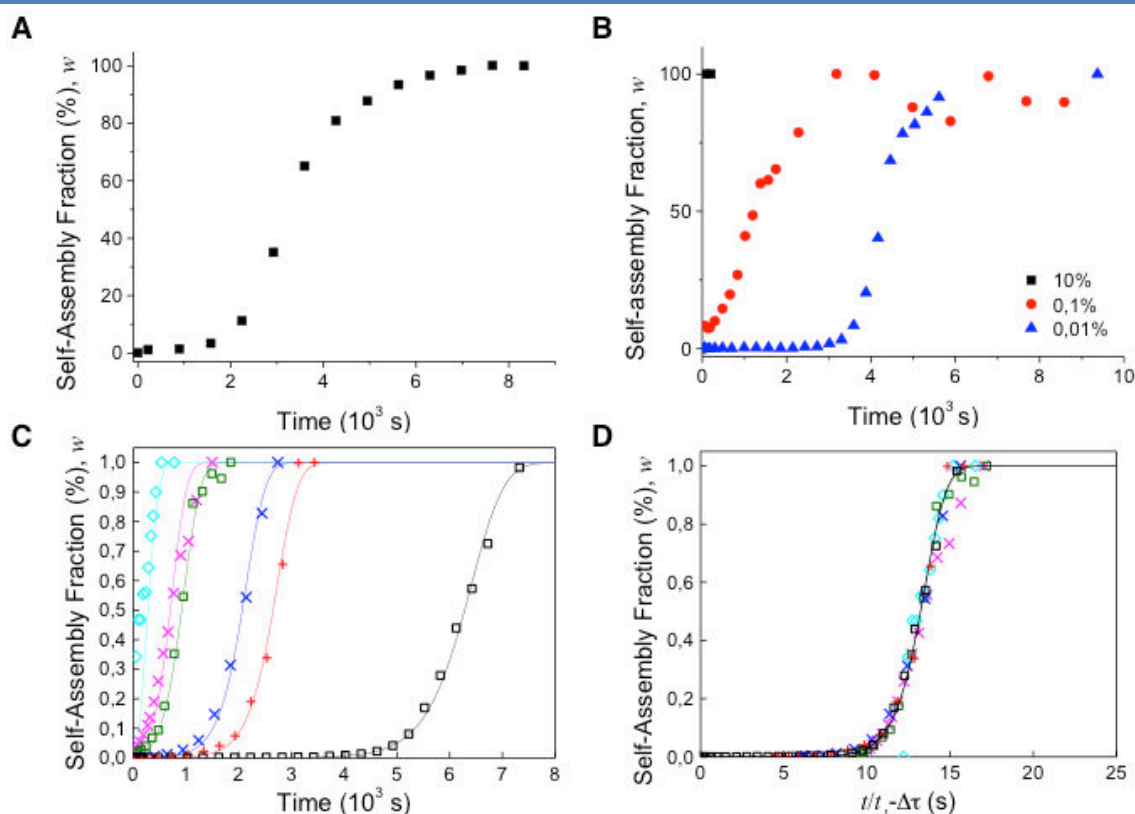


Figure 38 | Self-assembly kinetics as followed by NMR. Light-induced self-assembly after a 1s light pulse (a). self-assembly induced by seeding with preassembled molecules (b). Self-assembly induced by chemical oxidation fit with a master equation (c). Fit of the self-assembly kinetics with the master theory curve (d).

These self-assembly curves are critical for deriving information on the kinetic pathways. The early stages of self-assembly were elucidated through computational modeling. The radicals $\text{TAA}^{\bullet+}$ and oxidant anions form stable charge-transfer (CT) complexes $\text{TAA}^{\bullet+}\text{TBQ}^{\bullet-}$ (Figure 39a) with high dissociation energy, $E_{ca} \approx 58k_{\text{B}}T$, meaning that in practice the

dissociation is prohibited.⁵⁷ Being electric dipoles, the charge-transfer complexes can effectively assemble in supramolecular stacks: the scission energy stabilizing these stacks is $\approx 28k_B T$ for dimers and $\approx 31k_B T$ for long stacks (Figure 39b). Moreover, the initial cation–anion columns attract neutral TAAs at their ends *via* aromatic stacking and H-bond interactions (Figure 39c). The long enough single columns eventually form double columnar (DC) structures (Figure 39d) stabilized mainly by the intercolumnar H-bonding and side-to-side van der Waals attractions (the lateral attraction energy gain is $\approx 14k_B T$ per neutral TAA molecule involved in the H-bonding). The DC aggregates are very stable: they can effectively trap new TAA molecules at their ends (the corresponding energy gain is $E_{as}^{(2)} \approx 18k_B T$) serving as *nuclei* for the further end-growth of the fibrils, Figure 39e. As long as free $TAA^{+}TBQ^{-}$ complexes are still present in the solution, they can also enter into the growing fibrils producing *defects*, which are weak points in the fibril structure (see Figure 39f). On a long time scale it tends to break at a defect (Figure 39g);⁵⁸ the fibril scission energies are $\approx 55k_B T$ and $\approx 41k_B T$, respectively, for the regular double stack and for a defect point (corresponding to $\sim 10^6$ times higher probability to break at a defect).

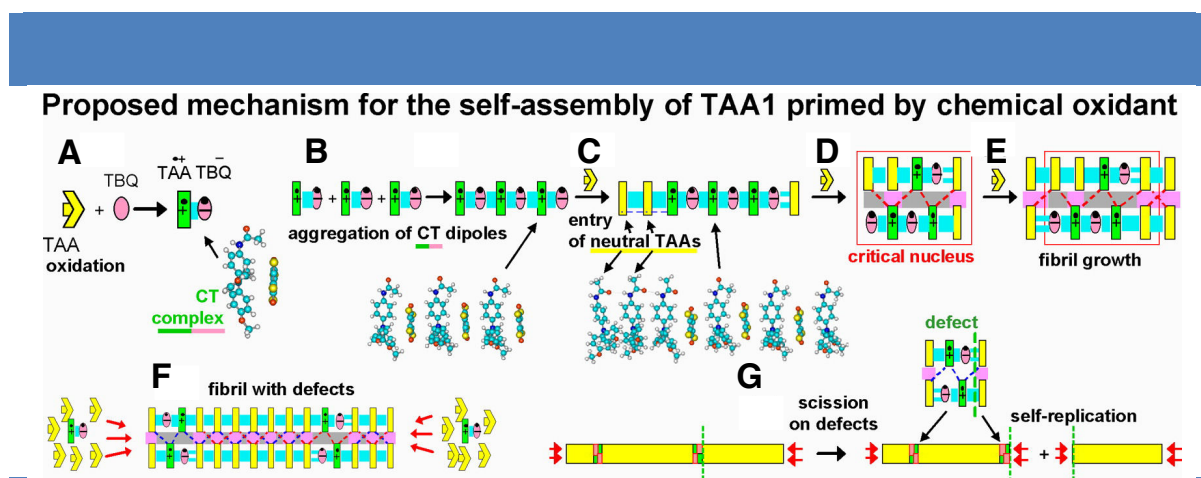


Figure 39 | Oxidant-induced aggregation kinetics in TAA solutions: (a) Oxidation of monomeric TAA by TBQ produces the radical ion pair $TAA^{+\bullet}TBQ^{-\bullet}$. (b–g) The main stages of the critical nuclei formation and subsequent fibril multiplication in TAA solutions with added TBQ: (b) Association of $TAA^{+\bullet}TBQ^{-\bullet}$ ion pairs. (c) End-attachment of neutral TAA molecules. (d) The critical nucleus formation with $n = 3$ $TAA^{+\bullet}$ radicals, and (e,f) further growth of the bicolumnar fibril by end-attachment of free amines. (g) Self-replication by scission at defect points.

⁵⁷ Here and below $k_B T$ is the thermal energy corresponding to the ambient temperature of 293 K, $1 \text{ kcal/mol} = 1.72k_B T$. The effective dielectric constant was chosen to be $\epsilon = 2.2$. The solvation energy contribution is taken into account both in the dissociation energy E_{ca} and in the fibril end- association energy E_{as} .

⁵⁸ More precisely, it is the bonds between CT dimers and the neighboring neutral TAA molecules that serve as weak points of the columnar structure.

4. Derivation of the Master Equation

The kinetics of this multistage self-assembly process can be described in terms of two basic quantities: the number of fibrils $m = m(t)$ and the total number of aggregated amines $M = M(t)$. If c_A and c_O are the total molar concentrations of TAA and **TBQ** in solution ($p_O \equiv c_O/c_A$ is the oxidant fraction, which is supposed to be low), and c , c_+ are concentrations of free TAA molecules and of free cation–anion complexes, respectively, then $c+M = c_A$; $c_+ \approx cp_O$. The kinetic equations are

$$\frac{dM}{dt} = k(c - c^*)m, \frac{dm}{dt} = \lambda Mp_O + \Gamma_n \quad (11)$$

Here kc is the rate of association of dissolved TAA molecules at a fibril end and $kc^* = \text{const}$ is the fibril dissociation rate, which is neglected hereafter since the critical association concentration c^* is extremely low: $c^* \ll c_A$ (see the next section). The λ -term in the second equation accounts for the formation of new fibrils by scission at the defects (Mp_O is the total number of radical-defects in the fibrils), $\Gamma_n = k'c_+^n c^v$ is the fibril nucleation rate, and k , k' and λ are the relevant rate constants.

The phenomenon of fibril *self-replication* is pronounced if the initial nucleation rate $\Gamma_n \approx k'p_O^n c_A^{n+v}$ is much lower than the maximum scission rate $\lambda c_A p_O$:

$$\gamma \ll 1, \gamma \equiv \Gamma_n / (\lambda c_A p_O) \approx \left(\frac{k'}{\lambda}\right) p_O^{n-1} c_A^{n+v-1} \quad (12)$$

In this case the self-assembly in accordance with eq 11 follows the universal curve:

$$w \approx 1 - e^{-\mu}, \tau = \text{arcosh}\left(1 + \frac{\mu}{\gamma}\right) + \varphi(\mu) \quad (13)$$

where the weight fraction of the aggregated amines $w \equiv M/c_A$ and the reduced time

$$\tau \equiv \frac{t}{t_1}, t_1 = k\lambda p_O c_A^{-1/2} \quad (14)$$

are related implicitly *via* an auxiliary variable μ and the universal function $\varphi(\mu)$:

$$\varphi(\mu) = \int_0^\mu (1/\sqrt{2} \sqrt{\mu + e^{-\mu} - 1} - 1/\mu) d\mu \quad (15)$$

This model reproduces very well (with fitted t_1 and γ) all the experimental NMR data on the kinetics of the TAA aggregation for various oxidant concentrations, p_O (see figure 38c for a plot of the data fit with the master equation). To perform a more detailed comparison, we note that the theoretical curves $w(\tau)$ eq 13 for various γ have nearly the same shape as long as $\gamma \ll 1$: the curves are simply shifted one with respect to another along τ giving the universal dependence

$$w = w_{\text{univ}}(\tau - \Delta\tau), \text{ with } \Delta\tau = \text{const}_\tau - \ln_\gamma \quad (16)$$

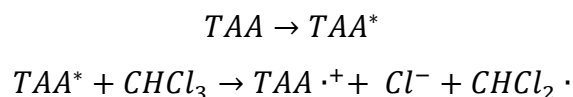
where $w_{\text{univ}}(\tau)$ is a universal function, independent of any material constant. Therefore, we

predict an essentially universal growth of the aggregated fraction w in terms of the appropriate time parameter $\tilde{\tau} = t/t_1 - \Delta\tau$ (*i.e.*, with appropriately shifted and rescaled time). In other words, the fibril growth time t_1 is nearly independent of γ ; it is just the lag-time before the growth that crucially depends on the nucleation rate, $t_{\text{delay}} \simeq t_1 \ln 1/\gamma$. The master curve representation, eq 16, of the NMR data is shown in Figure 38d.

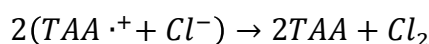
Finally, returning to the system without oxidant, we note that the same kinetic mechanism (fibril end-growth + scission) can explain the kinetics of TAA self-assembly in pure chloroform solutions triggered by a short pulse of light, or, alternatively, by a small amount of added fibril “seeds” (Figure 38a,b). In this case, both the scission rate and the end-growth rate constants are independent of the irradiation dose I , or of the amount of seeds, c_s . The TAA self-assembly in these systems can be described by the same eq 11, but with Γ_n replaced by $\text{const} \times \delta(t)$ (here $\text{const} \propto I, c_s$ and δ is the Dirac’s delta), and λp_O replaced with the homogeneous scission rate constant λ_h . Therefore, the characteristic aggregation time t_1 , eq 14, is predicted to be constant (independent of I or c_s) and similar to the time t_1 for low oxidant fraction p_O , in agreement with the NMR kinetic data giving $t_1 \sim (2 \div 3) \cdot 10^3$ s (Figure 38a,b). By contrast, c_s still defines the delay time for the seeded systems (Figure 38b).

5. Light-induced Mechanism and Self-assembled Structure

Computational results revealed that the neutral TAA molecules adopt a pyramidal conformation with strong out-of-plane rotation of the aromatic rings. However, the TAA amine pyramid becomes flat and the ring rotation angles decrease significantly after oxidation. The flat TAA radicals facilitate stacking, in agreement with the experimental evidence that the association of TAA molecules in solution is correlated with the TAA radical cation formation. The basic reaction stages of this light-induced oxidation process are (Figure 40a,b):



and for reduction (figure 40b):



Noteworthy, $TAA^{\cdot+}$ and Cl^- ions form a rather stable cation–anion complex. The ion-bond energy, E_{ca} , obtained by the simulation technique is $E_{ca} \approx 55k_B T$. This energy is high enough to practically suppress the dissociation: the fraction of dissociated radicals is about $e^{-E_{ca}/2k_B T} \sim 10^{-12}$.

TAA⁺Cl⁻ ion pairs are electric dipoles that can effectively assemble in supramolecular stacks. The optimal configuration of the stack depends on the number of TAA⁺Cl⁻ pairs in it. Formation of the supramolecular pile of dipoles starts with association of just two cation–anion pairs, the attraction energy stabilizing such dimers (Figure 40d) is $E_{11} \approx 15.5k_B T$. The energy gain for end-attachment of a dipole to a long stack of dipoles is even higher: $\tilde{E}_1^{(l)} \approx 16.5k_B T$ (Figure 40f). Hence, the dimers associate readily if their concentration is above $\sim 10^{-7}$ M.

Simulations suggest two principal arrangements of TAA⁺Cl⁻ pairs in long supramolecular stacks: a *loose* chain with symmetrically positioned chlorides (Figure 40f), and a *tight* chain with chloride counterions in the off-axis positions (Figure 40h), the latter being much more stable (as direct contacts between neighboring TAAs allow for their correct π -stacking and optimal van-der-Waals attraction). Indeed, the scission energy of the tight stack, \tilde{E}_{sc} , is higher by $\approx 12.7k_B T$ and its overall association energy (per charge-transfer complex) \tilde{E}_1 is stronger by $\approx 6.7k_B T$ in comparison with the values for the loose chain. However, a transformation from the “loose” to the more favored “tight” structure demands multiple rearrangements (Figure 40g) of chloride ions. The corresponding activation energy is on the order of $\Delta E_a \sim 8.6k_B T$. Such transformation is only possible for chains longer than a trimer since an isolated “tight” dimer is less favorable than a “loose” dimer (while the energies of the corresponding trimers are roughly the same).

Long aggregates of TAA⁺Cl⁻ pairs tend to form double columns stabilized by significant lateral attraction energy (including the H-bond energy). The minimal stable double-columnar aggregate involves $n^* \sim 3$ charge-transfer pairs per column. Its energy is lower by $\sim 15 \pm 5 k_B T$ than that of a single-columnar “tight” stack of $2n^*$ dipoles. Once a double-columnar nucleus (Figure 40i) is formed, it attracts neutral TAA molecules that attach at its ends by aromatic stacking and H-bonding, thus initiating proliferation of TAA aggregation without any further molecular oxidation (Figure 40j). The total energy gained when a neutral TAA molecule enters the most energetically favorable double-columnar “snowflake” TAA fibril (Figure 40B) is $E_{as}^{(2)} \approx 18k_B T$; it corresponds to an extremely low critical association concentration $c^* \sim 10^{-8}$ M. Therefore, practically all TAA molecules should eventually aggregate. On the other hand, the activation energy to transform a free TAA molecule into the association-ready state TAA' (flat and solvent-dissociated) is high, $E_{act} \approx 16k_B T$, so neutral TAAs cannot start the self-assembly on their own, hence a nucleus formed by radicals is required for that (otherwise, at least eight activated neutral molecules are needed to nucleate a

fibril leading to a prohibitive energy barrier of $\sim 128k_B T$).

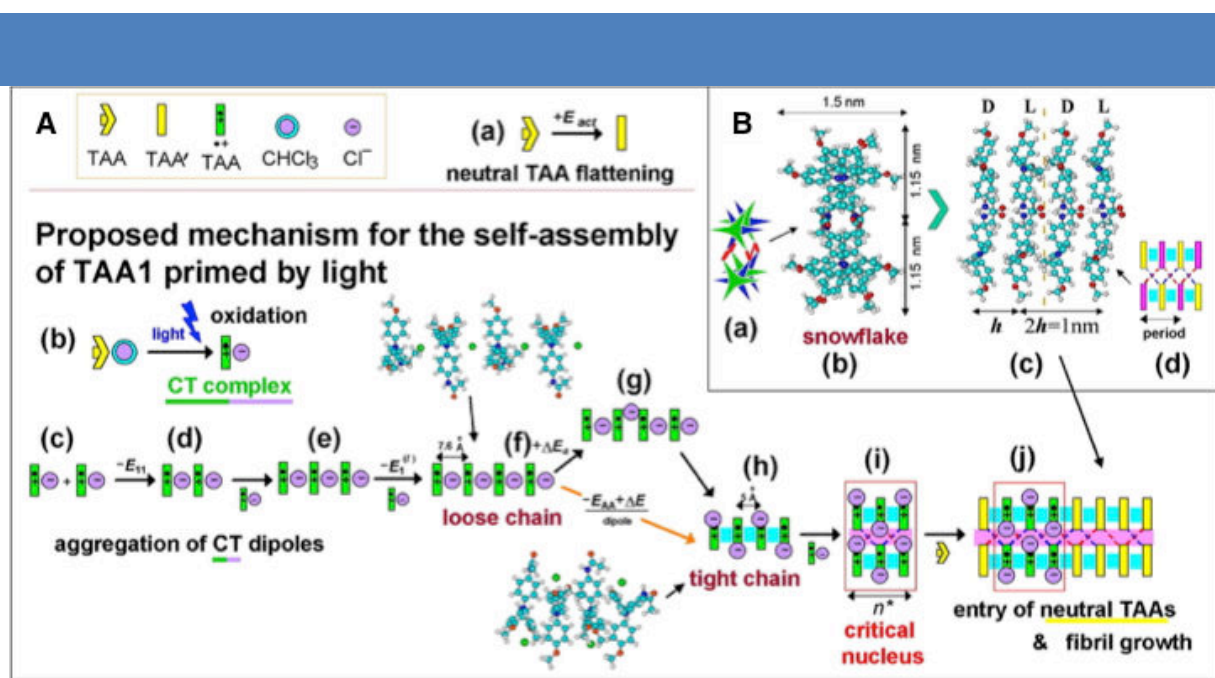


Figure 40 | (A) Light-induced aggregation kinetics in TAA solutions. (a) Highly improbable spontaneous flattening of isolated neutral TAA molecule (transition TAA \rightarrow TAA'). (b) Light induces oxidation of a neutral TAA molecule producing TAA^{•+} radical and Cl⁻ anion. (c,d) Two free radicals TAA^{•+} complexed with the Cl⁻ counterions attract each other head-to-tail. (e,f) A growing stack of radical dipoles. (f,g,h) Tightening of the stack: chloride ions move sideways (g); aromatic rings of TAA molecules benefit from closer contacts, while chloride anions are finally accommodated in the gaps between ether tails of TAA molecules (h). (i) Formation of double-columnar nuclei stabilized by H-bonds between the columns. (j) Growth of the structure by attachment of neutral TAA molecules. (B) Molecular arrangements in bicolumnar “snowflake” stacks from X-ray diffraction data: (a) A cartoon showing alternating molecular orientation in the columns. (b) The top view (along the main axis), and (c) the side view of the structure. (d) A cartoon with zigzag chain of H-bonds connecting the columns.

The TAA fibril structure involves the “snowflake” double columnar arrangement. While isolated neutral TAA has a pyramidal conformation with strong out-of-plane rotation of rings, the molecule adopts “propeller-like” conformation TAA' after entering the stack: the pyramid becomes flat and the ring rotation angles decrease. Two chiral geometries (L, D) are possible depending on the propeller twirl sense. In each single snowflake column, the twirl sense alternate so the aryl rings from neighboring TAA molecules closely approach each other. The amide groups facilitate stacking by intercolumnar H-bonds forming the double-columnar pattern. The primitive crystalline lattice cell for the double-columnar “snowflake” structure thus corresponds to at least 4 TAA molecules.

AFM images revealed that the assemblies form characteristic maize-like aggregates with their main motif being based on the columnar arrangement of “grains” of *ca.* 1.3 nm diameter, with in-columnar period of *ca.* 1.0 nm. These parameters are consistent with the “snowflake” morphology (Figure 40B(b,c)) obtained by simulations of the model molecules: the sizes of

one “snowflake” are ≈ 1.5 and ≈ 1.15 nm in two directions perpendicular to the main axis, and the ld-period along the column is $2h = 1.0$ nm.⁵⁹

6. Fibril Growth and Relaxation in the Dark

After light irradiation is switched off, the radicals decay relatively quickly while the fibrils are stable for a long time. In accordance with the established mechanisms of fibril nucleation and growth under irradiation, the kinetic equations are

$$\frac{dm}{dt} = k_n c_+^{2n^*}, \frac{dM}{dt} = k_c m \quad (17)$$

where m , M and $c = c_A - M$. The first equation describes formation of the critical double-filament nuclei, $(TAA^{*+})_{2n^*}$, with $n^* > 2$, and k_n is the corresponding nucleation rate constant. The second equation comes from eq 11 (c^* is neglected). From these relations, the time-dependence of the number of aggregates

$$m(t) = [2/(kn^*t^*)] \tanh\left(\frac{t}{t^*}\right) \quad (18)$$

the fraction of self-assembled molecules

$$w(t) \equiv \frac{M(t)}{c_A} = 1 - \frac{c(t)}{c_A} = 1 - \left(\cosh\left(\frac{tn^*}{t_c}\right)\right)^{-2/n^*} \quad (19)$$

and the current concentration of free radicals

$$c_+(t) = k_1 (c_A l)^{\frac{1}{2}} \cosh\left(\frac{tn^*}{t_c}\right)^{-1/n^*} \quad (20)$$

where

$$\frac{1}{t^*} = \sqrt{k k_n^* / 2 k_1} l^{n^*/2} c_A^{n^*/2}, t_c = n^* t^* \quad (21)$$

Note that the nucleation rate dm/dt decreases rapidly with time, so that $m(t) \approx m(\infty) = 2/(kn^*t^*)$ for $t \gg t^*$. The analogous time for concentration of free amines, $c(t)$, is longer, $\sim t_c = n^* t^*$. This means that nucleation virtually stops before the reservoir of amines is depleted, and for $t \gg t^*$ all fibrils should have roughly the same length $L(t) \approx hN/2$ ($h \approx 0.5$ nm, see Figure 40B(c)), where $N \approx M(t)/m(t)$ is the mean fibril aggregation number. It saturates at $N \approx N_\infty = c_A/m(\infty)$ for $t \gg t_c$, where

$$N_\infty = k_1^{-n^*} \sqrt{k n^* / 2 k_n} l^{-n^*/2} c_A^{1-n^*/2} \quad (22)$$

Thus, the nucleation stage (t^*) is always shorter than the growth stage (t_c). A lower nucleation rate constant (k_n) implies less but longer fibrils, leading to longer characteristic times t^* and t_c . A decrease of the light intensity I or of the amine concentration c_A leads to a similar effect (if $n^* > 2$). The physical origin of this effect is simple: doubling of c_A or I leads to a dramatic

⁵⁹ The period is doubled due to different orientations of L- and D-molecules alternating along the “snowflake” column.

increase of the nucleation rate (by a factor of 8 or more), so that much more fibrils are formed, hence they have to be shorter eventually. The number of fibrils grows nearly linearly in time, $m(t) \propto t$ for $t \lesssim t^*$, while the aggregated mass $M(t) \propto t^2$ for $t \lesssim t^*$ and $M(t) \propto t$ for $t^* \lesssim t \lesssim t_c$ (the last regime reflects the linear growth of fibril length with nearly constant number of fibrils). The NMR data on TAA solutions ($c_A = 10mM$) indicate that *the aggregation time t_c is shorter than 10 min.*

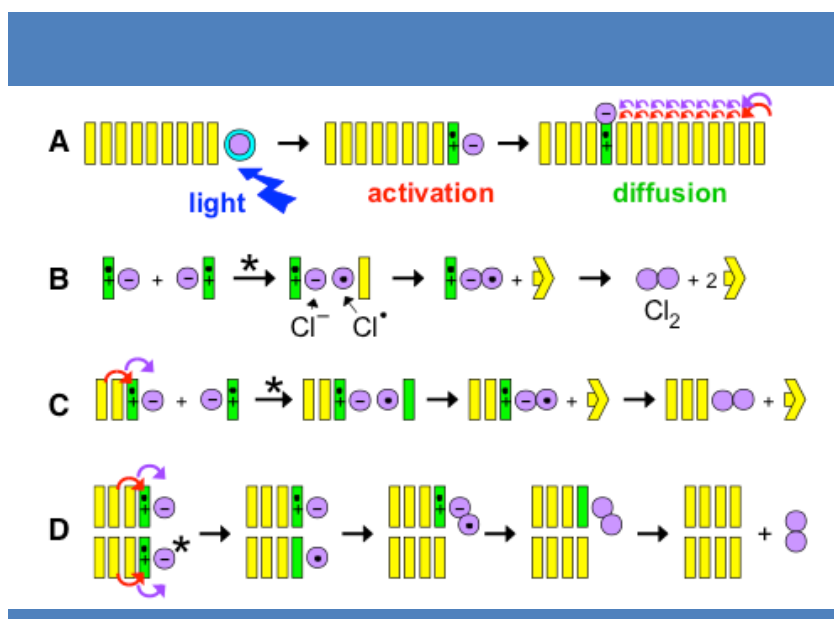
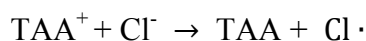


Figure 41 | Photo-oxidation of a TAA molecule at a fibril end followed by diffusion of the cation–anion pair inside the fibril (a). The chloride anion moves physically (see violet arrows), the TAA radical diffuses *via* electronic exchange with neighboring neutral TAA molecules (red arrows). Pairwise annihilation of two free cation–anion complexes (b). Annihilation of a radical at the end of a fibril aided by a free radical (c) Self-assisted reduction of two radicals at the end of a two-columnar fibril (d).

The observed nonlinear growth of f at $t \gtrsim t_c$ indicates that a *new* mechanism of radical formation becomes effective at longer t . The most reasonable conjecture is that the radicals are produced also among the aggregated amines (in addition to the free radicals). However, as photo-oxidation process implies an electron transfer from an amine to a solvent molecule, it seems highly improbable that it is effective for the amines buried inside STANW (the minimum distance, N to Cl, between TAA and CHCl₃ molecules is about 5 Å). Among all TAA units aggregated in STANW, only the *terminal* units are in close enough contact with the solvent, hence they can be converted to radical cations (Figure 41c,d). The rate of radical production (the probability that an amine unit at a given fibril end transforms to radical state in unit time) is $W_+ = k_+I$.

Let us turn to the reverse reaction of radical decay. The direct reaction



is prohibited energetically. The following channel is possible, however, Figure 41c: a *free*

radical complex $\text{TAA}^{+\cdot}\text{Cl}^-$ approaches the radical at the fibril end, and they annihilate with the rate $W_- = k_{-c+}$.⁶⁰ The balance of the two rates

$$W_+(1 - p) = W_-p \quad (23)$$

defines the probability p of the radical state at the fibril end: $p^{-1} = k_{-c+}/(k_+l) + 1$. As c_+ decreases exponentially for $t \gg t_c$, the linear radical decay rate k_{-c+} rapidly vanishes leading to a significant growth of p . However, precisely in this regime, $t \gtrsim t_c$, another, second-order, radical decay reaction comes into play. This reaction channel is related to the double-columnar structure of TAA aggregates. If p is not too small, there is a significant probability (p^2) that both neighboring end-units of a double fibril are in the radical state, so the two radicals can annihilate, Figure 41d. The rate of this reaction is $k_{2-}p^2$, where k_{2-} is expected to be rather small (as compared with k_{-}/d^3). The detailed balance gives now: $W_+(1 - p) = k_{2-}p^2$. This equation reads

$$p + \left(\frac{k_{2-}}{k_+l}\right)p^2 = 1 \quad (24)$$

It defines the probability $p = p_e$ of a radical at a column end for $t \gg t_c$. As k_{2-} is small as argued above, p_e can be high enough, so we can assume $p_e \gg f_2$ (recall that f_2 is the mean number concentration of trapped radicals in the fibrils right after their self-assembly. The overall fraction of radicals in the system changes then to $f \approx f_2 + 4p_e/N$, where 4 stands for the number of end-amines in a double-columnar aggregate, and the total aggregation number is $N \simeq N_\infty$ for $t \gg t_c$.

So far we assumed that concentration of radicals inside an aggregate does not change. This is, however, not the case as the radicals can hop from one amine site to a neighbor; such radical hopping was observed in the literature.^{61,62} The hopping process leads to radical diffusion with diffusivity $D = h^2/2t_h$, where t_h is the radical hopping time. The terminal relaxation time of this process is $t_m = L^2/(\pi^2 D)$, where $L \simeq L_\infty = hN_\infty/2$ is the fibril length. after 1 h of illumination the amount of trapped radicals approaches the saturation level (*i.e.*, $f \approx p_e$). Indeed, the data shown in Figure 42d demonstrate an apparent saturation for $t > 2000$ s (note also that the best fit time parameter $t_m = 1150$ s). If the light is then switched off, the equilibrium concentration of radicals jumps to 0, $p_e \rightarrow 0$ (eq 24), so the amount of radicals starts decreasing. As explained above, a radical located well inside the aggregate cannot disappear at once: it must first diffuse down to an end of the column, where the diffusive

⁶¹ Low, P. J.; Paterson, M. A. J.; Puschmann, H.; Goeta, A. E.; Howard, J. A. K.; Lambert, C.; Cherryman, J. C.; Tackley, D. R.; Leeming, S.; Brown, B. *Chem.—Eur. J.* **2004**, *10*, 83–91

⁶² Lambert, C.; Nöll, G.; Scheluter, J. *Nat. Mater.* **2002**, *1*, 69–73

current (D/h) ($\partial\rho/\partial x$) of radicals coming from the inner part of the fibril must be balanced by the end-radical decay rate $k_2\rho^2$. Here $\rho(x,t)$ is the local fraction of radicals within the fibril. The corresponding diffusion process can be analyzed taking into account that all the equations can be reduced to

$$\frac{\partial y}{\partial \tau} = \frac{\partial^2 y}{\partial \xi^2}; y(\xi, 0)|_{0 < \xi < \pi} = 1; \left. \frac{\partial y}{\partial \tau} \right|_{\xi=0} = - \left. \frac{\partial y}{\partial \xi} \right|_{\xi=\pi} = \kappa y^2 \quad (25)$$

using the substitution $\rho(x,t) = \rho_0 y(\xi,\tau)$ with $\xi = \pi x/L$, $\tau = t/t_m$. The initial condition (at the beginning of the dark stage, $t = 0$) is $\rho(x,0) \approx \rho_0$, where $\rho_0 \approx p_e$ is defined in eq 23. Thus, the only essential parameter defining the relaxation kinetics is the reduced end-decay rate constant:

$$\kappa = k_2 - \rho_0 L h / (\pi D) \quad (26)$$

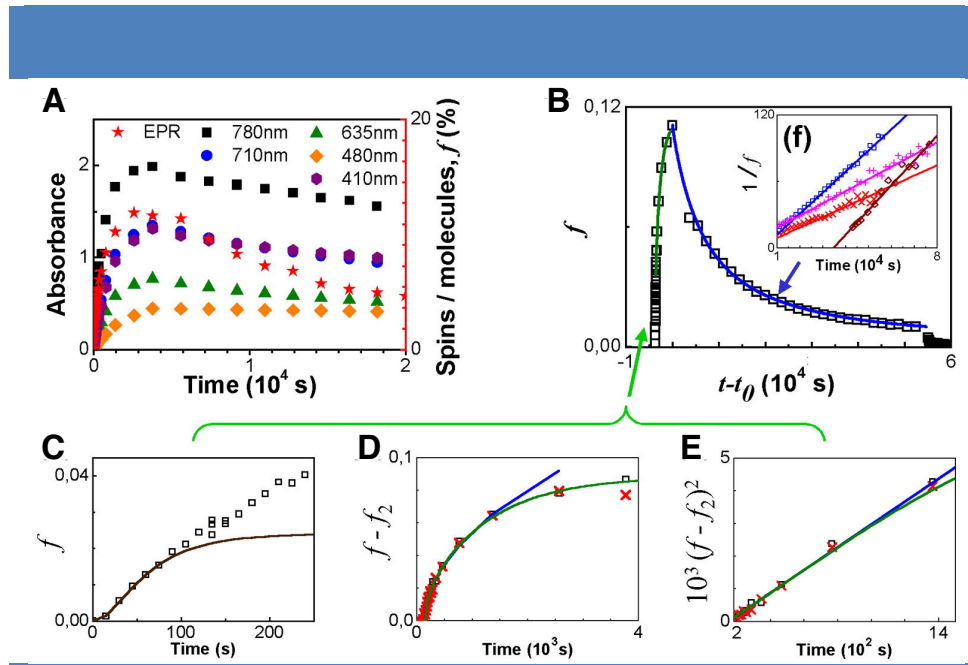


Figure 42 | Kinetics of light-induced radical formation and decay in the dark. (a) Time evolution of the UV absorbance at 5 different wavelengths and of the fraction f of the triarylammmonium radical (quantitative EPR data) for solutions in chloroform (at 1 mM) during both 1 h irradiation ($I = 0.06\text{W}/\text{cm}^2$) and overnight relaxation in the dark. (b) Time dependence of the number fraction of radicals, f vs $t - t_0$ for 10 mM TAA solution irradiated for 1 h at $t < t_0 = 3765$ s: EPR data (squares) and theoretical curves. The fraction of radicals at the beginning of the dark stage $\rho_0 = f(t_0) \approx 0.111$; the solution was heated up at $t > 62000$ s. (c–e): Radical formation in solutions of initially monomeric solution during 1 h irradiation stage ($I = 0.06\text{W}/\text{cm}^2$) in chloroform: EPR data for the fraction of radicals, f vs t at $c_A = 10$ mM (black squares) and at $c_A = 1$ mM (red crosses). The solid curves comes from the theory with $f_2 = 0.024$ ($c_A = 10$ mM) and $f_2 = 0.032$ ($c_A = 1$ mM). (c) The early stage data and the theoretical fit with $n^* = 3$, $t_c = 60$ s (brown curve) for $c_A = 10$ mM. (d) The excess relative number of radicals, $f - f_2$ vs t : the theory, with $p_e - f_2 = 0.088$, $t_m = 1150$ s and $t_f = 150$ s (green curve); the corresponding theoretical asymptote, $f - f_2 = 0.00187((t - t_f)/s)^{1/2}$ (blue curve). (e) The same data and the theoretical curves from (d) for the time range $t = 150 \div 1500$ s: the square of the excess radical amount, $(f - f_2)^2$, vs t . (f) Radical decay in the dark after 1 h of irradiation: $1/f$ vs t . EPR data sets (symbols) and the corresponding linear regression approximations for $t > 2 \times 10^4$ s for $c_A = 10$ mM (blue, data as in the plot (b)), 1 mM (two independent experiments, red (the data as in the plot (a)) and magenta), and for another solution, $c_A = 1$ mM, sonicated in the dark.

At long times, $t \gg t_m$, the diffusion relaxation within the fibril becomes faster than the reduction at its ends, so the profile $y(\xi, \tau)$ becomes nearly uniform along the coordinate ξ . Indeed, while the terminal diffusion relaxation time τ_m is constant, the end-reduction rate κy^2 slows down significantly as the radical concentration decreases ($y \rightarrow 0$). In this regime (for late stages $t \gg t_m$, when $\langle y \rangle \lesssim \kappa^{-1}$) the asymptotic solution for the mean fraction of trapped radicals inside the fibrils, $f = \rho_0 \langle y \rangle$, is *i.e.*, $1/f$ increases linearly in time. This prediction is successfully verified using EPR data for several dark-stage experiments (on samples with $c_A = 1$ mM and 10 mM, with and without sonication) as demonstrated in Figure 42. Thus, f does not tend to a finite saturation level at long times, rather it always decreases slowly as $1/t$.

5. Conclusions

Here we have elucidated through a combined experimental and theoretical treatment, the complex self-assembly process of mono-amide triarylamine molecules. Some important conclusions are that the basic mechanism is a nucleation-growth mechanism where the nucleation process is triggered by the formation of the triarylamine radical cation-anion complex that associates to form short stacks. The critical nucleus is predicted to be a minimum of 6 radicals in a double columnar assembly. Intercolumnar hydrogen bonding between two of these stacks leads to a double columnar self-assembly, onto which subsequent neutral molecules can attach. Importantly, hopping between the core units allow for diffusion of the radicals through the fibers, and continued oxidation of the formed fibrils can be affected from the ends. Likewise, reduction of the radicals happens in the dark from the fibril ends and ‘trapped’ radical species may diffuse towards the ends and be reduced.

The mechanism displays self-replication behavior due to the tandem scission/end-growth mechanisms. The resultant sigmoid growth of w in TAA systems with oxidant is characterized by the growth time t_1 , which is inversely proportional to the square root of the fibril scission rate defined by the oxidant concentration, and by the delay time $t_{\text{delay}} \approx t_1 \ln(1/\gamma)$, which gets longer for lower nucleation rate (γ). The sigmoid growth is characteristic of systems where the TAA self-assembly is triggered by a small amount of fibril seeds or by a short light pulse. These results are of interest for other self-replicating systems based on the fiber nucleation–growth processes.^{63,64} Additionally, the use of light as a spatially precise and noninvasive factor is of particular interest to trigger or modify the self-assembled architectures and to

⁶³ Takahashi, Y.; Mihara, H.. *Bioorg. Med. Chem.* **2004**, *12*, 693–699.

⁶⁴ Bissette, A. J.; Fletcher, S. P.. *Angew. Chem., Int. Ed.* **2013**, *52*, 12800–12826.

design responsive materials.^{65,66}

⁶⁵ Jochum, F. D.; Theato, P. *Chem. Soc. Rev.* **2013**, *42*, 7468–7483.

⁶⁶ Burnworth, M.; Tang, L.; Kumpfer, J. R.; Duncan, A. J.; Beyer, F. L.; Fiore, G. L.; Rowan, S. J.; Weder, C., *Nature* **2011**, *472*, 334–338.

Chapter III Triarylamine Self-Assembly at Electrode Surfaces

1. Introduction

Having elucidated in detail the self-assembly mechanism due to light and chemical triggers, we next set out to see whether we could extend this process to electrochemically trigger the self-assembly process in a collaboration performed with Tom Ellis and David Martel. As outlined in the previous chapter, the self-assembly mechanism involves *i*) the oxidation of a catalytic quantity of triarylaminines to their radical cations, with concomitant reduction of the chlorinated solvent producing chloride counterions; *ii*) the formation (above a critical concentration of 10 nM) of a nucleus of at least 6 triarylammonium radicals in a double columnar arrangement involving hydrogen bonds; *iii*) the stacking of neutral triarylaminines onto the nucleus and subsequent growth of the primary fibril; *iv*) the lateral secondary aggregations of fibrils by van der Waals forces to reach larger bundles of fibers. Since the initial process is an oxidation step, it seems logical that one could trigger this process at electrode surfaces. In the literature, there exists only a few examples of redox responsive supramolecular polymers.^{67,68,69} They all rely on an isodesmic mechanism of polymerization growth which implies a stoichiometric oxidation (or reduction) of the monomers. The redox event acts on the degree of polymerization by changing the association constants in host-guest recognition processes of (AB)_n type polymers.

In this chapter, we successfully demonstrate the electrochemically triggered self-assembly of mono-amide triarylaminines. Additionally, we show that we can suppress the self-assembly by using a redox couple to arrest the nucleation phase. We then demonstrate the self-assembly of tris-amide triarylaminines, whose full characterization will be further elucidated in a subsequent chapter. These self-assemblies form stable structures through the cooperative mechanism, i.e. there is no need to form the radicals first in order to form the self-assemblies. These molecules display quasi-reversible electrochemical behavior due to their efficient inter-assembly charge-transfer. Finally, we demonstrate the functionalization of electrodes with a

⁶⁷ D.-S. Guo, S. Chen, H. Qian, H.-Q. Zhang and Y. Lu, *Chem. Commun.*, **2010**, 46, 2620 - 2620

⁶⁸ X. Ma, R. Sun, W. Li and H. Tian, *Polym. Chem.*, **2011**, 2, 1068 - 1072

⁶⁹ B. Erdogan, B. J. Jordan, J. B. Carroll, G. Cooke and V. M. Rotello, *Polym. Preprints*, **2005**, 46, 1151 -1153

phosphonate derivative and attachment through supramolecular recognition to the electrode surface.

2. Electrochemically Triggered Self-Assembly of Mono-Amide Triarylamine Nanowires

The stability of the mono-amide triarylamine self-assembly was tested in the presence of commonly used electrochemical counterions as well as at high electrolyte concentrations commonly used in electrochemical experiments. Photo-induced self-assembly was observed in the presence of the various electrolytes and in several cases we actually found increased stability of the counterion. When irradiated with LED light (395 ± 5 nm), self-assembled triarylaminates have the characteristic feature of stabilizing the catalytic quantity of trapped radical cations for extended periods of time. These radicals produce a series of characteristic absorption bands, with the typical band around 800 nm as described in the previous chapter as originating from the triarylamine radical cation species. Photo-oxidation of the mono-amide triarylamine (MTAA, **4**) in a tetrachloroethane (TCE) solution containing 0.1M tetrabutylammonium chloride (TBACl) gave the same stable absorption spectrum as the control solution in pure TCE, indicating the generation of a stable self-assembly even at high concentrations of electrolyte. In order to test the effect of substituting different counter ions, **4** was then dissolved in a solution of TCE with either the common electrochemical tetrabutylammonium salts of perchlorate (TBAClO₄) or hexafluorophosphate (TBAHFP) (Figure 43). The absorption experiments suggest that the self-assembly is still present with all of the counter ions tested due to the stability of the radical cation peak

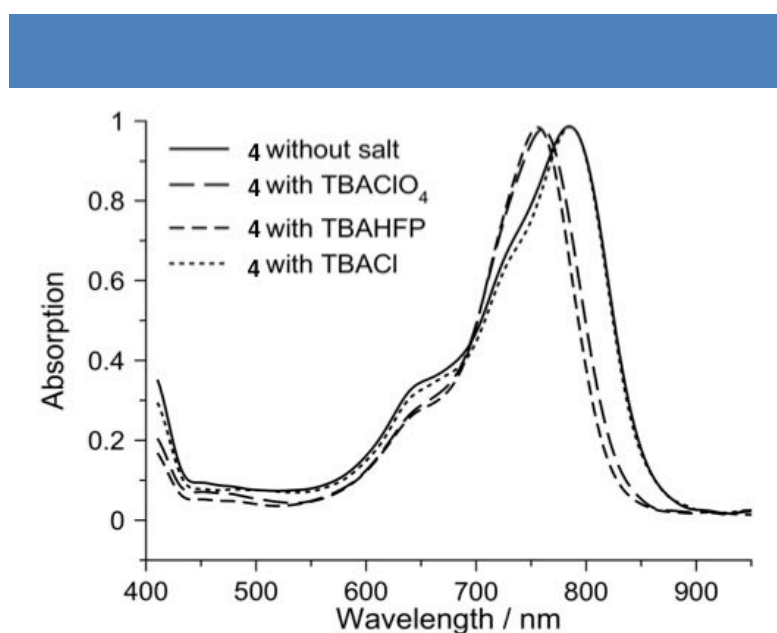


Figure 43 | UV-Vis spectra of **4** at 1 mM in TCE after photo-assembly in the presence (or the absence) of various counter ion salts. (All spectra normalized for clarity).

We then performed cyclic voltammetry (CV; figure 44a) at a scan rate of $100 \text{ mV}\cdot\text{s}^{-1}$ for **4** in TCE and TBAHFP, revealing the first oxidation associated with the radical cation $\mathbf{4}^{\bullet+}$ ($E_{1/2} = -71 \text{ mV vs Fc/Fc}^+$), and the second oxidation leading to the corresponding dication ($\mathbf{4}^{2+}$, $E_{1/2} = 704 \text{ mV vs Fc/Fc}^+$). Spectroelectrochemistry was also conducted on a solution of **4** showing the expected UV-Vis radical absorption peak at 800 nm as the potential moves past the first oxidation. As observed in figure 44b, the spectrum matches that observed upon photoirradiation.

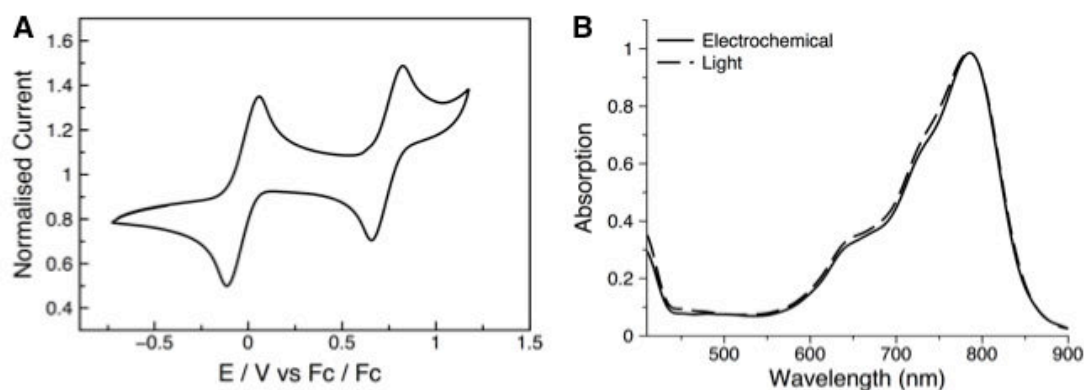


Figure 44 | Cyclic voltammetry on the mono-amide triarylamine **4** (1 mM in tetrachloroethane with 0.1M Tetrabutylammonium hexafluorophosphate; a). Absorption measurement comparing electrooxidized and photochemically oxidized wires in solution (b).

We then tested whether we could electrochemically trigger the formation of wires from **4** in the presence of an electrolyte. We thus probed by ^1H NMR spectroscopy the behavior of a solution of triarylamine in deuterated chloroform (5 mM), and in the presence of TBAHFP (0.1 M), while holding a potential of 0.2 V vs Fc/Fc^+ for 30 min. This involves the production of approximately 1% of $\mathbf{4}^{+\bullet}$ in the solution. After electrolysis, we observed the characteristic suppression of the NMR peaks, confirming the self-assembly process upon electrolysis. In order to get cleaner spectra without a signal from the contributing electrolyte, **4** was electrolyzed with platinum foils (separation 0.5 cm). The voltage was slowly increased until an increase in current was observed on *d*-TCE sample. After electrolysis, the characteristic suppression of the NMR peaks was also observed. The solution was then successfully imaged by TEM and AFM, confirming the formation of supramolecular triarylamine nanowires (Figure 45d,e).

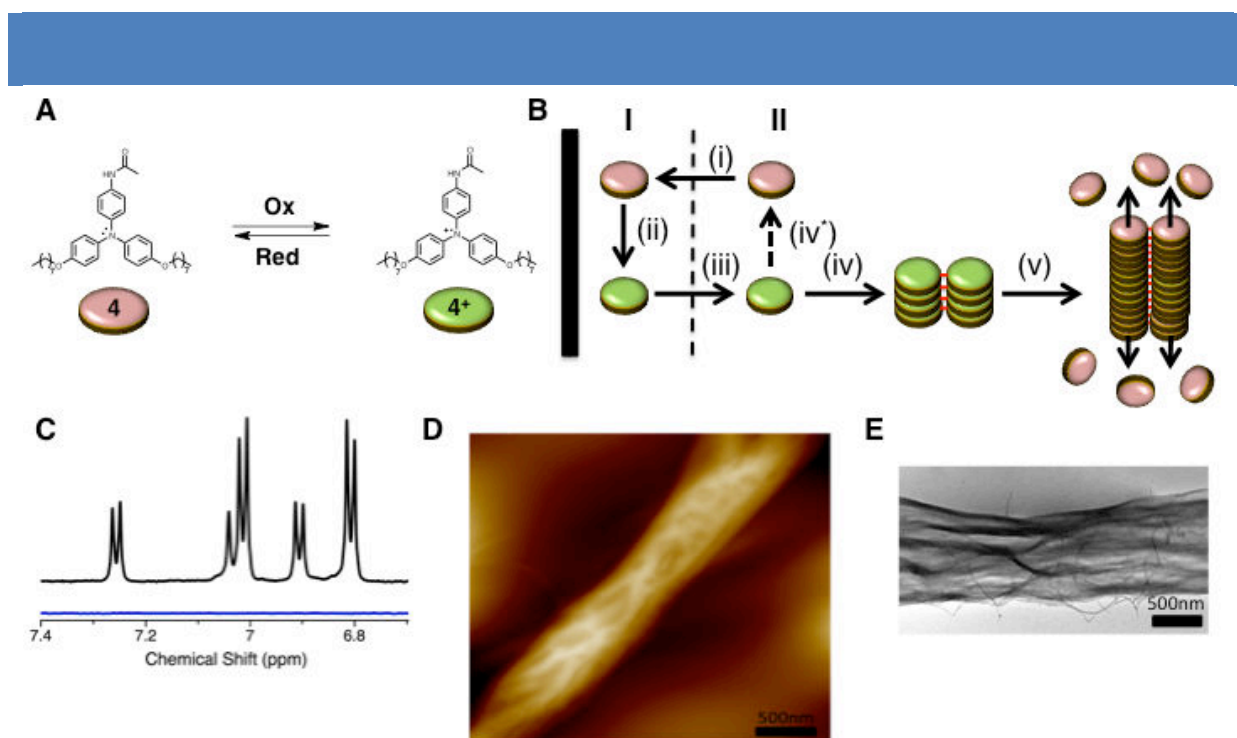


Figure 45 | (a) Oxidation and reduction of mono-amide triarylamine (MTAA). (b) Electrochemically triggered self-assembly via the nucleation and growth mechanism. (I) is the electrochemical double layer next to the electrode surface and (II) is the diffusion and bulk layers. The general process involves: (i) diffusion of a molecular species of neutral **1** into the double layer, (ii) oxidation of the neutral species at the electrode surface, (iii) diffusion of the oxidized radical cation molecule into the diffusion layer, (iv) nucleation of the radical species, (iv') an alternative pathway by which the self-assembly pathway is shunted through the presence of an excess of decamethylferrocene acting as a redox couple to reduce the radical cation, and (v) growth of the self-assembled fibers by the addition of neutral monomer species. (c) NMR of the aromatic peak region before (top) and after electrochemically induced self-assembly, (blue line). (d) AFM images of electrochemically formed fibers. (e) TEM images of the electrochemically formed fibers.

The self-assembly mechanism at the electrode surface is outlined in figure 45 and the general process involves: (i) diffusion of a molecular species of neutral **4** into the double layer, (ii) oxidation of the neutral species at the electrode surface, (iii) diffusion of the oxidized radical cation molecule into the diffusion layer, (iv) nucleation of the radical species, and (v) growth of the self-assembled fibers by the addition of neutral monomer species.

Alternatively, we found that we could shunt the self-assembly pathway by introducing a redox couple in excess, in this case decamethylferrocene (DmFc). DmFc has an oxidation potential well below the oxidation potential of the oxidized MTAA (Figure 46a), giving it the ability to reduce 4^{*+} upon formation in solution. To confirm this behaviour, the interaction of self-assembled wires made of $4/4^{*+}$ with decamethylferrocene was investigated by conducting a spectroscopic redox back-titration of the radical. We first exposed a solution of **4** to LED irradiation. Then a solution of decamethylferrocene was then added to the wires with stirring, and the UV-Vis absorbance was taken after sequential addition (Figure 46b). The linear relation of the plots suggests that decamethylferrocene does not interfere with the self-assembled system. The application of Beer's law to the back titration gave an extinction coefficient of $\epsilon = 31200 \pm 2600 \text{ L mol}^{-1} \text{ cm}^{-1}$ (95% confidence) for 4^{*+} . Using this extinction coefficient, we could estimate the charge saturation concentration of the wires by exposing **4** to UV for 20 minutes (until absorbance ceased to increase on illumination). The system approaches a saturation of $\sim 31.5\%$ of radical without electrolyte. The fact that it is well below unity supports that there must be neutral species to form the wires and stabilize the radical cation. Additionally, we observed a decrease in the peak heights of solutions which were preirradiated (Figure 46c,d) indicating less available species to be oxidized. Upon addition of decamethylferrocene, we observed a recovery of the oxidation peak height indicating complete reduction of MTAA in solution.

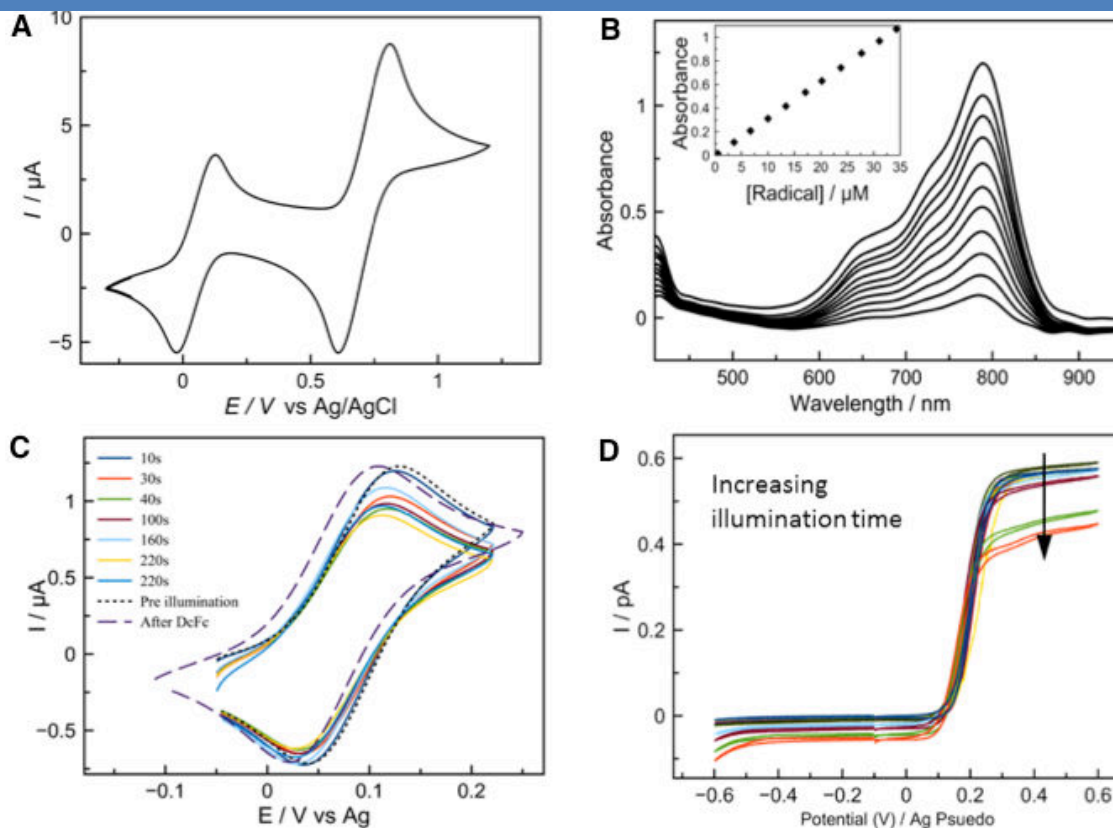


Figure 46 | (a) Cyclic voltammetry of decamethylferrocene ($E_{1/2} = 0.1$ V vs Ag/AgCl) and mono-amide triarylamine ($E_{1/2} = 0.6$ V vs Ag/AgCl). (b) Back titration of a solution of **4** with decamethyl ferrocene demonstrating the reduction of the radical cation. (c,d) Cyclic voltammetry after various illumination times with the standard electrode setup (c) and with a microelectrode setup (d).

We used this system to test the radical stability against various electrochemical salts (at 0.1 M) to probe the effect of the counter-ion on the oxidation and reduction processes. Using light-induced oxidation, we observed a saturation concentration mostly independent of the salt ions used (TBAHFP : 32.1%, TBAClO₄ : 35.6%). The notable exception is however TBACl, which could only introduce half as many charges as the others for the same experimental conditions (14.9%). Moreover, when using TBACl, the radical was strongly reduced within a day, while the typical green colour of the radical persisted for months in the presence of TBAHFP and TBAClO₄. This is in agreement with our previously proposed light-induced mechanism where the chloride plays an active role in the radical reduction by forming Cl₂ molecules at the tips of double columnar fibrils following a second order rate reaction. Here, in the presence of an excess chloride coming from the electrolyte, this reduction rate is enhanced.

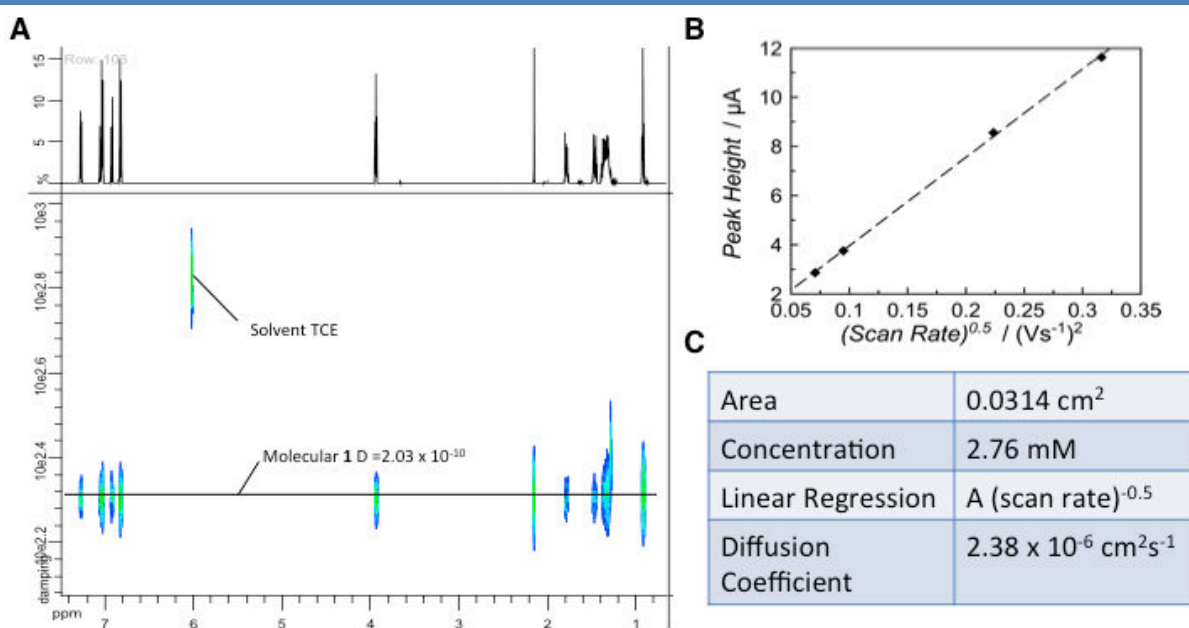


Figure 47 | (a) DOSY NMR of the unassembled triarylamine species. (b) Peak height versus the square root of the scan rate for the oxidation of the monoamide triarylamine in the presence of decamethylferrocene. (c) Calculation of the diffusion coefficient from the electrochemical data.

The diffusion constant of the MTAA in the presence of decamethylferrocene was determined using the Randles–Sevcik equation:

$$i_p = 0.446 nFAC \left(\frac{nFvD}{RT} \right)^{0.5} \quad (27)$$

where i_p = current maximum (A), n = number of electrons transferred (1), A = electrode area (cm²), F = Faraday's constant (C mol⁻¹), D = diffusion coefficient (cm²/s), C = concentration (mol/L), and v = scan rate in V/s. A diffusion coefficient of $2.38 \times 10^{-10} \text{ m}^2 \text{ s}^{-1}$ was determined from the electrochemical data. This was then compared with the diffusion constant determined by DOSY NMR of the unassembled, molecular species $2.03 \times 10^{-10} \text{ m}^2 \text{ s}^{-1}$ (Figure 47). This demonstrates that we observe the signal of the monomer, unassembled species in the presence of decamethylferrocene.

3. Electrochemical Behavior Of Tris-Amide Triarylamine Nanowires

We now move to examining the electrochemical behaviour of a tris-amide triarylamine (TATA, **6**, Figure 48a) self-assembly. A full description of this self-assembly will be addressed in a chapter 7. In contrast the monoamide triarylamine compound, the tris-amide derivative forms self-assembled fibers before irradiation.

Cyclic voltammetry (Figure 48c) displayed two redox peaks with the first oxidation occurring at 279 mV (vs. Fc) and the second oxidation occurring at 945 mV (vs. Fc).

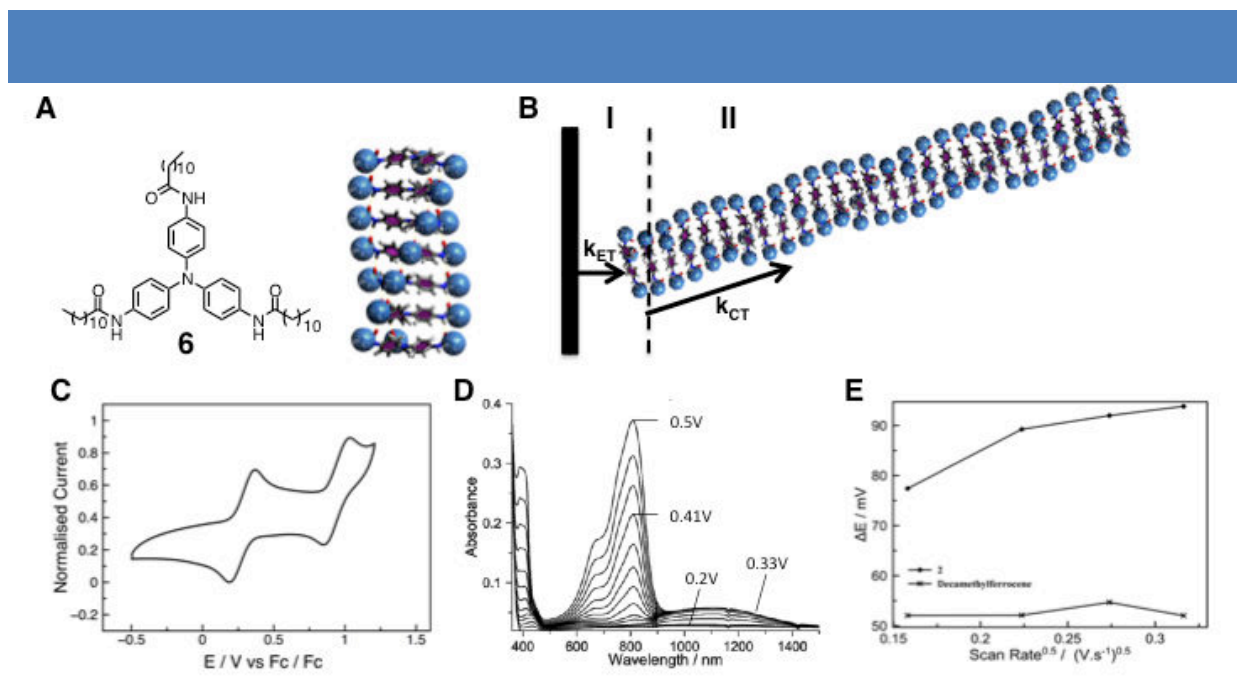


Figure 48 | (a) Chemical structure and self-assembly of tris-amide triarylamine (TATA). (b) Schematic depicting the electrochemical oxidation of molecules in the nanowires. k_{ET} is the rate of electron transfer from the electrode to the molecules. k_{CT} is the rate of charge transfer along the nanowires. k_D is rate of diffusion of the nanowires in solution. (c) CV of TATA in solution. (d) Spectroelectrochemistry of the TATA wires in solution demonstrating the appearance of the NIR charge transfer band associated with charge diffusion in the wires. (e) Quasi-reversible behaviour of the TATA wires after carefully controlling for the iR drop in the electrochemical setup.

Spectroelectrochemistry (Figure 48d) was performed on the first redox peak, which demonstrated the formation of a near-infrared charge transfer band, characteristic of through space charge-transfer within the TATA assembly and demonstrating that the self-assembly process occurs under the electrochemical conditions. Closer inspection of the electrochemical behaviour revealed that TATA nanofibers displayed quasi-reversible behaviour after carefully controlling for the IR drop in the electrochemical cell and using decamethylferrocene as an internal standard. The results are displayed in figure 48e and show peak splittings in the range of 75 mV to 95 mV depending on the scan rate. As a reference, the peak splittings of decamethylferrocene were between 52 mV and 60 mV. In contrast, cyclic voltammetry performed in a mixture of methanol and toluene (in which self-assembly is inhibited) demonstrated reversible behaviour with a peak splitting of 59 mV. This clearly demonstrates that the electrochemical quasireversibility is a consequence of the self-assembly of the individual molecules.

Quasireversibility is an indication of a kinetically controlled electrode redox process (as opposed to a diffusion controlled redox process). This result can be rationalized by examining the overall schematic of the electrochemical setup, as illustrated in figure 48b. Due to the stable stacking structure of TATA, not all of the molecules have equal access to the electrode surface. This implies that oxidation and reduction will be affected primarily from the ends of the wires, an assumption which holds equally for solution oxidation of triarylamine nanowires. Due to the facile ability of the charges inside the wires to migrate, we assign a radical diffusion rate constant, k_{CT} . The quasi-reversibility is a result of the formation of interacting redox centers with a slow diffusion rate through the fibers relative to the electron transfer rate at the electrode, i.e. $k_{ET} > k_{CT}$. This leads to unsuccessful oxidation events and a kinetically controlled electrode process. This also demonstrates adequate stability of the TATA nanowires within the electrochemical double layer, as opposed to the MTAA nanowires, for which we do not observe a quasireversible signal.

CV scans at scan rates between 200 mV/s and 5 mV/s are shown for 1 mM and 5 mM concentrations of **6** in figure 49a,b. There is a clear effect on the shape and the splitting potentials of the oxidation and reduction peaks. In figure 49c, we quantitated the splitting between the oxidation and reduction peaks as a function of the concentration and the scan rate. We observe at low concentrations (0.1 mM) we observe reversible splitting behaviour, indicated by splitting values close to the theoretical $59 \frac{1}{2}$ mV. As we increase concentration, we observe a corresponding increase in the splitting values at each scan rate. There is a huge jump in the splitting values when we move to the high concentration solutions of 5 mM and 10 mM.

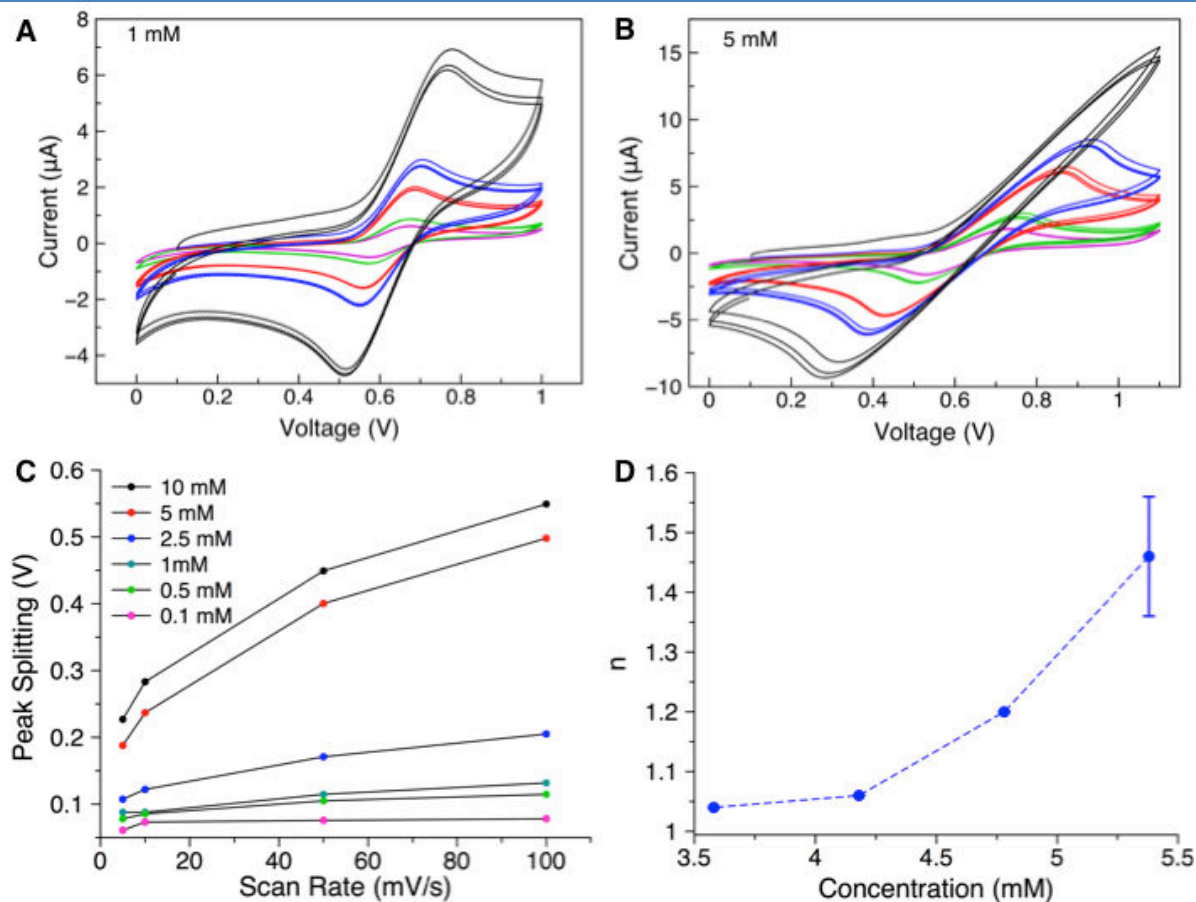
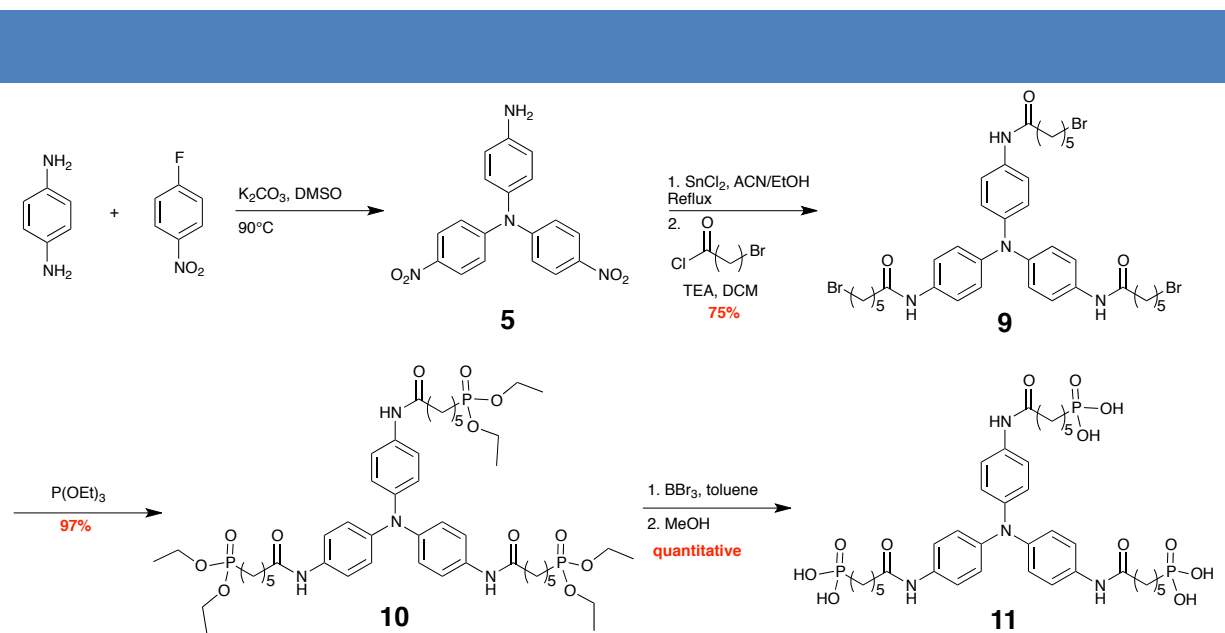


Figure 49 | (a) CV of **6** in 1 mM in TCE solution of TATA at various scan rates between 200 mV/s and 5 mV/s. (b) CV of a 5 mM solution of TATA at various scan rates between 200 mV/s and 5 mV/s. (c) Peak splittings for a range of concentrations and a range of scan rates demonstrating the effect of increasing the self-assembly size of TATA. (d) Relative viscosity for TATA solutions at various concentrations.

Figure 49d gives some more insight, as we performed viscosity measurements on **6** at varying concentrations in TCE. We can observe a large increase in the solution viscosity as we go from 3.5 mM to 5.5 mM solutions, which is due to the formation of large self-assembled fibers in the solution (as we will detail later, TATA fibers readily form organogels at sufficiently high concentrations). This is further proof that the quasi-reversible behaviour comes from the self-assembly, with larger and larger peak splitting observed for higher concentrations, which contain larger and larger fibers.

4. Electrode Functionalization and Attachment of Triarylamine Nanowires

Phosphonic acids are a well known functional group capable of binding to a wide range of surfaces with exposed hydroxyl groups.⁷⁰ The synthesis of molecule **11**, a tris-amide triarylamine substituted with phosphonic acid groups was accomplished in high yield, as displayed in scheme 1. The triarylamine core **5** was built up using a nucleophilic aromatic substitution reaction between 4-aminoaniline and 4-fluoronitrobenzene in DMSO under basic conditions (K_2CO_3) at 90°C. After chromatographic separation, the tris-amide compound **9** was synthesized by a tin chloride reduction followed by amidation with 6-bromohexanoyl chloride in the presence of triethylamine in DCM. The phosphonate ether derivative was synthesized in 97% yield in solvent free conditions with $P(OEt)_3$. Deprotection of the ether groups with boron tribromide resulted in the final product, **11**.



Scheme 1 | Synthetic scheme for the synthesis of the phosphonic acid derivative of tris-amide triarylamine.

Functionalization of SiO_2 and ITO covered glass slides followed the standard procedure of incubating the appropriate surface in a 1 mM solution of the TATA- PO_3H_2 **11** for 24 hrs in an aqueous solution, rinsing with milli-Q water, followed by baking at 120°C for 1 hr, and finally extensive rinsing with milli-Q water and organic solvents to remove unattached molecules (Figure 50a). Figure 50c shows the cyclic voltammetry response of a functionalized monolayer. In comparison to a

⁷⁰ Pujari, S. P.; Scheres, L.; Marcelis, A. T. M.; Zuilhof, H. *Ang. Chem. Int. Ed.* **2014**, 53, (25), 6322-6356.

control solution of TATA nanowires with the same electrode setup, we notice a much smaller peak splitting, as well as a large capacitive current response due to coverage of the electrode surface. A graph of the peak heights versus scan rate displayed linear behaviour for both the oxidation and the reduction peaks, indicating that the molecules are indeed surface confined (Figure 50d). One expects a linear relation between the peak height and the square root of the scan rate for freely diffusing species. Additionally, the functionalized ITO slide displayed absorbance due to the monolayer attachment (Figure 50b).

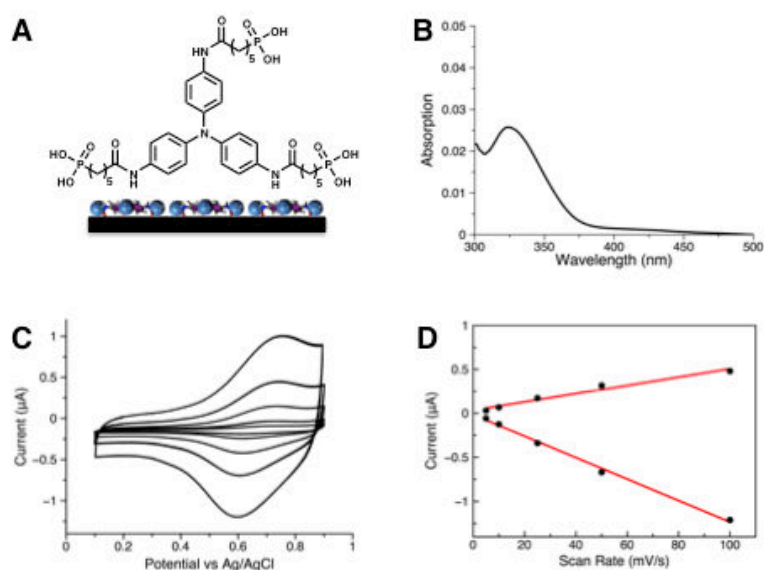


Figure 50 | Functionalization of an ITO surface with a tris-amide triarylamine functionalized with pendant phosphonic acid groups. chemical structure and schematic of monolayers formed from tris-amide triarylamine phosphonic acids. (b) Absorption spectrum after deposition onto ITO. (c) CV taken of a monolayer formed from 1mM deposition after extensive washing. (d) Peak heights versus scan rate display a linear dependence indicating that the molecules are surface confined.

Next, we investigated the supramolecular attachment of TATA **6** to monolayer-functionalized surfaces. Upon incubating functionalized ITO slides with TATA **6** for 24 hrs, we observed a noticeable increase in the absorbance indicating successful attachment of TATA **6** (figure 51a). In order to further investigate the supramolecular recognition and attachment of TATA fibers to the functionalized surfaces, we decided to use the quartz crystal microbalance technique on SiO₂ wafers. We first functionalized quartz QCM sensors with a SiO₂ surface with the TATA-PO₃H₂ following the standard incubation/baking procedure. Afterwards, we followed the effect of incubating the functionalized sensors in a 1 mM solution of TATA **6**. Figure 51b displays the initial deposition phase over the first hour

demonstrating a decrease in the frequency response due to adsorption of the molecules to the surface.

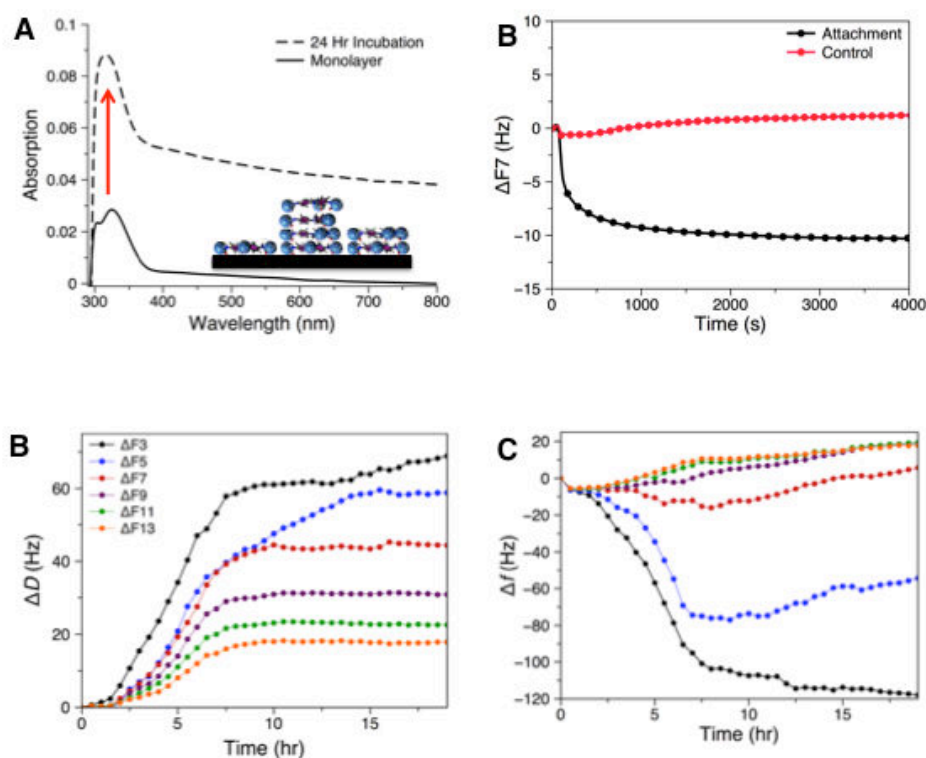
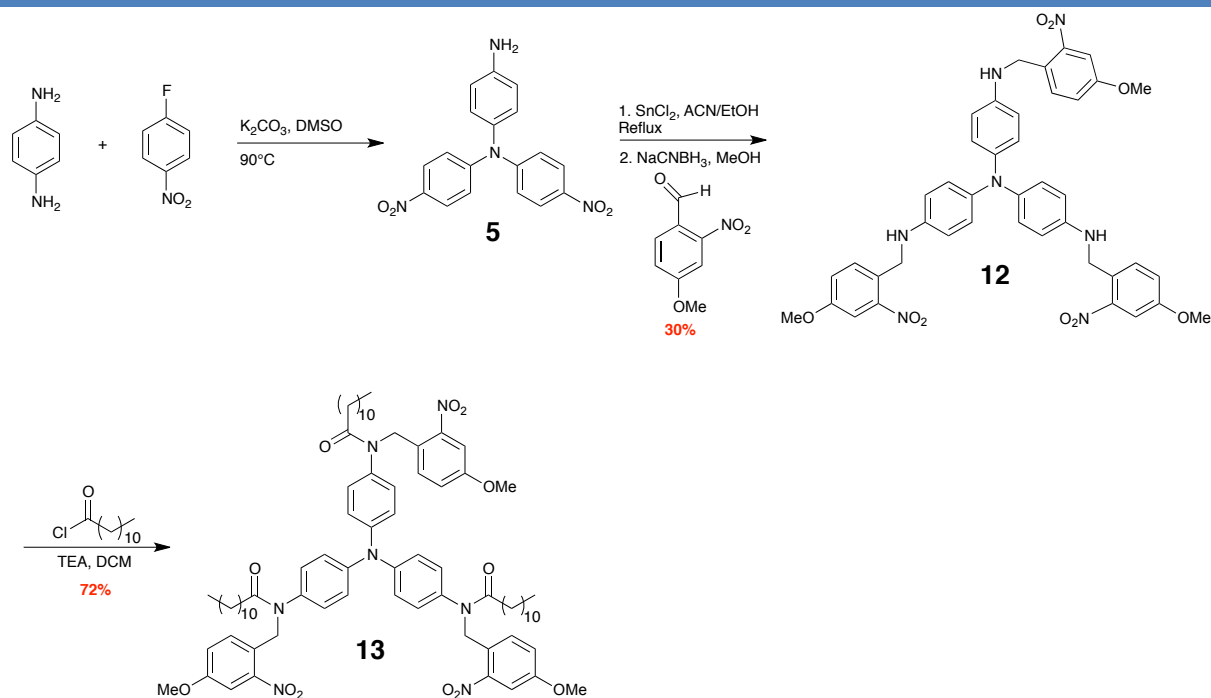


Figure 51 | (a) Absorption of a functionalized ITO substrate after 24hr incubation with TATA **6**. (b) QCM-D frequency shift of a SiO₂ surface with a monolayer of TATA-PO₃H₂ **11** and incubation with TATA **6** (attached) and a control molecule with protecting groups on the amide nitrogen to prevent supramolecular assembly. (c) QCM-D dissipation of attachment to functionalized surfaces over 19hrs. of incubation. (d) QCM-D frequency shift for the same experiment.

As a control, we synthesized molecule **13**, which due to bulky benzyl protecting groups on the amide nitrogen positions does not undergo self-assembly. The synthetic scheme is shown in scheme 2. Briefly, the triarylamine core unit **5** was reduced with tin (II) chloride to provide the tris-amine intermediate, which was then functionalized with a benzyl protecting group through a reductive amination reaction to give **12** in modest yield. Reaction with an acid chloride provides the protected tris-amide compound, **13**. We observed no deposition response with this molecule confirming that the effect we are indeed observing involves supramolecular recognition at the surface leading to attachment.



Scheme 2 | Synthetic scheme for the synthesis of the protected tris-amide triarylamine.

Over longer incubation times, we observed a noticeable effect on the QCM signal, which varied depending on the frequency that was followed. The lower frequencies displayed the largest frequency shifts, with the ΔF_3 frequency well in excess of -120 Hz, indicating multilayer formation at the surface. The ΔF_5 frequency follows the same path until around 7 hours, after which we start to observe an increase in the frequency. The ΔF_7 frequency likewise demonstrates a shallow initial decrease, followed by an increase in the signal around the same time. The higher frequencies give positive shifts after an initial decrease over the first hour and a half. This type of frequency-dependent behaviour has been observed with multilayer fibrillation on surfaces.⁷¹ Analysis of the dissipation shift demonstrates a large increase, indicative of soft, multilayer formation on top of the functionalized surface, and in line with what has been previously reported for surface fibrillation. We also performed QCM experiments over the same time period with the same TATA **6** solution on unfunctionalized QCM crystals. We observed no deposition from these QCM experiments. The signal was stable indicating the ability to stably attach TATA nanowires to electrodes for future applications

⁷¹ Hovgaard, M. B.; Dong, M.; Otzen, D. E.; Besenbacher, F. *Biophysical Journal* **2007**, 93, (6), 2162-2169.

5. Conclusions

In conclusion, we have demonstrated several key features which aid in the understanding and potential applications of triarylamine self-assemblies: (1) the ability to electrochemically trigger the self-assembly of MTAA nanowires, (2) using redox couples to suppress the self-assembly, (3) the ability to electrochemically distinguish TATA self-assembly in solution due to quasireversible behaviour, (4) the stability of TATA self-assemblies at the electrode surface, and (5) the ability to functionalize electrode surfaces and attach nanowires. Potential applications resulting from these experiments include: (1) spatial control over the self-assembly process, due to triggering the process near the electrode surface, (2) the ability to use redox couples to create out-of-equilibrium redox environments for the self-assembly, (3) probing TATA self-assembly for sensing applications, (4) electrode functionalization and attachment which is critical for work function matching and efficient charge transport for a variety of organic devices ranging from solar cells to OLEDs.

Chapter IV Self-Assembling Triarylamines as the Hole-Transport Layer In Perovskite Solar Cells

1. Introduction

This chapter details a collaborative effort within the group (including myself, Tom Ellis, a former postdoc, and Artem Osypenko, a more junior doctoral candidate who will continue the work) and with external groups (an industrial collaboration with BASF as well as an academic collaboration with the group of Michael Graetzel at the EPFL in Switzerland) to design and synthesize self-assembling triarylamines for use as the hole transport layer in perovskite solar cells. Perovskite solar cells are currently the most promising organic solar cell architecture being studied, with efficiencies as high as 15%.⁷² The device setup contains a semiconducting perovskite layer ($\text{CH}_3\text{NH}_3\text{PbX}_3$; X = Cl, Br, or I), as the light absorbing material. Photoirradiation induces charge separation within the perovskite layer while an adjacent hole transport layer transports the positive charge to a gold electrode and the perovskite layer transports the electron to the opposite electrode (Figure 52).

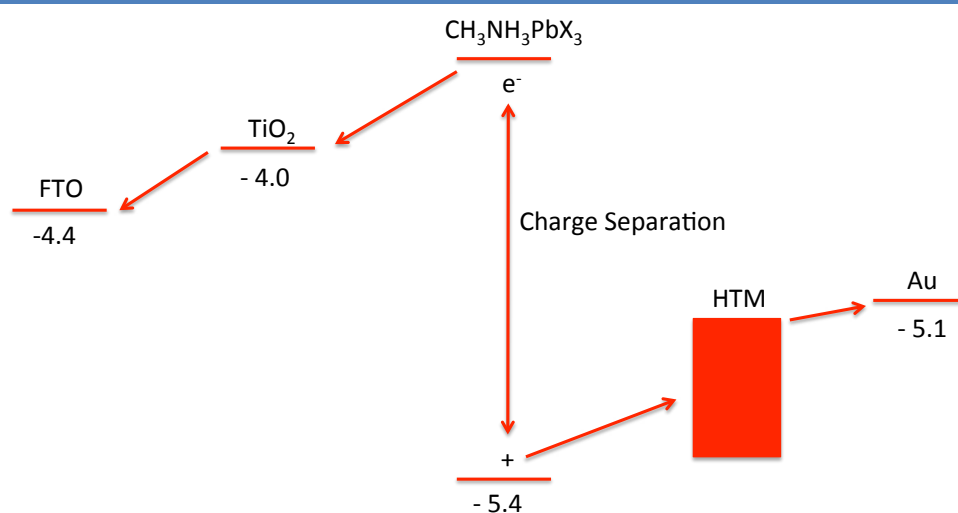


Figure 52 | Perovskite Solar Cell Energy Level Architecture The general perovskite mechanism involves photoinduced charge separation in the perovskite layer, followed by hole transport through the HTM to the gold electrode and electron transport to the FTO electrode.

The gold standard hole transport molecule in the field is 2,2',7,7'-tetrakis(N,N-di-p-methoxyphenylamine) 9,9'-spirobifluorene (spiro-OMeTAD)

⁷² Gratzel, M., *Nat Mater* **2014**, *13*, 838-842.

which contains a triarylamine redox center as the electroactive component. In this project, we tested the ability to replace the hole transport material (HTM) with triarylamines which have been carefully designed to produce conductive self-assemblies with the appropriate energy level offsets to match the perovskite solar cell design. Ideally, incorporation of conductive self-assemblies within the hole transport layer will lead to more efficient charge separation with less recombination and more efficient solar cell function overall. Towards this end, we have synthesized two sets of self-assembling molecules with triarylamine centers incorporating two or three redox centers designed specifically to have the appropriate energy level offsets for use in perovskite solar cells.

2. Synthesis And Characterization Of Self-Assembling Triarylamines With 2 And 3 Redox Centers

Triarylamine molecules containing two and three redox centers were designed for solar cell testing based on theoretical calculations of their energy levels (Figure 53). As was outlined in the introduction, it is critical to have appropriate energy level matching with the perovskite layer in order to have charge separation and consequently charge transport. Incorporation of the amide group was designed to aid in self-assembly by inducing a hydrogen bond interaction between molecules as well as to adjust the energy oxidation potential of the triarylamine redox centers. Subsequently, one may vary the pendant side-chain groups of the oxygen and observe the effect on the self-assembly and solar cell performance.

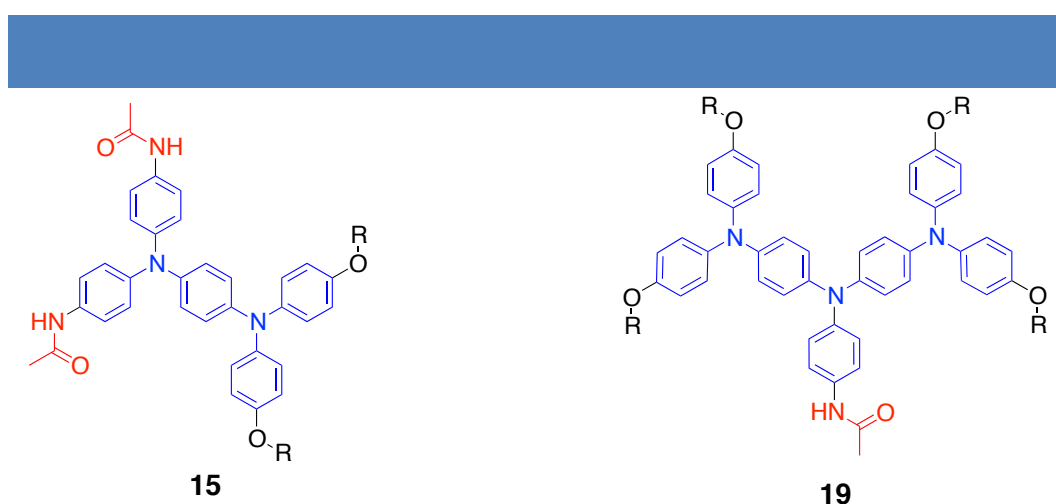
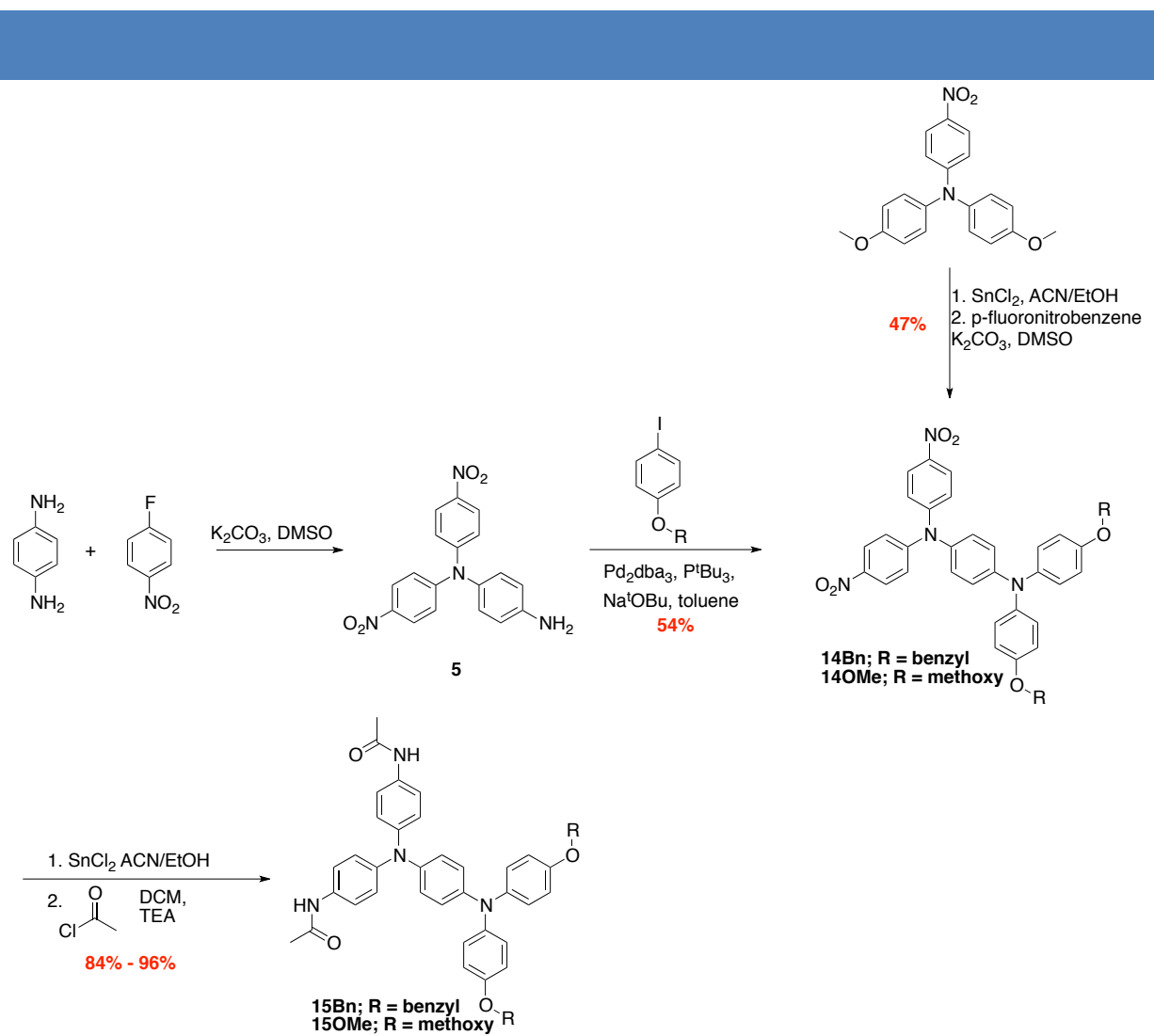


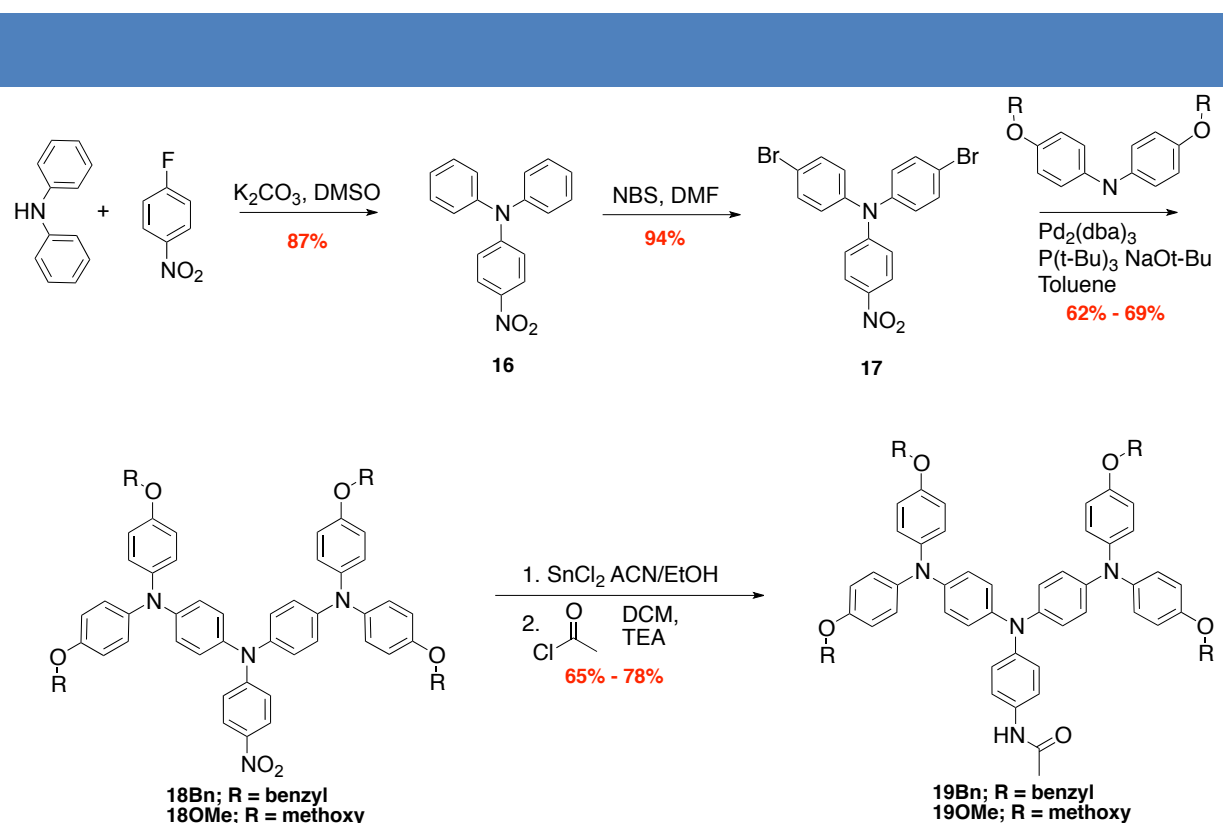
Figure 53 | General structure of the triarylamine derivatives used in this study. A two-redox centered version containing two amide groups (**15**) as well as a three-redox centered version containing one amide group (**19**). The synthesis of the benzyl ($R = \text{Bn}$) and methoxy ($R = \text{OMe}$) side-chains are reported.

The general synthetic scheme for the two-redox center triarylamine molecule is shown in scheme 3. The initial reaction is the same nucleophilic aromatic substitution used to synthesize the core unit for the tris-amide triarylamine molecule. Afterwards, the second redox center is built up by using a Buchwald-Hartwig palladium catalyzed cross-coupling. The iodinated benzene is prefunctionalized with the appropriate substitution at the phenolic position before the coupling. We were able to affect a double coupling to the aromatic amine in greater than 50% yield. Finally, the routine tin chloride reduction followed by amidation with acetyl chloride affords the final product. The synthetic details for the benzyl substituted and methoxy substituted compounds are reported in the appendix. Our experiments so far have been performed with the methoxy derivative, though we plan on testing the effect of different side-chain groups. We report the benzyl derivative synthetic procedure since it may be easily deprotected to the phenol derivative and subsequently functionalized with a variety of side-chain groups.



Scheme 3 | General synthetic scheme for the two-redox center triarylamine derivative **15**.

The general synthetic scheme for the three-redox center triarylamine is presented in scheme 4. The commercially available diarylamine is used to form the nitro substituted triarylamine building block **16** through the same nucleophilic aromatic substitution used in the previous synthesis. Next, bromination with N-bromosuccinimide at the free para positions gives the di-bromo triarylamine intermediate **17**. From here, the three-redox center molecule can be built up using the Buchwald-Hartwig coupling reaction with the diarylamine containing the appropriate substitution pattern. Finally, the reduction/amidation reaction sequence gives the amide-substituted product **19**.



Scheme 4 | General synthetic scheme for the three-redox centered triarylamine derivative, **19**. Two derivatives are described in the synthetic procedures, the benzyl and methoxy derivatives.

Absorption measurements were performed on the methoxy derivatives of the 2-center and 3-center triarylamine core molecules (**15OMe** and **19OMe**) in order to extrapolate the general behavior of these two groups of molecules. Samples were prepared in tetrachloroethane at a concentration of 0.05 mM. Figure 54a displays the non-irradiated absorbance spectra for these two molecules. The Tauc plot in figure 54b gives an optical energy gap of 3.0 eV for the 3-center molecule and 3.1 eV for the 2-center molecule. Figure 54c and figure 54d display the effect of photooxidation on the absorption spectra for the 3-center and 2-center compounds, respectively. Irradiation was performed with a 390 nm LED light 5 cm from the sample for up

to 30 s. Most notable is the appearance of a near infrared charge-transfer band due to intramolecular charge transfer between the redox centers in the triarylamine core. This implies incomplete oxidation of the molecules with the photoirradiation as there needs to be an unoxidized redox center to allow for charge transfer.

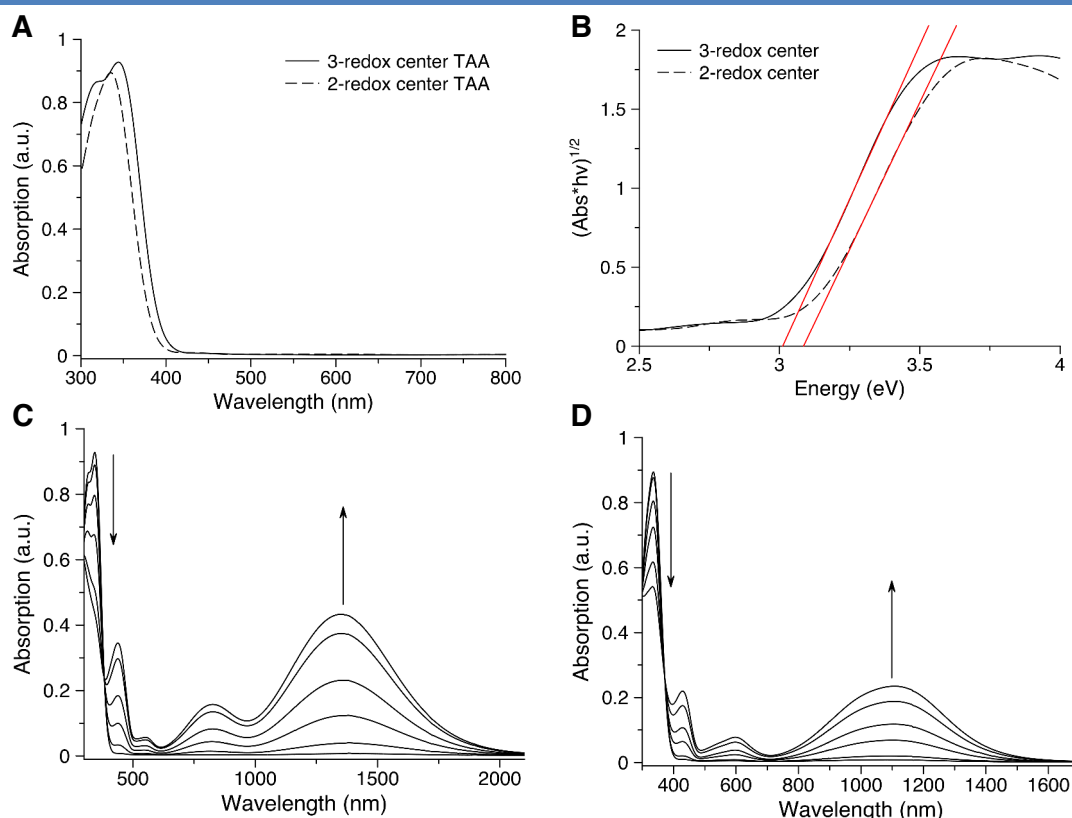


Figure 54 | Absorption spectrum of non-irradiated solutions of the methoxy-substituted versions of the 2-center **15OMe** and 3-center **19OMe** TAA compounds (**A**, 0.05 mM in tetrachloroethane). Tauc plot and extrapolation of the energy gap energy of the two molecules, 3.0 eV and 3.1 eV for the 3-center and 2-center molecule respectively (**B**). Absorption spectra during photooxidation with a 390nm LED light of the 3-center (**C**) and 2-center (**D**) TAAs (0.05 mM in tetrachloroethane). Illumination was performed 5 cm from the sample for a maximum of 30 seconds.

Cyclic voltammetry displayed two redox peaks for the 2-center compound **15OMe** and three redox peaks for the 3-center compound **19OMe** as shown in figure 55. From the onset of the first oxidation peak, one can calculate the HOMO level for each compound. The redox potential of the two-redox center compound is at 5.25 V (vs. vacuum). This corresponds to a HOMO energy level of 5.15 eV. For the three center compound, the initial oxidation occurs at 5.17 eV (vs. vacuum). This corresponds to a HOMO energy level of 5.04 eV. In contrast the tris-amide and mono-amide triarylamines display HOMO energy levels around 5.6-5.7 eV. For perovskite solar cells, we need a HOMO energy level below 5.4 eV. Clearly, the mono-amide and tris-amide substituted triarylamines are not valid candidates for use as hole

transport layers in perovskite solar cells, whereas the two-redox center and three-redox center molecules display the appropriate energy level offsets.

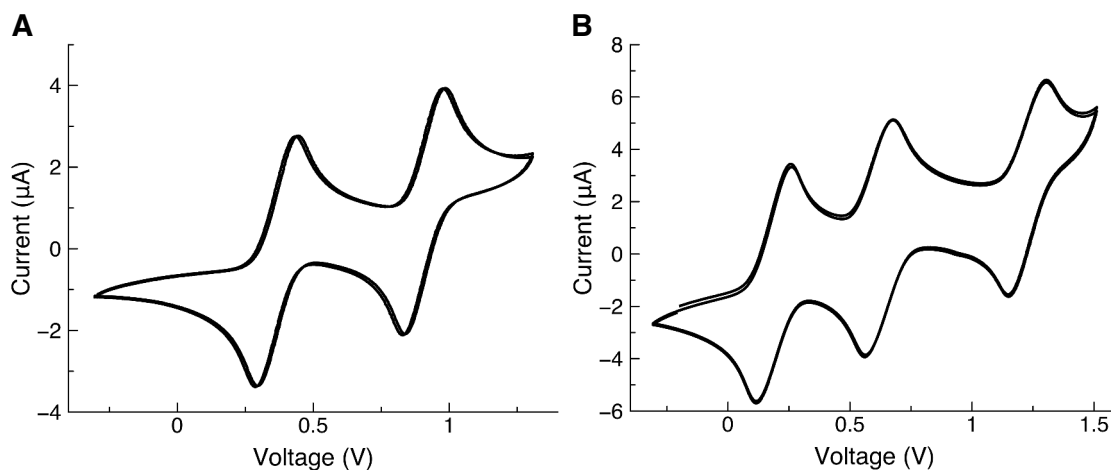


Figure 55 | Cyclic voltammetry runs were performed at 0.1V/s with 1mM tetrachloroethane solutions of the 2-center (A) and 3-center TAA (B) in TCE with 0.1M tetrabutylammonium hexfluorophosphate as the supporting electrolyte.

We tested the self-assembly of the molecules by irradiating in a solution of chloroform. The resulting TEM images, displayed in figure 56, demonstrates that both molecules undergo light-triggered self-assembly processes.

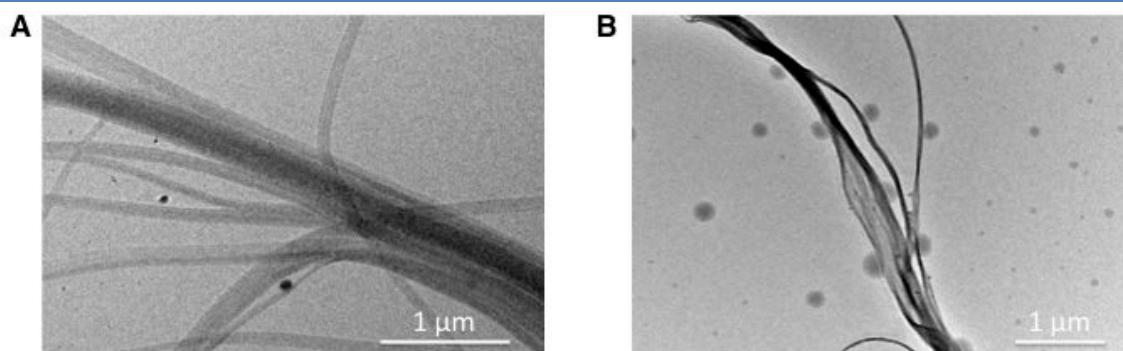


Figure 56 | TEM images of nanowires formed in solution from the two-center **15OMe** (a) and three-center **19OMe** (b) triarylamine molecules.

3. Solar Cell Performance

Initial results with perovskite solar cells incorporating self-assembling triarylamines as the hole-transport layer were prepared according to published procedures at the BASF facility in Ludwigshafen, Germany. Briefly, FTO (fluorine doped tin oxide) was coated on patterned

glass substrates upon which a layer of lead perovskite was spin coated (general formula $\text{CH}_3\text{NH}_3\text{PbX}_3$; X = Cl, Br, I). Then, self-assembling triaryamine molecules as the hole transport material (TAA-HTM) were spin-coated followed by evaporation of gold electrodes (see schematic below).

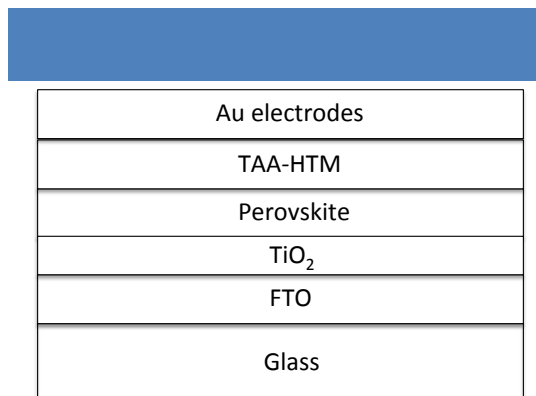


Figure 57 | General perovskite solar cell structural architecture.

Both the two-centered and three centered triaryamine compounds were tested in perovskite solar cells with this construction. Solutions for spin-coating were prepared in chlorobenzene and tetrachloroethane using the BASF recipe (60 mg/mL TAA + additives). Different oxidation techniques were tested: illumination in both chlorobenzene and tetrachloroethane as well as chemical oxidation in chlorobenzene. In general, chemical oxidation gave the worst results with illumination in tetrachloroethane giving the best results (Table 3, Figure 58).

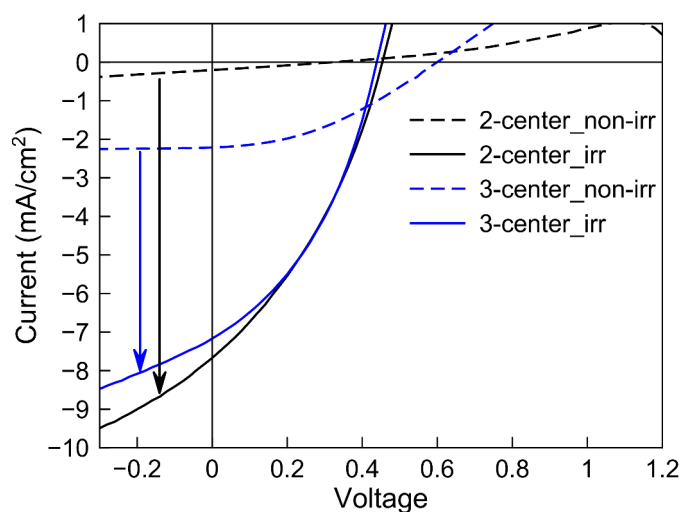


Figure 58 | Solar cell results on devices the day after fabrication showing a large increase in efficiency due to the light-triggered self-assembly (2-center is **15OMe** and 3-center is **19OMe**).

A control compound with an inappropriate energy level offset did not give a functioning solar cell under any of the conditions tested. The best results were obtained in tetrachloroethane which demonstrated a clear effect of photooxidation on the device output. The 3-center compound displayed an increase in efficiency from 0.6% to 1.2% upon illumination in tetrachloroethane. The 2-center compound needed to be codissolved with 10% methanol due to solubility issues at this concentration. The methanol should aid in inhibiting aggregation or assembly. Promisingly, the results displayed a change from a non-functioning device to 1.2% efficiency with the illuminated device. This is likely due to the effect of self-assembly as the 3-center compound has been observed to self-assemble without illumination. Additionally, the 2-center compound needed to be solubilized with 10% MeOH which may have aided in disrupting the assembly. Illumination had little effect on solar cells made from chlorobenzene solutions, with the three-center compound giving a 1.1% efficient cell and the two-center compound displaying 0.1%. Results are summarized in the table below along with the spiro-MeOTAD gold standard for comparison.

Sample (TCE)	Isc[mA/cm ²]	Voc[mV]	FF[%]	ETA[%]	ETA[%]	Sun[mW/cm ²]
Spiro gold standard	-16.04	780	63	9.2	7.8	101
2-center (15OMe)	-0.29	520	30	0	0	101
3-center (19OMe)	-3.36	540	35	0.4	0.6	101
3-center (19OMe) irradiated	-7.17	440	39	1	1.2	101
2-center (15OMe) irradiated	-7.67	460	34	0.8	1.2	101

Table 3 | Solar cell results for devices made from TCE solutions as measured the day after manufacturing. I_{sc} is the short circuit current, V_{oc} the open circuit voltage, FF the fill factor, and ETA the device efficiency. Efficiency recorded the same day of device manufacturing (first column). Efficiency recorded the day after device manufacturing (second column).

We have subsequently continued testing these molecules in collaboration with professor Michael Graetzel's group at the EPFL, in Lausanne Switzerland. When tested as before, with the additives that are standard in perovskite cell manufacturing, namely tert-butyl pyridine and lithium bis-trifluoromethanesulfonimide, we observed similar solar cell efficiencies as the first devices made at BASF (1.22%). However, when fabricating devices without the additives, we have observed large increases in the solar cell efficiencies. While the testing is

still ongoing, we have seen a vast improvement in the solar cell results, with upwards of 10% power conversion efficiencies.

4. Ongoing Work

We are continuing to work on improving the solar cell device results. Aside from finding conditions which give us the optimum working conditions for the solar cells, we are also trying to prove the effect of the self-assembly on the device performance. So far we have we have demonstrated a clear increase coming from light irradiation. The problem is trying to distinguish whether the increased performance derives from the partially oxidized triarylamine hole transport layer or from the self-assembly process. Towards finding a solution to this problem we are performing control experiments in solvents where we are sure the molecules do not self-assemble. By comparing the device performance from these molecules with the device performance from the non-irradiated and irradiated molecules, we should have a fairly good idea of the role of both oxidation and self-assembly plays on the efficiency of hole transport.

Chapter V Triarylamine-Nitronyl Nitroxide Derivatives as Stable Diradicals With Applications Towards Molecular Spintronics

1. Introduction

Due to the ability of the triarylamine core unit to be readily converted to its radical cation, we investigated the effect of attaching a pendant nitronyl nitroxide radical group. The rationalization behind this strategy is that due to the extensive delocalization of the triarylamine radical amongst the aromatic core units, there should be a strong through-bond coupling when a stable radical species is attached. Additionally, it has been shown that organic diradicals can be engineered to provide strong through-bond coupling by altering the conjugation and distance between the radical units.⁷³ The ultimate goal would be to create materials displaying organic magnetoresistance from these molecules.⁷⁴ Therefore, our objectives for this project were threefold: (1) to demonstrate a strong coupling between the oxidized triarylamine and the nitronyl nitroxide, (2) to control the strength and sign of the coupling by changing the substitution pattern on the molecule, and (3) to test whether we can observe a magnetoresistance effect with assembled stacks of these molecules.

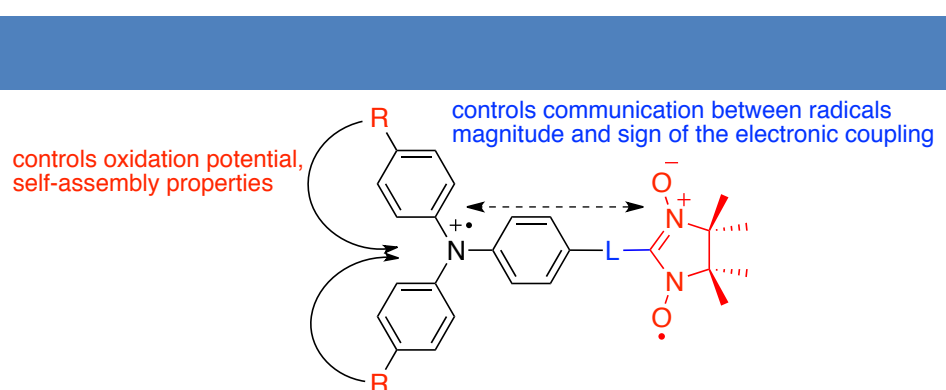


Figure 59 | General molecular design of the triarylamine-nitronyl nitroxide biradical species.

Towards these ends, extensive theoretical calculations were performed various triarylamine-nitronyl nitroxide (TAA-NN) derivatives that demonstrated very high ferromagnetic couplings (Figure 59). Additionally, a prototype TAA-NN molecule was successfully synthesized with high stability in ambient conditions. Additionally, the crystal

⁷³ Abe, M., Diradicals. *Chem. Rev.* **2013**, *113*, 7011-7088.

⁷⁴ Gu, H.; Zhang, X.; Wei, H.; Huang, Y.; Wei, S.; Guo, Z., *Chem. Soc. Rev.* **2013**, *42*, 5907-5943

structure was determined and initial magnetic measurements have confirmed the ferromagnetic interaction between the diradical species.

2. Density Functional Theory Calculations on Various Triarylamine-Nitronyl Nitroxide Derivatives

Diradicals are molecular compounds containing two spatially separated, unpaired electrons, which, depending on the nature of the bonding and geometry of the molecule can experience a coupling. This interaction is modeled by the Heisenberg-Dirac-Van Vleck Hamiltonian:⁷⁵

$$\hat{H} = -\sum_{i<j} J_{ij} \hat{S}_i \hat{S}_j \quad (28)$$

where \hat{S}_i and \hat{S}_j are the spin angular momentum operators on magnetic sites i and j and J_{ij} is the exchange coupling constant between them. The sign indicates whether the coupling is ferromagnetic or antiferromagnetic and the magnitude reveals the strength of the coupling. The strength of the coupling constant may be derived from the energy difference of the singlet and triplet states. Conveniently, density functional theory (DFT) methods may be used to compute the coupling values with relatively good accuracy. We performed calculations on triarylamine-nitronyl nitroxide derivatives in order to assess the strength and sign of the magnetic coupling between the oxidized triarylamine radical core and the nitronyl nitroxide radical. First, geometry optimizations were carried out using spin-polarized unrestricted density functional theory (UB3LYP) with the 6-311G(d,p) basis set on the uncharged and charged triplet states. Frequency calculations, stability checks, as well as population analysis were performed using these geometries. Single-point energy calculations were performed with the larger 6-311++G(d,p) basis set for the purposes of calculating the coupling constants. More accurate J-coupling values have been reported when using larger basis sets.^{76,77} The magnetic coupling constants were calculated using the broken symmetry approach proposed by Yamaguchi.⁷⁸

$$J = (E_{BS} - E_T) / \langle S^2 \rangle_T - \langle S^2 \rangle_{BS} \quad (29)$$

where E_{BS} and E_T are the energy of the broken symmetry singlet states and triplet states, respectively. While $\langle S^2 \rangle_T$ and $\langle S^2 \rangle_{BS}$ are the average spin square values. Therefore, the calculations were carried out on the triplet ($S = 1$) and singlet ($S=0$) states. In broken

⁷⁵ Paul, S.; Misra, A., *J. Chem. Theory and Computation* **2012**, *8* (3), 843-853.

⁷⁶ Ko, K. C.; Cho, D.; Lee, J. Y., *J. Phys. Chem. A* **2012**, *116* (25), 6837-6844

⁷⁷ Ko, K. C.; Son, S. U.; Lee, S.; Lee, J. Y., *J. Phys. Chem. B* **2011**, *115* (26), 8401-8408.

⁷⁸ Yamaguchi, K.; Jensen, F.; Dorigo, A.; Houk, K. N., *Chem. Phys. Lett.* **1988**, *149* (5-6), 537-542.

symmetry state calculations, to generate the appropriate BS wave functions, we used both “stable=opt” and “guess=mix” keywords. The “guess=mix” keyword allows the highest occupied molecular orbitals (HOMO) and the lowest unoccupied molecular orbitals (LUMO) to be mixed, and this removes the α,β spatial symmetries and generates a new initial guess, thereby generating the broken symmetry solution. This was a solution proposed by Noodleman to avoid the problem of spin contamination.⁷⁹

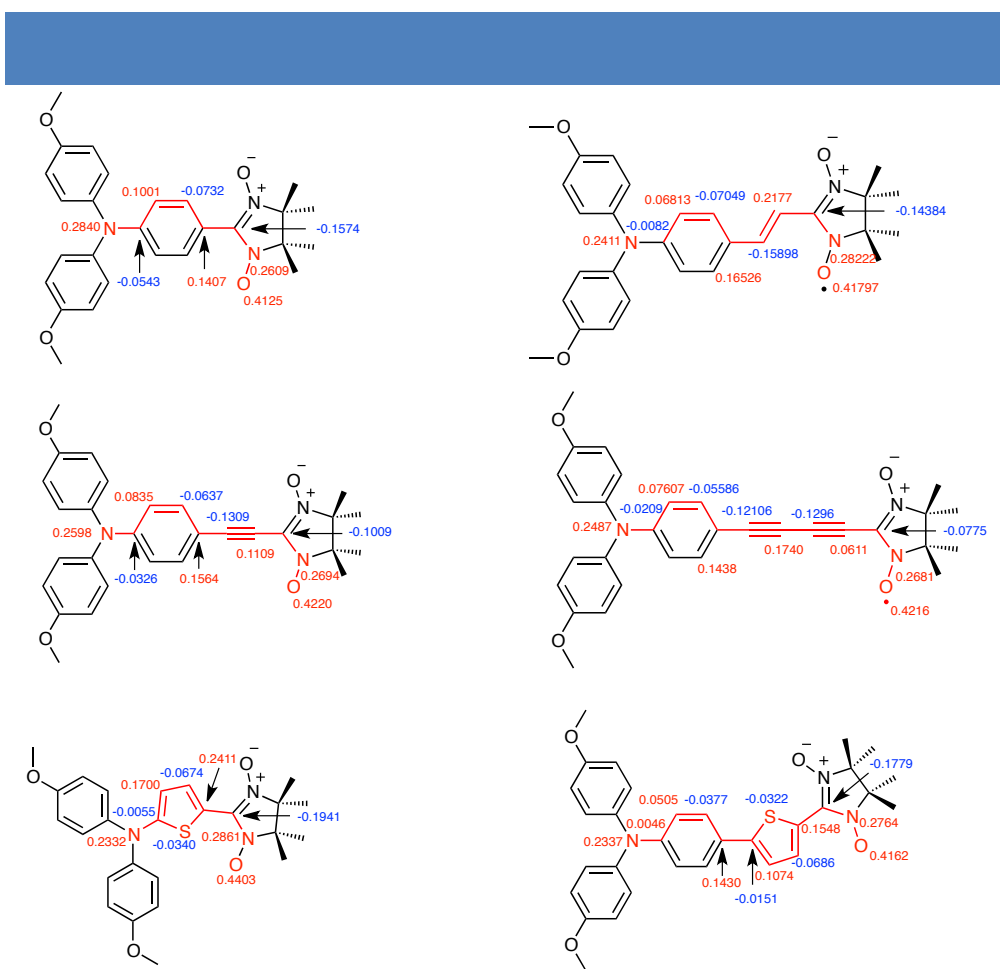


Figure 60 | Mulliken atomic spin densities from the triplet state calculated at the 6-311++G(d,p) level of six different triarylamine-nitronyl nitroxide derivatives. The sign on the respective atoms tells us the relative quantum number (+1/2 or -1/2).

In figure 60, the mulliken atomic spin density for the triplet state of six different triarylamine-nitronyl nitroxide derivatives are shown. The molecules all retain a two para-methoxy substitution on the aromatic rings adjacent to the nitronyl nitroxide aromatic ring, with only a change in the linking unit between the two. There are two important pieces of information to glean from the spin density distributions. First, is the magnitude of the values at the various atoms between the two radical centers is indicative of the strength of

⁷⁹ Noodleman, L.; Baerends, E. J. *J. Am. Chem. Soc.* **1984**, *106*, 2316 - 2320.

coupling. Specifically, the spin density at the connecting carbon on the nitronyl nitroxide has been directly linked to the coupling strength, something we can also confirm from our experimental calculations. The second important trait of the spin density calculations is the sign of the values. According to the spin alternation rule, the sign should flip at every atom, which is exactly what we observe. Qualitatively, without doing any calculations, the spin alternation rule predicts ferromagnetic coupling between the two radicals due to an odd number of atoms in between (likewise, an even number of atoms will give rise to antiferromagnetic couplings).

The values of the energies in the triplet and singlet form as well as the derived coupling constants are displayed in table 4. These values predict large ferromagnetic couplings for the structures. Larger linkers give lower coupling constants, as one would rationalize due to the larger distance between the two radicals. For example, the TAA-NN without a linker unit has a coupling value of 1284 K, whereas the molecule with an alkyne linker has a lower coupling value at 724 K, and the bisalkyne even lower still at 552 K. Interestingly, the largest projected coupling constant is between the diarylthiophene-nitronyl nitroxide molecule at 1708 K.

Linker	E_T	$\langle S^2 \rangle_T$	E_{BS}	$\langle S^2 \rangle_{BS}$	J (cm ⁻¹)	J (K)
None	-1512.13583021	2.075989	-1512.13093524	0.872188	892.4413022	1284.088205
Alkene	-1589.568902	2.097943	-1589.566081	0.752405	460.125232	662.051
Alkyne	-1588.304893	2.091337	-1588.3018548	0.765832	503.0428968	723.8027292
Bisalkyne	-1664.480316	2.105649	-1664.477978	0.768882	383.778137	552.199
Diarylthiophene	-1832.9055633	2.063596	-1832.8990783	0.864704	1187.173639	1708.16351
TAA-thiophene	-2064.0218286	2.085093	-2064.016808	0.958059	977.6550086	1406.697854

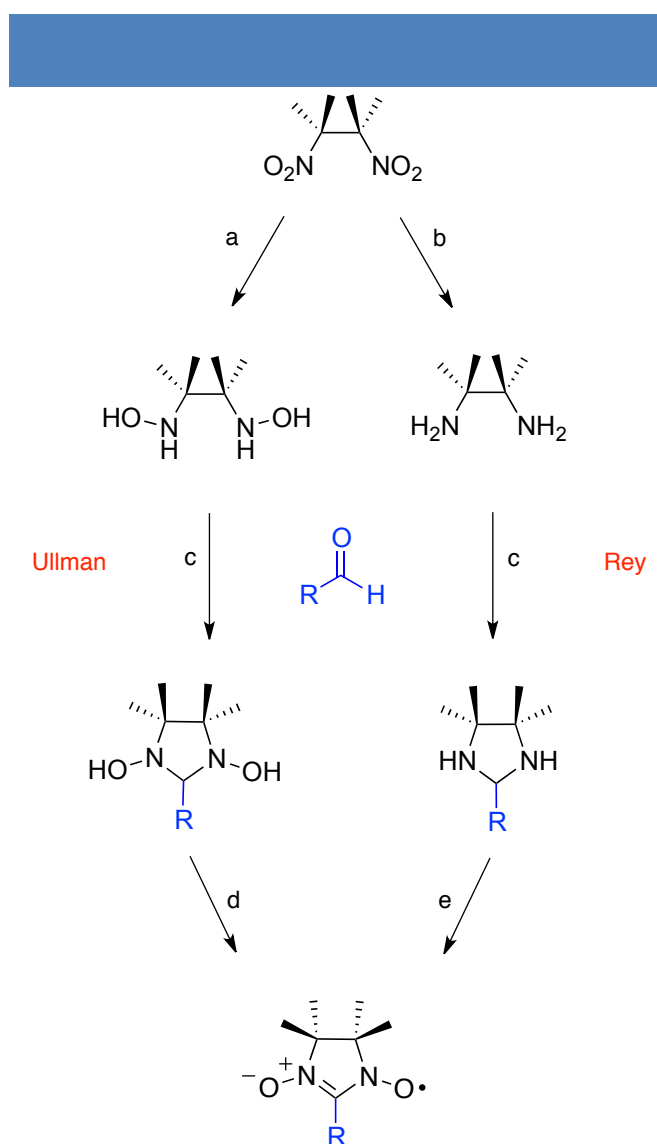
Table 4 | Energy values for the six derivatives as well as the coupling constants, all predicting strong ferromagnetic interactions between the radicals.

3. Synthesis of Triarylamine-Nitronyl Nitroxide Derivatives

There are two synthetic strategies towards synthesizing nitronyl-nitroxide derivatives. In scheme 5 the outline of two synthetic methods is shown from the literature. The first method was devised by Ullman⁸⁰ in 1972 and involves the reduction of the commercially available

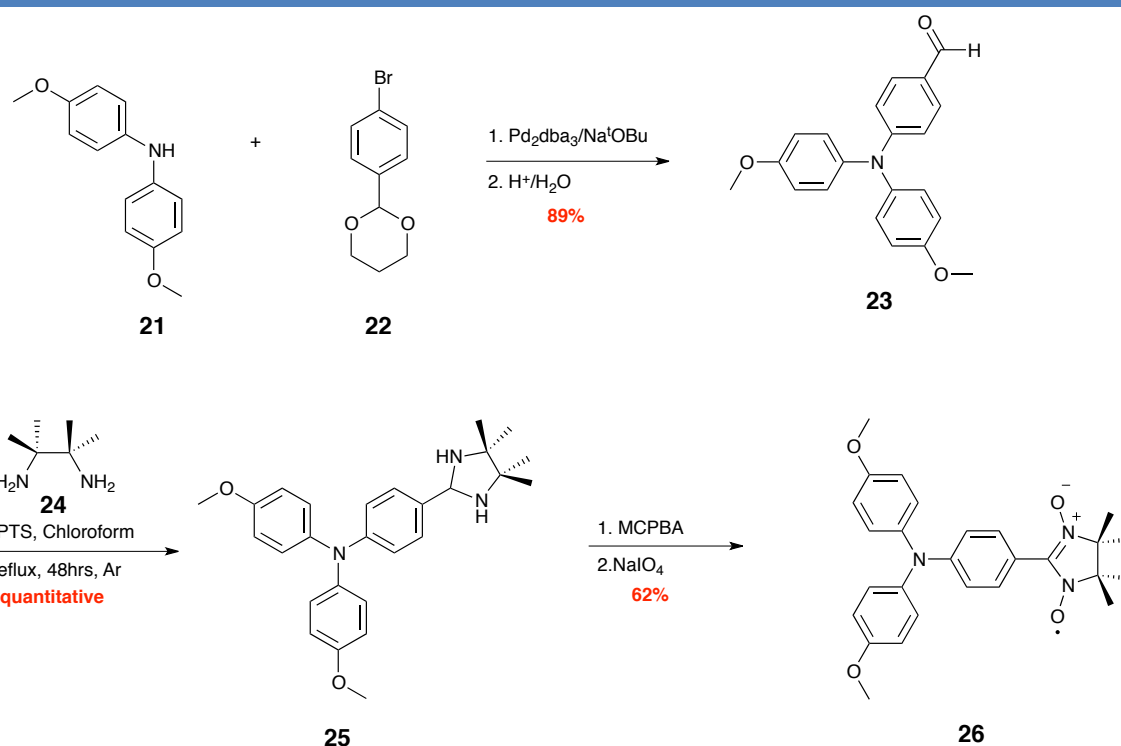
⁸⁰ Ullman, E. F.; Osiecki, J. H.; Boocock, D. G. B.; Darcy, R., *J. Am. Chem. Soc.* **1972**, *94* (20), 7049-7059.

dinitro compound into the dihydroxylamine, which is then reacted with an aldehyde to form the cyclic intermediate, which can be easily oxidized with NaIO_4 or MnO_2 . An alternative procedure has been proposed by Rey⁸¹ in 2001 and it involves the formation of the cyclic aminal through the diaminobutane instead of the dihydroxylamine. Though, higher yields have been reported with this method, the oxidation involves the use of MCPBA, which has compatibility issues with a wide variety of functional groups. Thus both methods useful to the synthetic chemist depending on the molecule one is trying to synthesize.



⁸¹ Hirel, C.; Vostrikova, K. E.; Pécaut, J.; Ovcharenko, V. I.; Rey, P., *Chem. Eur. J.* **2001**, 7 (9), 2007-2014.

The triarylamine-nitronyl nitroxide without a linking group was synthesized in high yield according to scheme 6. First, precursor **21** was synthesized in 87% yield by a copper catalyzed Ullman reaction between 4-aminoanisole and 4-iodoanisole, while protected precursor **22** was synthesized in 97% yield through the reaction of 4-bromobenzaldehyde and 1,3-propanediol in a Dean-Stark apparatus. The triarylamine-aldehyde **23** was then synthesized through a Buschwald-Hartwig palladium catalyzed reaction, followed by an acid deprotection in 89% yield. Refluxing for 48 hours in chloroform with 2,3-diamino-dimethyl butane gave the cyclic aminal **25** in quantitative yield. Finally, oxidation with MCPBA, followed by sodium periodate gave the TAA-NN product **26** which was purified by column chromatography and then crystallized from acetonitrile to afford purple needles in 62% yield.



Scheme 6 | Synthetic route to the methoxy substituted triarylamine-nitronyl nitroxide compound.

4. Crystal Structure

X-ray quality crystals were grown by dissolving the triarylamine-nitronyl nitroxide **26** in acetonitrile close to the saturation point. The solution was degassed with argon for several minutes and then heated to 50°C and allowed to slowly cool to room temperature to initiate nucleation. After several days of slow evaporation, crystals large enough for X-ray diffraction

were recovered. The examined crystal was a purple prism with dimensions of 3.5 mm x 2 mm x 1.2 mm. The crystal system is orthorhombic and the space group is Pbcn (Table 5). The R-factor is 4.1% demonstrating an excellent fit of the structural model with the diffraction pattern.

Molecular Formula	C ₂₇ H ₃₀ N ₃ O ₄
Formula Weight	460.54
Temperature (K)	173 K
Crystal System	Orthorhombic
Space Group	Pbcn
Unit Cell dimensions	a = 16.2532 (11) b = 14.1068 (10) c = 10.5920 (7)
	$\alpha = 90^\circ$
	$\beta = 90^\circ$
	$\gamma = 90^\circ$
Volume (Å ³)	2428.5 (3)
Z	4
Number of reflections	2935
R	0.0411
Goodness of Fit	1.007

Table 5 | X-ray diffraction data for the TAA-NN crystal.

The crystal structure packing depicts the formation of stacks of triarylamine cores in a snowflake configuration with alternating nitronyl nitroxide arrangement (180° dihedral angle; figure 61). This stacking structure is critical to ensure minimum stacking distance between the triarylamine cores while removing steric interference due to the bulky nitronyl nitroxide groups. Additionally, from the magnetic perspective, separating the nitronyl nitroxide groups cuts down on possible through-space magnetic coupling that might occur between nitronyl nitroxides if they were in close proximity. Relevant intermolecular stacking distances include (1) a nitrogen-nitrogen distance of 5.309 Å and (2) a 3.722 Å distance between the carbon adjacent to the nitrogen on the aromatic ring functionalized with the nitronyl nitroxide and an ortho carbon on a non-functionalized aromatic ring. This distance is important, as it is short enough to allow coupling between the triarylamine centers, and therefore a conductive pathway through the crystal.

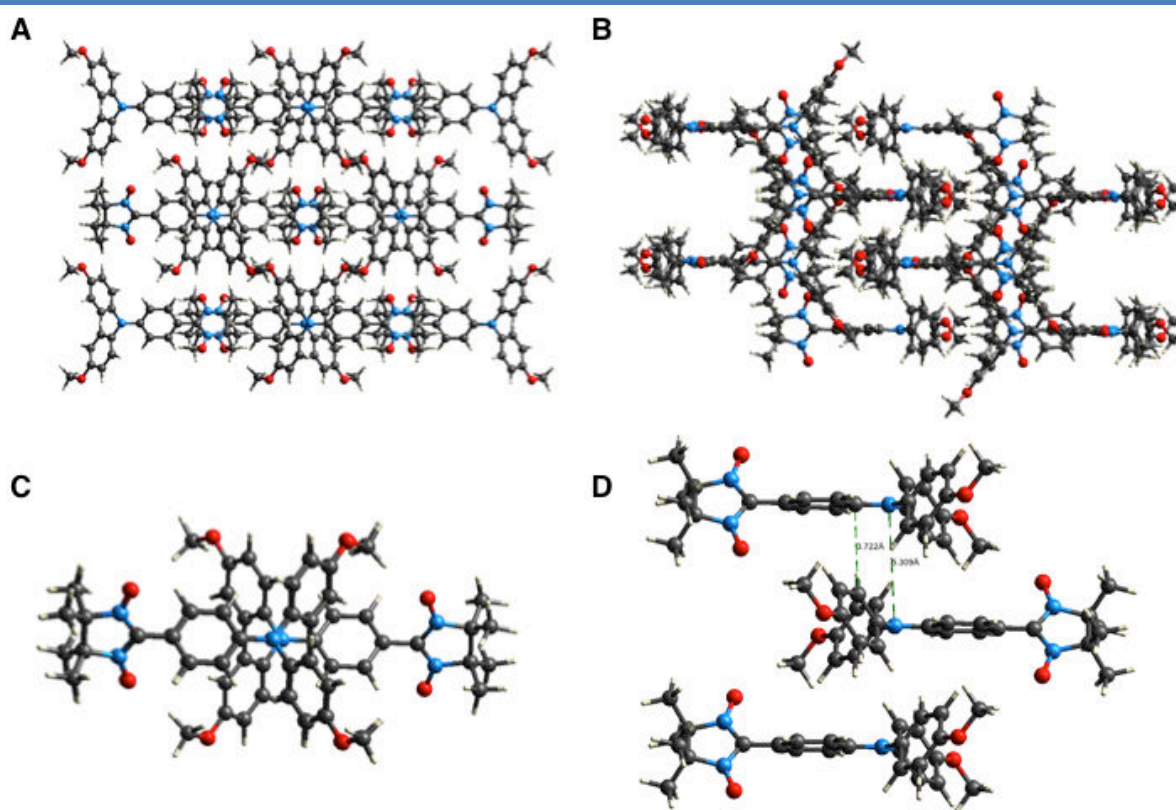


Figure 61 | Crystal structure packing of the TAA-NN. Views along the stacking direction (a, c) and cross-sectional view of the columnar stacking (b, d).

The Hirshfeld surface of a molecule within the crystal is presented in figure 62 (an overview of the method of defining the Hirshfeld surface is presented in chapter 8). The red spots indicate regions of closest packing to adjacent molecules, followed by the regions colored in white, and finally the blue regions are relative distant from neighboring molecules. The crystal structure packing appears to be driven by the hydrogens located at the meta position on each aromatic ring as well as the methoxy oxygens and the nitronyl nitroxide oxygens. Overall, close interactions seem to occur laterally on the molecule, i.e. on the plane perpendicular to the stacking direction. It is interesting to note the contrast in the stacking structure of this molecule with the TSOF stacking structure (see chapter 8). In that case the amide groups drove the crystal structure arrangement. Additionally, the triarylamine molecules were situated more closely together in the columns than with this molecule. Here, it is apparent that the stacking structure is likely driven to minimize steric repulsion due to the bulky nitronyl nitroxide group, which is achieved by placing the bulky side group at alternating 180° positions along the stacks. The fact that we still observe columnar assembly and not a ladder type stacking arrangement also indicates the relatively strong aromatic stacking driving force present in these molecules. This is likely enhanced, not just from the

point of view of aromatic stacking, but also from the point of view of the propeller shape (geometry) of the triarylamine core unit that lends itself to stacking arrangements as opposed to off-center ladder type structures.

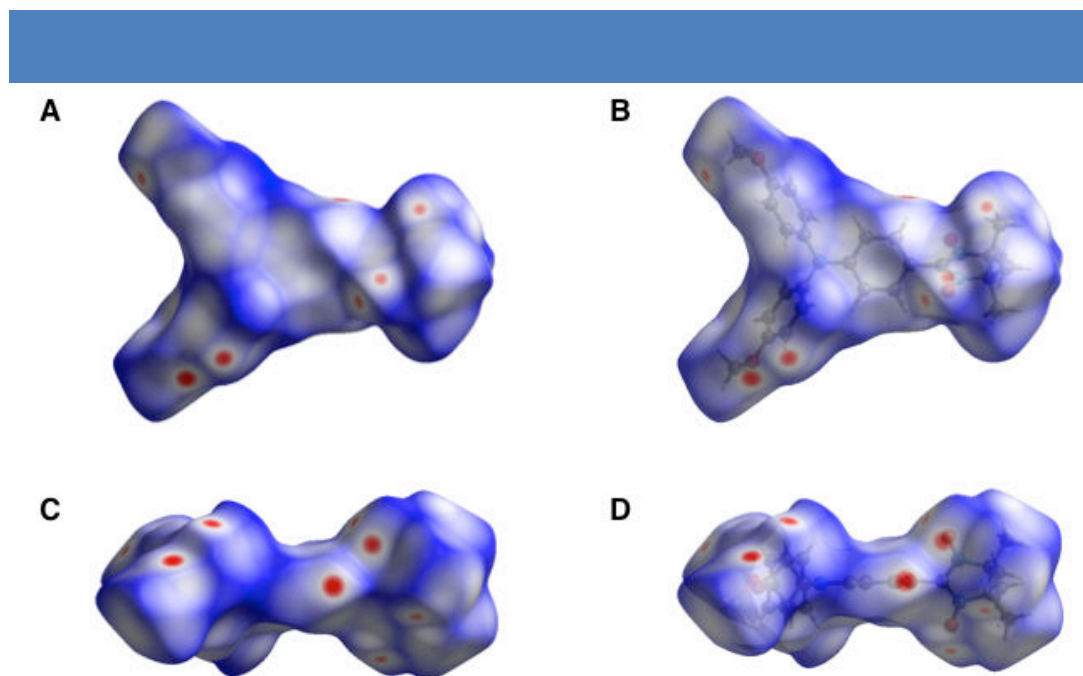


Figure 62 | Hirshfeld surfaces depicting the tight packing of the TAA-NN molecule inside the crystal.

5. Characterization

Absorption measurements of **26** were taken in a DCM solution (Figure 63a). Aside from the main triarylamine peak around 350 nm, we observe the weak absorbance signal from the nitronyl nitroxide in the region of 600 nm – 750 nm.

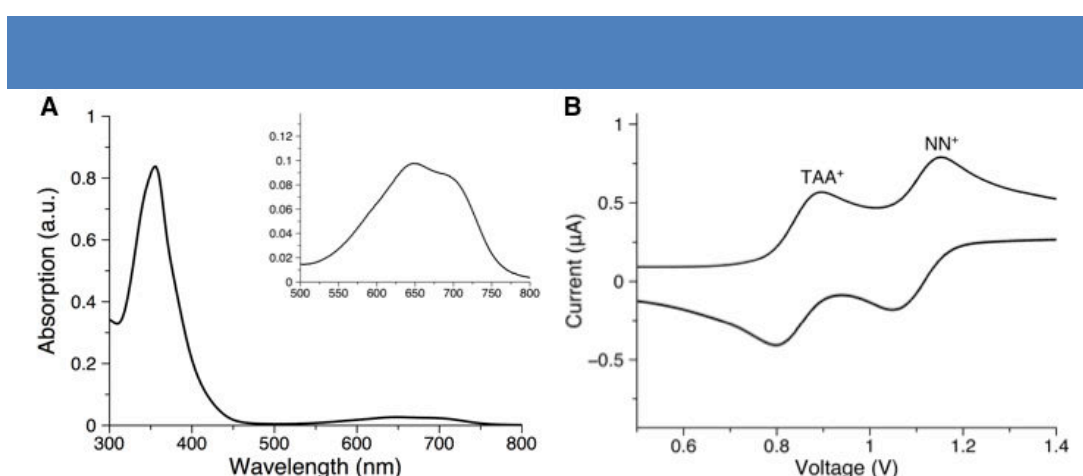


Figure 63 | Absorbance measurements of a 0.025mM dichloromethane solution (a; insert: 0.1mM solution highlighting the lower energy transitions due to the nitronyl nitroxide). Cyclic voltammety in dichloromethane referenced against decamethylferrocene as an internal standard (b).

Cyclic voltammetry (Figure 63b) displayed two reversible peaks corresponding to the triarylamine oxidation followed by the nitronyl nitroxide oxidation peak. Importantly, the fact that the triarylamine peak comes before the nitronyl nitroxide oxidation peak supports the ability to oxidize the triarylamine core and have a stable diradical species. If the triarylamine oxidation potential were higher than the nitronyl nitroxide peak, we would not be able to attain the diradical species, as the nitronyl nitroxide radical would be oxidized to the oxide species by the time the triarylamine was oxidized. Initial EPR experiments have been performed on the oxidized TAA, which was oxidized by SbCl_5 . Low temperature measurements detected a half field signal indicative of a diradical species exhibiting exchange coupling (Figure 64a). A plot of the temperature dependence confirms a ferromagnetic interaction between the radical species (see chapter 6 for a full description of the variable temperature magnetic measurements).

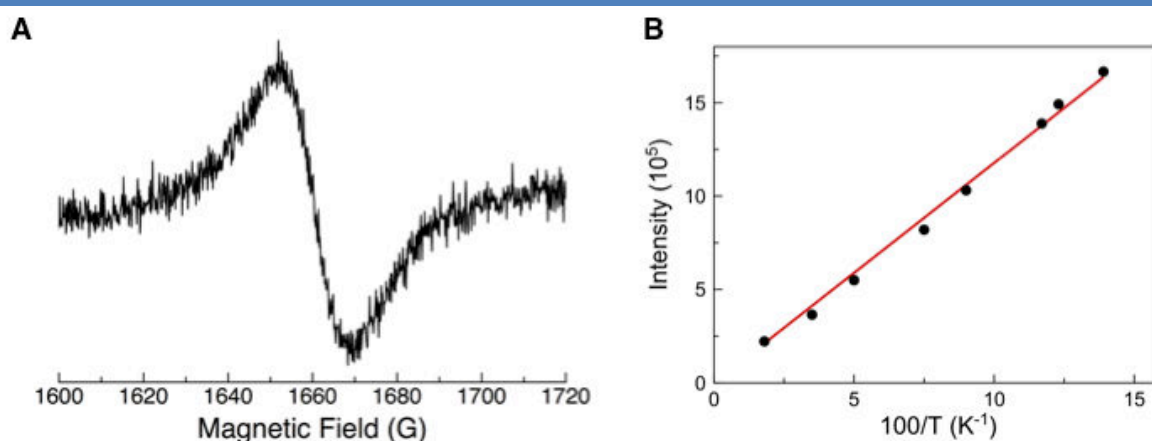


Figure 64 | Half-field EPR signal indicating exchange coupling between the two radicals (a). Curie plot indicating a ferromagnetic interaction between the triarylamine radical cation and the nitronyl nitroxide moiety (b).

6. Conclusions

We have successfully been able to elucidate through computational calculations and the synthesis of a TAA-NN prototype molecule that triarylaminines can be used as building blocks for organic magnetic materials. The molecule presented here can be stably oxidized to the diradical species with a ferromagnetic interaction. Theoretical calculations support the strong ferromagnetic coupling achievable by using this motif. We hope that future experimental magnetic measurements can elucidate the precise coupling value for comparison to the

computational calculations. Additionally, we hope that future experiments will be able to demonstrate a magnetoresistance behavior over the conductivity through the crystal due to the exchange coupling interaction.

Chapter VI: Healable Supramolecular Polymers As Organic Metals

1. Introduction

In this chapter, we elucidate another class of self-assembling triarylaminines, specifically those based on tris-amide substituted triarylaminines (TATA) that display magnetic, optical, and electrical signatures of delocalized, metallic band structure. Metallic organic polymers sharing the electrical, electronic, magnetic, and optical properties of metals are still very scarce although very promising for the development of a number of technologies such as transparent electrodes,⁸² printed electronic circuits and interconnects,^{83,84} thermoelectric materials,^{85,86} or memory devices.⁸⁷ To reach such properties, oxidative or reductive doping should produce unpaired electrons that open a partially filled conduction band where charge carriers drift with minimal scattering, as is the case in metals.⁸⁸ Defects enormously affect such conductivity, resulting in localized electronic states which alter the transport mechanism from band-like to undesired thermally activated hopping.⁸⁹ There currently exist only a few organic structures have reached the landmark of metallic conductivity.⁹⁰ For conjugated polymers, chain-ordered polyaniline with a low density of structural defects was recently obtained by dispersion synthesis, showing a dramatic transition from an insulating to a metallic material upon doping, and with an increase in conductivity over 9 orders of magnitude.⁹¹ Still, the poor solubility of doped polyaniline limits its use for a number of processing techniques. Another kind of organic metal is based on charge transfer complexes such as TTF-TCNQ salts,⁹² which are single-crystals and lack the processability and

⁸² MacDiarmid, A. G. *Angew. Chem., Int. Ed.* **2001**, *40*, 2581–2590.

⁸³ Fabretto, M. V.; Evans, D. R.; Mueller, M.; Zuber, K.; Hojati-Talemi, P.; Short, R. D.; Wallace, G. G.; Murphy, P. J. *Chem. Mater.* **2012**, *24*, 3998–4003.

⁸⁴ Xia, Y.; Sun, K.; Ouyang, J. *Adv. Mater.* **2012**, *24*, 2436–2440.

⁸⁵ Singh, M.; Haverinen, H. M.; Dhagat, P.; Jabbour, G. E. *Adv. Mater.* **2010**, *22*, 673–685.

⁸⁶ Siringhaus, H.; Kawase, T.; Friend, R. H.; Shimoda, T.; Inbasekaran, M.; Wu, W.; Woo, E. P. *Science* **2000**, *290*, 2123–2126.

⁸⁷ Bubnova, O.; Khan, Z. U.; Wang, H.; Braun, S.; Evans, D. R.; Fabretto, M.; Hojati-Talemi, P.; Dagnelund, D.; Arlin, J.-B.; Geerts, Y. H.; Desbief, S.; Breiby, D. W.; Andreasen, J. W.; Lazzaroni, R.; Chen, W. M.; Zozoulenko, I.; Fahlman, M.; Murphy, P. J.; Berggren, M.; Crispin, X. *Nat. Mater.* **2014**, *13*, 190–194.

⁸⁸ Bubnova, O.; Khan, Z. U.; Malti, A.; Braun, S.; Fahlman, M.; Berggren, M.; Crispin, X. *Nat. Mater.* **2011**, *10*, 429–433.

⁸⁹ Hoffmann, S. T.; Jaiser, F.; Hayer, A.; Bäessler, H.; Unger, T.; Athanasopoulos, S.; Neher, D.; Köhler, A. *J. Am. Chem. Soc.* **2013**, *135*, 1772–1782.

⁹⁰ Kohlman, R. S.; Zibold, A.; Tanner, D. B.; Ihas, G. G.; Ishiguro, T.; Min, Y. G.; MacDiarmid, A. G.; Epstein, A. *J. Phys. Rev. Lett.* **1997**, *78*, 3915–3918.

⁹¹ Lee, K.; Cho, S.; Heum Park, S.; Heeger, A. J.; Lee, C.-W.; Lee, S.-H. *Nature* **2006**, *441*, 65–68.

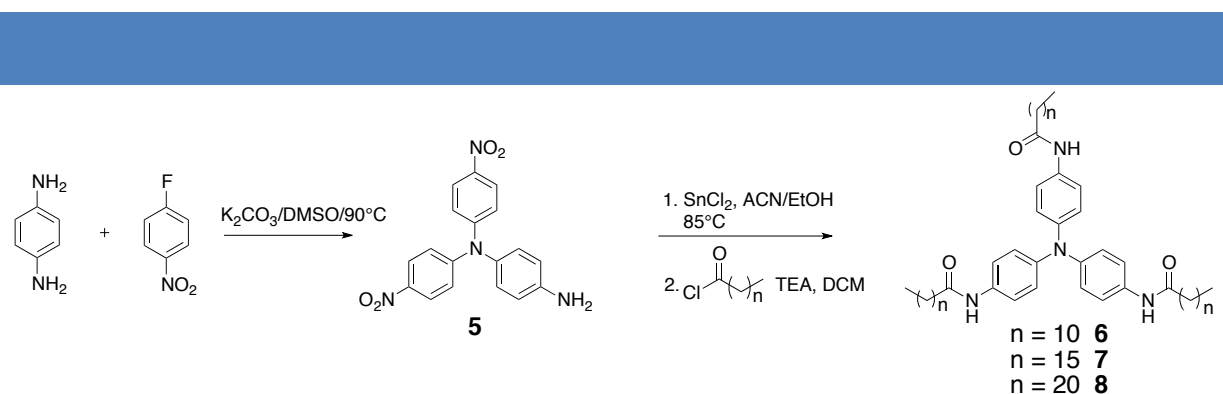
⁹² Cohen, M. J.; Coleman, L. B.; Garito, A. F.; Heeger, A. *J. Phys. Rev. B* **1974**, *10*, 1298–1307.

mechanical properties required by flexible electronic devices.

The TATA self-assemblies that we describe are very soft and kinetically labile supramolecular triarylamines, i.e., in which reorganization of the molecular units can take place with a relatively low activation energy. In such a configuration, the reversible nature of the supramolecular interactions can in principle correct structural defects (i.e., lateral or rotational misalignments of the stacks) by reaching a lower energetic state under thermodynamic control (self-healing polymers).^{93,94} A proper balance between order and mobility leads to materials presenting a unique combination of functionalities, namely extended metallic character with soft mechanical and defect-healing properties.

2. Physical Characterization of Tris-amide Triarylamine Self-assemblies

Tris-amide triarylamines (TATA) were synthesized with an average three-step yield between 49% and 61%. Scheme 7 depicts the synthetic route, where the triarylamine core is built up using a nucleophilic aromatic substitution reaction between p-phenylenediamine and 1-fluoro-4-nitrobenzene. Reduction with tin chloride affords the quasi-stable tris-amino triarylamine intermediate, which is quickly amidated to afford the corresponding tris-amide triarylamine. The generality of this synthetic route allows for a myriad of functionalized TATA molecules to be synthesized using the same core synthetic sequence, which can then be coupled to the desired functionalization through robust amidation methodology.



Scheme 7 | Synthetic route to tris-amide triarylamines (TATA: $n = 10, 15, 20$ for TATA **6**, **7**, **8**). The average yield for the three-step process was between 49% and 61%.

Three symmetrical TATA derivatives were synthesized for this study with varying alkyl chain lengths, **6** (10 methylene carbons), **7** (15 methylene carbons), and **8** (20 methylene carbons). At a concentration of 5 mM in a deuterated 5:3 methanol:toluene mixture, **6** is

⁹³ Cordier, P.; Tournilhac, F.; Soulie-Ziakovic, C.; Leibler, L. *Nature* **2008**, *451*, 977–980

⁹⁴ Yang, Y.; Urban, M. W. *Chem. Soc. Rev.* **2013**, *42*, 7446–7467

soluble and a full NMR spectrum can be recorded (Figure 65). Interestingly, upon the addition of deuterated chloroform (5 vol %) as an electron acceptor, it is possible to trigger a self-assembly process by a pulse of white light which oxidizes a catalytic quantity of TATA to its radical cation TATA^{•+}. Aggregation of these radicals at a critical nucleation concentration promotes the stacking of neutral TATA molecules in a subsequent growth process. The clear signature of this self-assembly is the disappearance of the **a**, **b**, and **c** resonance signals due to a strong π -stacking between TATA cores and resulting in an anisotropic columnar system kept soluble by lateral flexible alkyl chains (Figure 65). In a variety of pure organic solvents (chloroform, acetonitrile, acetone, or toluene), ¹H NMR reveals the direct self-assembly of **6-8** without the need of light. Evidence for intermolecular hydrogen bonding was observed by infrared spectroscopy, which displays the characteristic shifts of the amide stretching frequencies with the N–H and C=O stretching vibration occurring at 3291 and 1654 cm⁻¹, respectively.⁹⁵

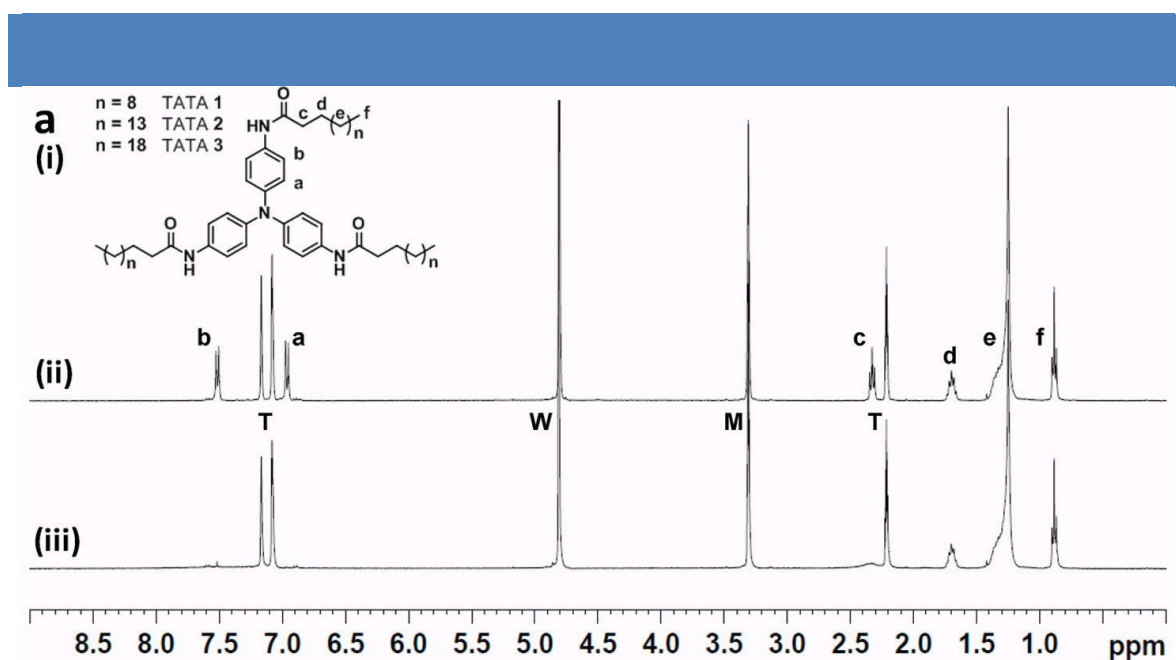


Figure 65 | ¹H NMR spectra of TATA **6** in a 5:3 methanol-*d*₄:toluene-*d*₈ mixture, in the presence of CDCl₃ (5 vol %) before (ii) and after (iii) light irradiation (W, M, and T are the residual resonance peaks for water, methanol, and toluene, respectively).

Organogelation was observed for the TATA compounds, which was investigated using tube-inversion and differential scanning calorimetry (DSC) experiments. A decreasing critical

⁹⁵ Non-hydrogen-bonded amides have N-H stretching frequency between 3400 and 3500 cm⁻¹ as opposed to 3350–3100 cm⁻¹ for hydrogen bonded amides. Likewise the C=O stretch shifts from around 1685 to 1650 cm⁻¹ upon hydrogen bonding. The IR frequency shifts we report for both functional groups correspond to the presence of hydrogen bonded amides. See: Pretsch, E.; Bühlmann, P.; Badertscher, M. *Structure Determination of Organic Compounds*, 4th ed.; Springer: New York, 2009.

gelation concentration and an increasing melting enthalpy was observed as the alkyl chain length was increased, with **6** displaying a melting enthalpy of 7.6 kJ/mol at 35.7°C, **7** displaying a melting enthalpy of 14.4 kJ/mol at 42.05°C, and **8** displaying a melting enthalpy of 22.3 kJ/mol at 47.86°C. Likewise, the critical gelation concentrations decrease with increasing alkyl chain length from 17.9 mM to 9.1 mM to 5.6 mM, respectively for **6**, **7**, and **8** gels in chloroform. The DSC profiles display a sharp endothermic peak for the melting process, while the cooling curves display first a shallow endothermic event about 20°C below the melting temperature, which is immediately followed by a broad exothermic transition (Figure 66). This points to a gelation occurring, as a second order process upon cooling while melting is a first order process.

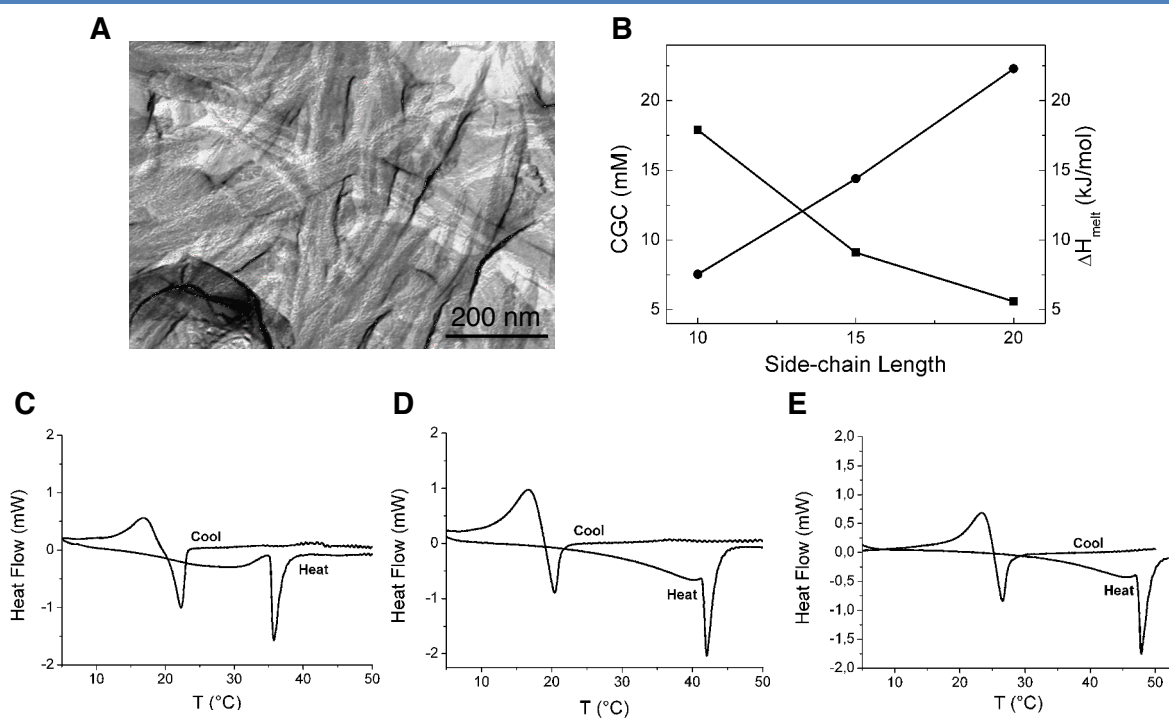


Figure 66 | Organogelation properties of TATA **6/7/8**. (a) Freeze-fracture TEM images of native TATA **7** fibers in the gel state. (b) Decreasing critical gelation concentration (CGC; chloroform) and increasing melting enthalpy were observed as the side-chain length was increased. (c-e) Differential Scanning Calorimetry (DSC) traces from the second pass of chloroform gels taken at 1 °C/min for (c) TATA **6** (d) TATA **7** and (e) TATA **8**.

Insight into the structure of this self-assembly is first given by freeze fracture transmission electron microscopy (FFTEM) in the gel state (Figure 66), and by atomic force microscopy (AFM) of cast films obtained from dilute chloroform solutions (Figure 67). Well-defined fibers of more than ten micrometers long and of high persistence length are characteristic of such compounds. For **6**, high resolution AFM shows a diameter of 16(\pm 3.0)

Å for the individual fibers (Figure 67d), which also present a twisted periodic pattern of $30.0(\pm 2.0)$ Å along their main axis.

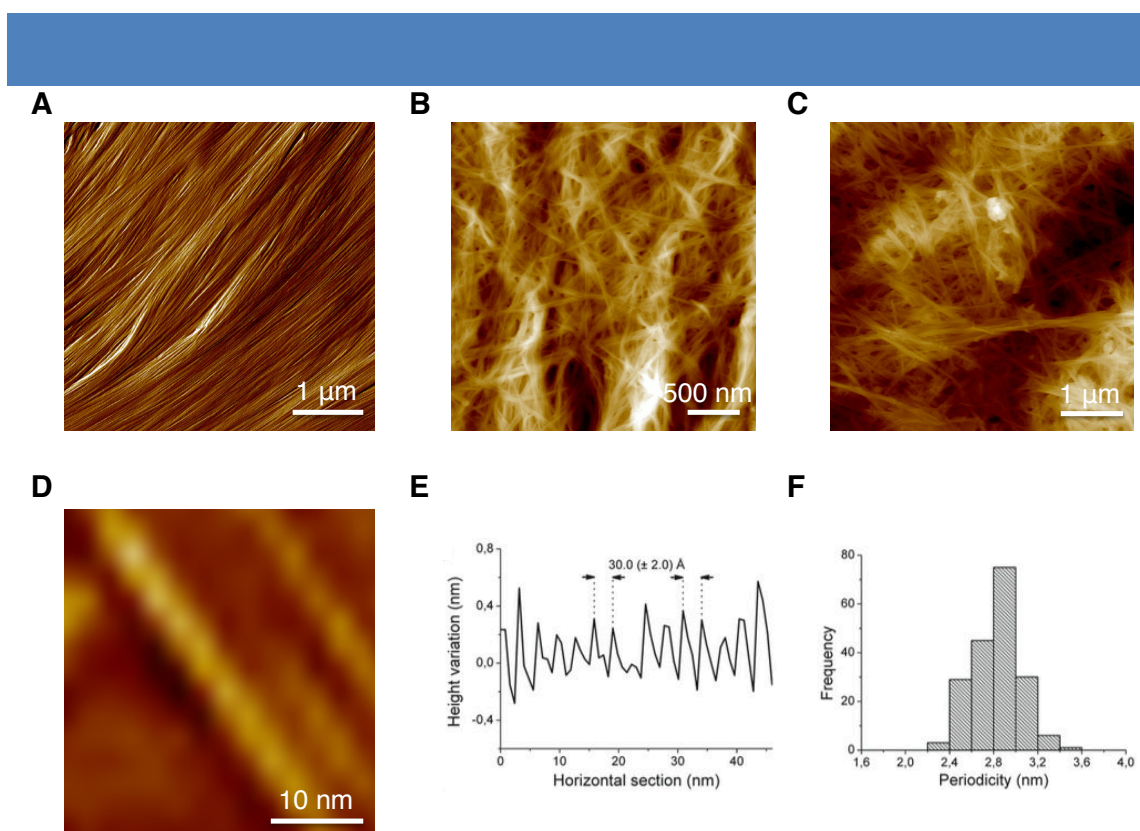


Figure 67 | AFM characterization of the TATA fibers. (a) Peak force image of fibers formed from TATA **6**. (b,c) AFM height images of fibers formed from TATA **7** (b) and TATA **8** (c). (d) High resolution AFM image of a single nanofiber. (e) Height variation profile along the longitudinal direction of a single fiber. (f) Histogram of the observed periodicity observed by AFM.

A model of the molecular assembly was built up using complementary small angle and wide-angle X-ray scattering (SAXS and WAXS; Figure 68), together with density functional theory (DFT).^{96,97,98} Strong 100 scattering peak at 0.215 \AA^{-1} as well as weaker 200 and 300 reflections are characteristic of a smectic-type packing with a periodicity of 29.1 \AA along the one-dimensional ordering of the molecules (similar to the periodicity observed by AFM, Figure 67e). The large peak at 1.30 \AA^{-1} corresponds to a distance of 4.85 \AA between nitrogen centers of adjacent triarylaminines, in agreement with DFT results. The apparent pitch (which is due to the 3-fold symmetry of the TATA core), together with the stacking distance, imply that 7 molecules are contained in a single period with a dihedral angle of 20° between them, a value also in agreement with DFT calculations. The broad scattering peak centered at 1.40 \AA^{-1}

⁹⁶ Zhao, Y.; Truhlar, D. G. *Acc. Chem. Res.* **2008**, *41*, 157–167

⁹⁷ Zhao, Y.; Truhlar, D. *Theor. Chem. Acc.* **2008**, *120*, 215–241

⁹⁸ Steinmann, S. N.; Piemontesi, C.; Delachat, A.; Corminboeuf, C. *J. Chem. Theory Comput.* **2012**, *8*, 1629–1640

corresponds to amorphous packing of the alkyl chains, and the small peak around 2 \AA^{-1} corresponds to an aryl π - π stacking distance of 3.1 – 3.2 \AA .

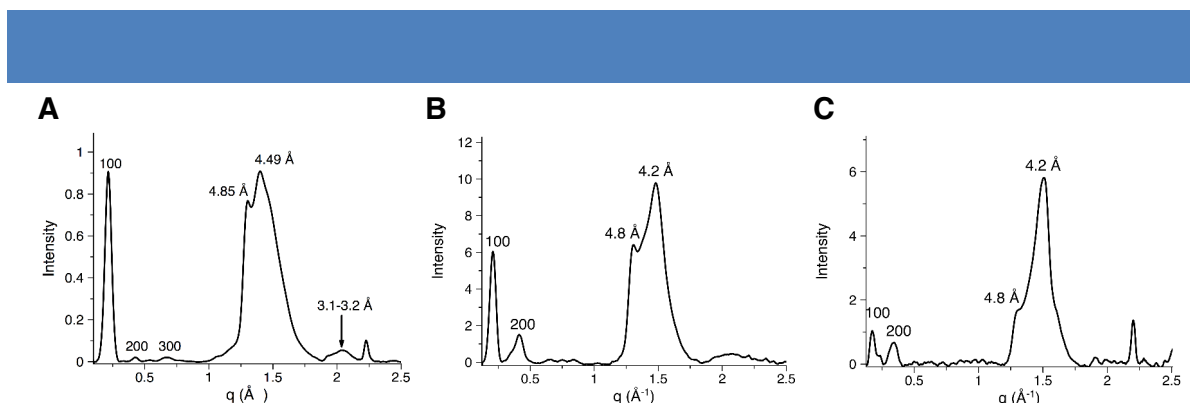


Figure 68 | X-ray scattering data (SAXS/WAXS) of a thin film prepared from TATA 6 (a), TATA 7 (b), and TATA 8 (c).

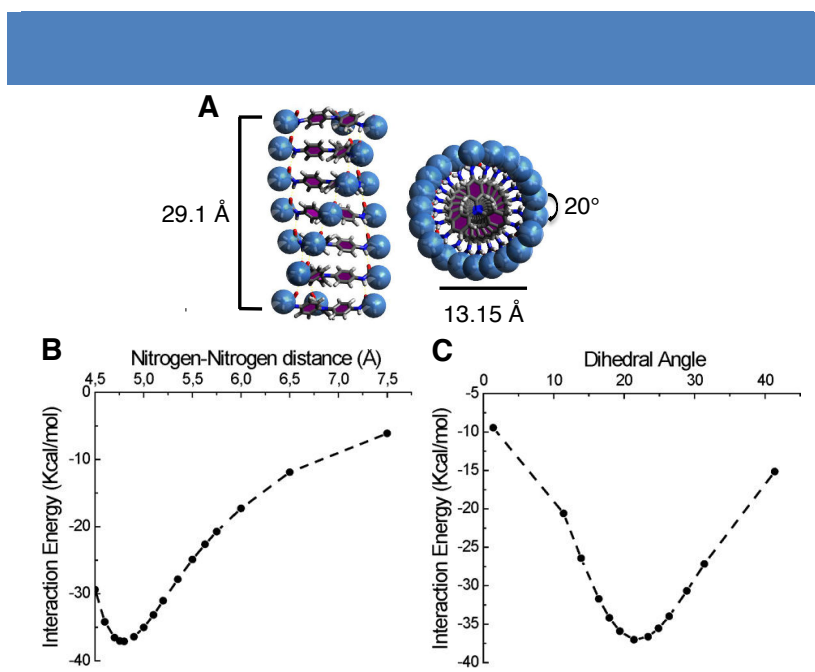


Figure 69 | (a) Proposed assembly geometry of long-chain TATA compounds displaying a longitudinal periodicity of 29.1 \AA , a nitrogen–nitrogen distance of 4.85 \AA between adjacent molecules, and a dihedral angle of 20° between each molecular unit. (b, c) Interaction energies between two stacked TATA molecules as determined by DFT calculations using the M062/6-31G(d) level of theory as a function of separation distance along the stacking axis (b) and dihedral angle (c). (d) Frontier orbitals of a radical cation dimer from DFT calculations.

3. Intermolecular Charge-Transfer Induced Error Correction and Self-Healing

Exposure of preassembled TATA fibers to visible light in chloroform leads to the appearance of an absorption band in the near-infrared (NIR), with a complex behavior as a function of

irradiation time (Figure 70a,b). Similar bands have been described in the literature for mixed valence charge transfer between bis-triarylamine molecules linked by conjugated covalent bonds.⁹⁹

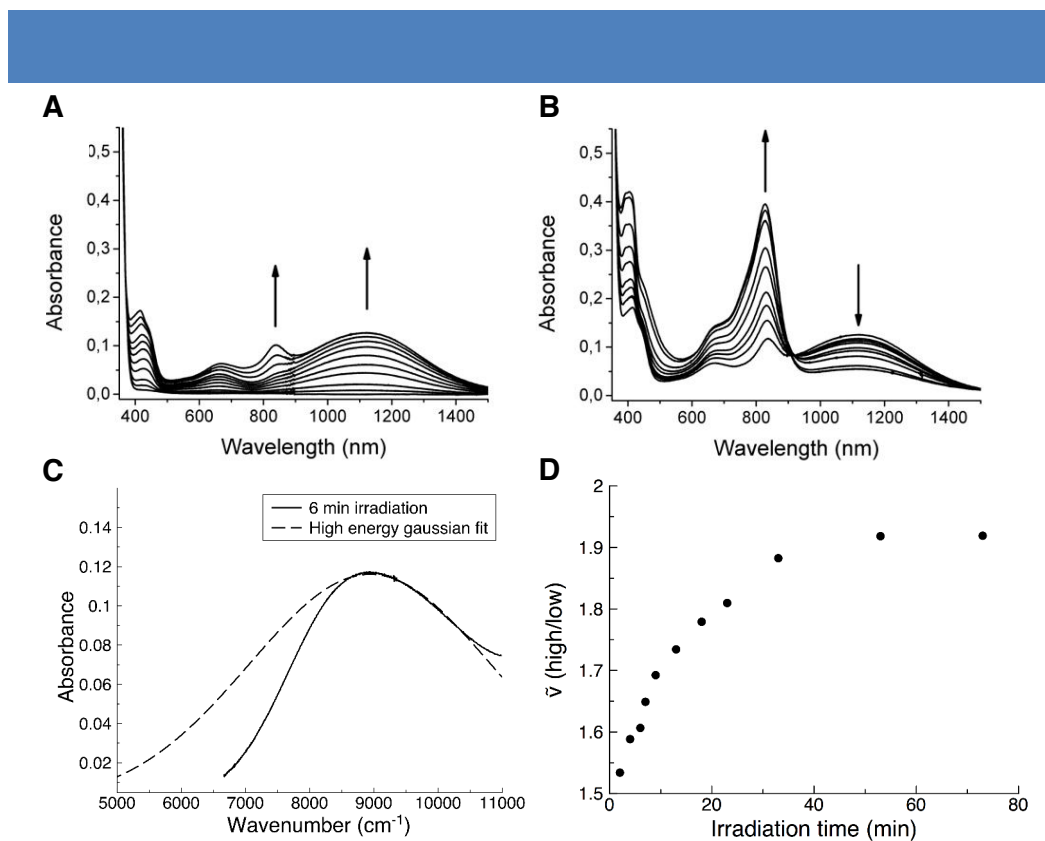


Figure 70 | Effect of light irradiation on TATA self-assemblies. (a,b) Sequential absorbance spectra taken during light irradiation (with a halogen lamp; 10 W cm^{-2}) of a 0.1 mM solution of TATA **6** in CHCl_3 ; (a) first 6 min of light irradiation, (b) from 7 to 73 min of light irradiation. (c) Example of a Gaussian fit (dashed line) for the high energy side of the charge transfer band after 6 minutes of irradiation of TATA **6**. (d) Peak asymmetry of the NIR absorption band versus time of an irradiated solution of TATA **6** in chloroform (0.1 mM).

Interestingly, in our system, the presence of such a characteristic absorption band ($\lambda_{\text{max}} = 1100 \text{ nm}$) can only arise from an intermolecular through-space charge-transfer between stacked triarylamine cores. In the literature, mixed-valence charge transfers have been classified depending on the nature of the electronic delocalization between the redox centers.¹⁰⁰ Class I systems consist of localized redox centers, while class II are partially delocalized, and class III fully delocalized. The shape of the charge transfer band can give insight into the nature of the interaction, with a Gaussian shaped band expected for a class II charge transfer and an asymmetric band expected for a class III. The optically induced charge-transfer band provides

⁹⁹ Heckmann, A.; Lambert, C. *Angew. Chem., Int. Ed.* **2012**, *51*, 326–392.

¹⁰⁰ Robin, M. B.; Day, P., Emel us, H. J.; Sharpe, A. G., Eds.; Academic Press Inc.: New York, 1968; Vol. 10, pp 274–422.

a convenient way to probe the interaction between redox centers. While both class II and class III systems should give rise to NIR optical absorption bands, a gaussian shaped band is expected for class II charge transfers and an asymmetric band is expected for a class III charge transfer. This effect is related to the increase in the electronic coupling between the redox centers and the corresponding decrease in the barrier to charge transfer. An analysis of the charge transfer band at various points in the irradiation cycle was performed by applying a separate gaussian fit to the high energy side and the low energy side of the band. Comparison of the half width at half max of the respective fits reveals an increase in asymmetry for longer irradiation times which levels off after 30 minutes (Figure 70d). This behavior may be explained if the NIR band contains both class II and class III charge transfers, where gradually more and more of the transitions exhibit class III behavior. The absorption band at 800 nm, starting at 5 min and increasing in intensity for the remainder of the irradiation experiment, corresponds to a higher contribution of localized class I triarylamine cation.

The two critical parameters are the electronic coupling (V), which is a measure of the extent of orbital overlap between the two redox centers, and the reorganization energy (λ), which is a result of the change in the redox centers' geometry as the charge is transferred. The relationship between the values of V and λ may be used to describe the extent of delocalization of the mixed-valence system, where $0 < V < \lambda/2$ for class II transitions and $V > \lambda/2$ for class III transitions. One can take the optical absorption maximum from a class III transition as being equal to $2V$, giving a value of 4470 cm^{-1} for the electronic coupling. DFT calculations predict an electronic coupling of 4070 cm^{-1} , within 8.9 % of the experimental value. The calculated reorganizational energy is 1301 cm^{-1} , predicting a class III charge transfer with $\lambda < 2V$. Assignment of the main band as a class III charge transfer is further supported by the lack of solvent dependence on the peak maximum, a typical characteristic.

Electronic paramagnetic resonance spectroscopy (EPR) provides both a quantification of the amount of radicals within the fibers as well as an alternative means of investigating the nature of the charge transfer relative to the EPR time scale. The hyperfine splitting of the EPR signal, arising from a through-space hyperfine coupling of adjacent triarylamine nitrogen centers, displays an evolution with the time of light irradiation (Figure 71). Three distinct although partially overlapped periods are observed with (i) the growth of a smooth five line signal corresponding to irradiation times from 15 s to 7 min (0–15 mol % of radicals); (ii) an evolution toward a one line pattern from 7 to 18 min (15–25 mol % of radicals), and (iii) the emergence of a 3-line pattern from 23 to 73 min (29–44 mol % of radicals). In the literature, EPR studies of covalently linked mixed-valence bis-triarylaminines show similar splitting

patterns.¹⁰¹ By analogy, the five line pattern corresponds to partially delocalized unpaired electrons between two triaryl amines; the one line pattern, to a fully delocalized system with no energetic barrier to charge transfer; and the three line pattern, to unpaired electrons which are localized on one triaryl amine.

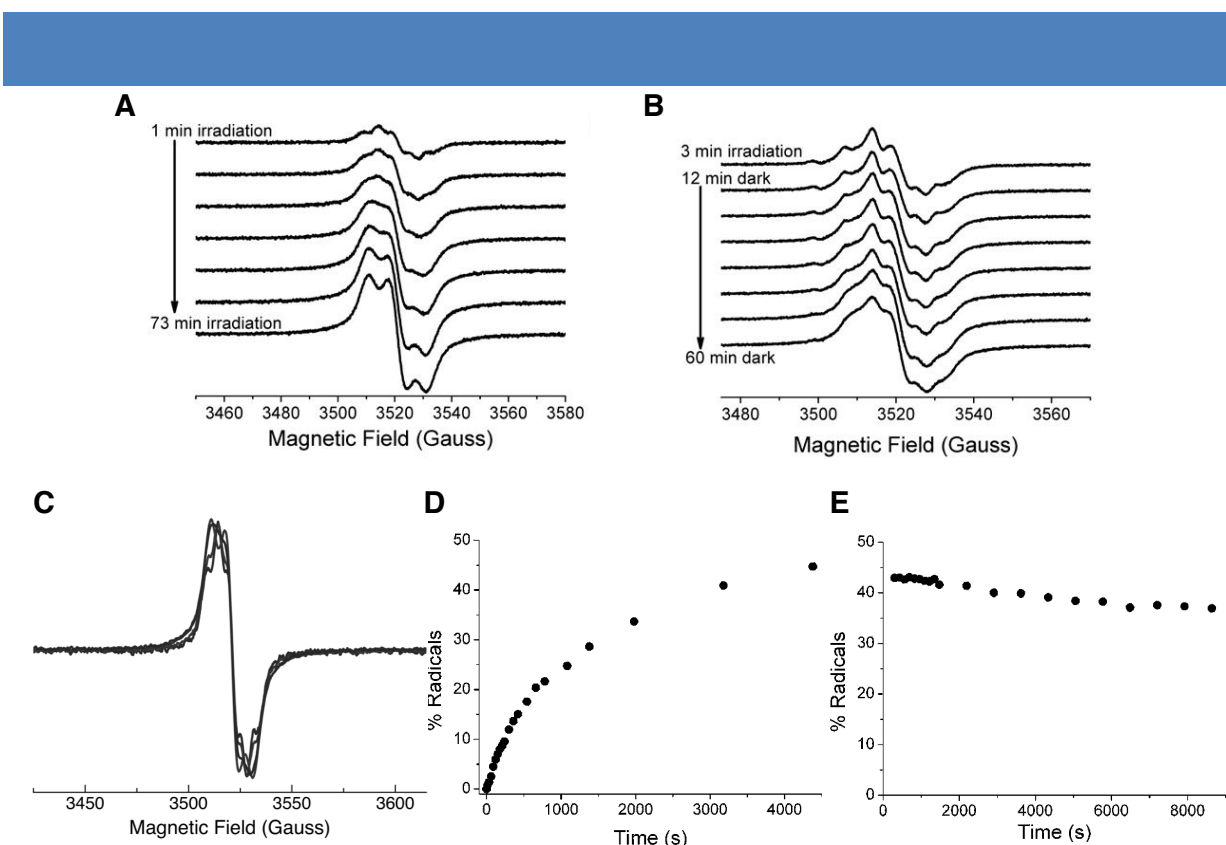


Figure 71 | EPR characterization of TATA during photooxidation. (a) Room temperature EPR spectra taken while irradiating (with a halogen lamp; 10 W cm^{-2}) a 1 mM solution of TATA **6** in CHCl_3 from 1 to 73 min. (b) Room temperature EPR spectra taken for a sample irradiated for 3 minutes, and subsequently put in the dark for 60 min. (c) Overlay of the normalized EPR signals at 3.5 min, 7 min, 23 min, and 73 min of irradiation. Quantitative EPR (d) during irradiation and (e) after irradiation in the dark of a 1 mM chloroform solution of TATA **6**.

Thus, both EPR and absorption data demonstrate the initial formation of a mixed population of classes II and III charge transfers, followed by a transition to a single population of class III, which then tends to a localized class I as the higher number of charges in the one-dimensional fiber leads to electrostatic repulsion. A complementary experiment was performed by irradiating a solution for 3 min and by then following the evolution of the radicals in the dark (Figure 71b). Interestingly, the change of the EPR signal toward a one-line pattern was observed over 1 h. This indicates that the transformation from class II to class III

¹⁰¹ Lancaster, K.; Odom, S. A.; Jones, S.; Thayumanavan, S.; Marder, S. R.; Bredas, J.-L.; Coropceanu, V.; Barlow, S. *J. Am. Chem. Soc.* **2009**, *131*, 1717–1723.

charge transfers is not related to the number of radicals, and suggests an intrinsic structural evolution of the system with time.

To understand the relationship between the nature of the charge transfer and the irradiation time, we compared the X-ray scattering profiles of two thin films; one made from a nonirradiated solution, and the other one from a solution irradiated for 15 min (Figure 72). A Gaussian fit of the peak at 0.215 \AA^{-1} revealed a noticeable decrease in the peak width at half-maximum, demonstrating an increase of the fiber correlation length (ξ) of 49%, going from 163 \AA in the dark to 243 \AA upon irradiation. The 300 reflection of the irradiated sample also displays a noticeable sharpening, indicating a decreasing cumulative disorder, i.e. a fewer number of structural defects with light.¹⁰²

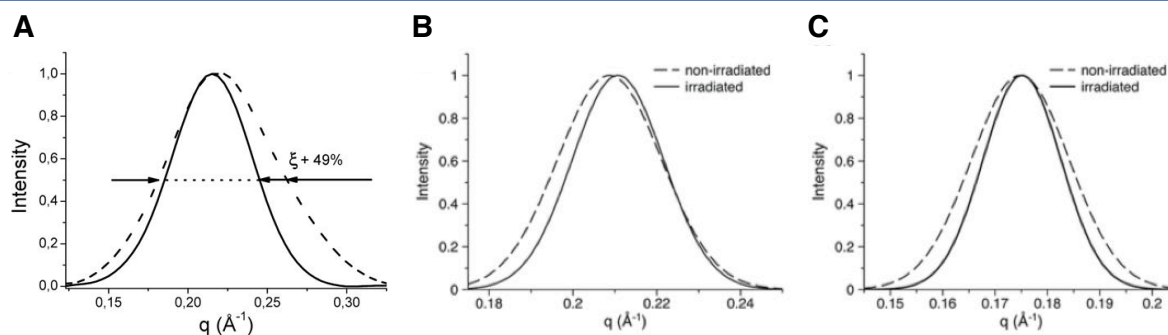


Figure 72 | (a) SAXS of nonirradiated (dotted line) and irradiated (full line) thin films of **6** demonstrating a 49% increase in the correlation length (calculated as $4\pi/\text{fwhm}$). (b) A 12% decrease in the HWHM was observed from the non-irradiated to the irradiated state for **7**, which corresponds to an increase of the coherence length (ξ) of 14%. (c) A 20% decrease in the HWHM was observed from the non-irradiated to the irradiated state for **8**, which corresponds to an increase of the coherence length (ξ) of 25%.

Characterization of numerous samples using high resolution AFM unambiguously confirmed the improved ordering of the fibers, as well as the self-healing of the gel in the 100 nm range, upon light irradiation (figures 73 and 74). Additionally, the EPR signal did not reveal a change in the EPR linewidth with increasing irradiation, indicating that there is not a uniform change in the charge transfer rates across the whole assembly, but that the signal arises from an overlay of several different charge transfer events. This was supported by the X-ray data as well, which does not show a global rearrangement of the stacking structure upon irradiation. Altogether, these results strongly suggest that class III charge transfer occurs between molecules in a thermodynamic minimum while class II charge transfer occurs at small structural defects in the self-assembly where the electronic coupling and reorganization

¹⁰² Rivnay, J.; Mannsfeld, S. C. B.; Miller, C. E.; Salleo, A.; Toney, M. F. *Chem. Rev.* **2012**, *112*, 5488–5519.

energy are less efficient.

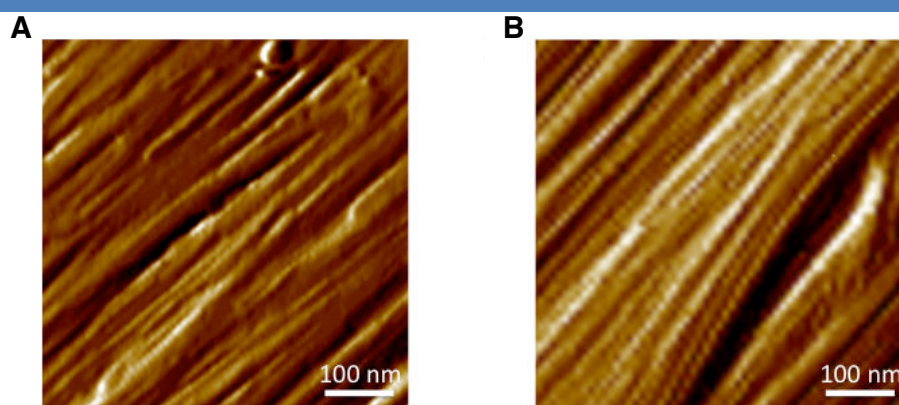


Figure 73 | AFM image of TATA **6** obtained from the drop cast of a chloroform solution before light irradiation (a) and after 15 min of light irradiation (b) showing the healing of structural defects. The nonirradiated solutions were kept 15 min in the dark to discriminate the effect of light from a possible aging effect.

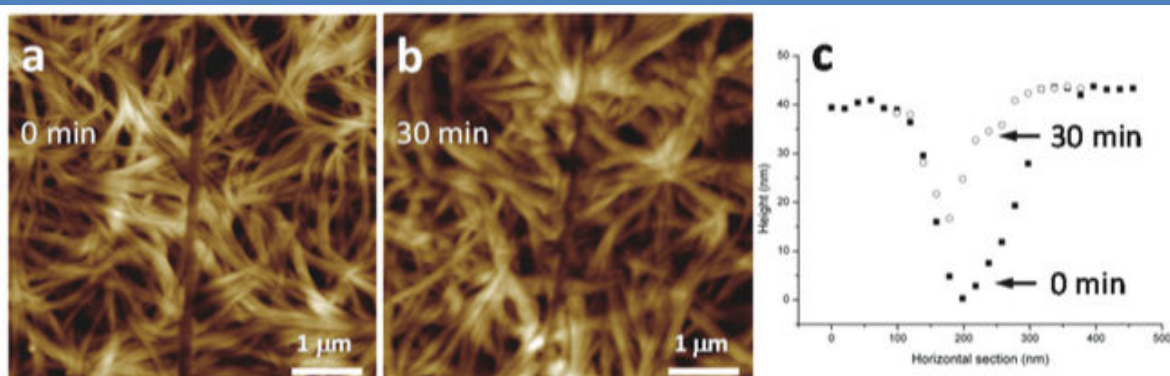


Figure 74 | AFM height images of TATA **6** obtained from chloroform samples (20 mg/mL) drop cast on mica. Irradiation times under vapors of chloroform (with a halogen lamp; 10 W.cm⁻²) vary from 0 minutes (a) to 30 minutes (b). c, A self-healing of the cut is measured along its height profile with an observed reparation in the order of 100 nm.

To gain further insight into the thermodynamics of the assembly process, we performed calculations using density functional theory (DFT). All calculations were performed with the M062X functional using the 6-31G(d) basis set and carried out with Gaussian 09. The M062X functional is a hybrid DFT functional that has been shown to effectively model non-covalent interactions.¹⁰³ Geometry optimizations were performed on the single molecule (neutral and radical cation; Figure 75), the stacked dimer (neutral and radical cation; Figure 76), and a stacked trimer (radical cation; Figure 77). The alkyl chains were omitted during calculations.

¹⁰³ Zhao, Y.; Truhlar, D. G., *Acc. Chem. Res.* **2008**, *41*, 157-167.

The *reorganization energy* (λ) was calculated using the energy of the monomers:¹⁰⁴

$$\lambda = E^{+n} - E^{++} + E^{n+} - E^{nn} \quad (30)$$

where E^{+n} is the energy of the cation in the geometry of the optimized neutral species, E^{++} is the energy of the cation in its optimized geometry, E^{n+} is the energy of the neutral species in the geometry of the optimized cation, and E^{nn} is the energy of the neutral monomer in its optimized geometry. The *electronic coupling* (V) was calculated using the energy splitting-in-dimer method, involving the energies of the HOMO and HOMO-1 orbitals of the neutral dimer.¹⁰⁵

$$V = 1/2(E_{\text{HOMO}} - E_{\text{HOMO-1}}) \quad (31)$$

The *interaction energy* for the dimer species was performed using the counterpoise correction to correct for the basis set superposition error commonly found in DFT calculations of molecular ensembles. Single-point interaction energies were computed for the optimized radical cation dimer while varying the stacking distance and the dihedral angle between the two molecules.

The *frontier orbitals* were calculated as follows: the HOMO was taken from the neutral monomer calculation, and the band gap was taken from the first excitation energy from time-dependent DFT calculations.¹⁰⁶

Analysis of the molecular orbital output from the single molecule calculation of the neutral and radical cation species reveals extensive delocalization of the molecular orbitals over the entire aromatic core structure. The optimized radical cation dimer displays delocalized orbitals over the two stacked molecules as compared with the neutral dimer species. Dimer calculations predict a N-N distance of 4.8 Å and a dihedral angle of 21.4°. In the optimized geometry, the interaction energy of the cation dimer is of 37.1 Kcal/mol, which is a gain of 20.9 Kcal/mol over the neutral dimer. The nearest contact point of the triarylamine core occurs with the outer aromatic carbons, with a predicted distance of 3.26 Å and significant density of the LUMO orbital between these carbons. The optimized trimer cation gave a nitrogen-nitrogen stacking distance of 4.84 Å and a dihedral angle of 19.9°, in very close agreement with the X-ray scattering data of 4.85 Å and a 20° dihedral angle. The frontier orbitals were calculated to be 5.75 eV and 1.62 eV for the HOMO and LUMO orbitals, respectively, giving a band gap of 4.13 eV. The reorganization energy and electronic coupling are 1301 cm⁻¹ and 4070 cm⁻¹, respectively. This is consistent with a class III,

¹⁰⁴ Lambert, C.; Nöll, G., *J. Am. Chem. Soc.* **1999**, *121*, 8434-8442.

¹⁰⁵ Coropceanu, V.; Cornil, J.; da Silva Filho, D. A.; Olivier, Y.; Silbey, R.; Brédas, J. L., *Chem. Rev.* **2007**, *107*, 926-952.

¹⁰⁶ McCormick, T. M.; Bridges, C. R.; Carrera, E. I.; DiCarmine, P. M.; Gibson, G. L.; Hollinger, J.; Kozycz, L. M.; Seferos, D. S., *Macromolecules* **2013**, *46*, 3879-3886.

delocalized charge transfer where $\lambda < 2$ V.

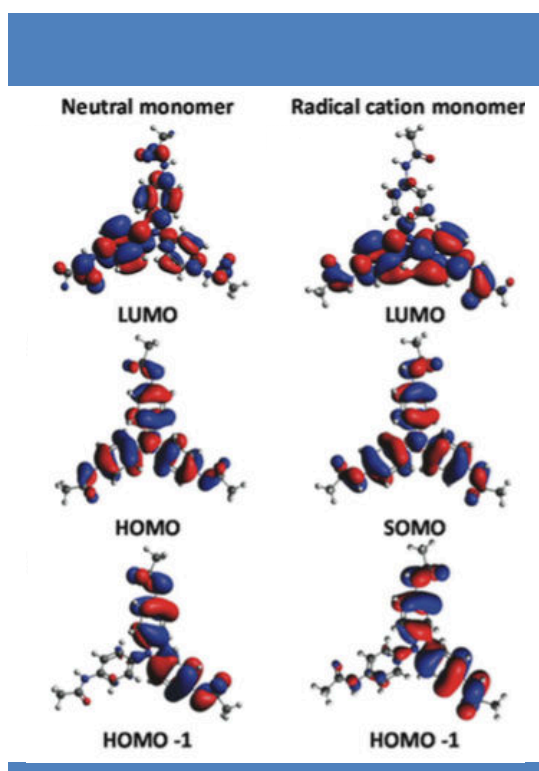


Figure 75 | DFT-calculated molecular orbitals for a single generic TATA molecule. Neutral monomer LUMO, HOMO, and HOMO-1 and radical cation monomer LUMO, SOMO, and HOMO-1 optimized with the MO62X-6-31G(d) basis set. The term generic is used as the alkyl chains of TATA **6-8** are replaced by a methyl group.

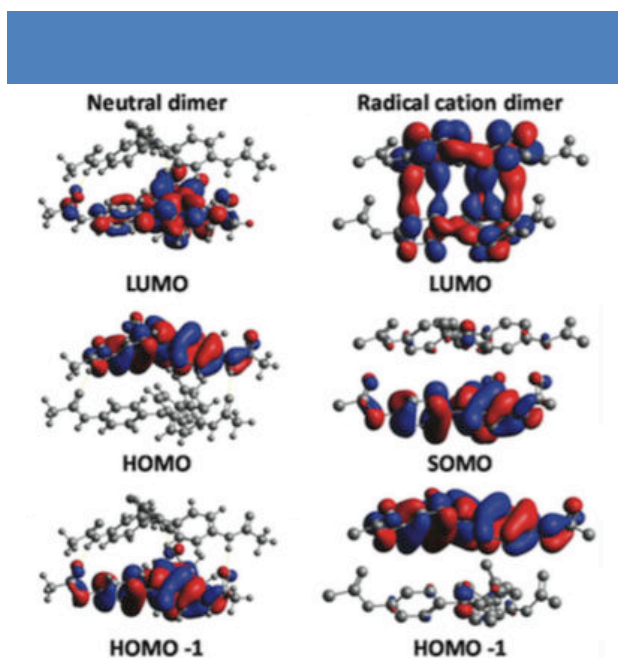


Figure 76 | DFT-calculated molecular orbitals for a stacked dimer of generic TATA molecules. Neutral dimer LUMO, HOMO, and HOMO-1 and radical cation dimer LUMO, SOMO, and HOMO-1 optimized with the MO62X-6-31G(d) basis set.

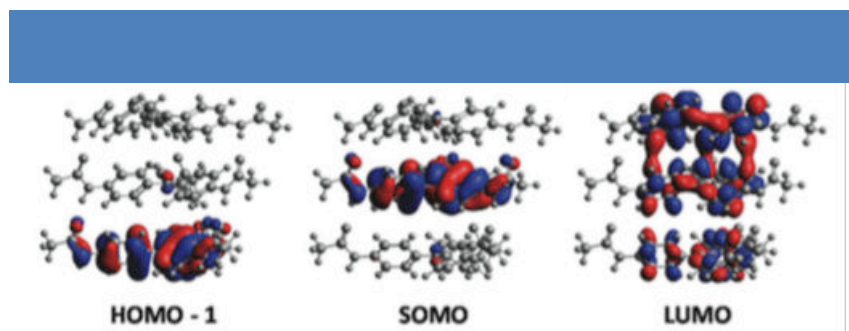


Figure 77 | DFT-calculated molecular orbitals for a stacked trimer of generic TATA molecules. The HOMO-1, SOMO, and LUMO orbitals for cation trimer assembly optimized with the MO62X-6-31G(d) basis set.

In conclusion, analysis of the data in the context of Marcus-Hush theory shows that there is a mixed population of class II and class III transitions, the proportion of which changes with increasing irradiation time to give predominately class III species. As the optimally stacked structures should give rise to delocalized, class III transition, the class II transitions come from defects in the stacking structure where the electronic coupling is decreased. During the process of photo-induced oxidation of the molecular units of the fibers, we induce a charge-transfer process (a migration of charges) through the fibers. We propose to describe this type of charge transfer complex migrating through the fibers as a “supramolecular polaron”, which consists in a “through-space” version of the polarons observed in conjugated polymers, and where the radical cation is associated with a lattice deformation.¹⁰¹ This is also in agreement with further fluorescence experiments which show exciton quenching by the supramolecular polarons as is commonly observed with polarons in conjugated polymers (Figure 78).^{107,108}

¹⁰⁷ Scheblykin, I. G.; Yartsev, A.; Pullerits, T.; Gulbinas, V.; Sundström, V. *J. Phys. Chem. B* **2007**, *111*, 6303–6321.

¹⁰⁸ Lin, H.; Tabaei, S. R.; Thomsson, D.; Mirzov, O.; Larsson, P.-O.; Scheblykin, I. G. *J. Am. Chem. Soc.* **2008**, *130*, 7042–7051.

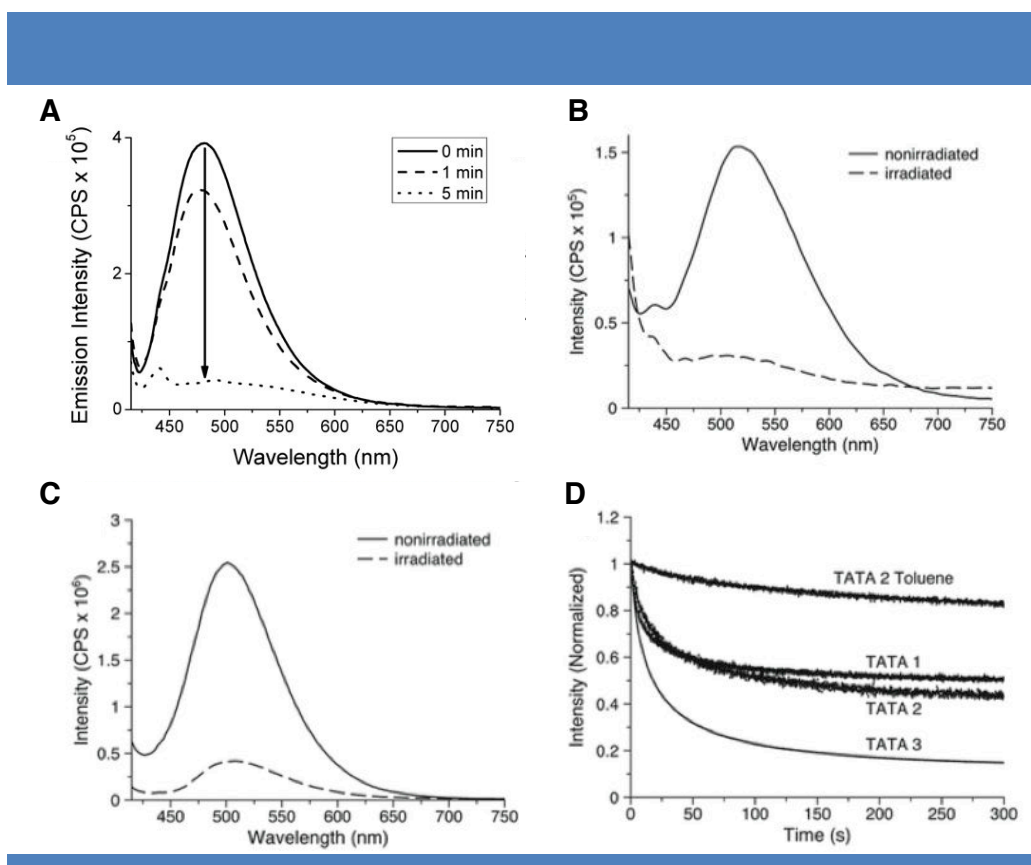


Figure 78 | (a) Fluorescence emission of TATA 6 upon light irradiation showing the quenching induced by the polaron formation. The same effect observed with both TATA 7 (b) and TATA 8 (c); Relative fluorescence quenching demonstrating the largest quenching for TATA 8 compared with a control of TATA 7 in toluene.

4. TATA As An Organic Metal

The temperature-dependent EPR measurements were performed down to 4 K on the powder obtained from irradiated fibers, and a plot of the inverse EPR signal versus temperature displays two distinct regions (Figure 79). The EPR signal intensity is proportional to the magnetic susceptibility (χ) of a sample, and can therefore be used to analyze the Curie behavior of a paramagnetic material. For a paramagnetic material in the doublet state ($S = 1/2$) with non-exchange coupled electrons, the magnetic behavior of the material should conform with the Curie-Weiss law. The plot of the inverse signal intensity versus temperature in Fig. 4a of the main text displays a linear relationship from 4 K to 80 K, confirming Curie-Weiss behavior in this temperature range. Curie-Weiss behavior is given as follows:

$$\chi = C/(T - \Theta) \quad (32)$$

where C is the Curie constant and Θ is the Weiss constant (units in Kelvin). The Weiss constant is indicative of either an antiferromagnetic or ferromagnetic interaction among the magnetic moments, with Θ being either negative or positive, respectively. The Curie constant

can be given by

$$C = Ng^2\mu_B^2S(S+1)/3k_B \quad (33)$$

where N is the number of spins/mole, g is the g -value of the EPR signal, μ_B is the Bohr Magneton, S is the electron spin quantum number, and k_B is the Boltzman constant. Collecting the constants, one can simplify the calculation as follows:

$$C = 0.125g^2S(S+1) \text{ emu}\cdot\text{K/mol} \quad (34)$$

For a spin=1/2 system and a g -value of 2.003, $C = 0.375 \text{ emu}\cdot\text{K/mol}$. From the quantitative EPR measurements, after 1 hr of irradiation 44% of the molecules are in the oxidized form. Therefore, factoring this into the above value gives $0.165 \text{ emu}\cdot\text{K/mol}$ as the Curie constant. The χ^{-1} versus T plot is shown in Fig. 81a with the data fit according to the Curie-Weiss law. The data points at the high end of the temperature spectrum were normalized to $0.165 \text{ emu}\cdot\text{K/mol}$.

The lower temperature region below 90 K shows a linear dependence, indicating that the signal is arising from unpaired Curie spins within the fibers. Then, starting at 90 K and above, a deviation from Curie behavior indicates a contribution from Pauli spins, which should display temperature independent behavior and which are commonly observed in materials containing metallic electrons. In particular, a similar transition between low temperature Curie behavior and higher temperature Pauli or mixed Curie and Pauli behavior has been observed in films of metallic polyaniline.¹⁰⁹ Additionally, by fitting the curve in the low temperature region using the Curie–Weiss law, a value of -1.81 K was found for the Weiss constant which indicates a weak antiferromagnetic interaction between radicals within the fibers.

The weak half-field signal ($g \approx 4$), observed around 10 K and below, demonstrates exchange-coupling of the doublet electrons giving rise to singlet ($S = 0$) and triplet ($S = 1$) states. This interaction is modeled by the Heisenberg-Dirac-Van Vleck Hamiltonian:

$$H_{ij} = -2J_{ij}S_iS_j \quad (35)$$

where the interaction parameter J_{ij} is positive for ferromagnetic coupling (triplet ground state) and negative for antiferromagnetic coupling (singlet ground state). Though the signal was low, a modest fit was obtained with the Bleaney-Bowers expression:¹¹⁰

$$\chi = 0.375 (g^2/T) * 2/(3+e^{(-2J/kT)}) \quad (36)$$

to give $J = -0.48 \text{ K}$, indicative of weak antiferromagnetic exchange-coupling and a singlet ground state within the fibers. Following the method of Eaton, a distance of 3.73 \AA was calculated between coupled spins at cryogenic temperatures indicating most of the spin

¹⁰⁹ Krinichnyi, V. I.; Konkin, A. L.; Monkman, A. P. *Synth. Met.* **2012**, *162*, 1147–1155

¹¹⁰ Bleaney, B.; Bowers, K. D.. *Proc. R. Soc. A* **1952**, *214*, 451-465.

density is on the aromatic carbons, in line with our DFT calculations.¹¹¹

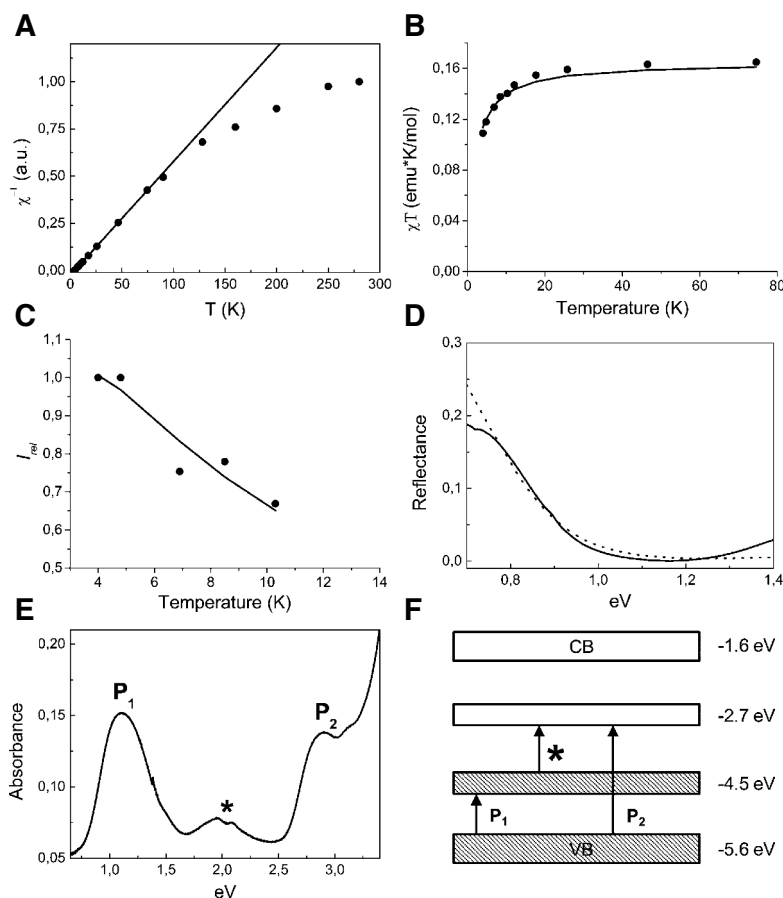


Figure 79 | Metallic characteristics of TATA self-assemblies. (a) Temperature-dependent EPR measurement of TATA **6** displaying a low-temperature region consisting entirely of localized Curie spins (see linear behavior) and a higher temperature region displaying a mixture of Curie and delocalized Pauli spins. (b) Fit of χT vs T with the Curie–Weiss law for data between 4 and 80 K ($r^2 = 0.999$). (c) Relative intensity of the half-field EPR transition versus temperature. The data were fitted with the Bleaney–Bowers model giving a weak antiferromagnetic coupling with $J = -0.48$ K ($r^2 = 0.998$). (d) Reflectance measurements of an irradiated thin film of TATA **6** displaying a plasma resonance near 1.2 eV, typical of delocalized metallic electrons and theoretical fit of the reflectance with the Drude model (dotted line), $\epsilon(\omega) = \epsilon^\infty - \omega_p^2 \tau^2 (1 + \omega^2 \tau^2)^{-1}$. (e) Absorption spectrum of an irradiated thin film of TATA **6** displaying optical signatures of polaronic bands. (f) Determined band structure calculated from absorbance measurements in (e) and showing a half-filled polaronic band at -4.5 eV.

Quantitative EPR measurements displayed a consistent increase in radicals up to a maximum of 44 % by photoirradiation. No evidence of a bipolaron regime was observed (this would lead to a decrease in the EPR signal due to spin pairing), indicating that the radical cations exist as polarons within the fibers. This is important for potential spintronic applications, where bipolaron formation would be detrimental due to the loss of coherent spins.

¹¹¹ Eaton, S. S.; More, K. M.; Sawant, B. M.; Eaton, G. R. *J. Am. Chem. Soc.* **1983**, *105*, 6560–6567

Finally, a further signature of the metallic behavior comes from the reflectance measurements displaying a minimum around 1.2 eV. These data are well-fitted by the Drude model for a true metallic behavior which gives the values of the plasma frequency ($\omega_p = 1.16$ eV) and of the relaxation time ($\tau = 1.16 \times 10^{-14}$ s; Figure 79d).¹¹² In an irradiated thin film, and by using both EPR and absorption spectroscopy (Figure 79e), we observed a high stability of the radical which remains unchanged for at least six months. It is striking to observe a classic polaronic absorption signature as described for conducting conjugated polymers¹¹³ and, from the two main absorptions, a polaronic conduction band with a half-filled energy level located at 1.1 eV above the valence band (Figure 79f).

Analysis of the behavior of the radical cations within the nanowires requires extrapolation of the charge transfer theories over larger scales. First, we look at the radical cations within the fibers in the context of supramolecular polaron formation, where a polaron is defined as the unpaired electron and the surrounding lattice deformation. According to the 1D Holstein molecular model,¹¹⁴ polarons can exist in two varieties, as a ‘small’ polaron or a ‘large’ polaron. A small polaron is essentially localized on one molecule, while a large polaron is delocalized over several molecules. From the Marcus-Hush analysis, the delocalized nature of the charge transfer band for optimally stacked molecules implies delocalization and the formation of ‘large’ polarons within the self-assembled structures, and delocalization over at least two molecules. Transport of this polaron through the fibers may occur as either adiabatic transitions, where the electron remains in the same eigenstate, or as non-adiabatic transitions, between two distinct potential energy surfaces.¹¹⁵ In perfectly stacked molecules, there will be delocalized adiabatic transitions, which are supported by the observations of electron transfer rates in the fast regime relative to the EPR timescale (greater than 10^{13} s⁻¹).¹¹⁶ At defects, non-adiabatic transitions will occur with an energetic barrier equal to the reorganization energy. It means that the larger the stacking defect, the larger the reorganization energy, and the larger the energetic barrier to charge transfer. The reorganization of the stacking geometry after charge transfer leads to a lower energy in the stacking structure, which remains after the polaron has passed, thereby leading to defect healing. For optimally stacked segments of the nanowires, band formation takes over, leading

¹¹² Lee, K.; Heeger, A. J. *Synth. Met.* **1997**, *84*, 715–718

¹¹³ Beljonne, D.; Cornil, J.; Sirringhaus, H.; Brown, P. J.; Shkunov, M.; Friend, R. H.; Brédas, J.-L. *Adv. Funct. Mater.* **2001**, *11*, 229–234

¹¹⁴ Coropceanu, V.; Cornil, J.; da Silva Filho, D. A.; Olivier, Y.; Silbey, R.; Brédas, J. L. *Chem. Rev.* **2007**, *107*, 926–952.

¹¹⁵ Stafstrom, S. *Chem. Soc. Rev.* **2010**, *39*, 2484–2499.

¹¹⁶ Lancaster, K.; Odom, S. A.; Jones, S. C.; Thayumanavan, S.; Marder, S. R.; Brédas, J.-L.; Coropceanu, V.; Barlow, S., *J. Am. Chem. Soc.* **2009**, *131*, 1717–1723.

to the signatures of 1D metallic electrons within the wires, as shown by the reflectivity and temperature-dependent EPR experiments.

Fluorescence studies of self-assembled triarylaminines have revealed a characteristic fluorescence emission related to the self-assembly. Irradiation of the TATA fibers leads to fluorescence quenching within 5 minutes of irradiation. Polaron-induced quenching of excited states is a well described phenomenon in conjugated polymers^{117,118} and is typically described by Förster energy transfer.¹¹⁹ Irradiation induces exciton formation in the fibers with mobility dependent upon delocalization over the molecules. After formation, relaxation to the ground state occurs either by emission of a fluorescence photon around 500 nm or by quenching from a nearby polaron within the Förster interaction range. Accordingly, with five minutes of irradiation, the polarons are arranged in the fibers within the Förster interaction range. From quantitative EPR spectroscopy, five minutes of photooxidation corresponds to 12% radicals in the fibers. If charge propagation is assumed to be reasonably efficient, the radicals will be maximally spaced from one another, with an average position every 8.4 molecules. Using the stacking distance of 4.85 Å from X-ray scattering, a minimum Förster interaction range of 20.5 Å is estimated within the fibers, in agreement with typical Förster energy transfer distances. The quenching observed after 5 minutes of irradiation appears to be related to the appearance of the 800 nm band in the absorbance spectrum. This may indicate the optimal number of radicals within the fibers to achieve interaction between the polarons and to begin forming band structure. Conductivity experiments appear to confirm this behavior as the optimal, steady conductivity was achieved with 5 minutes of irradiation. Further irradiation displayed a transient increase with the light irradiation, followed by a decrease back to the 5 min level.

In order to probe the effect of light on the fibers' conduction properties directly in a device, we have then used transparent ITO electrodes separated by a 4 μm gap. Conductivity measurements were performed with a dc current on fibers made of TATA **6**, **7**, and **8** (all at a concentration of 17 mM in tetrachloroethane), and on a non self-assembling tri(bromophenyl)amine for control experiments (Figure 80). Compared to this control, previous to light irradiation and under a 0.1 V bias (which is far below the oxidation potential of the triarylamine derivatives), conductivities of 2 orders of magnitude higher for **3**, and **4**

¹¹⁷ Scheblykin, I. G.; Yartsev, A.; Pullerits, T.; Gulbinas, V.; Sundström, V. *J. Phys. Chem. B* **2007**, *111*, 6303-6321.

¹¹⁸ Yan, X. Z.; Pawlas, J.; Goodson, T.; Hartwig, J. F., *J. Am. Chem. Soc.* **2005**, *127*, 9105-9116.

¹¹⁹ Lin, H.; Tabaei, S. R.; Thomsson, D.; Mirzov, O.; Larsson, P.-O.; Scheblykin, I. G., *J. Am. Chem. Soc.* **2008**, *130*, 7042-7051.

orders of magnitude higher for **6** and **7** are observed, demonstrating conduction through the preformed fibers. Upon subsequent irradiation for 50 s, an increase of 2 orders of magnitude in conductivity is observed for TATA **6** and **7**, while the gel of **8** exhibits nearly a four-orders-of-magnitude increase, leading to a similar conductivity for the three TATAs after irradiation. This observation can be correlated to a larger fluorescence quenching in the case of TATA **8**. The measured conductivity then remains very stable in the dark, 6 orders of magnitude higher than the control molecule. We here consider that the contribution of ionic current is negligible because, in addition to its stability in the dark under a dc field and to the negligible response of the control molecule, the measured electronic conductivity remains unchanged when adding 10% of tetrabutylammonium chloride to the gel of **6**. It was also possible to affect the conductivity of the organogel without light irradiation but, instead, by applying a difference of electric potential comprised between 0.6 and 0.8 V (that is crossing the oxidation potential of TATA).

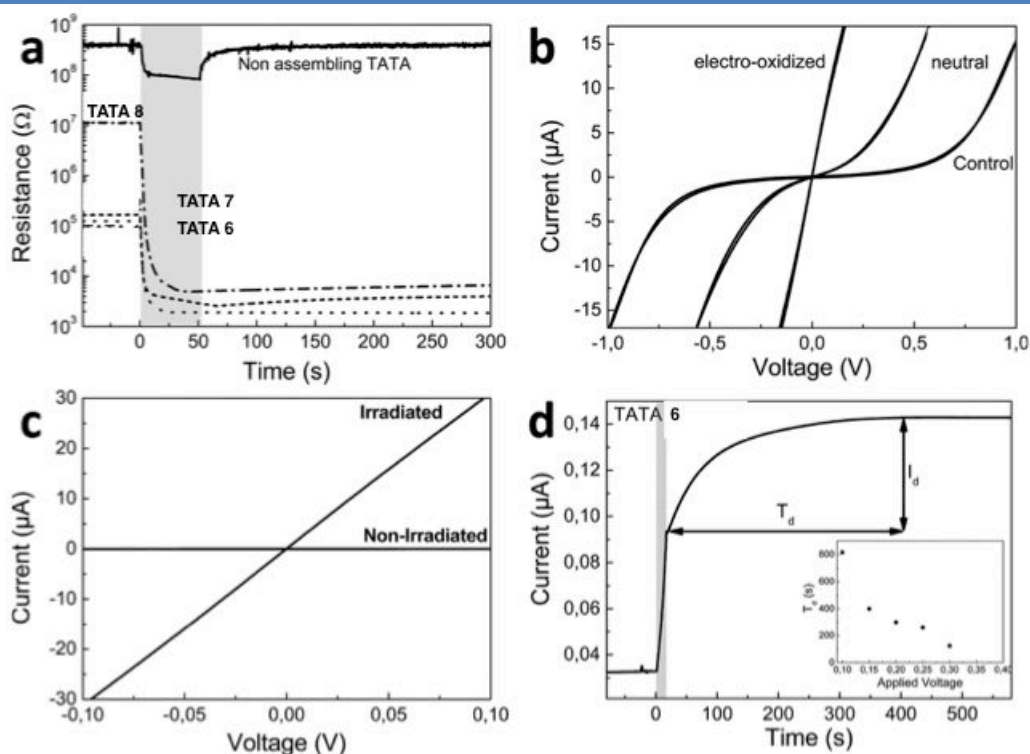


Figure 80 | Combined influences of polarons' formation and diffusion on the conductivity of TATA self-assemblies. (a) Resistance versus time for 17 mM TATA samples in tetrachloroethane, and for a nonassembling tri(bromophenyl)amine as a control molecule. The gray background corresponds to the light irradiation time (halogen lamp; 10 W cm^{-2}). (b) I - V curves for samples subjected to electrochemical oxidation. The control tri(bromophenyl)amine was subjected to an I - V scan up to 2 V to ensure electrochemical oxidation. (c) I - V curves before and after light-induced fibers formation of TATA **1** in a mixed solvent system of 5:3 methanol:toluene +5 vol % tetrachloroethane. (d) Dark conductivity increase time (T_d) after 15 s irradiation of TATA **1** (halogen lamp; 10 W cm^{-2}); the gray background corresponds to the light irradiation time.

The I - V curves demonstrate a transition toward an ohmic behavior upon electrochemical oxidation, illustrating the change in the conduction mode going from a semiconducting to a conducting state (figure 80b). The nonself-assembling control triarylamine was also oxidized by performing I - V sweeps up to 2 V, yet no change to the I - V curve shape was observed. In addition, it was possible to form the nanowires directly inside the device by first inserting a solution of nonassembled TATA **6** (5:3 methanol:toluene with 5% tetrachloroethane) and by subsequent light irradiation. The 4 orders of magnitude increase of the conductivity and the characteristic linear I - V curve remained after the light was turned off (Figure 80a), demonstrating a self-construction process in a gap as large as 4 μm between simple commercially available ITO plates.

We finally probed the conductivity improvement afforded by the light-induced healing process in the fibers. After irradiation of the initial gel of TATA **6** with a short pulse of light (15 s with the voltage held at 0.1 V), an increase of the conductivity was measured afterward in the dark, with a gain comprised between 30 and 50%. This value can be correlated with an increase of the coherence length and a decrease of structural defects in the polymer, as determined by SAXS and AFM (see above). We also measured a delay time (T_d) between switching the light off and reaching the maximum conductivity value, and interestingly an inverse dependence of T_d on the applied voltage was noticed (inset in Figure 80d). We postulate that this further increase reflects the supramolecular optimization of the fibers thanks to the increased photoinduced charge injection linked to the polarons' diffusion in the electric field.

5. Conclusions

In conclusion, we have described the synthesis and the unique properties of a new class of soft supramolecular polymers made of columnar stacks of tris-amide triarylamine. These one-dimensional fibers can be oxidized to their radical cation by light (photodoping) or electrochemically. The resulting presence of delocalized Pauli spins and polaronic absorption band shows that this supramolecular system has similar charge-transport characteristics to those observed in metallic conducting conjugated polymers. This first demonstration that supramolecular polymers can present electronic, magnetic, and optical signatures similar to those measured through-bond in the best conjugated polymers extends the current understanding of both fields and unifies them. In addition, we have shown that the induced

through-space mixed-valence charge-transfer within their structure behave as “supramolecular polarons” which diffuse along the fibers and fix structural defects of the stacked structure, representing a novel cooperative healing mechanism thanks to the presence of the charge carrier itself. The capacity of soft supramolecular self-assemblies to self-optimize their conduction properties provides alternatives to conventional organic metals in terms of responsiveness, healing, and processability, which is of interest for applications in organic electronics and spintronics.

Chapter VII: Supramolecular Plasmonic Interconnects and their Directed Self-Assembly into Optical Nanocircuits

1. Introduction

In this chapter, we take advantage of the metallic and self-assembling properties of the TATA molecules which we elucidated in the previous chapter to connect gold nanoclusters and demonstrate that the TATA nanowires may act as plasmonic interconnects. As outlined in the introduction, metallic nanoparticles exhibit localized surface plasmon resonances in the presence of electromagnetic fields because free electrons in their conduction band are set in coherent oscillations at the interface with a dielectric.¹²⁰ Transmission of the induced displacement current and coupling with nearby nanoparticles through metallic interconnects provides the basis to achieve optical nanocircuits. However, practical realization of plasmonic interconnects has yet to be reported in the literature. When the resonance modes of these metallic nanoparticles are coupled through the TATA interconnects, the optical conductivity of the plasmonic layer dramatically increases from $259 \text{ W}^{-1} \cdot \text{cm}^{-1}$ to $4271 \text{ W}^{-1} \cdot \text{cm}^{-1}$. The whole system can be described by using the lumped circuit theory as a fuzzy AND logic gate. This supramolecular bottom-up approach opens the possibility to implement processable, soft, and low cost organic plasmonic interconnects into a large number of applications going from sensing to metamaterials and information technologies.¹²¹

2. Hierarchical Construction of Nanoparticle Arrays Connected Via Tris-amide Triarylamine Nanowires

The plasmonic devices for the present study were constructed by a hierarchical three-step strategy involving: *i*) the formation of an array of gold nanoclusters on an insulating surface, *ii*) the functionalization of these nanoclusters with a monolayer of tris-thiol triarylamine **29**, and *iii*) the directed crosslink of these functionalized nanoclusters by STANWs made of **6** (Figures 81).

¹²⁰ Halas, N. J., Lal, S., Chang, W.-S., Link, S. & Nordlander, P., *Chem. Rev.* **2011**, *111*, 3913-3961.

¹²¹ Editorial, *Nature Nanotech.*, **2015**,*10*, 1.

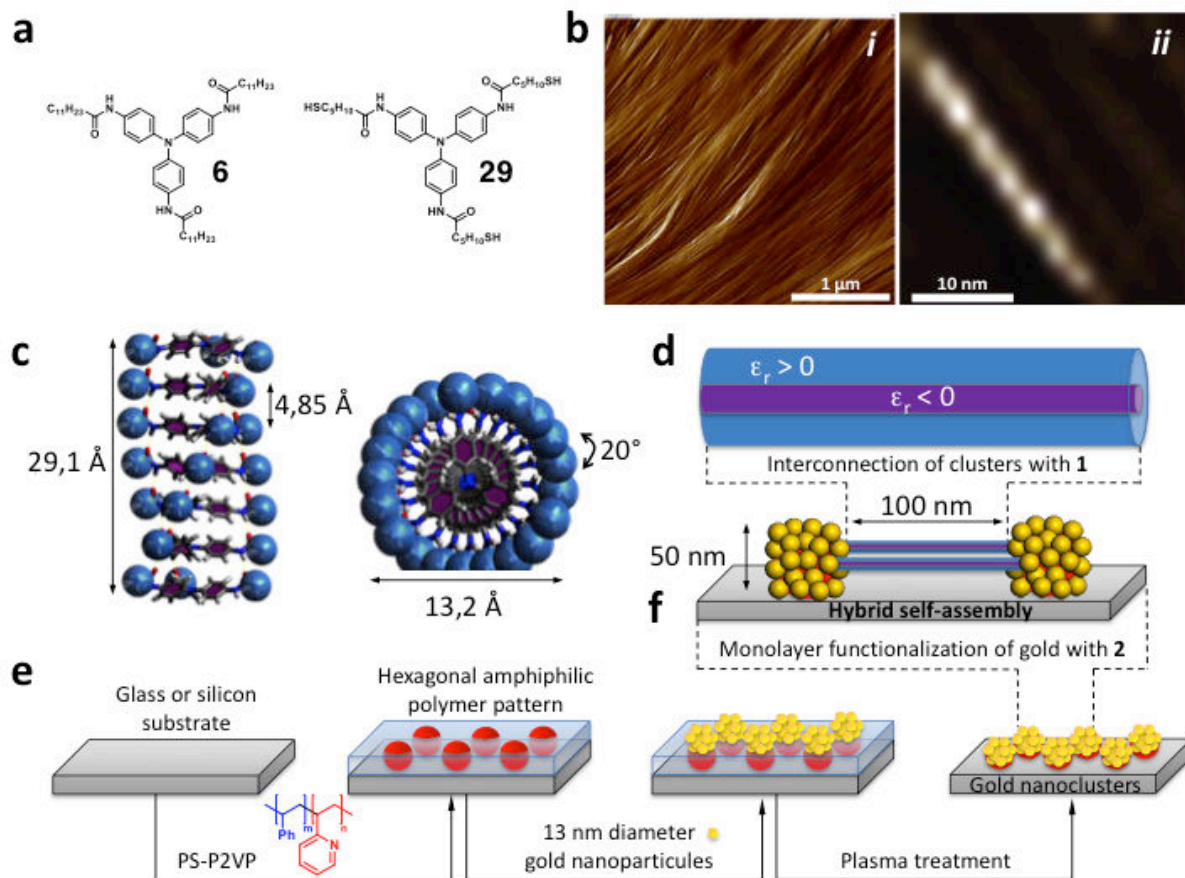


Figure 81 | a, Chemical structures of compounds **6** and **29** which are used to form the nanowires and to functionalize the gold surface, respectively. b, Two AFM images of STANWs made of **6** at the micrometer scale (i) and at the nanometer scale for a single fiber (ii). c, Side view and top view of the STANWs structure, and characteristic dimensions, as determined by AFM, small-angle and wide-angle X-ray scattering (SAXS and WAXS), and density functional theory (DFT) calculations. d, Coaxial structure of STANWs with a metallic triarylamine core (purple) surrounded by an aliphatic insulating sheath (blue). e, Schematic construction of the array of gold nanoclusters, using the amphiphilic patterning of the substrate by microphase separation of a block copolymer, selective deposition of nanoparticles, and plasma treatment. f, After proper functionalization of the gold surface by **29**, the array of gold nanoclusters is incubated with STANWs and leads to a fully interconnected network.

First, the array of nanoparticles was obtained using a templating strategy involving block copolymers (Figure 81e).^{122 123} A solution of self-assembled reverse micelles of polystyrene-poly-2-vinylpyridine (PS-P2VP) was spin coated onto either glass or silicon substrates to pattern an hexagonal amphiphilic mesostructure. Then, 13 nm gold nanoparticles were selectively adsorbed onto the hydrophilic polymer domains, producing clusters of gold nanoparticles. Subsequent plasma treatment removed the exposed hydrophobic polymer from the surface, leaving isolated gold nanoclusters with an average height of 48.9 ± 4.3 nm, and an

¹²² Mistark, P. A. Park, S.; Yalcin, S. E.; Lee, D. H.; Yavuzcetin, O.; Tuominen, M. T.; Russell, T. P.; Achermann, M. *ACS Nano* **2009**, *3*, 3987-3992.

¹²³ Yap, F. L., Thoniyot, P., Krishnan, S. & Krishnamoorthy, S., *ACS Nano*, **2012**, *6*, 2056-2070.

edge-to-edge distance of 94.5 ± 15.5 nm between nearest neighbors, as determined by atomic force microscopy (AFM) and scanning electron microscopy (SEM) (Figure 82).

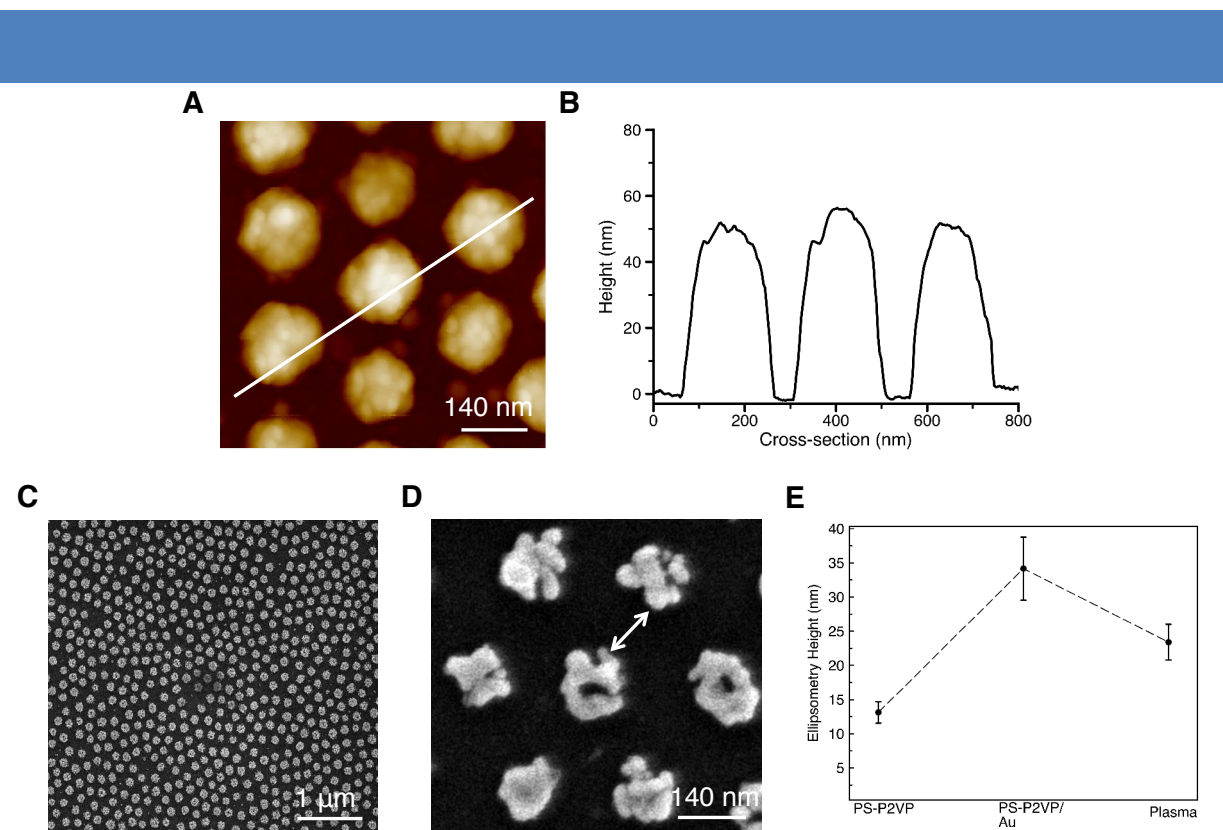
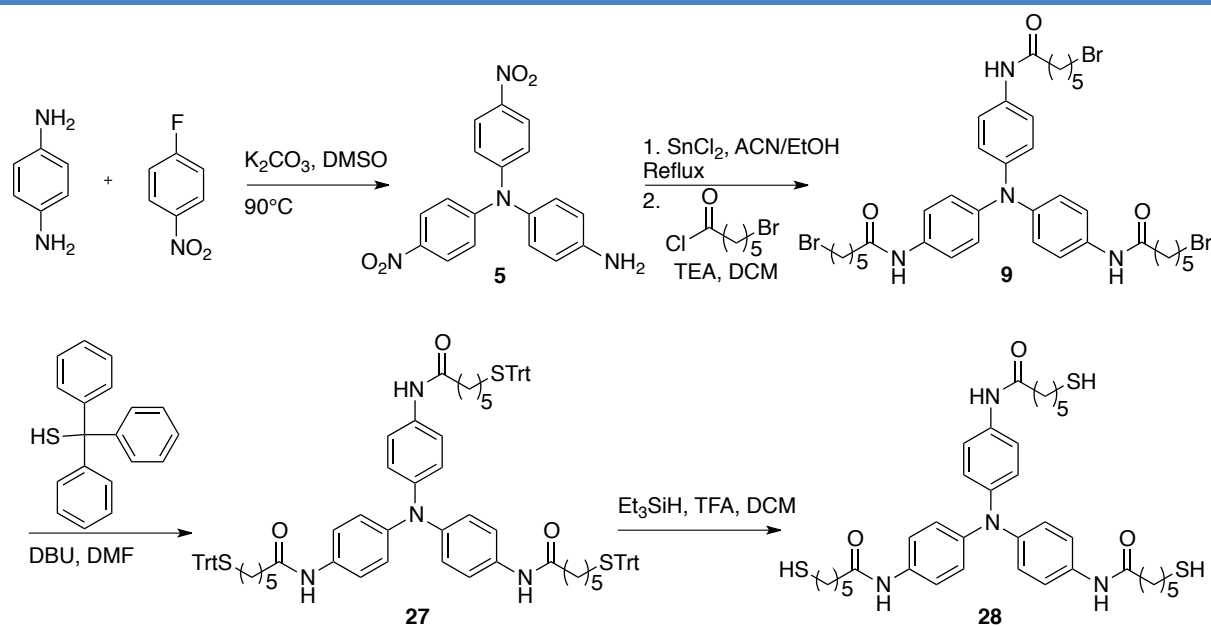


Figure 82 | (a) AFM height imaging of a typical gold nanocluster array obtained from a PS-P2VP template surface. (b) Height profile obtained along the white line depicted in (a). (c), Magnification of a cluster containing on average 10 nanoparticles. (d,e) SEM images at different magnifications and used to determine the average distance between gold nanoclusters ($94.5 \text{ nm} \pm 15.5 \text{ nm}$ ($n = 114$)). (f) Height of the substrate as determined by ellipsometry at different stages in the process: PS-P2VP layer, after addition of gold nanoparticles, and after plasma treatment of the surface.

Next, the nanocluster array was covered with a monolayer of tris-thiol triarylamine (**8**), which was synthesized according to the procedure in scheme 8. This is a good example of the versatility of the reaction pathway described in the previous chapter. After forming the triarylamine core, amidation gives the tris-amide molecule **9** with terminal bromine substitution on the alkyl chains. This allows a facile substitution with triphenylmethane thiol to give the protected thiol compound **27** in high yield. Careful deprotection under inert atmosphere gives the resulting free thiol **28**.



Scheme 8 | Synthetic route to tris-amide thiol triarylamine, **28**.

Monolayer deposition was effected from methanolic solutions, which preclude the formation of stabilizing intermolecular hydrogen bonds, and likewise any self-assembly. Moreover, the critical aspect of this step was to achieve the desired parallel orientation (*versus* the undesired perpendicular one) of the triarylamine core with the nanoparticle surface (Figure 83a). Formation of the triarylamine monolayer was investigated using quartz crystal microbalance with dissipation (QCM-D) and atomic force microscopy (AFM). The QCM technique is commonly used to probe surface attachment,¹²⁴ and is particularly useful for monitoring thiol adsorption to gold.¹²⁵ The advantages of this technique are that they allow the real time monitoring of the rate of deposition as well as the mass of deposited material. A negligible dissipation signal was observed during the deposition experiments (see blue data in Figure 83b), indicating the formation of a rigid monolayer and allowing the amount of material deposited on the surface to be estimated from the Sauerbrey equation:

$$m_f = -C \cdot \Delta f \quad (37)$$

where m_f is the area mass density of the film and C is the mass sensitivity constant (17.7 ng cm⁻² Hz⁻¹). Monolayers formed from low concentration (10 μM) and high concentration (1 mM) solutions of **28** resulted in mass densities of 0.55 molecules nm⁻² and 2.34 molecules nm⁻², respectively. Subsequent deposition from a 1 mM solution onto the monolayer prepared

¹²⁴ Reviakine, I.; Johannsmann, D. & Richter, R. P. *Anal. Chem.*, **2011**, 83, 8838–8848.

¹²⁵ Schneider, T. W.; Buttry, D. A., *J. Am. Chem. Soc.* **1993**, 115, 12391–12397.

from the 10 μM solution gave an additional mass loading of 0.939 molecules nm^{-2} . The combined mass from this sequential deposition was 1.489 molecules nm^{-2} , demonstrating a difference of 0.851 molecules nm^{-2} with the high concentration deposition on a clean substrate.

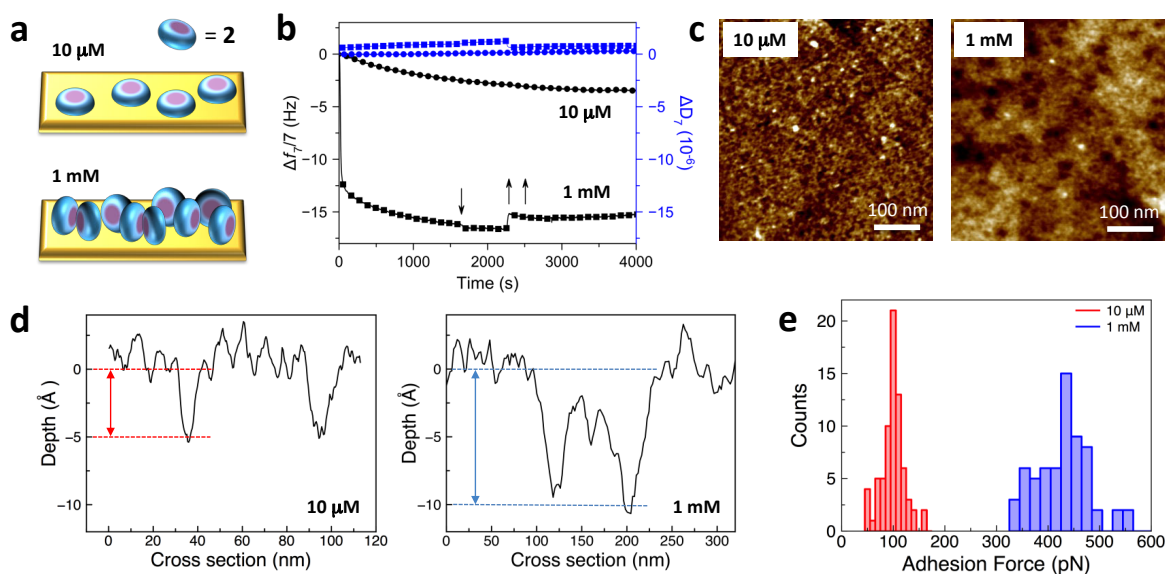


Figure 83 | **a**, Two possible orientations of **28** at the gold surface. These orientations are sensitive to the concentration of the solution during the deposition process because of the tripodal nature of the molecule: (top) desired parallel orientation at low concentration with the three thiols attached, and (bottom) undesired perpendicular orientation at higher concentration, leaving free alkyl chains pointing out of the surface. **b**, QCM monitoring of the functionalization from a 10 μM solution (circles) and a 1 mM solution (squares) of **28** with the corresponding frequency shifts (black) and dissipations (blue). **c**, AFM imaging of the surfaces obtained after incubation of a crystalline (111) gold surface with a 10 μM solution of **28** (left) and a 1 mM solution of **28** (right). **d**, AFM depth profiles of the surface for a 10 μM solution (left) and a 1 mM solution (right) of **28**. **e**, AFM adhesion force measurements (statistical distribution on $n = 100$ values) at the surface for a 10 μM solution of **28** (red) and a 1 mM solution (blue) of **28**.

These data are indicative of a significant change in the monolayer packing depending upon the concentration of the depositing solution. From DFT calculations, the core of a triarylamine molecule oriented parallel to the surface will take up approximately 1.4 nm^2 , giving a maximum concentration of 0.71 molecules nm^{-2} . In contrast, perpendicular orientation to the surface will take up an area of 0.4 nm^2 , giving a maximum concentration of 2.48 molecules nm^{-2} . Overall, the low concentration solution is consistent with a parallel orientation of the triarylamines with all three thiol groups anchoring to the surface, while the high concentration deposition is consistent with a perpendicular orientation with either one or two of the thiol groups bonded to the surface.

Analysis of the deposition kinetics also demonstrated a marked difference between the two deposition concentrations (Figure 84).

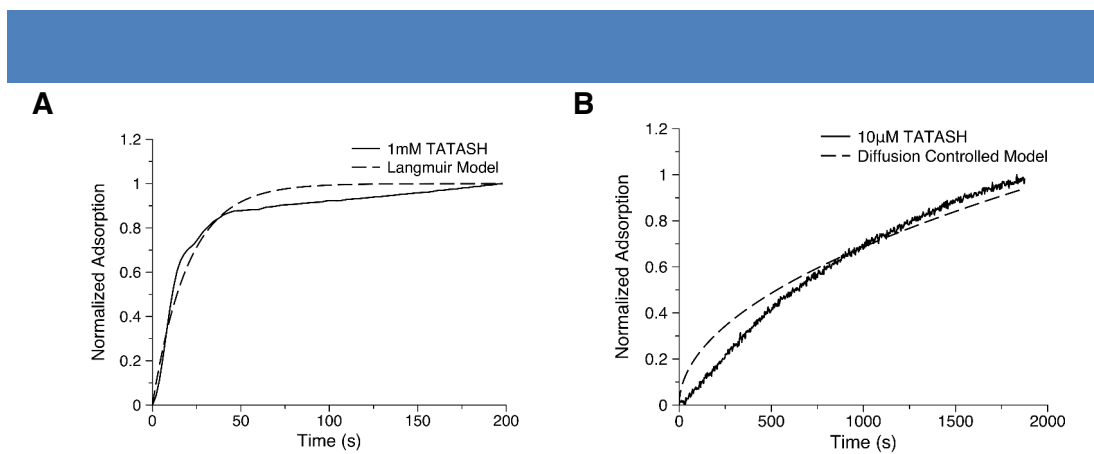


Figure 84 | **a**, Adsorption kinetics from a 1 mM solution of TATASH **28** along with the fit of the data to the Langmuir model giving a rate constant of $0.255 \text{ s}^{-1/2}$. **b**, Adsorption kinetics from a $10 \mu\text{M}$ solution fit with a combination of linear mass transport regime for the first 500 s ($k=6.875 \cdot 10^{-4} \text{ s}^{-1}$), followed by a diffusion controlled model giving a rate constant of $0.0165 \text{ s}^{-1/2}$.

The monolayer formed from a high concentration solution of the thiol was modeled using a diffusion-limited Langmuir model:

$$\theta(t) = [1 - e^{-kt^{0.5}}] \quad (38)$$

giving a rate constant of $0.255 \text{ s}^{-1/2}$. This indicates that the adsorption kinetics are influenced by the fraction of available surface area on the gold substrate indicative of molecular crowding at the surface. By contrast, the $10 \mu\text{M}$ concentration fit includes two regimes, an initial linear regime due to the mass transport of the thiol molecules along a concentration gradient from the bulk solution to the surface followed by a diffusion-controlled regime. The linear fit resulted in a rate constant of 0.0006875 s^{-1} . After the surface functionalization had reached 40% of the final coverage, the deposition kinetics transitioned to a diffusion-controlled regime:

$$\theta(t) = k_d \sqrt{t} \quad (39)$$

with a rate constant of $0.0165 \text{ s}^{-1/2}$. Thus, deposition affected from a low concentration solution does not incur the kinetic limitation observed from high concentration solutions. The results indicate that the concentration of the depositing solution influences the kinetics of the deposition process which in turn gives rise to two predominant orientations on the surface: (1) the thermodynamically favored parallel orientation with all three thiol groups attached to the surface, and (2) the perpendicular orientation which is kinetically controlled due to rapid deposition from high concentration solutions. The relatively strong (ca. $50 \text{ kcal}\cdot\text{mol}^{-1}$) gold-thiol bonds are able to trap the kinetically controlled perpendicular orientation, while

providing the energetics to make the parallel orientation thermodynamically favorable.¹²⁶

These results were correlated with high resolution AFM profiles of monolayers on crystalline gold (111) surfaces (Figure 83c). The average height of the deposited monolayer from high concentration (1 mM / 1 nm) was twice that of low concentration (10 μ M / 0.5 nm), corresponding to the expected difference between vertical and horizontal orientations. Additionally, adhesion force measurements ($n \approx 100$) gave mean values of 430 ± 52 pN for the high concentration protocol, and of 99 ± 22 pN for the low concentration deposition (figure 85e). This difference can be explained by the more sticky interaction of the tip with the free alkyl side-chains in the vertical orientation.

Finally, the functionalized nanoclusters were connected with STANWs through supramolecular recognition with the monolayer made of **28** (Figures 85 and 87).

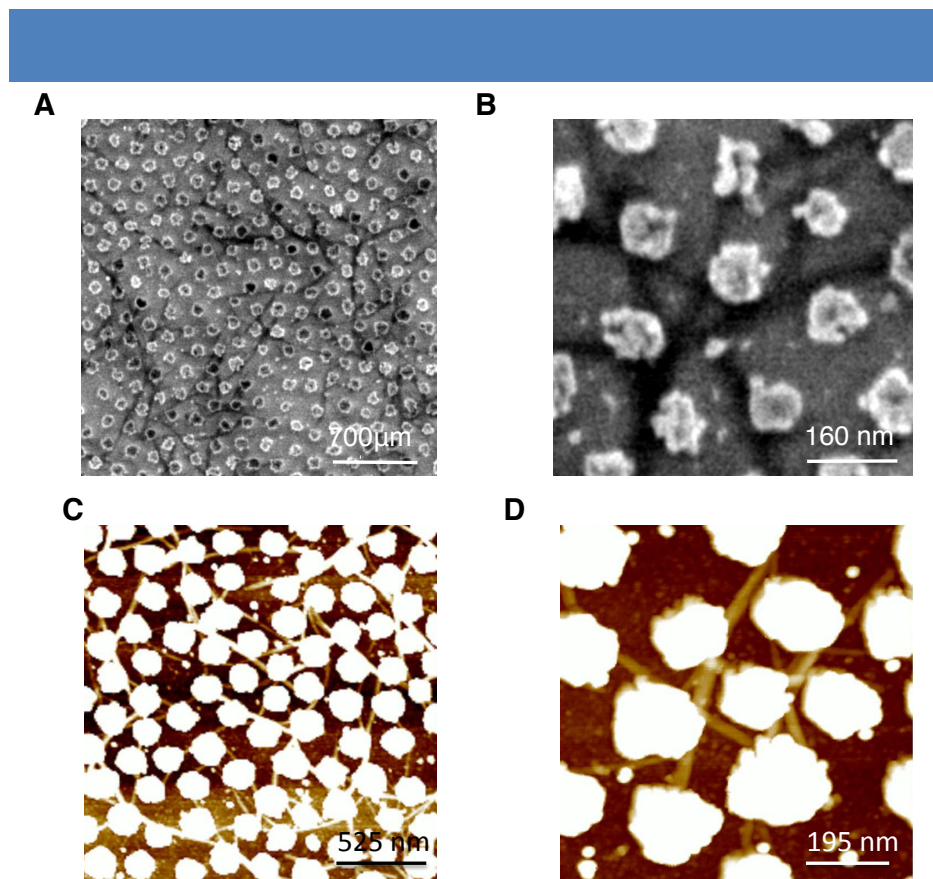


Figure 85 | (a, b) SEM images of an array of nanoparticle clusters after incubation with attached doped nanowires (a) and after washing (b). (c, d) AFM images of an array of nanoparticle clusters after incubation with attached doped nanowires (c) and after washing (d).

Attachments were performed under thermodynamic equilibration by incubation of the substrate for 24 h in a chloroform solution of **6** ($c = 1$ mM). In this solvent, the fibers can be

¹²⁶ Bain, C. D., Troughton, E. B., Tao, Y. T., Evall, J., Whitesides, G. M. & Nuzzo, R. G., *J. Am. Chem. Soc.* **1989**, *111*, 321-335.

oxidized by simple light irradiation with a 10 W.cm^{-2} halogen lamp, leading to conducting organic metals. In the following, the terms of “undoped” (or “doped”) wires will refer to the absence (or the presence) of such light irradiation applied during the first 10 min of the incubation process. Various techniques were used to probe the STANWs–nanoclusters connections. For instance, AFM images immediately after incubation display a network of nanoparticles and dense fibers (Figures 87 b,c). Upon washing the substrates with chloroform, only fibers strongly connected to nearby nanoparticles remained (Figure 85). Control experiments highlighted the necessity of this hierarchical process in order to achieve the desired outcome. A substrate incubated with a 1 mM chloroform solution of TATA fibers **6** for 24 hours displayed no fibers remaining after washing (Figure 86). A second control experiment involving pre-functionalization with a high concentration of molecule **28** in chloroform displayed amorphous deposition of the molecules that were resistant to washing. Additionally, high concentrations of **28** in methanol (1 mM) led to displacement and aggregation of the nanoclusters without any wire attachment, as seen by AFM using peak force error image. On average, one can determine a ratio of fibers over clusters is of 1.25, which means on average 12.5% of connected fibers per nanoparticle, as clusters contain on average 10 nanoparticles.

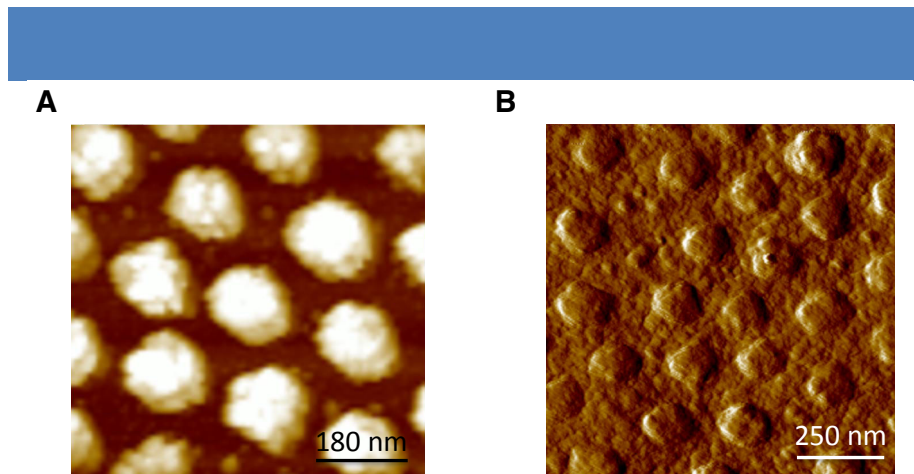


Figure 86 | (a) Substrate incubated with nanowires of **6** but without the thiol pre-functionalization step (and washed). (b) Substrate incubated in 1 mM chloroform solution of **28** and washed (peak force error image).

Surface Enhanced Raman Scattering (SERS) was also used as an ultrasensitive method for probing the local chemical environment at the gold surface. Raman signals in figure 87d display a clear signature for the monolayer of **28**, demonstrating effective functionalization of the nanoclusters. Notably, there is no observable Raman signal for the substrate covered by STANWs without surface pre-functionalization with **28**, demonstrating their inefficient

attachment to naked nanoclusters. However, functionalized nanoclusters with doped nanowires display an enhancement of Raman modes at 1175 cm^{-1} and 1600 cm^{-1} , together with a suppression of other modes, thus showing an effective connection through the monolayer.

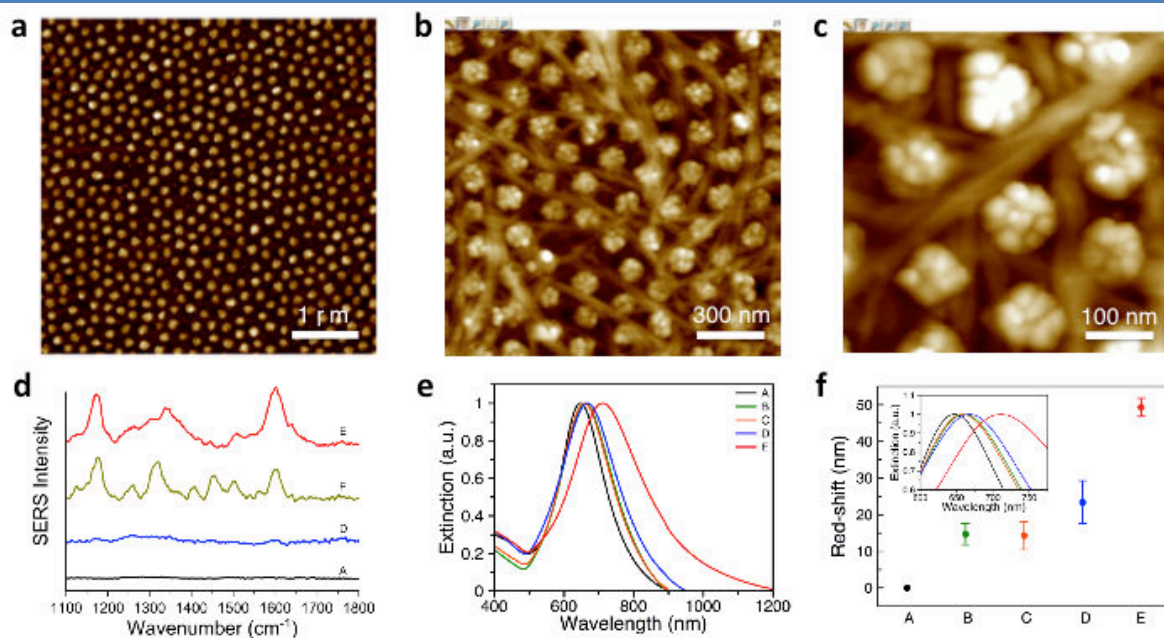


Figure 87 | Throughout this figure and Figure 88, the following color code is used for the plotted data: A (black), naked gold nanoclusters; B (green), unfunctionalized with **28** and undoped fibers; C (orange), functionalized with **28** and undoped fibers; D (blue), unfunctionalized with **28** and doped fibers; E (red), functionalized with **28** and doped fibers. **a**, AFM height image of the patterned array of naked gold nanoclusters, as obtained after the construction process depicted in Figure 1e. **b**, AFM height image of the hybrid array of organic fibers with gold nanoclusters, as obtained after the construction process depicted in Figure 1f, that is including STANWs as interconnects. **c**, Magnification of the AFM height image obtained in (b) showing details of the hybrid network. **d**, SERS responses of the gold nanoparticle surfaces depending on the surface treatment and on the doping of fibers (see color code above). **e**, Extinction spectra of the plasmonic array, depending on the surface treatment of the gold and on the doping of fibers (see color code above). **f**, Details of the plasmonic red shifts, depending on the surface treatment of the gold and on the doping of fibers (see color code above).

3. Optical Properties of Connected Nanocluster Arrays

The various plasmonic responses of these substrates were studied in their interconnected *versus* disconnected configurations. Far-field scattering spectrum (Figure 87) of the reference array of nanoparticles covered only by a monolayer of the thiolated compound exhibited a plasmonic peak at $651\pm 4.5\text{ nm}$, similar to the naked nanoparticles $647\pm 2.8\text{ nm}$. Substrates prepared with undoped fibers displayed equivalent red-shifts, regardless of the pre-functionalization of the nanoclusters ($14.7\pm 2.9\text{ nm}$ unattached; $14.3\pm 3.8\text{ nm}$ attached). An increase in the red-shift of $23.4\pm 5.9\text{ nm}$ was observed with doped fibers on

unfunctionalized substrates and, finally, functionalized nanoclusters connected by doped nanowires displayed the largest red-shifts (49.3 ± 2.5 nm). This displays a remarkable effect of doping on the plasmonic resonance of the nanocluster array, along with a huge increase resulting when the nanoclusters are connected through the monolayer functionalization strategy.

Optical constants of the substrates were determined from spectroscopic ellipsometry by modeling the plasmonic oscillations with a Lorentzian behavior.^{127,128} The pseudodielectric function may be obtained from the following expression:⁷²

$$\varepsilon(\omega) = \sin^2\theta \left[1 + \left(\frac{1-\rho}{1+\rho} \right)^2 \tan^2\theta \right] \quad (40)$$

and is thus dependent upon the incident angle (θ) and the reflection ratio (ρ):

$$\rho = \tan\Psi e^{-i\Delta} \quad (41)$$

where Ψ and Δ are the amplitude ratio and phase difference of the reflected polarized light. A three-phase model was used to fit the data consisting of the incident medium (air), the plasmonic layer, and the silicon substrate. The thickness of the plasmonic layer was fixed to match the height obtained by AFM imaging. The plasmonic layer was assumed to be isotropic with Lorentzian behavior, due to the spatial confinement of the surface plasmons by the nanoparticle dimensions.⁷¹ Accordingly, the dielectric response was fit by a Drude-Lorentz function with three Lorentzian oscillators:

$$\varepsilon(\omega) = \varepsilon_\infty + \sum_{j=1}^3 \frac{f_j \omega_{0j}^2}{\omega_{0j}^2 - \omega^2 + i\gamma_j \omega} \quad (42)$$

where ω_0 is the resonance frequency, γ is the damping parameter, and f is the fractional strength of the j^{th} oscillator. Measurements were taken between 40° and 80° , with the final data coming from a combined fit of three angles (40° , 60° , 80°).

Figure 88 displays the real and imaginary parts of the dielectric function for nanoarrays prepared with undoped attached nanowires, doped unattached nanowires, and doped attached nanowires, respectively. The imaginary part of the dielectric constant was used to derive the real part of the optical conductivity (σ_r) which directly relates to the number of electrons undergoing oscillations in the plasmonic layer.¹²⁹ The data displays a massive increase of σ_r going from $259 \Omega^{-1} \cdot \text{cm}^{-1}$ for the undoped nanowires, to $3193 \Omega^{-1} \cdot \text{cm}^{-1}$ for the doped unattached nanowires. This demonstrates a significant coupling of the metallic

¹²⁷ Yang, Y.; Akozbek, N.; Kim, T.-H.; Sanz, J. M.; Moreno, F.; Losurdo, M.; Brown, A. S.; Everitt, H. O.. *ACS Photonics*, **2014**, *1*, 582-589.

¹²⁸ Verre, R.; Modreanu, M.; Ualibek, O.; Fox, D.; Fleischer, K.; Smith, C.; Zhang, H.; Pemble, M.; McGilp, J. F.; Shvets, I. V., *Physical Review B* **2013**, *87*, 235428.

¹²⁹ Vakil, A. & Engheta, N., *Science*, **2011**, *332*, 1291-1294.

electrons in the STANWs to the plasmonic oscillations of the gold nanoclusters, which are in turn coupled to the incident electromagnetic field. Pre-functionalization of gold with the thiol monolayer gave an additional 34% increase in the oscillator strength ($4271 \Omega^{-1} \cdot \text{cm}^{-1}$), emphasizing the benefit of supramolecular attachment of the doped wires at the gold surface to couple the plasmonic nanoparticles. Convergenly, a significant red-shift of the resonance frequency of the oscillator (ω) was observed with the peak position going from 548 nm for the undoped nanowires, to 623 nm and 633 nm for the doped unattached and doped attached nanowires, respectively (Figure 88). Moreover, the damping parameter (γ), which is related to interactions at the particle surface, was equivalent for the doped and undoped nanowires with the unfunctionalized substrates (100 nm), but was found to increase to 109 nm for the thiol-functionalized substrate, demonstrating again an increased coupling of the oscillations at the interface. We also measured an increase in the dissipation factor¹³⁰ when doping and further attaching the STANWs on the array of nanoclusters (Figure 88f).

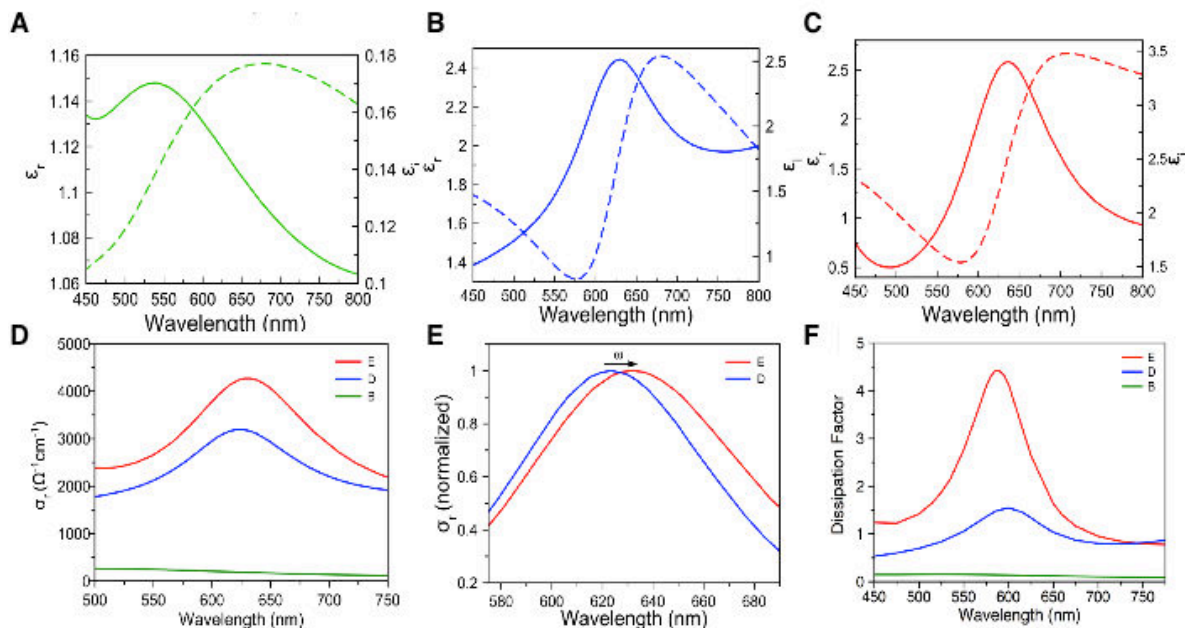


Figure 88 | **a**, Real (dashed) and imaginary (plain) parts of the dielectric constant, as determined by ellipsometry, for the undoped attached fibers. **b**, Real (dashed) and imaginary (plain) parts of the dielectric constant, as determined by ellipsometry, for the doped unattached fibers. **c**, Real (dashed) and imaginary (plain) parts of the dielectric constant, as determined by ellipsometry, for the doped attached fibers. **d**, Overlay of the real optical conductivities, derived from ellipsometry measurements, depending on the surface treatment of gold nanoparticles and on the doping of fibers (see color code above). **e**, Normalized real optical conductivities for the unattached (D) and attached doped (E) fibers showing the resonance frequency of the oscillator ω . **f**, Overlay of the dissipation factors, depending on the surface treatment of the gold and on the doping of fibers (see color code above).

¹³⁰ Tassin, P., Koschny, T., Kafesaki, M. & Soukoulis, C. M., *Nature Photon.*, **2012**, 6, 259-264.

The doped, unattached substrate and the doped attached substrates gave standard deviations of 1.29% and 3.79%, respectively, from the raw ellipsometry data (n=5).

The dielectric constant of the plasmonic layer is composed of a real and imaginary part. In general, the real part indicates the strength of polarization induced by an applied electromagnetic (EM) field, while the imaginary part indicates the losses incurred when polarizing the material. Here, the imaginary dielectric constant corresponds to the absorptive effect of inducing plasmonic oscillations within the nanoparticles. The imaginary part of the dielectric constant can also be used to determine the real part of the optical conductivity from the following relation:

$$\sigma_r = \frac{\varepsilon_i \omega}{4\pi} \quad (43)$$

Since the conduction electrons in the gold are bound spatially, they will exhibit Lorentzian behavior in response to the driving electromagnetic field. Thus, the real part of the optical conductivity corresponds to the induced current in phase with the driving EM field. The description of Lorentzian oscillators depicts three key variables. First, the resonant frequency is ω_0 which determines the oscillator position. In Lorentzian theory, this is proportional to the force constant on the system which is the electric field vector experienced by the conduction electrons in the nanoparticles. Contributions from local fields, i.e. electric fields emanating from nearby electron oscillations can disrupt the incident EM field, thus altering the restoring force of the oscillator and shifting the plasmonic resonance frequency. Next, the oscillator strength, f , is a sum rule of the number of electronic interactions and directly relates the number of electrons undergoing oscillations. The damping parameter will depend on the size of the nanoparticles and can also be due to interactions of the plasmonic oscillations with molecules near the nanoparticle surface.^{131,132} Finally, the dissipation factor (Figure 88f) was determined by taking the ratio between the imaginary part and the real part of the dielectric constants for the respective substrates. It gives how much energy supplied by an external EM field is dissipated in a system. Here, the dissipative losses depict the efficiency of coupling between the plasmonic resonances in the gold nanoparticles and the metallic electrons in the STANWs nanowires.

¹³¹ Berciaud, S.; Cognet, L.; Tamarat, P.; Lounis, B. *Nano Lett.* **2005**, *5*, 515–518

¹³² Bosbach, J.; Hendrich, C.; Stietz, F.; Vartanyan, T.; Träger, F. *Phys. Rev. Lett.*, **2002** *89*, 257404

4. Optical Nanocircuit Theory

The lumped circuit abstraction is used to model physical systems by ignoring nonessential physical parameters and defining the parts of a system as discrete elements. Optical nanocircuits rely on displacement currents and not on conduction current that are the basis of conventional electrical circuits. These displacement currents are directly related to the scattered field and therefore depict the response of the far-field spectrum to changes in the circuit. Application of an EM field induces an oscillating polarization of the electrons in the metallic nanoparticle with the displacement current defined as:

$$J_d = -i\omega\epsilon E \quad (44)$$

Kirchoff's laws may be satisfied by taking the current I to be the flux integral of J_d across the nanoparticle and the voltage V to be the potential between the two ends of the nanoparticle. The extinction spectra from an isolated gold nanoparticle resonating at its plasmonic frequency may be modeled as an LC circuit (figure 88a). The two impedance elements in the model are the capacitance due to the propagating near-field around the nanoparticle and an inductor due to the negative dielectric constant of gold:

$$Z_c = (-i\omega 2\pi R \epsilon_0)^{-1} \quad (45)$$

$$Z_l = (-i\omega \pi R \epsilon_r)^{-1} \quad (46)$$

where ω is the frequency, ϵ_0 is the permittivity of the region surrounding the nanoparticle, ϵ_r is the real part of the dielectric constant of gold and R is the radius of the nanoparticle.

The coupling of the plasmonic resonances of two nanoparticles was modeled by placing the inductive elements either in series (I_s) (Figure 89b) or in parallel configuration (I_p) (Figure 89c) The series configuration corresponds to excitation perpendicular to the axis of connection, while the parallel configuration corresponds to excitation parallel to the axis of connection.⁷ Due to the isotropic nature of our substrate, there should be an even distribution between the two configurations, therefore the total contribution from coupled nanoparticles comes from a linear combination of the two circuits ($I_c = \frac{1}{2} I_s + \frac{1}{2} I_p$). The red-shift of the substrate is then dependent on the proportion of current flowing through the isolated nanoparticle circuit (I_i) and the connected circuits: $I_{total} = aI_i + bI_c$ where $a + b = 1$. The coefficients a and b represent the fractions of current flowing through the constituents of the circuit, and are related to the proportion of efficient interconnects. This combined circuit description of the substrate is displayed in figure 89d. The circuit will be directly related to the number of connections between the nanoparticles on the substrate, therefore we can represent the entire substrate as a fuzzy AND logic gate (figure 89e) where the number of

connections will change the proportion of current flowing through the two loops with a change in the corresponding output (the far-field scattering spectrum; figure 89f).

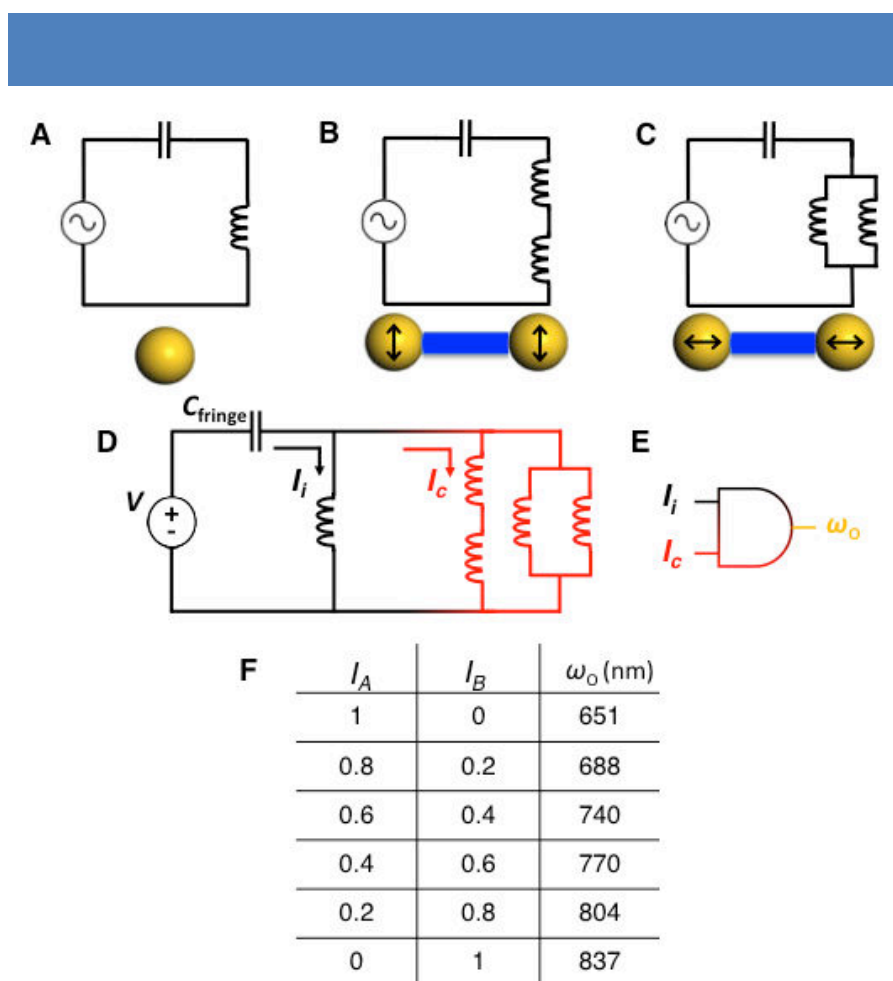


Figure 89 | Circuit models based on optical nanocircuit theory for (a) an isolated nanoparticle, (b) two connected nanoparticles with incident light polarized along the interparticle axis, and (c) connected nanoparticles with incident light polarized perpendicular to the interparticle axis. (d) Proposed circuit model of the nanoparticle arrays connected by the nanowires. AND logic gate representation corresponding to the circuit diagram with the resonance frequency of the circuits as the output (e). Logic table of values for different current proportions through the loops I_i and I_c (f).

The circuit model was applied to our substrates by first fitting the bare gold nanocluster extinction spectrum by adjusting the permittivity of the polymer-supported nanocluster (Figure 90a). The values of the gold dielectric constant were taken from literature.¹³³ A constant value for the resistance in the circuit was applied to achieve the requisite broadening of the peak. Next, the extinction spectrum from the nanoclusters with undoped nanowires was fit to take into account the change in dielectric constant surrounding the nanoparticles (Figure 90b). This resulted in a dielectric of $1.4\epsilon_0$ for the undoped

¹³³ Johnson, P. B. & Christy, R. W. *Phys. Rev. B*, **1972**, 6, 4370–4379

nanowires and a nanocapacitance value of 2.46 attoF. Subsequently, the extinction spectra for the doped substrates were fit by holding the value of the inductances constant and adjusting the proportion of current flowing through the three circuits displayed in Figure 89c. In this circuit model, the plasmonic interconnects are taken to be ideal wires with no impedance contribution.^{56,57}

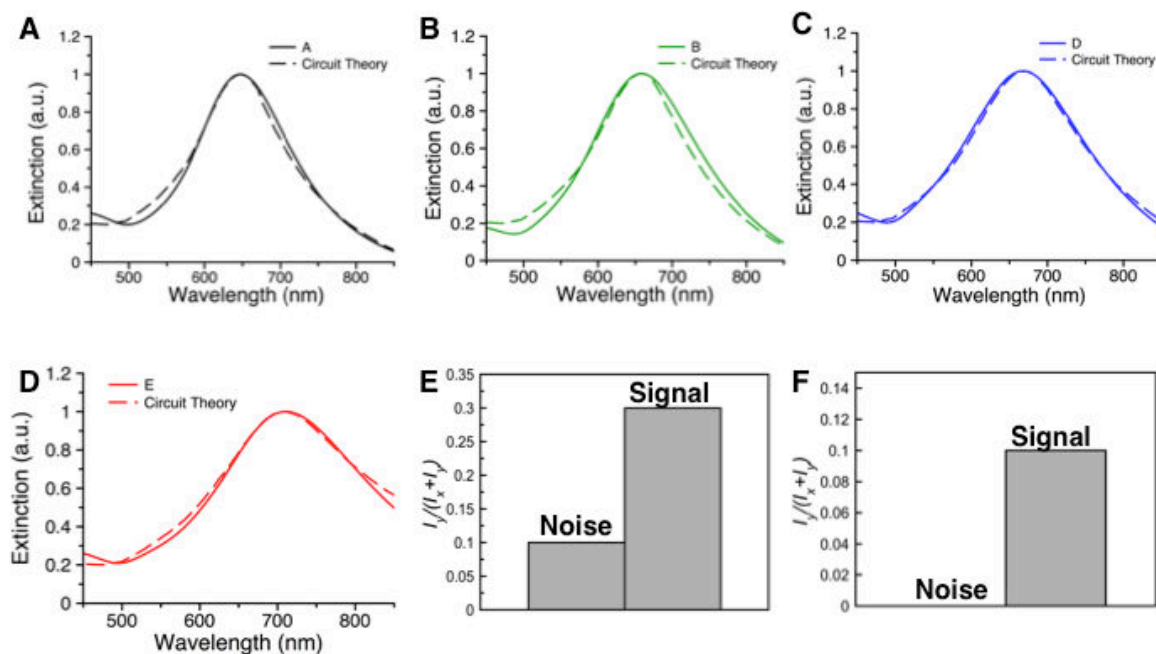


Figure 90 | Circuit theory fits to the experimental scattering data for substrates A (a), B (b), D (c), and E (d). Signal to noise ratio for unwashed and washed substrates, demonstrating the ability to detect in the far-field the connected nanocircuits (e, f).

The attached doped substrate extinction spectrum (Figure 90e) was fit with 90% of the current flowing through the connected circuits and 10% flowing through the isolated nanoparticles. A similar procedure was used to fit the washed substrates. First, the fringe capacitance was adjusted to fit the washed samples from the undoped, attached substrate resulting in a surrounding dielectric of $1.1\epsilon_0$. Then, the washed, doped/attached substrate was fit using the circuit theory model giving 13% of the current flowing through the connected circuits. This can be thought of as a way to detect the ‘signal’ coming from connected nanoparticles over the ‘noise’ coming from unconnected nanoparticles (Figure 90e,f). Importantly, this demonstrates the ability to detect, with simple far-field methods, attached nanowires from unattached background noise. The ratio is a factor of 3 for unwashed substrates, while the washed substrates exhibit no noise contribution (since all of the fibers have been removed). From this extraction we see the creation of fuzzy circuits (many-valued logic) wherein the number of connections will dictate the output value (the far-field extinction spectrum). One

can also view it as the creation of a non-linear circuit with a switching function resulting in a fuzzy AND logic gate. Additionally, by finite difference time domain (FDTD) simulations, and using two gold nanoparticles connected by a nanowire having the permittivity determined by ellipsometry for attached doped fibers, one can observe a propagation along the waveguide when the incident electric field is perpendicular to the wire direction (Figure 91). This is important to future applications of this because it means that by controlling the orientation of the incident light, one should be able to control whether two nanoparticles are coupled or not. This should result in the ability to switch the circuit on and off.

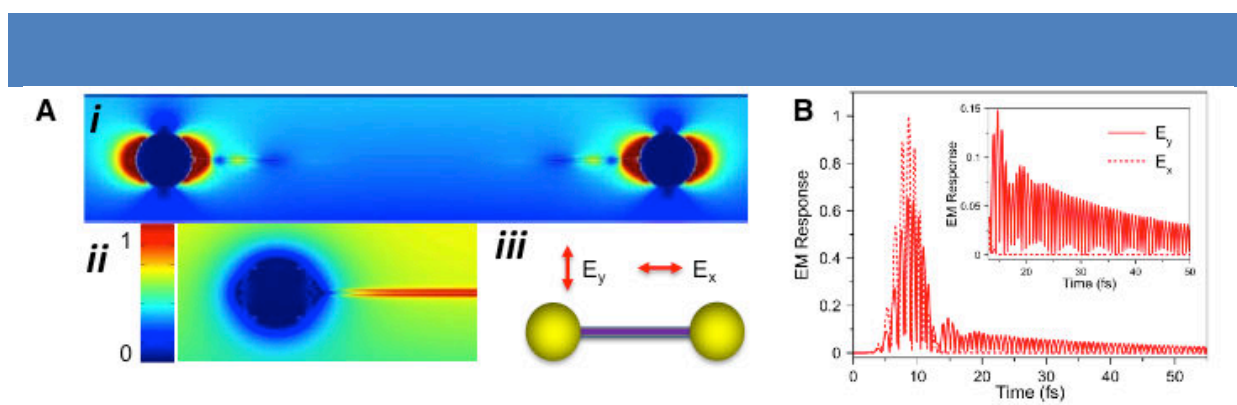


Figure 91 | FDTD simulations of coupling through the nanowires based upon the dielectric constants determined from the ellipsometry data.

5. Conclusions

The data presented in this chapter demonstrates the coupling of plasmonic modes between metallic nanoparticles through the oscillation modes of TATA nanowires, demonstrating the ability to act as subwavelength optical interconnects. This proof of principle is important because plasmonic interconnects are predicted as key tools to reach complex nanocircuit topologies, and because they should solve the problem of undesired displacement current ‘leakage’ that occurs when nanoparticles are brought in direct contact. Furthermore, the organic and self-assembled characters of STANWs open an entirely new field of research towards “plastic” and “supramolecular” plasmonics, providing a large number of opportunities to implement soft and processable 2D and 3D nanophotonic devices and metamaterials.

Chapter VIII: A Triarylamine Supramolecular Organic Framework As Plasmonic Waveguide

1. Introduction

In this chapter we introduce a supramolecular organic framework based on the tris-amide triarylamine core structure. Additionally, we are able to expand upon the observations seen in the previous chapter by analyzing the waveguiding properties of single crystals large enough to be examined with an optical microscope. As outlined in the introduction, organic materials have become increasingly investigated for their optical waveguiding properties. The dominant waveguiding mechanism is the photoluminescence mechanism, whereby an incident laser induces an excited state in the molecules which then, due to the close packing of the chromophoric part of the molecule, leads to energy transfer in the form of exciton polaritons along the coherently stacked structures.¹³⁴ Such a mechanism is strongly wavelength dependent and only a few examples of energy transport over 10 nanometers have been reported.^{135,136,137} Meanwhile, metallic nanostructures such as gold nanowires have been demonstrated to produce optical waveguiding effects due to plasmonic coupling, coupling between incident light and metallic electrons.¹³⁸ Indeed metallic nanostructures are the subject of intense research efforts towards light harvesting and energy transport.¹³⁹ Here, we propose the conceptual advance of using organic metals, organic materials with band-like electronic structure with delocalized electrons, as waveguides for light and energy transport. In addition, we show the clear energy transport on the micron scale due to this mechanism. This proof-of-principle should be readily extended to other organic metals allowing the formation of organic plasmonic waveguides as a novel photonic material.

¹³⁴ Yan, Y.; Zhao, Y. S. *Chem. Soc. Rev.* **2014**, *43*, 4325-4340.

¹³⁵ Haedler, A. T.; Kreger, K.; Issac, A.; Wittmann, B.; Kivala, M.; Hammer, N.; Kohler, J.; Schmidt, H.-W.; Hildner, R. *Nature* **2015**, *523*, 196-199.

¹³⁶ Avakian, P.; Merrifield, R. E. *Phys. Rev. Lett.* **1964**, *13*, 541-543.

¹³⁷ Dubin, F.; Melet, R.; Barisien, T.; Grousson, R.; Legrand, L.; Schott, M.; Voliotis, V. *Nat Phys* **2006**, *2*, 32-35.

¹³⁸ Lal, S.; Hafner, J. H.; Halas, N. J.; Link, S.; Nordlander, P. *Accounts of Chemical Research* **2012**, *45*, 1887-1895.

¹³⁹ Atwater, H. A.; Polman, A. *Nat Mater* **2010**, *9*, 205-213.

2. A Triarylamine Supramolecular Organic Framework (TSOF)

The use of supramolecular synthons to control crystallization structure is becoming a key technique to design packing structure in organic molecules.^{140 141} The triarylamine supramolecular organic framework (TSOF) is formed from tris-amide substituted triarylamine **29** (Figure 92).

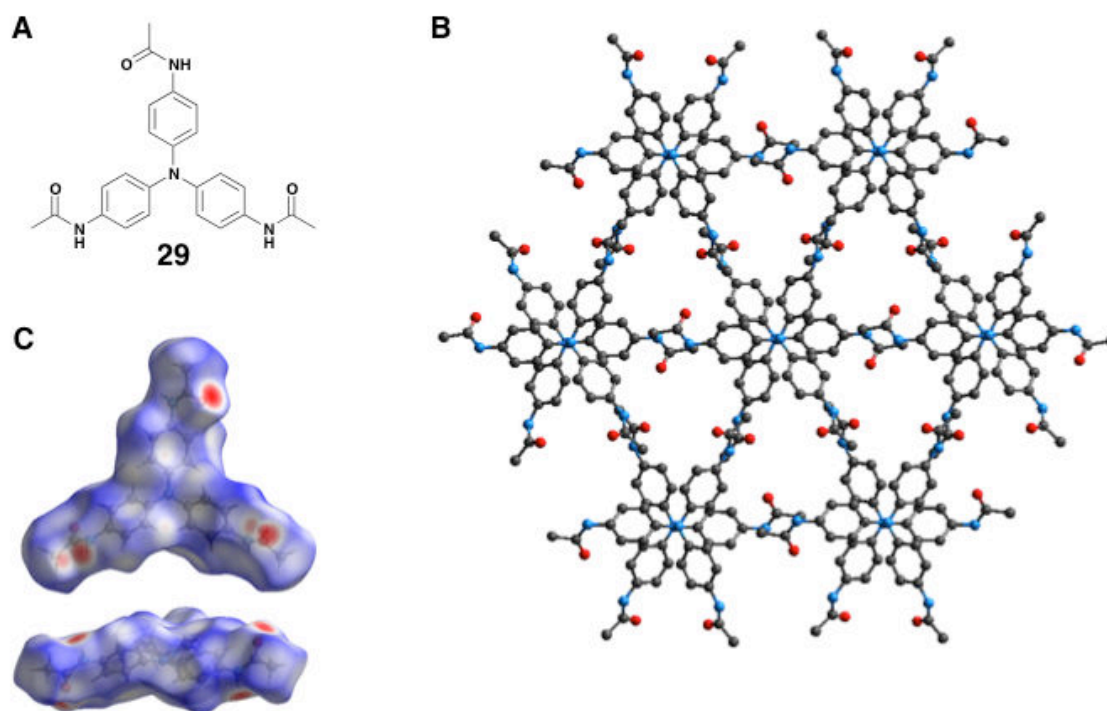


Figure 92 | Molecular structure of tris-amide triarylamine **29** (a) Crystal structure of the Triarylamine Supramolecular Organic Framework (TSOF) (b). Hirshfeld surface of an isolated molecule displaying the close contacts of the three amide groups (red) and the three aromatic rings (white) driving the crystallization structure (c).

In order to control the crystallization of TSOF, a solvent mixture of methanol (75%) and toluene (25%) was employed to ensure the absence of any self-assembly. NMR studies confirmed the presence of the monomer, unassembled species with this solvent mixture. Crystallization of TSOF was induced by slow evaporation, which favors the removal of the ‘bad’ solvent, methanol (b.p. = 64.6°C) while the ‘good’ solvent, toluene (b.p. = 110.6°C), increases in concentration thereby favoring self-assembly and ensuring thermodynamic control over the crystal structure packing. The triarylamine units are arranged in columns displaying an alternating AB type stacking (60° dihedral angle) in contrast to the helical stacking structure (20° dihedral angle) previously described for TATA nanowires. Relevant

¹⁴⁰ Desiraju, G. R. *J. Am. Chem. Soc.* **2013**, 135, (27), 9952-9967.

¹⁴¹ Mukherjee, A. *Crystal Growth & Design* **2015**, 15, (6), 3076-3085.

intermolecular stacking distances include (1) a nitrogen-nitrogen distance of 4.173 Å as well as (2) a stacking distance of 3.608 Å from the ortho carbons (Figure 92 and 93).

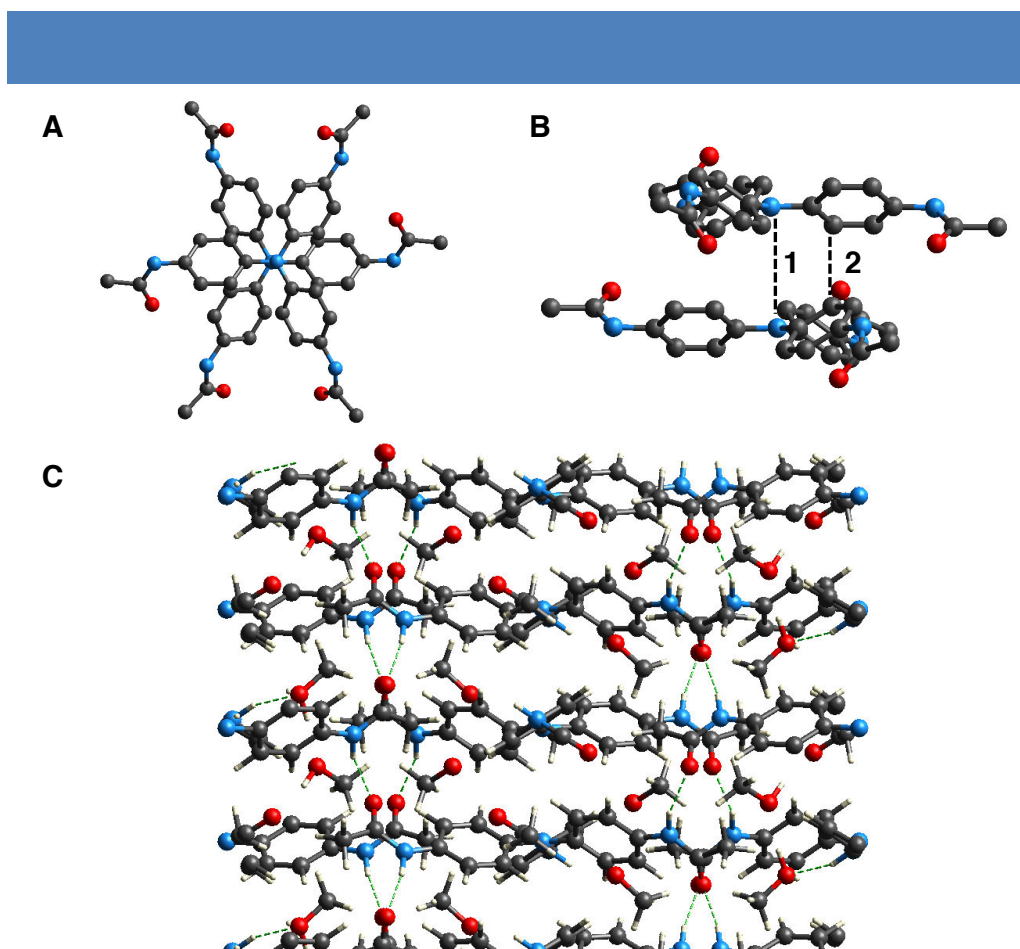


Figure 93 | AB stacking motif with a 60° dihedral angle between molecules (a). Horizontal view of two stacked molecules. (1) represents a distance of 4.173 Å between nitrogen centers and (2) represents a distance of 3.608 Å between the ortho carbons (b). Demonstration of the *intercolumnar* hydrogen bonding network driving the formation of the supramolecular organic framework (c).

Due to the tilt of the aromatic rings, the aromatic hydrogen on the ortho carbon points towards the adjacent ortho carbon on the ring below giving a minuscule separation of 2.708 Å. The supramolecular organic framework is constructed via an *intercolumnar* hydrogen bonding network, with each amide group participating in two hydrogen bonds to adjacent triarylamines in a neighboring column on the plane above and the plane below. Additionally, the framework structure depicts cavities of 7.9 Å in diameter, and the crystal structure demonstrated the facile inclusion of methanol molecules within the cavities (Figure 94).

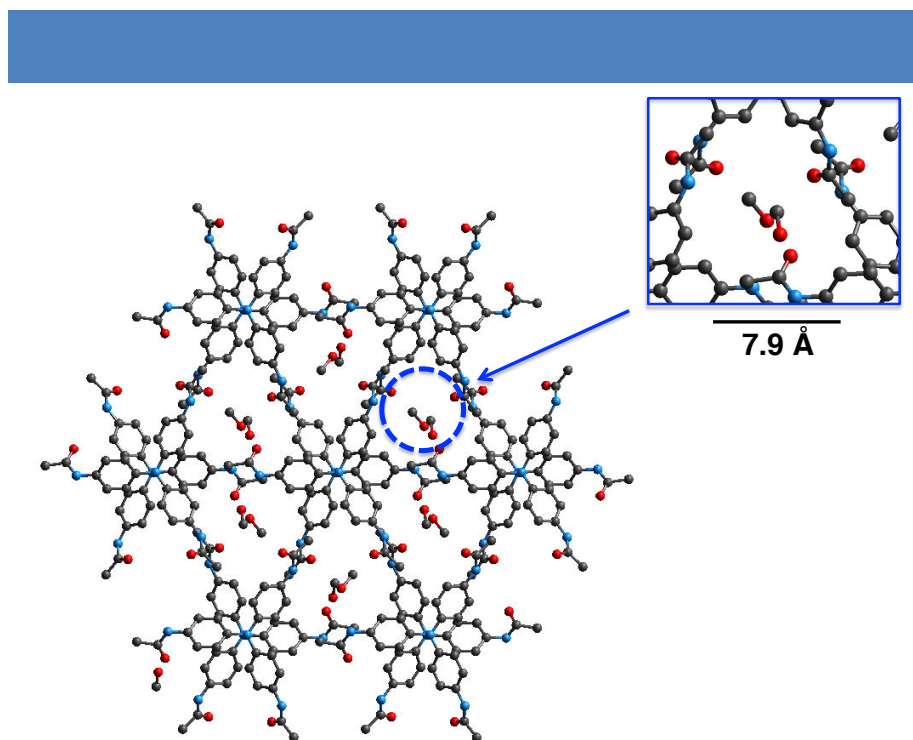


Figure 94 | Crystal Structure displaying incorporation of methanol molecules inside the cavities of TSOF.

Hirshfeld analysis is a method of quantitating close contacts between molecules in molecular crystals.¹⁴² As opposed to other methods of generating molecular surfaces which depend only on the molecule itself, the Hirshfeld surface is defined by the molecule and the proximity of the neighboring molecules, thereby portraying information about intermolecular interactions. Technically, the Hirshfeld surface is defined as $w(\mathbf{r})=0.5$ where the weight function $w(\mathbf{r})$ is defined as

$$w(\mathbf{r}) = \sum_i \text{molecule} \rho_i(\mathbf{r}) / \sum_i \text{crystal} \rho_i(\mathbf{r}) \quad (47)$$

where $\rho_i(\mathbf{r})$ is the spherical atomic electron distribution located at the i^{th} nucleus; The weight ratio represents the ratio a particular molecule's electron distribution in relation to the the general electron distribution of other molecules inside the crystal. The two key parameters of every point on the Hirshfeld surface are (d_i) the distance from the surface to the nearest atom *interior* to the surface (d_e) the distance from the surface to the nearest atom *exterior* to the surface. This information can be displayed in the fingerprint plots of d_e vs. d_i . The Hirshfeld surfaces displayed in the figure come from the normalized surface d_{norm} :

$$d_{\text{norm}} = \frac{d_i - r_i^{\text{vdW}}}{r_i^{\text{vdW}}} + \frac{d_e - r_e^{\text{vdW}}}{r_e^{\text{vdW}}} \quad (48)$$

The Hirshfeld surface of **29** inside TSOF is displayed in figure 92c. Hydrogen bonding

¹⁴² Spackman, M. A.; Jayatilaka, D. *CrystEngComm* **2009**, 11, 19-32.

interactions account for 18% of the surface area and display the closest packing to adjacent atoms (indicated by the red color around the amide oxygen and hydrogen). This indicates the primary influence of the amide groups in dictating the structural geometry. Secondly, interactions due to close contact of the aromatic groups contribute to 21% of the surface area (indicated by the white color over the aromatic groups). The central amine as well as the terminal methyl groups play little to no role in the packing structure. A scatter diagram for each of the interactions is shown in figure 95 where the d_e is on the y-axis and d_i is on the x-axis.

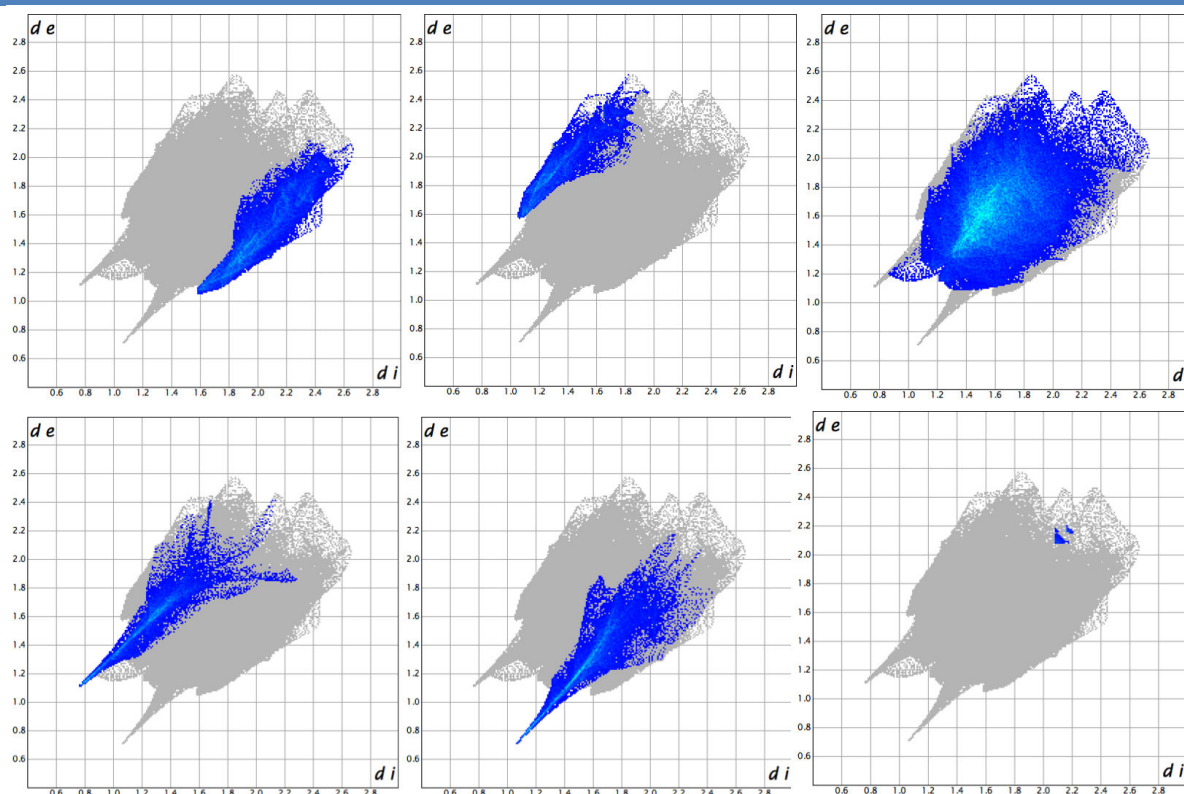


Figure 95 | Fingerprint plots from the Hirshfeld analysis for C-H (top left), H-C (top middle), H-H (top right), H-O (bottom left), O-H (bottom middle), and N-N (bottom right) close contacts.

Secondarily, interactions occur over between the three aromatic groups of the triarylamine core. The central amine as well as the terminal methyl groups play little to no role in the packing structure. This can be nicely contrasted with the helical columnar structure which longer chain triarylaminines assume. There the side chains play a critical role by (1) inhibiting lateral hydrogen bonding, thereby forcing hydrogen bonding to be intracolumnar and (2) forcing van der Waals interactions with neighboring fibers, thereby leading to bundling. The specific Hirshfeld interactions are broken down in the following table by interaction type. We

observe a large contribution from C-H interactions (21%) arising from the stacking of the aromatic rings as well as a large contribution from the hydrogen bonding (18%). SEM imaging of the needle-like crystals are displayed in figure 96.

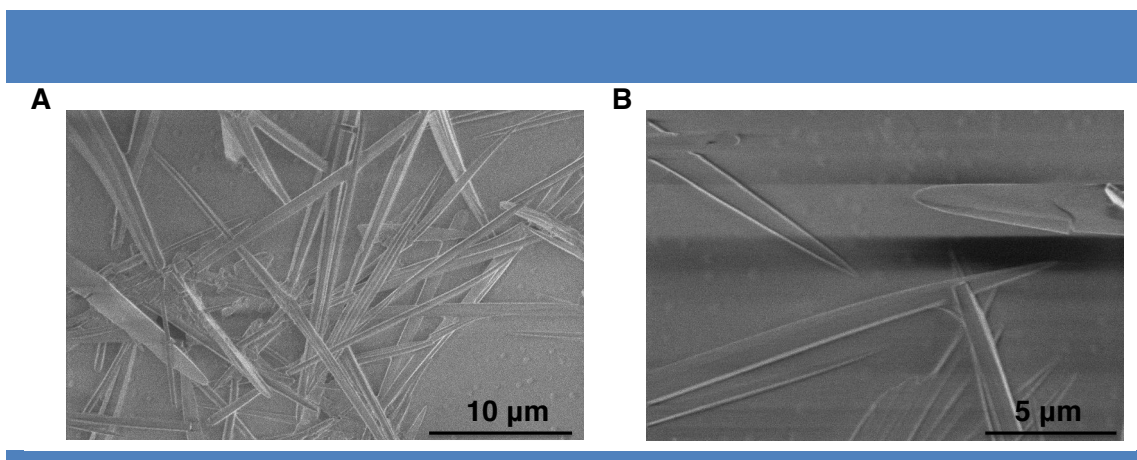


Figure 96 | SEM imaging of TSOF crystals.

3. Properties of doped TSOF

NMR of resuspended crystals in chloroform demonstrated that TSOF made of **29** remained intact as there was no signal apparent from isolated molecules. Irradiation with a 20 W halogen lamp induced the formation of stable radical cations inside the SOF as demonstrated in figure 97. Visually, photooxidation turns the suspension from colorless to green as the radical cations are formed. Irradiated solutions maintained their green color for weeks, indicating the high stability of the doped TSOF. Initially, irradiation gives rise to a band around 800 nm, typical of triarylamine radical cations. Interestingly, a large band appears around 500 nm which is not observed in the oxidized individual molecule (Figure 97b). This band appears linked with the radical cation band as the band at 800 nm begins to decrease while this band continues to increase. This is likely an *intracolumnar* charge transfer band due to electronic interactions between oxidized and neutral molecules inside the SOF. Reflectance and transmission measurements were made on crystalline thin films of the oxidized and unoxidized crystals (Figure 97c). The oxidized crystals displayed absorption bands around 0.8 eV, 2.1 eV, and 2.7 eV displaying the optical signature of delocalized polaron formation within TSOF.¹⁴³ Similar polaron formation was observed with the TATA nanowires, though the transition energies between the bands are shifted down in energy due to the crystalline nature of the columns allowing for better structural ordering.

¹⁴³ Beljonne, D.; Cornil, J.; Sirringhaus, H.; Brown, P. J.; Shkunov, M.; Friend, R. H.; Brédas, J. L. *Adv. Funct. Mat.* **2001**, 11, 229-234.

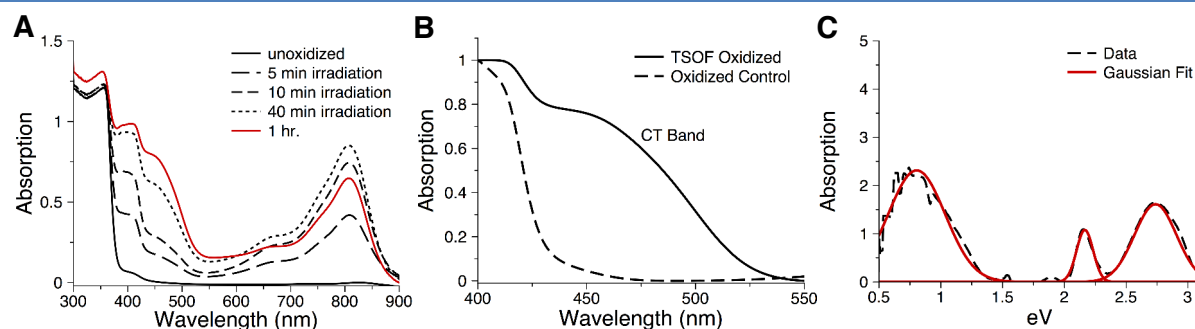


Figure 97 | Absorption measurements during various stages of photodoping of TSOF (a). Close up of the charge transfer band present in the oxidized TSOF (b). Absorption bands of oxidized crystals and the Gaussian fit for each peak demonstrating energy transitions at 0.80 eV, 2.17 eV, and 2.74 eV (c).

The electronic coupling between molecules along the stacking direction was determined to be 393.3 cm^{-1} from DFT calculations on the crystal structure coordinates of a stacked dimer, using the energy splitting approach.¹⁴⁴ Further investigations of the charge transport properties determined an electronic interaction of 618.95 meV between the HOMO and SOMO of neutral and charged species inside the SOF. This leads to an effective transfer integral of 63.36 meV (511.03 cm^{-1}), in line with typical values for TCNQ charge-transfer crystals.¹⁴⁵ These results depict strong coupling between stacked molecules giving rise to large electronic couplings comparable with the most efficient synthetic and natural systems displaying long-range energy transport.^{79,146} The effect of photodoping on the conductivity of TSOF was observed by dropcasting the crystals over interdigitated electrodes (Figure 98).

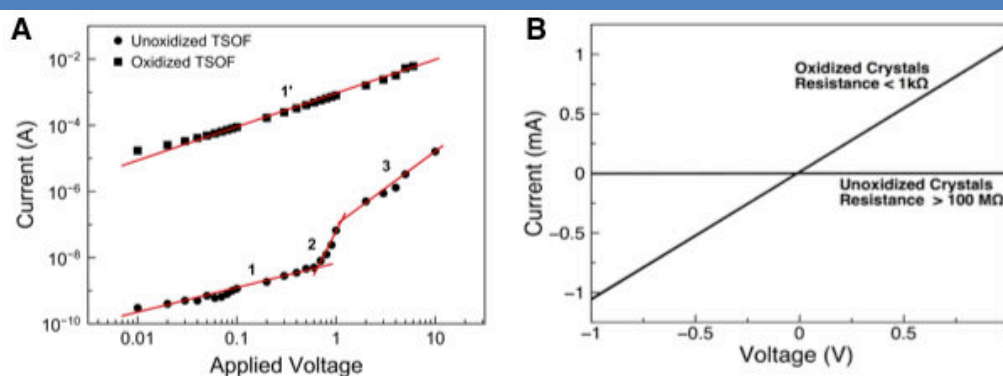


Figure 98 | I-V curve of oxidized and unoxidized crystals on interdigitated crystals.

The applied voltage was varied between 10 mV and 5 V. The oxidized TSOF displayed ohmic

¹⁴⁴ Zhu, L.; Yi, Y.; Li, Y.; Kim, E.-G.; Coropceanu, V.; Brédas, J.-L. *J. Am. Chem. Soc.*, **2012**, 134, 2340-2347.

¹⁴⁵ Zhu, L.; Yi, Y.; Fonari, A.; Corbin, N. S.; Coropceanu, V.; Brédas, J.-L. *J. Phys. Chem. C*, **2014**, 118, 14150-14156.

¹⁴⁶ Cogdell, R. J.; Gall, A.; Houmlhler, J. *Quarterly Reviews of Biophysics* **2006**, 39, 227-324

behavior throughout the entire voltage window in contrast to the unoxidized TSOF which displayed three distinct regimes indicating charge-trap limited behavior. The resistance of the oxidized TSOF was around 500 ohms at 10 mV voltage. In contrast the resistance of unoxidized TSOF was around 100 Mohms. The I-V curves between 1V and -1V were linear for the oxidized species, whereas the unoxidized crystals displayed some hysteresis.

4. Plasmonic Waveguiding From A Supramolecular Organic Framework

Birefringence was observed with TSOF crystals under crossed polarizers, demonstrating a net orientation of the molecules in the crystal along the long axis of the crystal – i.e. the stacking direction is indeed parallel to the long axis of the crystal. Physically, this means that there is a non-zero difference in the two refractive index planes of the crystal, the parallel and perpendicular planes which leads to a net rotation of incident plane polarized light. The TSOF crystals were tested for their ability to act as photonic waveguides using a confocal microscope with the incident laser (532 nm or 785 nm) focused through a 100x objective. The crystals were prepared on glass slides from the appropriate suspensions. Non-oxidized TSOF crystals were dropcast from a suspension of 1 mg of **29** in 750 μ L MeOH and 250 μ L toluene. Oxidized TSOF was prepared by irradiating for 1 hr. with a halogen lamp (1 mg in 500 μ L CHCl_3 and 80 μ L MeOH).

The lengths of the crystals varied between 4 μ m and 40 μ m with an average width between 1 μ m and 3 μ m. Upon focusing the laser at the tip of the crystals, we could observe output at the distal end with both the 532 nm and 785 nm lasers (Figure 99d,e). Optical waveguiding was observed in over 90% of the TSOF crystals regardless of whether they were oxidized or not. No waveguiding was observed when the laser was focused on top of the crystal away from the ends (Figure 99f). Multiple waveguiding outputs were routinely observed with crystals displaying defects (Figure 99g). We are able to rule out the photoluminescent mechanism, which is responsible for almost all reported active organic waveguides, for three reasons: (1) the incident laser source is in a region where the unoxidized crystal does not absorb (532 nm and 785 nm), (2) we do not observe any fluorescence when directly irradiating both the oxidized and unoxidized crystals with both laser sources (Figure 99d), and (3) we do not observe waveguiding behavior unless the SOF is illuminated at the tip.

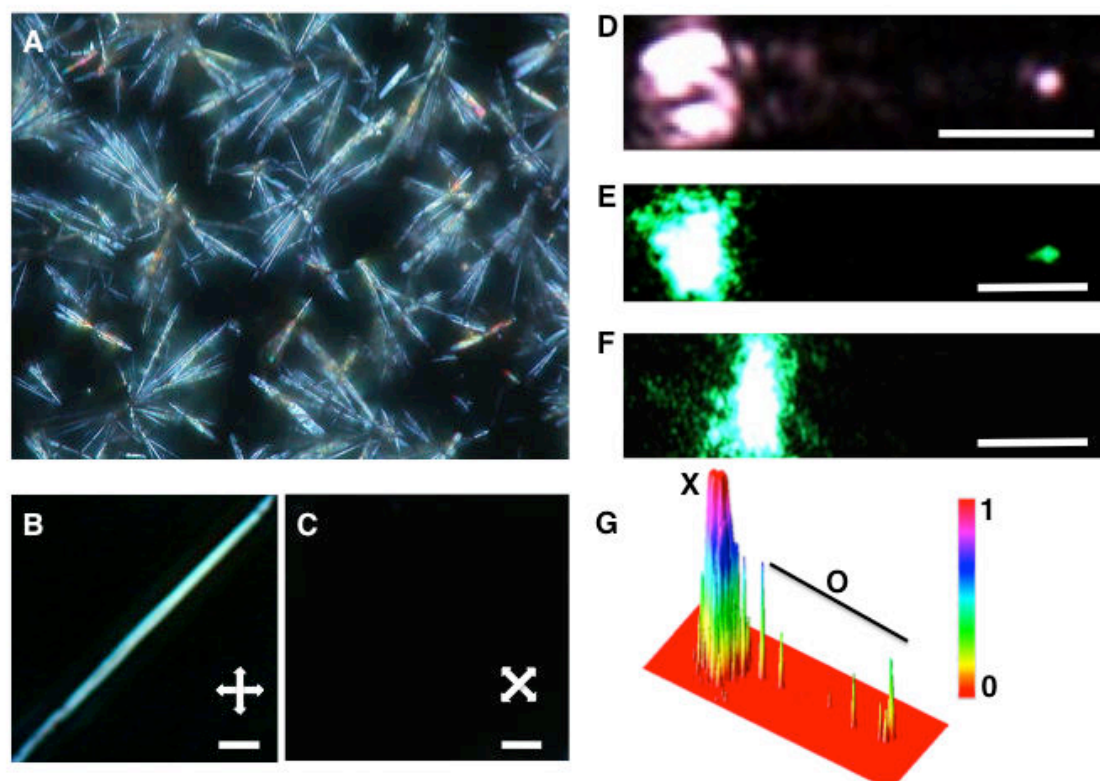


Figure 99 | Birefringence of TSOF under crossed polarizers (a). A single crystal observed under crossed polarizers before (b) and after 45° rotation of the sample (c; scale bars = $10\ \mu\text{m}$). Optical waveguiding of an incident 785nm laser (d) and a 532nm laser (e) focused at one end of the crystal displaying an output at the distal end. No waveguiding was observed when the laser was focused in the middle of the crystal (f; scale bars = $4\ \mu\text{m}$). Multiple output along a single crystal at defects in the crystal (g, X = excitation, O = outputs).

To further elucidate the waveguiding behavior, fluorescence bleaching experiments were performed on the oxidized TSOF crystals. These experiments were performed in a similar manner as the Bleach-Imaged Plasmon Propagation (BLIPP) technique used to identify plasmon propagation in metallic waveguides.⁴⁷ Oxidized and unoxidized crystals were both tested by irradiating with a laser for 10 minutes and then recording the fluorescence signal at various points on the crystal. Upon spin coating indocyanine dye on top of the crystals, we no longer observed the waveguiding phenomenon with the unoxidized crystals, but continued to observe it with the oxidized ones (figure 100b,c).

We observed a clear increase in the dye bleaching distance along the crystal for the oxidized crystal in comparison with the unoxidized crystals (figure 100a). The unoxidized crystals essentially correct for any effect of scattering along the surface of the crystals. They displayed a similar propagation distance as a dye control on glass substrate. This demonstrates the efficient energy transfer over 4 microns with the oxidized TSOF when coupled with incident

light at the crystal tip. This clearly displays the ability of the TSOF to couple with the incident light and transfer the energy over micron length distances. This strongly suggests that coupling of the incident laser light with the free metallic electrons within the crystals, akin to what is commonly observed in metallic nanowires, is giving rise to the waveguiding effect observed with the oxidized crystals.

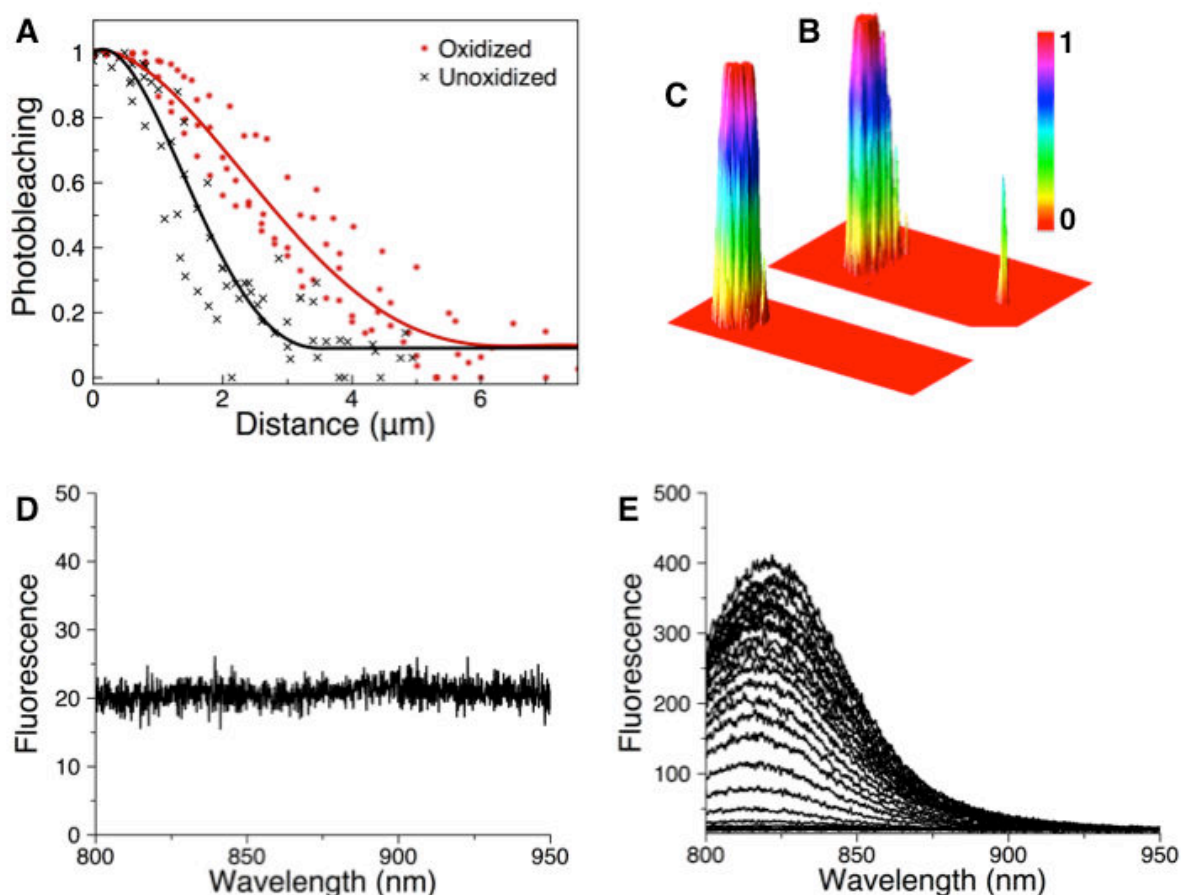


Figure 100 | Photobleaching of a dye spin coated on top of unoxidized and oxidized crystals (a). Images of light propagation in an oxidized crystal covered with dye and absence of light propagation in an unoxidized crystal covered with dye (b, c; scale bars = 3 μm , data taken from 8 crystals). Fluorescence measurement on an oxidized TSOF crystal with a 785nm laser focused through a 100x objective with a confocal microscope (d). Fluorescence on an oxidized TSOF crystal after irradiation with a 785nm laser displaying increasing fluorescence as the confocal microscope is moved along the crystal away from the point of irradiation (e).

For the unoxidized TSOF, the observations match a passive waveguiding mechanism. Upon addition of the dye, quenching of the passive waveguiding mechanism occurs for two reasons: (1) the increase in the refractive index of the environment resulting in a similar value as the organic crystal (1.5-2), passive waveguiding is dependent upon the refractive index of the material being larger than the refractive index of the surroundings to take advantage of total internal reflection at the interface, and (2) the surface is covered with a molecule which

highly absorbs at the wavelength of energy being propagated, this should lead to large losses and retarded waveguiding propagation lengths.

On the other hand, the oxidized TSO_F displays an active waveguiding mechanism as highlighted by the continued waveguiding output with the dye on top of the crystal. The BLIPP experiments clearly efficient energy transport mechanism due to the coherent polaronic band structure introduced in the crystal upon doping. Additionally, the photobleaching effect ends before the end of the crystal even though we still observe light output at the distal end. This indicates the existence of multi-modal waveguiding, where higher modes decay rapidly away from the excitation point leaving the lower modes to propagate through the columns. We have observed the effect on crystals as narrow as 750nm thereby ruling out the possibility of multimodal passive waveguiding.

5. Conclusions

These results demonstrate the formation of supramolecular organic frameworks displaying dual waveguiding mechanisms. The first mechanism is due to passive waveguiding at the interface between the crystal and air. The second waveguiding mechanism is plasmonic in nature, due to coupling between the incident light and the delocalized metallic electrons within the structures. This extends the results on the nanoparticle array to demonstrate that the TATA based organic crystals can exhibit energy transfer and waveguiding due to an organic-plasmonic mechanism.

Chapter IX Ordered Plasmonic Assemblies At A Liquid-Liquid Interface

1. Introduction

The self-assembly of plasmonic nanoparticles is being actively explored due to the novel electronic and optical properties that results from plasmonic coupling between nanoparticles at close distance.¹⁴⁷ Strategies towards plasmonic assemblies can be summarized as either solution methods, including DNA functionalization¹⁴⁸, templating methods, including block copolymer¹⁴⁹ and virus templating¹⁵⁰, or interfacial methods, which can be further broken down into assemblies at liquid-air, liquid-liquid, and liquid-solid interactions. While there are well known methods for aligning nanoparticles at a liquid-air interface, such as with a Langmuir trough, or at a liquid-solid interface, such as using block copolymers to pattern surfaces,¹²⁴ there do not exist any methods for organizing nanoparticles at a liquid-liquid interface (LLI). Nanoparticle assemblies at liquid-liquid interfaces are being investigated for use as optical devices, sensors, and catalysis.¹⁵¹ Indeed, LLI assemblies have recently been demonstrated to produce conductive mirror-like coatings¹⁵² as well as sensors for the trace detection of analytes via in-situ surface-enhanced raman scattering (SERS).¹⁵³

At the same time, another challenge involves the interfacial ordering of nanofibers into two-dimensional liquid crystalline lyotropic materials. While the subject has been theoretically treated^{154,155,156}, there are only a few examples in the literature.^{157,158,159} While at the core a fundamental science problem, there are important medical implications, namely in the area of amyloid fibril aggregation. The accumulation at biological interfaces is crucial in the formation of plaques leading to membrane-associated amyloid diseases such as

¹⁴⁷ Nie, Z.; Petukhova, A.; Kumacheva, E. *Nat Nano* **2010**, *5*, 15-25.

¹⁴⁸ Tan, S. J.; Campolongo, M. J.; Luo, D.; Cheng, W. *Nat Nano* **2011**, *6*, 268-276.

¹⁴⁹ Wang, H.; Lin, W.; Fritz, K. P.; Scholes, G. D.; Winnik, M. A.; Manners, I. *J. Am. Chem. Soc.* **2007**, *129*, 12924-12925.

¹⁵⁰ Dujardin, E.; Peet, C.; Stubbs, G.; Culver, J. N.; Mann, S. *Nano Lett* **2003**, *3*, 413-417.

¹⁵¹ Edel, J. B.; Kornyshev, A. A.; Urbakh, M. *ACS Nano* **2013**, *7*, 9526-9532.

¹⁵² Fang, P.-P.; Chen, S.; Deng, H.; Scanlon, M. D.; Gumy, F.; Lee, H. J.; Momotenko, D.; Amstutz, V.; Cortés-Salazar, F.; Pereira, C. M.; Yang, Z.; Girault, H. H. *ACS Nano* **2013**, *7*, 9241-9248.

¹⁵³ Cecchini, M. P.; Turek, V. A.; Paget, J.; Kornyshev, A. A.; Edel, J. B. *Nat Mater* **2013**, *12*, 165-171.

¹⁵⁴ Vink, R. L. C. *Phys. Rev. Lett.* **2007**, *98*, 217801.

¹⁵⁵ Chen, Z. Y. *Phys. Rev. Lett.* **1993**, *71*, 93-96.

¹⁵⁶ Marrucci, G.; Maffettone, P. L. *Macromolecules* **1989**, *22*, 4076-4082.

¹⁵⁷ Lepère, M.; Chevillard, C.; Brezesinski, G.; Goldmann, M.; Guenoun, P. *Angew. Chem. Int. Ed.* **2009**, *48*, 5005-5009.

¹⁵⁸ Jordens, S.; Isa, L.; Usov, I.; Mezzenga, R. *Nat Commun* **2013**, *4*, 1917.

¹⁵⁹ Yoo, P. J.; Nam, K. T.; Qi, J.; Lee, S.-K.; Park, J.; Belcher, A. M.; Hammond, P. T. *Nat Mater* **2006**, *5*, 234-240.

Alzheimer's disease or type II diabetes mellitus.¹⁶⁰ In general, ordering of high aspect ratio materials is driven entropically – the translational entropy gained by the alignment orientation entropy loss, thereby reducing the free energy of the system.¹⁶¹

Herein we demonstrate the first example of ordering plasmonic nanoparticles into anisotropic assemblies at a liquid-liquid interface. Furthermore, this is accomplished without the need of surface functionalization of the nanoparticles, but is induced by lyotropic templating with doped supramolecular nanowires. This allows the nanoparticles, once assembled, to retain their ability to plasmonically couple, forming plasmonic waveguides at the LLI. We anticipate that the general principles outlined here can be applied to a variety of systems in the future opening the possibility of novel device designs at interfacial surfaces.

2. Formation Of Triarylamine/Gold Nanoparticle Film At A Liquid-Liquid Interface

Film formation was observed at the liquid-liquid interface of a biphasic system consisting of (1) supramolecular tris-amide triarylamine (TATA **6**) nanowires suspended in chloroform (bottom phase) and (2) an aqueous suspension of 13 nm citrate coated spherical gold nanoparticles (top phase). It is a necessary condition that the triarylamine nanofibers are preirradiated before mixing. As we have previously demonstrated, light irradiation with a halogen lamp in chloroform induces the stable oxidation of TATA nanowires, reaching a maximum of 44% of the molecules converted to the radical cation form. Afterwards, an interfacial film may be easily obtained by shaking the biphasic system for 15 seconds. There is no film formed when only unoxidized, neutral fibers are present in solution, indicating that the driving force for film formation is strong coulombic interaction between the positively charged nanofibers and the negatively charged gold nanoparticles (zeta potential of -34.1 ± 1.54 mV). This is shown schematically in figure 101b, along with a photo of a bubble trapped by the interfacial film. Depending on the viewing angle, the film appears either blue or a very reflective metallic gold color. Absorbance measurements displayed a red shift of 90 nm from the colloidal nanoparticle suspension to the interfacial film (Figure 101d). This is a typical effect of aggregated plasmonic nanoparticles.¹⁶²

¹⁶⁰ Selkoe, D. J. *Nature* **2003**, 426, (6968), 900-904.

¹⁶¹ Onsager, L. *Ann. N.Y. Ac. Sci.* **1949**, 51, 627-659.

¹⁶² Halas, N. J.; Lal, S.; Chang, W.-S.; Link, S.; Nordlander, P., *Chem. Rev.* **2011**, 111, 3913-3961.

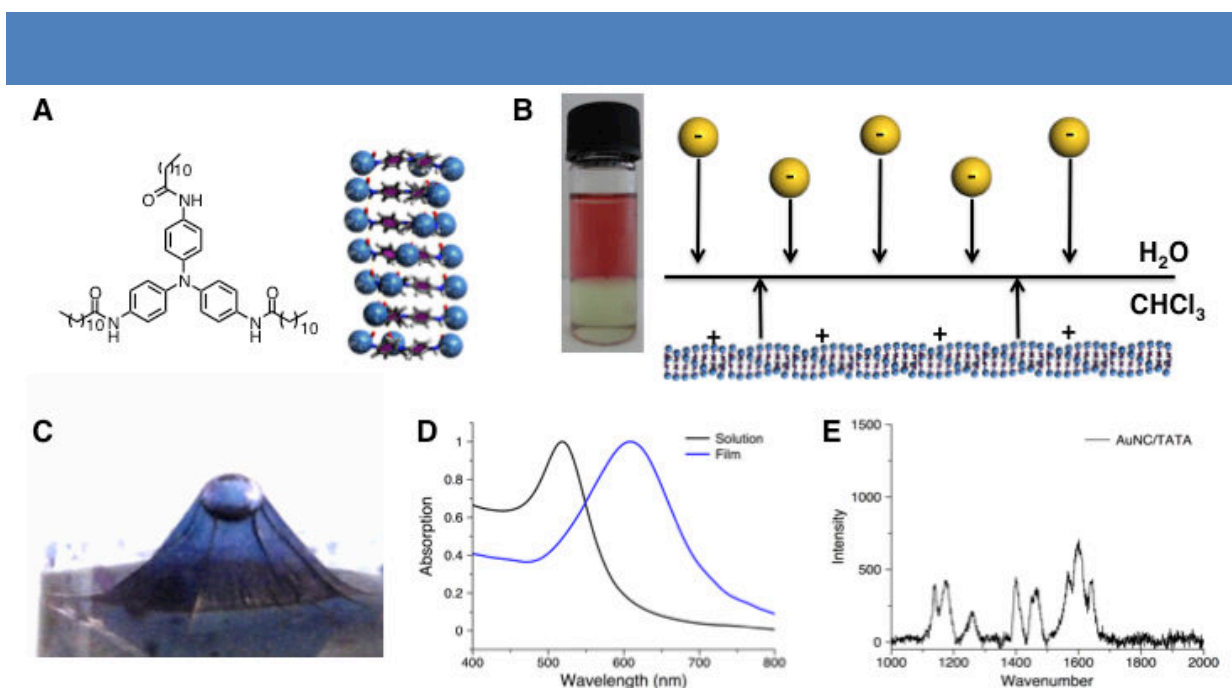


Figure 101 | Chemical structure and nanofiber structure of self-assembling tris-amide triarylamine **6** (TATA, a). Image of a vial containing the biphasic system with the aqueous nanoparticle suspension on top and the irradiated triarylamine solution on the bottom with graphical depiction of the film formation due to the negatively charged gold nanoparticles and the positively charged TATA nanowires (b). Photo of the interfacial film with a bubble caught in the middle of the film (c). Absorption measurements of a solution of the gold nanoparticles in comparison with the thin film absorption displaying a red-shift of 90nm due to aggregation of the plasmonic nanoparticles (d). Surface enhanced raman scattering (SERS) signal due to the close proximity of the TATA nanowires to the gold nanoparticles (e).

TEM imaging of the film showed the simultaneous presence of both TATA fibers and gold nanoparticles, confirming that film formation is a result of a strong interaction between the two components. There appeared to be a random distribution of the nanoparticles with no signs of ordering of neither the nanoparticles nor the fibers. Further analysis by AFM imaging showed that the nanoparticles remained on one side of the film while the nanowires remained on the other side. This demonstrates that the film is not a mixture of nanowires engulfing the nanoparticles, but the two components remain in separated domains in their respective solvents. Figure 102 shows optical images of the film taken with a microscope through a 100x objective. The reflective metallic surface comes from the aggregated nanoparticles, whereas the dark spots come from areas of the film with only fibers. We examined the film with the confocal Raman microscope and observed surface enhanced raman scattering (SERS) effect (figure 101e). We observed a signal arising from the triarylamine nanowires upon focusing the laser on areas with intact gold film, meanwhile there was no signal observed when focusing the laser on areas with only exposed fibers. This demonstrates (1) close contact between the nanoparticles and the triarylamine nanofibers, and (2) the ability to use these films for SERS detection of small molecules.

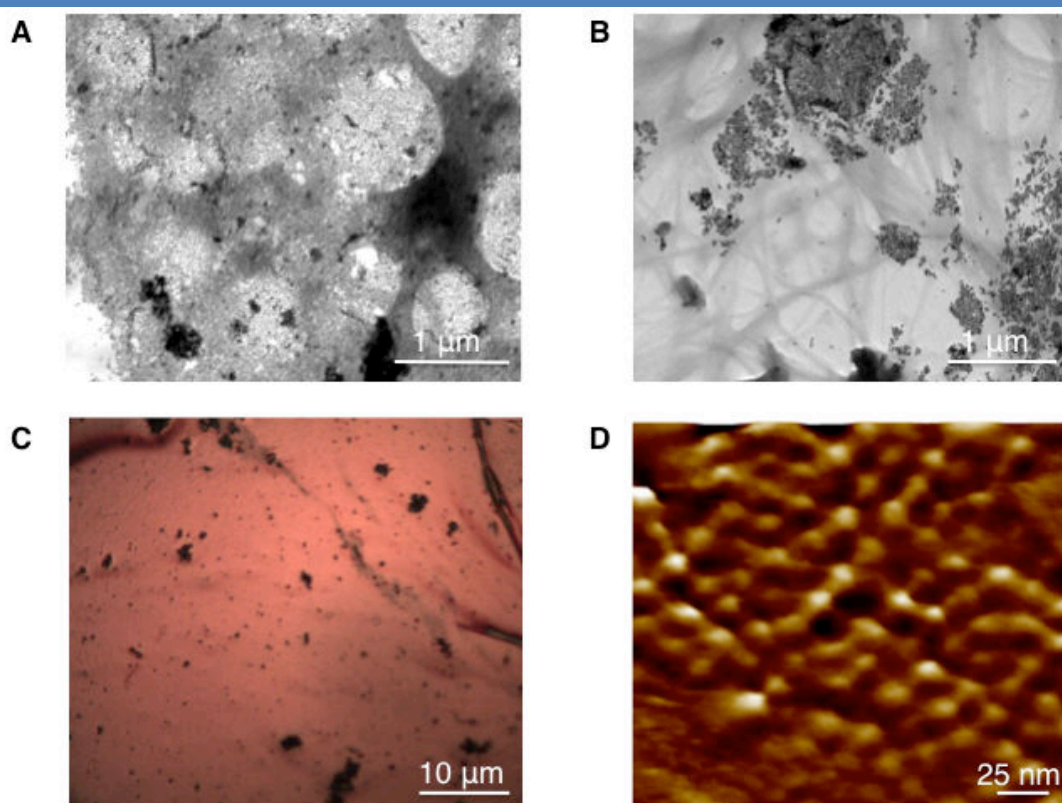


Figure 102 | TEM (a,b), optical (c), and AFM imaging of the aqueous face of the film formed by shaking the biphasic system displaying exposed gold nanoparticles (d).

3. Formation of Ordered Nanoparticle/Nanofiber Assemblies At A Liquid-Liquid Interface

a) Film Formation Through Stirring Leading to Aligned Nanoparticle Films

An initial pilot study was performed to explore the effect of changing the different variables in the system. Three factors were deemed critical for the initial study: (1) agitation method, ranging from no agitation, to stirring to shaking, (2) irradiation time, ranging from 30 s to 1 hr., and (3) TATA concentration, 0.1 mM to 1 mM. The outline of the three experiments were as follows:

Experiment	agitation	irradiation	TATA 6 conc
1	No agitation	1 hr.	1 mM
2	stirring	10 min.	0.5 mM
3	shake	30 sec.	0.1 mM

Table 6 | Pilot study investing the effects of various parameters on film formation.

The first experiment involved irradiation of the TATA solution by itself for 1 hr. followed by careful addition of the AuNP solution. The solution was left undisturbed for 14 hr. A thin blue optically homogenous film could be observed by eye. TEM imaging showed some organization of the nanoparticles and alignment with the fibers, though the film was thin and not many nanoparticles were observed. The second experiment was performed at a low concentration (0.1 mM), under intermediate irradiation times (10 minutes), and with vigorous shaking as the agitation method. The initial test with a sample irradiated for 30 s did not result in film formation, therefore we increased the irradiation time until film formation was apparent. Upon 1 min of irradiation, the beginning of a fibrous film was observed. After two minutes some blue coloration was observable at the interface indicative of nanoparticle aggregation. Finally, after 5 minutes of irradiation a distinct blue film at the interface was visible. TEM imaging showed random aggregation on the film, in line with the initial results of film formation. The third experiment involved an intermediate concentration (0.5 mM) that where agitation was induced by a stir bar. It should be noted that all of the experiments took place in cylindrical screw cap glass vials with a diameter of 1.2 cm. Initially the TATA solution was irradiated for 10 min, followed by stirring at 200 RPM with the NP solution. No film could be optically observed after an hour of stirring. The rate of stirring was then increased to 800 RPM (the point at which vortexing of the 2 layers could be observed without a significant disruption of the interface) and the solution irradiated continuously for 1 hr. An optically homogenous film could be observed after 1 hr. TEM imaging displayed alignment and aggregation of the nanoparticles into chains in multiple locations (Figure 103). It was clear from the TEM images that the film consisted of mixed domains of aligned nanoparticles and unaligned nanoparticles in close proximity. The aligned regions displayed impressive domains where the nanoparticles were clearly aligned with the orientation of the fibers.

Subsequent experiments examined in detail the effect of experimental conditions on film formation. In general, the observation of aligned domains in the film is favored by higher concentrations, longer irradiation times and high stirring speeds. For a disordered film initially formed by shaking, subsequent stirring did not induce ordering of the film thereby indicating that the film is a static construct as opposed to a dynamic one. However, we consistently observed a minority of the film displaying ordered regions and the majority displaying unordered regions without much of an improvement in the distribution. A simple thought experiment examining the forces on the film that could be inducing alignment and those forces that may be inhibiting it led to the hypothesis that the centrifugal force perpendicular to the film interface when the vortex is created was responsible for the

nanoparticle alignment. Additionally, the inhomogeneity of the film was likely due to turbulent forces from the stirring method as well as the uneven application (and in some places lack thereof!) of the centrifugal force.

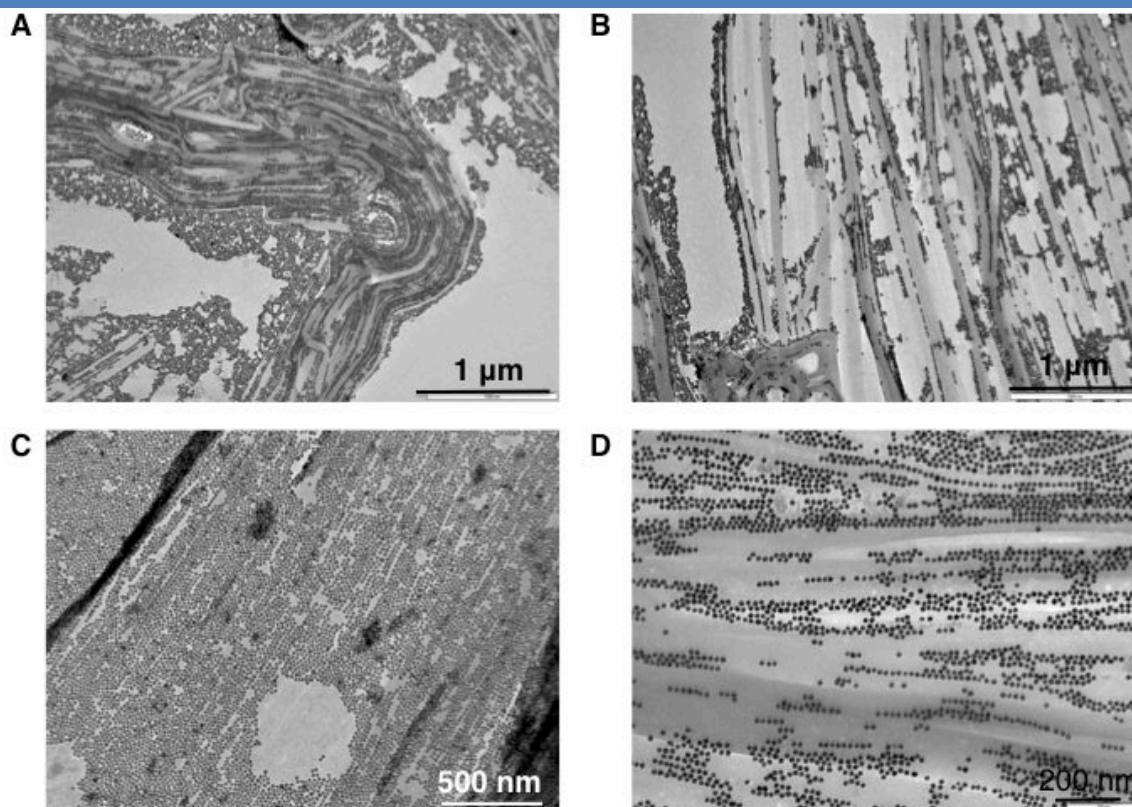


Figure 103 | Initial results from displaying regions of pseudoalignment of nanoparticles and nanofibers induced by stirring at 800 RPM for 1 hr.

b) Centrifugation as an External Ordering Force

Due to the critical requirement of forming a vortex while stirring in order to induce alignment, it appeared that the resulting centrifugal force was responsible for the ordering. In order to test this hypothesis, we calculated the approximate centrifugal force being created inside the vial during stirring at 800 RPM. The relative centrifugal force (RCF) may be calculated as

$$RCF = \frac{r\omega^2}{g} \quad (49)$$

where r is the radius from the center of the angular rotation, ω is the angular frequency, and g is the force due to gravity. By taking the distance from the center of the vial to the interfacial surface while vortexing as 0.3 cm, setting the frequency to 800 RPM, we get an

approximate centrifugal force in units of ‘g’

$$RCF = 1.118 \times 10^{-5} * 0.3(\text{cm}) * 800^2 = 2.15 \text{ g} \quad (50)$$

Therefore, to test the hypothesis we setup an experiment inside a centrifuge applying 2g of centrifugal force on the interfacial layer. Gratifyingly, we observed oriented nanofibers and nanoparticles throughout the film, successfully demonstrating that the ordering force on the system resulted from the perpendicular application of force.

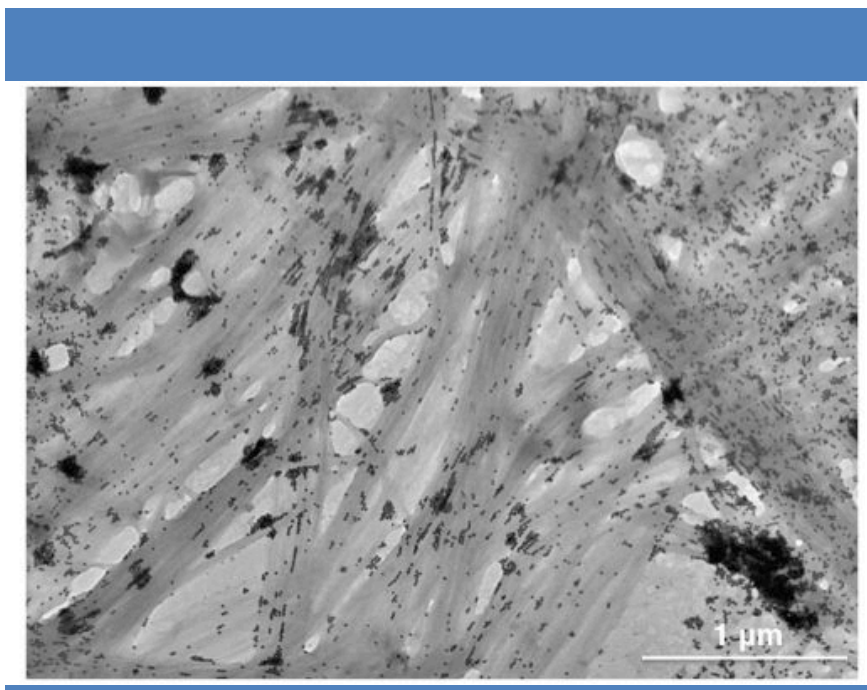


Figure 104 | Initial results from centrifugation experiments at 2g of applied force demonstrating alignment of the nanofibers as well as alignment of the nanoparticles with the nanofiber direction.

Having identified the ordering force on the system, we set about maintaining the other experimental variables as constants. For the concentration, we used either 1mM or 5mM solutions of TATA fibers, which were irradiated for 1 hour before centrifugation. Experiments were performed at pH 6.0, the native pH of the NP suspension after synthesis, though we observed film formation and alignment from pH 4.65 to 10.83. At lower pH, the citrate molecules around the gold nanoparticles become protonated, and we actually observed penetration into the chloroform layer at these low pH values, likely due to complexation and stabilization by the nanofibers. We also determined the stoichiometric ratio of gold nanoparticles to available interfacial film surface area. The SPR absorption peak was at 518 nm with a value of 0.86542 to give a AuNP concentration of 6.23×10^{-9} M (using the appropriate extinction coefficients). Using an average NP cross-sectional diameter of 13nm, a stoichiometric ratio of AuNP 2D surface area (1mL solution volume)/available thin film

surface area (diameter of 1.2 cm) was achieved by diluting 8.8 times the original concentration. Subsequent experiments demonstrated the importance of maintaining close to a stoichiometric ratio of nanoparticles to surface area. For a 0.5x surface area ratio of AuNPs it was visibly difficult to observe a film as it did not take on the usual characteristic blue-metallic color. The thin film made from the 2x concentration of NP solution gave large regions of multilayers of NPs. Even higher ratios (3x, and 10x) additionally displayed multilayer formation, however, the aqueous phase remained red after film formation demonstrating that there was incomplete transfer of the nanoparticles to the surface. We therefore reduced the NP surface area ratio to 1x for further experiments to avoid multilayer formation. Finally, the films were deposited onto TEM grids using a modified Langmuir-Schaffer deposition method allowing undisturbed film sections to be analyzed.

A comparison of films formed at varying centrifugal ‘g’ forces for 5 mM concentration of TATA is displayed in figure 105. The first image comes from a film formed without centrifugation, by letting the biphasic system equilibrate overnight.

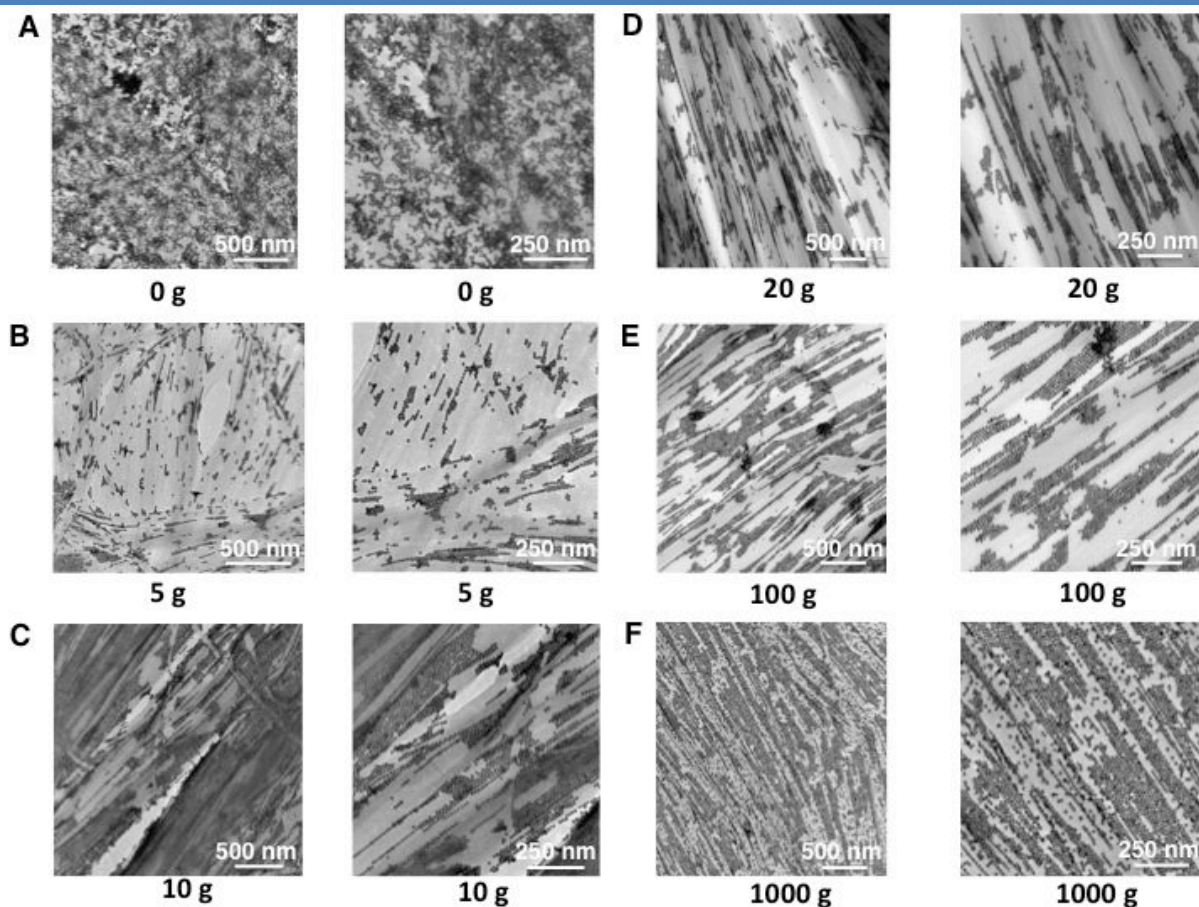


Figure 105 | Centrifugation experiments with a 5mM TATA solution: no centrifugation control left to rest undisturbed overnight (a), 5g (b), 10g (c), 20g (d), 100g (e), and 1000g (f).

Overall, there was very little ordering observed with this film. As the centrifugal force is increased, we see a corresponding increase in the ordering of the nanoparticles at the interface. From the 2g (figure 105) and 5g films we observe alignment of the nanowires leading to some nanoparticle ordering along the fibers. While there are larger aggregates demonstrating coherent ordering, isolated nanoparticle chains are quite limited in length (< 10 NPs). Upon moving to 10g and higher, we can observe now the emergence of isolated nanoparticle chains on the order of hundreds of nanometers, and clusters of nanoparticles exhibiting a coherent direction on the micron length scale. This demonstrates the ability to coherently order more than 100 nanoparticles into one-dimensional chains through the application of a perpendicular force.

This experiment was also repeated for 1 mM TATA **6** solution (Figure 106). Interestingly, below 1 mM we had a difficult time forming the film indicating a concentration limitation to the effect. Overall, there was increased ordering apparent on the small scale with the control without centrifugation. Increased ordering was observed with increasing centrifugal force, which was clearly apparent over larger scales where ordering well in excess of a micron was apparent.

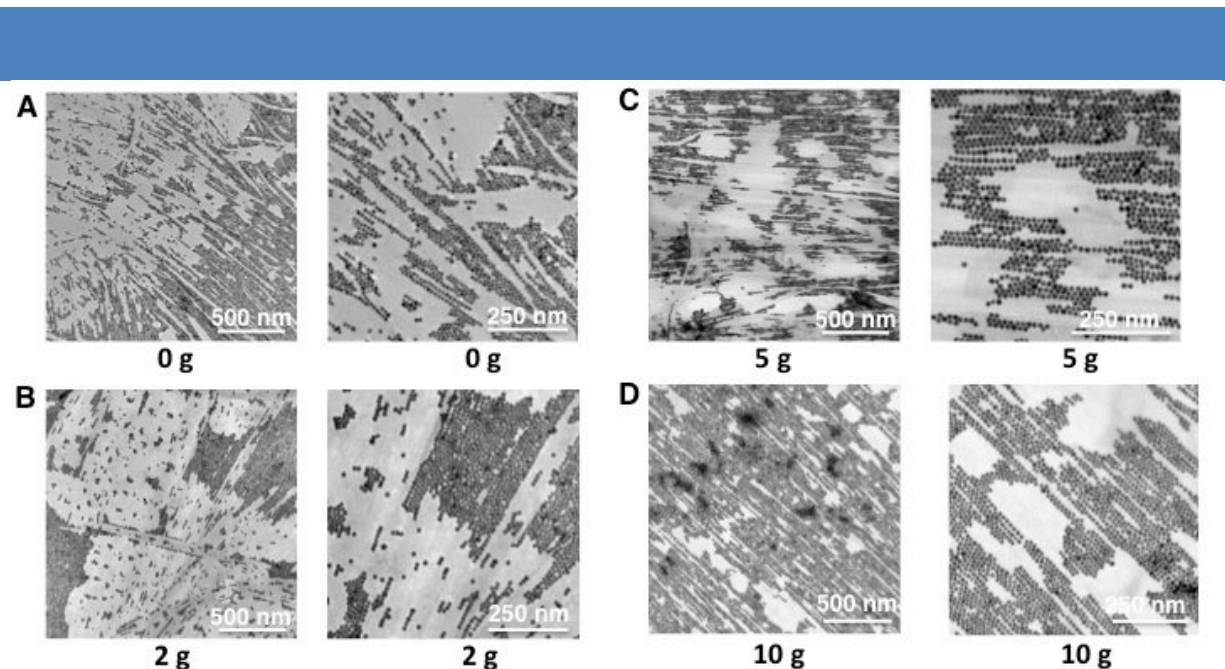


Figure 106 | Centrifugation experiments with a 1mM TATA **6** solution: no centrifugation control left to rest undisturbed overnight (a), 2g (b), 5g (c), 10g (d).

The NP film could also be easily transferred to surfaces through a modified Langmuir-Schaffer method. SEM images (Figure 107) display the successful transfer of the film onto silicon wafers. The images display that the aligned nanoparticle chains remained

intact during the transfer procedure.

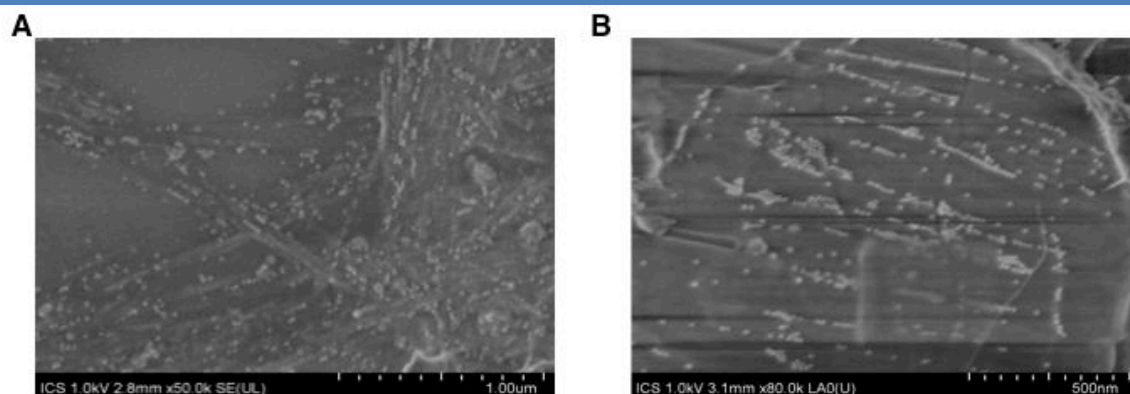


Figure 107 | SEM imaging of the film transferred to a silicon substrate via the Langmuir-Schaffer method.

c) Quantitation of Alignment

A quantitative examination of the alignment was undertaken by examining the ordering parameter at different centrifugal forces over different TEM image sizes for images taken at various parts of the film. The order parameter (S) was determined as follows:

$$S = 2(\cos^2\theta) - 1 \quad (51)$$

The ordering parameter for the 1 mM TATA **6** sample ($25 \mu\text{m}^2$ area) increased from 0.13 (no ordering) for the 0g sample to 0.83 for the 2g sample to 0.96 for the 10g sample (Figure 108). Analyzing smaller zone sizes demonstrated locally increased ordering, with a $9 \mu\text{m}^2$ area giving values of 0.64 (0g), 0.87 (2g), and 0.96 (10g). Even smaller zone sizes of $2.25 \mu\text{m}^2$ gave values of 0.73 (0g), 0.87 (2g), and 0.96 (10g). The largest effect was observed for the sample not exposed to the ordering force, where on small scales ($2.25 \mu\text{m}^2$) we observe some ordering of the nanofibers and nanoparticles (0.73 S -value), but as we go to larger scales ($25 \mu\text{m}^2$) we no longer observe the ordering. This is in stark contrast to the ordering observed at 10g, which was consistent across the three length scales that were measured. Here we see the clear influence of the centrifugal force inducing ordering of the film over large distances. Moving to the 5 mM sample we see the same effect, although the ordering parameter was smaller in this case due to the large fibers present at the higher concentration. At the large area dimension ($25 \mu\text{m}^2$) we see a steady increase in the film ordering from 0.184 (0g) to 0.47 (2g) to 0.72 (5g), and finally to 0.76 (10g). The intermediate size gave 0.34 (0g), 0.53 (2g), 0.72 (5g), and 0.85 (10g). Meanwhile, the smallest area gave 0.41 (0g), 0.61 (2g), 0.74 (5g), and 0.86 (10g).

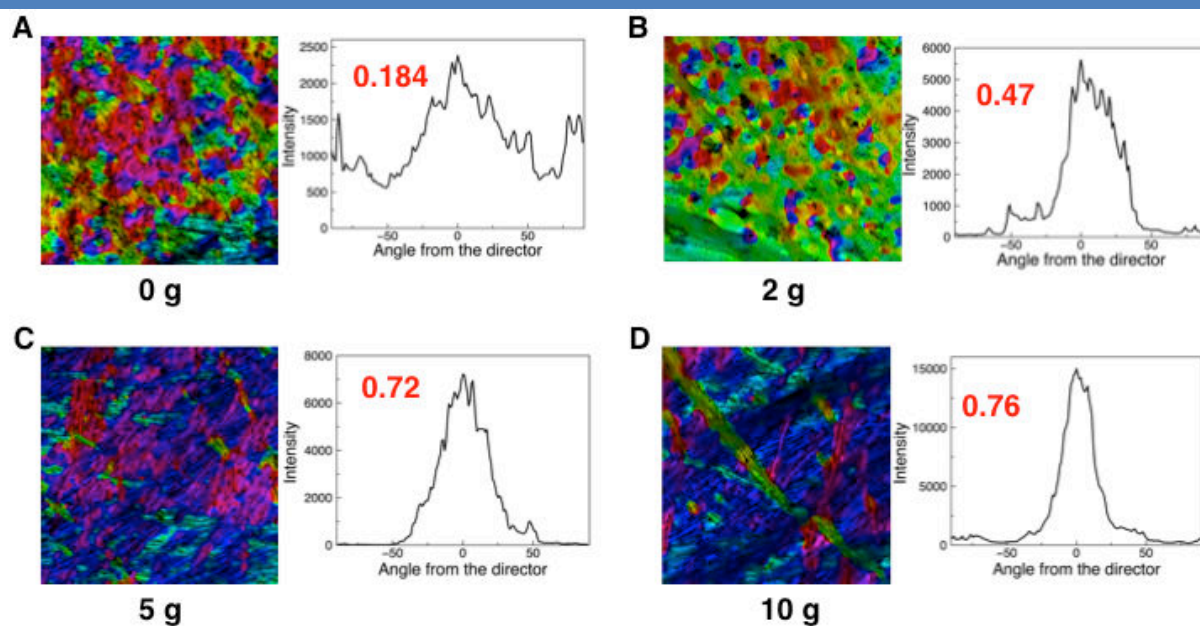


Figure 108 | Ordering for films formed from 5mM TATA solutions with 0g (a), 2g (b), 5g (c), and 10g (d). The colors in the TEM images demonstrate ordering in a certain direction. Homogenous coloring is indicative of homogenous alignment. Images are from the $25 \mu\text{m}^2$ samples.

Figure 109 demonstrates an example of an analysis of the ordering at the $25 \mu\text{m}^2$ scale. The colors in the TEM image correspond to angles of uniform direction in the film. Therefore, regions with a homogenous color scheme are indicative of a homogeneity in the alignment. Additionally, the angle from the director is also included. For $S = 1$, there would be theoretically a single peak at 0° with no width. For $S = 0$, there is an even distribution across all of the angles. The image analysis was performed using imageJ software. In order to determine if there was any intrinsic alignment of the nanofibers, we examined TEM grids with only fibers (Figure 110). Experiments were performed on fibers at a range of concentrations (0.1, 0.5, 1, 2, 3, 4, 5, 10 mM), which were irradiated, and then a TEM grid was placed at the top layer to remove via Langmuir-Schaffer method the fibers which rested at the air-liquid interface. Analysis of the ordering parameter revealed no significant alignment, even at 10 mM, the highest concentration tested which is on the verge of gelation. The ordering parameter for this sample was 0.19, while the ordering parameter for the 1 mM sample was 0.07 (Figure 111).

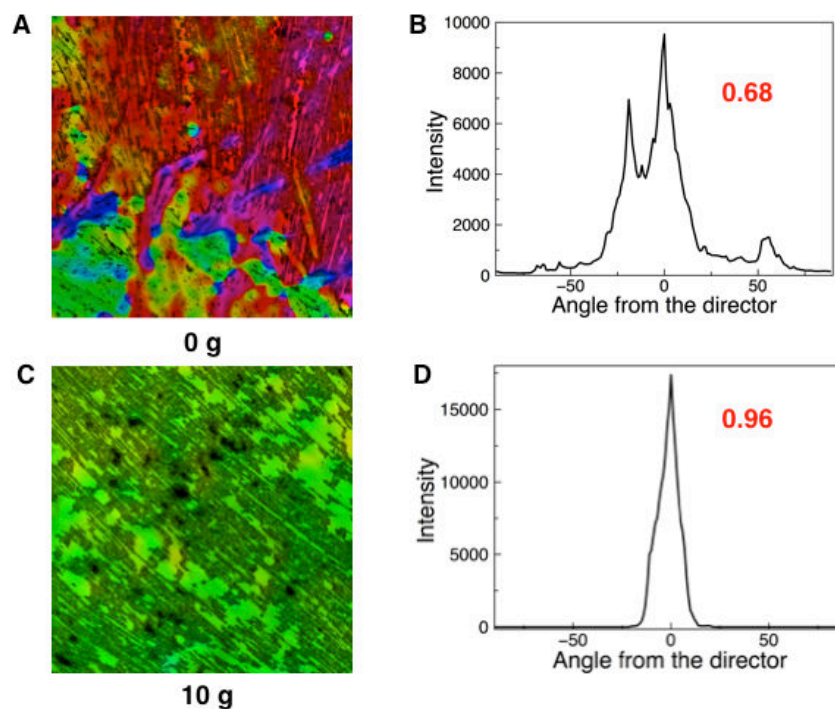


Figure 109 | Ordering for films formed from 1mM TATA solutions with 0g (a, b) and 10g (c, d). The colors in the TEM images demonstrate ordering in a certain direction. Homogenous coloring is indicative of homogenous alignment. The angle from the director is shown in b and c displaying the quantitative alignment. Images are from the $9 \mu\text{m}^2$ samples.

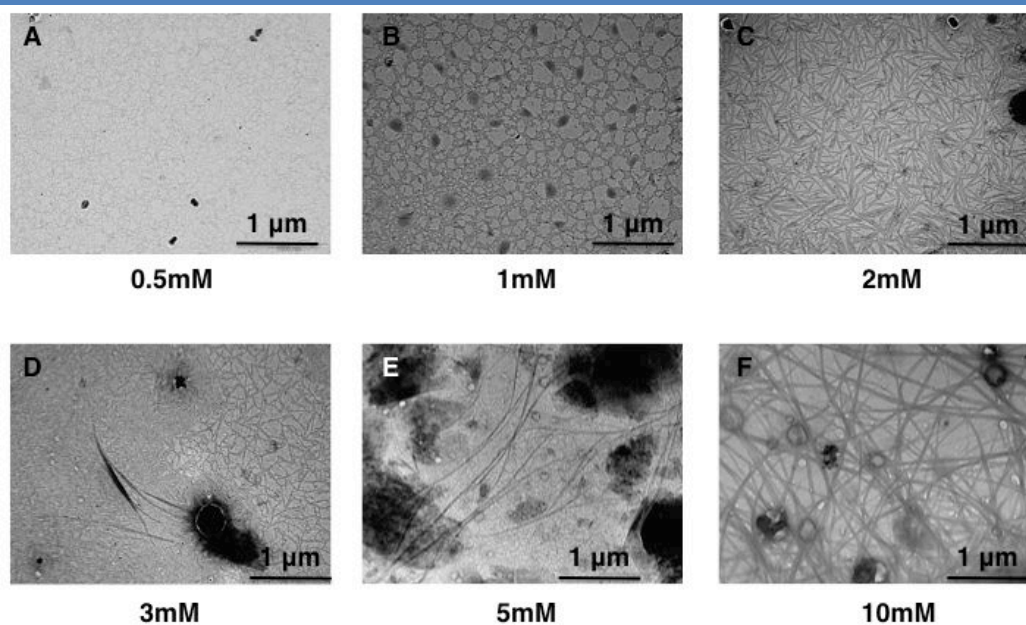


Figure 110 | TEM images taken from solutions at various concentrations of irradiated TATA: 0.5mM (a), 1mM (b), 2mM (c), 3mM (d), 5mM (e), and 10mM (f).

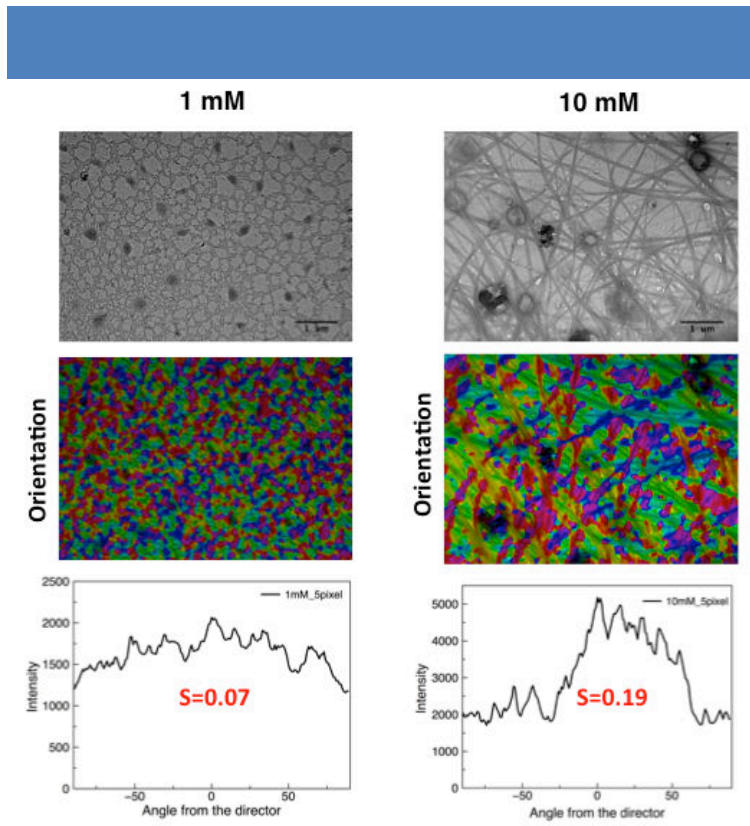


Figure 111 | Lack of orientation observed in pure TATA solution up to 10mM (close to the gelation point).

The aligned films also displayed liquid crystal phases under crossed polarizers with an optical microscope. Films formed by shaking did not display liquid crystalline domains. As we increased the centrifugation rate, we observed an increasing effect under the microscope with crossed polarizers, indicating the formation of larger and larger domain sizes (Figure 112).

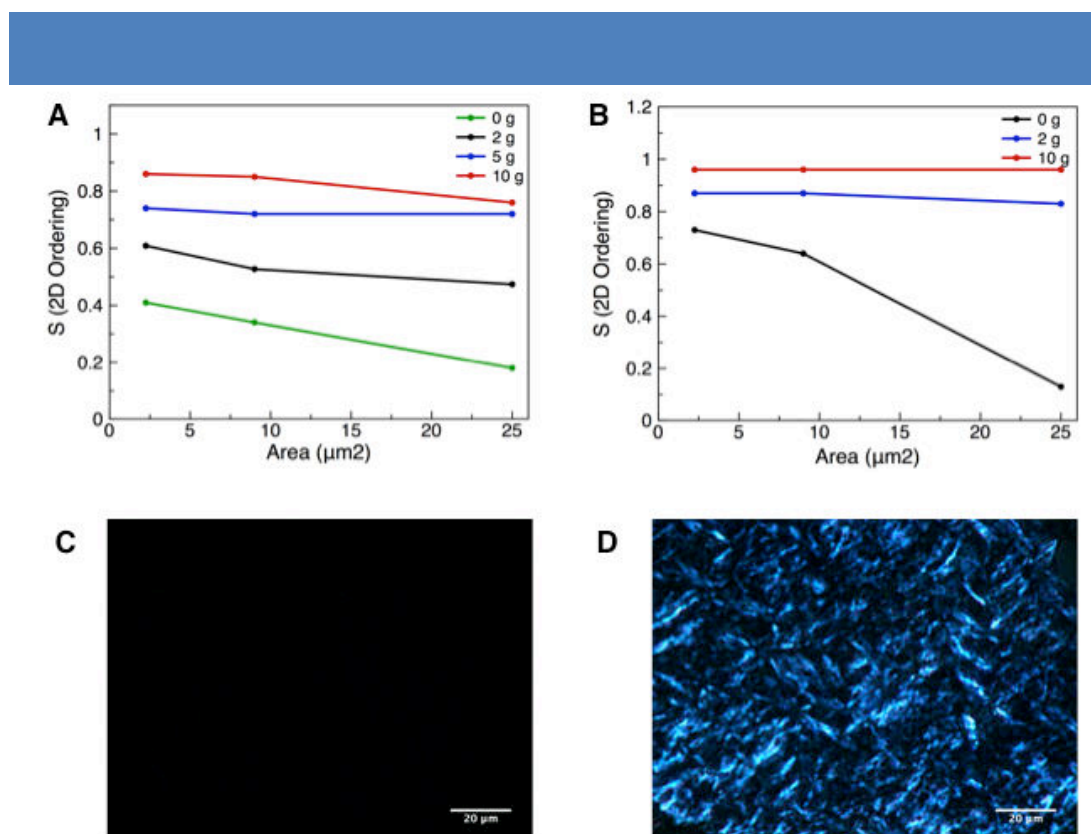


Figure 112 | Ordering parameter (S) as a function of applied centrifugal force and domain size for films formed from 5mM (a) and 1mM (b) TATA solutions. Optical microscope images under crossed polarizers demonstrating the formation of liquid crystalline domains only under the application of high enough centrifugal force: 0 g (c), and 1000 g (d).

4. Future Directions

Currently, we are working towards finishing a complete theoretical description of the film formation. This will give us better insight into the driving force of film formation and perhaps allow for the application of the basic principles into other systems, perhaps even by using different forces than we demonstrate here. Additionally, we have performed electron energy loss spectroscopy on the film with Raul Arenal at the University of Zaragoza, Spain. We have initial results demonstrating plasmonic coupling between the nanoparticles in the film in various orientations. Though we are still waiting on the data treatment which precludes inserting the data here. Besides being the first example of ordering of nanoparticles at a liquid-liquid interface, the ability to achieve liquid crystal like domains over many square microns attests to the strong effect that centrifugation has on the film.

Conclusions

In this thesis, I have described my progress over the past four years towards further understanding triarylamine self-assemblies as well as towards the development of novel applications. In chapter 2, I have elucidated the detailed mechanistic and structural aspects of the mono-amide triarylamine self-assemblies. This has demonstrated a novel self-assembly mechanism of nucleation and growth initiated by photogenerated radicals to produce a unique double columnar structure. I believe that elucidation of this mechanism contributes to further understanding of self-assembling supramolecular polymers in general. In chapter 3, I have detailed the ability to electrochemically trigger the self-assembly process. Additionally, the electrochemical behavior of the TATA self-assembly as well as electrode functionalization and attachment is shown. Potential applications resulting from these experiments include: (1) spatial control over the self-assembly process, due to triggering the process near the electrode surface, (2) the ability to use redox couples to create out-of-equilibrium redox environments for the self-assembly, (3) probing TATA self-assembly for sensing applications, (4) electrode functionalization and attachment which is critical for work function matching and efficient charge transport for a variety of organic devices ranging from solar cells to OLEDs. In chapter 4, I have written about a collaborative project working towards the development of triarylamine for use as the hole transport layer in perovskite solar cells. The goal is to use the self-assembling properties to make charge-transport conduits in the hole transport layer leading to efficient solar cell design.

Chapter 5 described the conceptual work of making diradical species from triarylamine functionalized with nitronyl nitroxide radicals. The strong intramolecular ferromagnetic coupling makes these molecules candidates as ferromagnetic materials. Additionally, magnetic control over the conductivity through the triarylamine stacks may be possible, leading to a conductive magnetoresistive material. Chapter 6 gave a detailed analysis of the tris-amide triarylamine self-assemblies and their unique charge-transfer properties giving rise to optical, magnetic, and electronic signatures of band-like metallicity. Additionally, we coin the term ‘supramolecular polaron’ to describe the through-space charge transfer within the stacks. The ability to fix defects in the stacked structures due to charge delocalization has not been reported before in the literature, demonstrating a novel driving force for self-repair. Chapter 7 develops the properties described in chapter 6 towards the application of plasmonic interconnects for use in plasmonic circuits. The development of a prototype plasmonic device

consisting of well-defined gold nanocluster arrays connected with TATA fibers was used to demonstrate plasmonic coupling through the fiber. This is the first demonstration of (1) the coupling of two nanoparticles together through a plasmonic waveguide and (2) the ability to use organic materials as plasmonic waveguides. This is an important first step towards the realization of functional plasmonic circuits. Chapter 8 gives an account of using a supramolecular framework based on TATA as a photonic material for waveguiding. We demonstrated that the photoluminescence mechanism is not responsible for the waveguiding, but the origin of the effect is actually plasmonic. We see this as the demonstration of a novel class of organic photonic materials. Finally, chapter 9 details the formation of ordered plasmonic assemblies at a liquid-liquid interface. Again, this is the first demonstration of ordering at a liquid-liquid interface in the literature, made all the more impressive by the fact that there is no ligand functionalization of the nanoparticles, thereby leaving the ability to form plasmonically coupled chains intact. Overall, I would say that this work contributes in a small way to both the understanding and advancement of research in the field of organic supramolecular chemistry. From my point of view, the actual experiments are but a small drop in the ocean of research, but it is my hope that some of these concepts may inspire others to build metaphorical pyramids where now there only lay sand.

So far my PhD work has resulted in the following publications:

Published:

1. Armao, J. J.; Maaloum, M.; Ellis, T.; Fuks, G.; Rawiso, M.; Moulin, E.; Giuseppone, N., Healable Supramolecular Polymers as Organic Metals. *Journal of the American Chemical Society* **2014**, *136*, 11382-11388.
2. Nyrkova, I.; Moulin, E.; Armao, J. J.; Maaloum, M.; Heinrich, B.; Rawiso, M.; Niess, F.; Cid, J.-J.; Jouault, N.; Buhler, E.; Semenov, A. N.; Giuseppone, N., Supramolecular Self-Assembly and Radical Kinetics in Conducting Self-Replicating Nanowires. *ACS Nano* **2014**, *8*, 10111-10124

Under Revision:

3. Armao, J.J.; Domoto, Y.; Umehara, T.; Maaloum, M.; Contal, C.; Fuks, G.; Moulin, E.; Decher, G.; Javahiraly, N.; Giuseppone, N.; Supramolecular Plasmonic Interconnects and their Directed Self-Assembly into Optical Nanocircuits. *under revision with Nat. Commun.*

To be submitted:

4. Armao, J.J.; Giuseppone, N.; *et al* A Supramolecular Organic Framework As Plasmonic Waveguide
5. Armao, J.J.*; Ellis, T.*; Martel, D.; Fuks; Maaloum, M.; Moulin, E.; Giuseppone; Triarylamine Self-Assemblies at Electrode Surfaces

Additionally, the work from chapters 4, 5, and 9 are in the process of being finished and/or in the early draft stage.

Appendix

Procedures

1. General Procedures

a. Solvent and chemical reagents

All reagents and solvents were purchased at the highest commercial quality and used without further purification unless otherwise noted. Dry solvents were obtained using a double column SolvTech purification system. Water was deionized by using a milli-gradient system (Millipore, Molsheim, France).

b. Chromatographic methods

Thin Layer Chromatographies were performed using silica on TLC Al foils (silica gel matrix with fluorescent indicator 254 nm, thickness: 500 μm , Sigma-Aldrich). In most cases, irradiation using a *Bioblock VL-4C* UV-Lamp (6 W, 254 nm and/or 365 nm) as well as *p*-anisaldehyde, phosphomolybdic acid and Cerium ammonium molybdate stainings were used for visualization. *Preparative Adsorption Flash Column Chromatographies* were performed using silica gel (60 \AA , 230 - 400 mesh, 40 - 63 μm , Sigma-Aldrich) or aluminium oxide 90 (standardized activity II, 70 - 230 mesh, Merck). *Preparative Ultra Performance Liquid Chromatographies* were performed using a *Waters AutoPurify* system equipped with a UV detector (set at 300 nm, 500 nm or 600 nm), a *3100* mass spectrometer, reverse phase columns (Waters, Sun Fire Prep C_{18} 5.0 μm , 19 \times 150 mm; Waters, XBridge Prep C_{18} 5.0 μm , 19 \times 150 mm) running with a water/methanol gradient as eluent, and the MassLynx 4.1 – XP software.

c. Analytical methods and instruments

i. Nuclear Magnetic Resonance (NMR)

^1H NMR spectra were recorded on a *Bruker Avance 400* spectrometer at 400 MHz and ^{13}C NMR spectra at 100 MHz. The spectra were internally referenced to the residual solvent peaks (CDCl_3 : 7.26 ppm, Toluene- d_8 : 7.09, 7.01, 6.97 and 2.08 ppm, CD_3OD : 3.31 ppm, CD_3CN : 1.94 ppm, $\text{DMSO-}d_6$: 2.50 ppm and D_2O : 4.80 ppm for ^1H spectrum, and CDCl_3 : 77.16 ppm, Toluene- d_8 : 137.48, 128.87, 127.96, 125.13 and 20.43 ppm, CD_3OD : 49.00 ppm, CD_3CN : 118.26 and 1.32 ppm and $\text{DMSO-}d_6$: 39.52 ppm for ^{13}C spectrum). For ^1H NMR

assignments, the chemical shifts are given in ppm. Coupling constants J are given in Hz. Peaks are described as singlet (s), doublet (d), triplet (t), quartet (q), multiplet (m) and broad (br).

ii. Mass spectrometry

Ultra Performance Liquid Chromatographies coupled to Mass Spectroscopy (UPLC-MS) were carried out on a *Waters Acquity UPLC-SQD* apparatus equipped with a PDA detector (190–500 nm, 80Hz), using a reverse phase column (Waters, BEH C₁₈ 1.7 μ m, 2.1 x 50 mm), the MassLynx 4.1 – XP software and a gradient (water-acetonitrile + 0.1% TFA) as eluent.

iii. Optical Spectroscopies

UV-VIS-NIR spectra were recorded on a Varian Cary 5000 apparatus.

Fluorescence experiments were recorded on a FluoroMax-4 (Horiba Jobin-Yvon) spectrofluorometer with the following settings: slit width = 5 nm, inc = 1, integration time = 0.1 s.

InfraRed (I. R.) spectra were recorded on a Fourier transform infrared spectrometer VERTEX 70 (Bruker).

iv. TEM

TEM was performed using a CM12 Philips microscope equipped with a MVIII (SoftImaging System) CCD camera. Samples were analyzed in Bright Field Mode with a LaB₆ cathode and 120 kV tension. Image treatments were performed by using analySIS (Soft Imaging System) software. Samples were either dropcast onto copper TEM grids (for triarylamine fiber solutions) or a modified Langmuir-Schaffer method was used (for the interfacial films in chapter 9) by placing the copper grids horizontally on the interface and lifting up.

Freeze Fracture Electron Microscopy (FFTEM) was performed with the same microscope. The gel samples were placed between two copper holders and rapidly frozen in liquid nitrogen. The sample was kept frozen and transferred into a freeze-fracture apparatus (developed by J.-C. Homo) where the sample was cleaved. Pt was then evaporated onto the sample which was allowed to warm to room temperature afterwards. The replica was rinsed with chloroform and deposited on 400 mesh grids. This technique preserves the native structure of the supramolecular polymer as solvated in the gel state.

v. AFM

Atomic force microscopy (AFM) images were obtained by scanning the samples using a Nanoscope 8 (Bruker) operated in Peak-Force tapping mode. Peak-Force AFM is based on Peak force tapping technology, during which the probe is oscillated in a similar fashion as it is in tapping mode, but at far below the resonance frequency. Each time the tip and the sample are brought together, a force curve is captured. These forces can be controlled at levels much lower than contact mode and even lower than tapping mode allowing operation on even the most delicate soft samples, as is the case here. Ultra-sharp silicon cantilevers were used. During AFM imaging, the force was reduced in order to avoid dragging of molecules by the tip. Integral gain was adjusted to give sharp images. All analyses of the images were conducted in integrated software.

vi. EPR

EPR measurements were performed on a Bruker EMX spectrometer operating at X-band. Quantitative EPR experiments were made by comparing the integrated EPR spectra of the sample with the integrated EPR spectra of a TEMPO standard. Low temperature measurements were performed with a liquid helium cooled cryostat down to 4K.

vii. Conductivity Measurements

Conductivity measurements were performed with a Keithley 2400 Sourcemeter connected to Instec SA100A040UNOPI(A35) parallel plate ITO cells for the conductive gel measurements.

viii. Confocal Raman Microscopy

Measurements were performed on a Horiba Jobin Yvon LabRAM ARAMIS confocal raman microscope with either a 532nm YAG laser or a 785 nm diode laser focused through Olympus 50x and 100x objectives. The sample was placed on a motorized Märzhäuser Wetzlar scanning stage allowing fine control over the position of the sample on the order of 100 nm. The signal was fed through a Synapse CCD detector with an image size of 1024 x 256 pixels.

ix. Electrochemistry

All samples were degassed with argon prior to analyze. Electrochemical measurements were performed on a PGstat101. For spectroelectrochemistry, UV-Vis spectra were acquired on either an Avaspec-2048 with an Avalight-DH-S-Bal light source and a Thorlabs GG420nm Glass longpass filter, or a Cary 5000 instrument from Agilent Technologies, and potential was

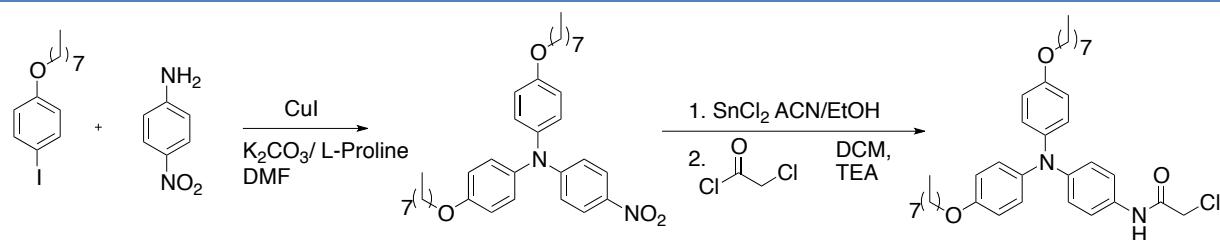
controlled using Keithley 2400 sourcemeter in a 3 probe configuration. Spectroelectrochemistry was performed using a platinum wire mesh transmission with a silver wire pseudo electrode and platinum foil counter electrode. All electrolyte salts were electrochemical grade from Aldrich. Working electrode for electrochemical studies were performed on a platinum 2 mm diameter working electrode, a platinum wire counter electrode with a silver wire pseudo-reference electrode. The counter and reference electrodes were separated from solution with a Vicor glass bridge. Reported redox values were internally referenced against decamethylferrocene. TCE was run through a dry packed column of basic alumina before use.

x. X-ray Diffraction

Crystal structures were determined using a CCD Bruker Kappa APEX II DUO at the crystallographic service of the Université de Strasbourg.

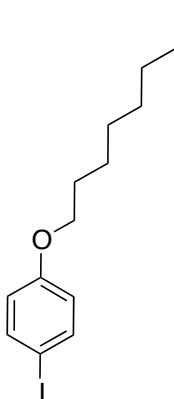
2. Organic Synthesis Procedures

a. Mono-amide triarylamine synthesis



Scheme S1 | Synthetic route to the mono-amide substituted triarylamine.

Compound 1

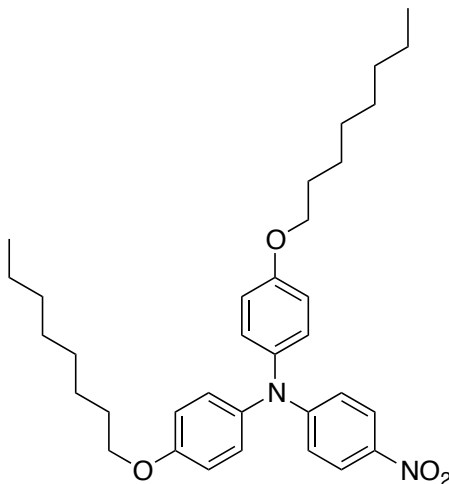


1-iodo-4-octyloxybenzene was synthesized by dissolving a mixture of 4-iodophenol (5.0 g, 23mmol), 1-bromooctane (3.97 mL, 23 mmol), and potassium carbonate (19.1 g, 138 mmol) in acetone (150 mL) and heating to reflux over night. The reaction mixture was diluted with diethylether (300 mL) and the organic layer was washed with 1M KOH (2 x 200 mL) and brine (200 mL) and further dried over Na₂SO₄. Further evaporation under reduced pressure afforded pure compound **1** (6.88 g, 90% yield) as a white powder .

¹H NMR (5:3 MeOD:Toluene-*d*₈, 400 MHz, 300 K): δ = 7.53 (d, ³J = 8.8 Hz, 2H), 6.67 (d, ³J = 8.8 Hz, 2H), 3.91 (t, ³J = 13.1 Hz, 2H), 1.43 – 1.39 (m, 2H), 1.34 – 1.25 (m, 10H), 0.89 (t, ³J = 6.9 Hz, 3H).

ESI-MS: m/z calculated for C₁₄H₂₁IO [M]⁺ 332.06; found 332.12

Compound 2



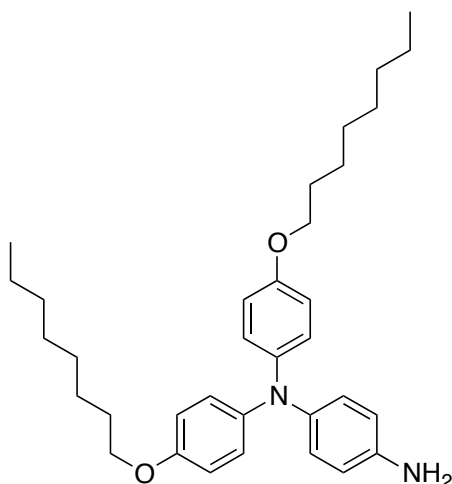
1-iodo-4-octyloxybenzene (6.88 g, 20.7 mmol) was mixed with 4-nitroaniline (0.71 g, 5.2 mmol), CuI (0.4 g, 2.07 mmol), K₂CO₃ (5.73 g, 41.4 mmol), and L-proline (0.471 g, 4.14 mmol) in DMF (40 mL) and heated at 115°C for 15 days. Afterwards, the reaction was diluted with diethylether (400 mL) and run over a pad of silica gel to remove the insoluble salts. Further purification by column chromatography (SiO₂, pentane → pentane/ether 3/1) afforded compound **2** (2.07 g, 73% yield) as an orange oil.

¹H NMR (CDCl₃, 400 MHz, 300 K): δ = 7.99 (d, ³J = 9.4 Hz, 2H), 7.12 (d, ³J = 9.0 Hz, 4H), 6.89 (d, ³J = 9.0 Hz, 4H), 6.75 (d, ³J = 9.4 Hz, 2H), 3.95 (t, ³J = 6.6 Hz, 4H), 1.82 – 1.75 (m, 4H), 1.50 – 1.43 (m, 4H), 1.35 – 1.27 (m, 16H), 0.89 (t, ³J = 6.9 Hz, 6H);

¹³C NMR (CDCl₃, 100 MHz, 300 K): δ = 157.3, 154.2, 138.9, 138.0, 128.1, 125.6, 115.7, 115.6, 68.3, 31.8, 29.3, 29.2, 29.2, 26.0, 22.6, 14.1;

ESI-MS: m/z calculated for C₃₄H₄₆N₂O₄ [M+H]⁺ 547.35; found 547.32

Compound 3



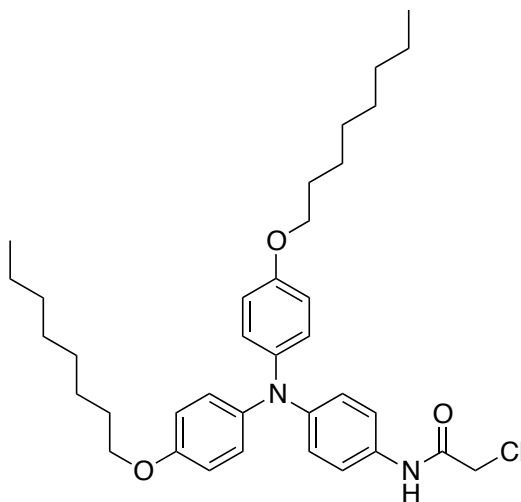
Triarylamine **3** was synthesized by mixing the precursor **2** (2.05 g, 3.79 mmol) and tin chloride (8.57 g, 28 mmol) in a mixture of acetonitrile (50 mL) and ethanol (61 mL) and refluxing overnight. The reaction mixture was diluted with ethyl acetate (600 mL), and the organic layer was washed with saturated Na_2CO_3 (2 x 300 mL) and saturated NaCl (2 x 150 mL), and then dried over MgSO_4 to give compound **3** (1.64 g, 84% yield) which was pure enough to be used as such in the next step.

^1H NMR (CDCl_3 , 400 MHz, 300 K): δ = 6.96 (d, 3J = 8.9 Hz, 4H), 6.89 (d, 3J = 8.5 Hz, 2H), 6.77 (d, 3J = 8.9 Hz, 4H), 6.58 (d, 3J = 8.6 Hz, 2H), 3.92 (t, 3J = 6.5 Hz, 4H), 3.56 (brs, 2H), 1.82 – 1.75 (m, 4H), 1.51 – 1.44 (m, 4H), 1.40 – 1.28 (m, 16H), 0.93 (t, 3J = 6.5 Hz, 6H);

^{13}C NMR (CDCl_3 , 100 MHz, 300 K) δ = 154.0, 142.0, 141.6, 140.1, 125.5, 124.1, 115.9, 114.9, 68.1, 31.7, 29.3 (2C), 29.1, 26.0, 22.5, 14.0;

ESI-MS: m/z calculated for $\text{C}_{34}\text{H}_{48}\text{N}_2\text{O}_2$ $[\text{M}]^+$ 516.38; found 516.59

Compound 4



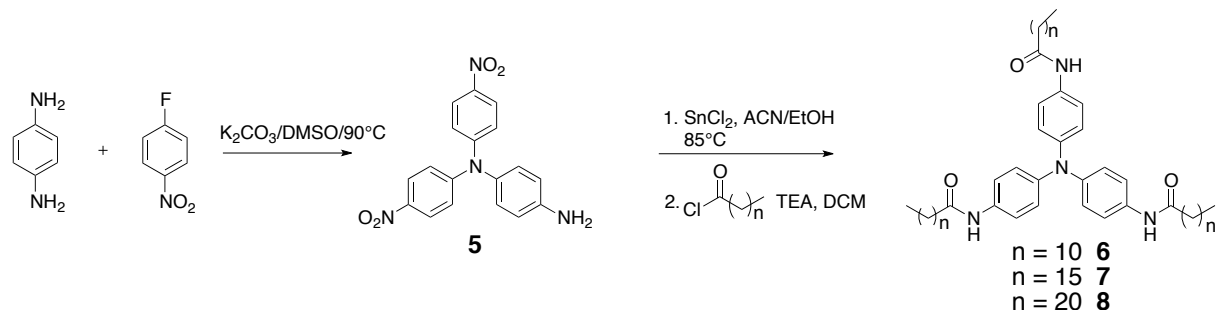
Compound **4** was synthesized by dissolving the amine precursor **3** (1.43 g, 2.76 mmol) and triethylamine (385 μ L) in dichloromethane (55 mL). After cooling down with an ice bath, chloroacetyl chloride (219 μ L, 2.76 mmol) was added dropwise, and the reaction mixture was then allowed to stir for 2 hours at room temperature. Afterwards, the reaction mixture was diluted with diethylether (180 mL) and the organic layer was washed with saturated ammonium chloride (2 x 200 mL) and a saturated brine solution (200 mL). Further purification by column chromatography (SiO₂, cyclohexane \rightarrow cyclohexane:ethyl acetate 1:1) was afforded compound **4** (1.56 g, 95% yield) as an off-white powder.

¹H NMR (CDCl₃, 400 MHz, 300 K): δ = 8.18 (s, 1H), 7.32 (d, ³*J* = 9.0 Hz, 2H), 7.01 (d, ³*J* = 8.9 Hz, 4H), 6.92 (d, ³*J* = 8.9 Hz, 4H), 6.81 (d, ³*J* = 8.9 Hz, 2H), 4.16 (s, 2H), 3.93 (t, ³*J* = 6.6 Hz, 4H), 1.81 – 1.74 (m, 4H), 1.50 – 1.43 (m, 4H), 1.38 – 1.28 (m, 16H), 0.91 (t, ³*J* = 6.9 Hz, 6H);

¹³C NMR (CDCl₃, 100 MHz, 300 K): δ = 163.6, 155.3, 146.2, 140.7, 129.4, 126.1, 121.4, 121.1, 115.2, 68.2, 42.8, 31.8, 29.6, 29.3, 29.2, 26.0, 22.6, 14.0;

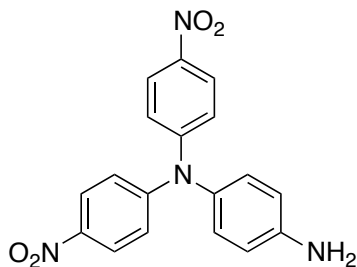
ESI-MS: *m/z* calculated for C₃₆H₄₉ClN₂O₃ [M]⁺ 592.34; found 592.33

b. Tris-amide triarylamine synthesis



Scheme S2 | General synthetic route to tris-amide triarylamines.

Compound 5



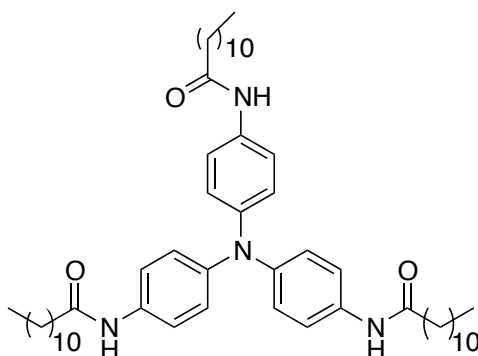
The tris-amide precursor was synthesized by stirring 4-aminoaniline (1.08 g, 10 mmol) and 4-fluoronitrobenzene (2.82 g, 20 mmol) and K_2CO_3 (5.5 g, 40 mmol) in DMSO (30 mL) for three days at 90°C under Argon. The reaction mixture was then cooled down to room temperature, and poured into a beaker containing 400 mL of deionized water. The resulting orange-brown precipitate was then filtered and left to dry overnight. Further purification by column chromatography (SiO_2 , dichloromethane) provided compound **5** (2.45 g, 70% yield) as an orange solid.

$^1\text{H NMR}$ (**5:3 MeOD:Toluene- d_8** , 400 MHz, 300 K): $\delta = 8.11$ (d, $^3J = 9.1$ Hz, 4H), 7.13 (d, $^3J = 9.1$ Hz, 4H), 6.96 (d, $^3J = 8.6$ Hz, 2H), 6.73 (d, $^3J = 8.5$ Hz, 2H);

$^{13}\text{C NMR}$ (**5:3 MeOD:Toluene- d_8** , 100 MHz, 300 K): $\delta = 152.2, 146.1, 142.4, 135.2, 129.1, 125.6, 121.6, 116.6$;

ESI-MS: m/z calculated for $\text{C}_{18}\text{H}_{14}\text{N}_4\text{O}_4$ $[\text{M}+\text{H}]^+$ 351.10, found 351.24

Compound 6



Compound **5** (5.0 g, 14.3 mmol) was reduced with tin (II) chloride (32.0 g, 143 mmol) in a mixture of acetonitrile (300 mL) and ethanol (360 mL) by refluxing overnight under argon. The next day, the reaction was allowed to cool and then it was diluted with ethyl acetate (500 mL) and washed with Na_2CO_3 (2 x 300 mL) and a brine solution (2 x 300 mL) before being dried over Na_2SO_4 . The brownish-red tris-amine intermediate was recovered after removal of solvent in vacuum. This intermediate (415 mg, 1.43 mmol) was then dissolved in dichloromethane (50 mL) along with triethylamine (660 μL , 4.72 mmol) under argon. This mixture was stirred inside of an ice bath and lauroyl chloride (1.1 mL, 4.72 mmol) was added dropwise. The next day, the reaction was diluted with diethylether (500 mL), washed with 1M HCl (2 x 200 mL) and brine (2 x 200 mL), dried over Na_2SO_4 before concentrating under reduced pressure. The material was then concentrated with celite and loaded on a silica column, which was subsequently washed with cyclohexane and ethyl acetate. The pure product was retrieved from the top of the column, dissolved in methanol:toluene (5:3, 200 mL), filtered, dried under reduced pressure, brought up in ether (500 mL) and washed with water (2 x 200 mL). The final product was obtained as an off-white powder after concentrating under reduced pressure for an 87% yield (1.03 g, 1.24 mmol).

^1H NMR (5:3 MeOD:Toluene- d_8 , 400 MHz, 300 K): δ = 7.54 (d, 3J = 9.0 Hz, 6H), 6.97 (d, 3J = 8.9 Hz, 6H), 2.33 (t, 3J = 7.5 Hz, 6H), 1.74 – 1.68 (m, 6H), 1.34 – 1.26 (m, 48H), 0.89 (t, 3J = 6.9 Hz, 9H);

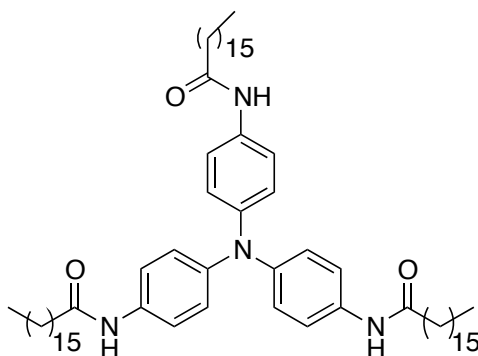
^{13}C NMR (5:3 MeOD:Toluene- d_8 , 100 MHz, 300 K): δ = 174.0, 145.1, 134.8, 125.0, 122.2,

37.9, 32.9, 30.7, 30.6 (x 2), 30.5, 30.4, 30.3, 26.9, 23.6, 14.6;

ESI-MS: m/z calculated for $C_{54}H_{84}N_4O_3$ $[M]^+$ 836.65, found 836.89;

IR: $\nu=3291\text{ cm}^{-1}$ (amide N-H stretch), 1654 cm^{-1} (amide carbonyl stretch), 1599 cm^{-1} (amide N-H bending).

Compound 7



Compound **5** (5.0 g, 14.3 mmol) was reduced with tin (II) chloride (32 g, 143 mmol) in a mixture of acetonitrile (300 mL) and ethanol (360 mL) by refluxing overnight under argon. The next day, the reaction was allowed to cool and then it was diluted with ethyl acetate (500 mL) and washed with Na_2CO_3 (2 x 300 mL) and a brine solution (2 x 300 mL) before being dried over Na_2SO_4 . The brownish-red tris-amine intermediate was recovered after removal of solvent in vacuum. This intermediate (189 mg, 0.65 mmol) was then dissolved in dichloromethane (30 mL) along with triethylamine (304 μ L, 2.18 mmol) under argon. This mixture was stirred inside of an ice bath and heptadecanoyl chloride (629 mg, 2.18 mmol) was added dropwise. The next day, the reaction was diluted with diethylether (300 mL), washed with 1M HCl (2 x 100 mL) and brine (2 x 100 mL), dried over Na_2SO_4 before concentrating under reduced pressure. The material is then concentrated with celite and loaded on a silica column, which is subsequently washed with cyclohexane and ethyl acetate. The pure product is retrieved from the top of the column, dissolved in methanol:toluene (5:3, 200 mL), filtered, dried under reduced pressure, brought up in ether (500 mL) and washed with water (2 x 100 mL.). The final product is obtained as an off-white powder after concentrating under reduced

pressure for an 70% yield (477 mg, 0.455 mmol).

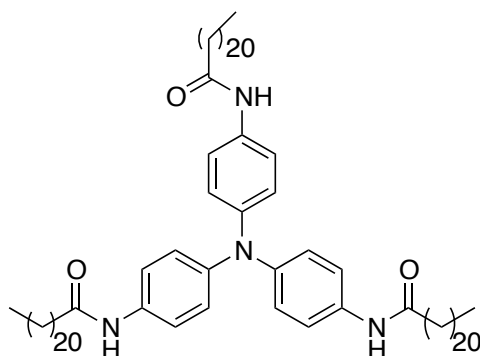
¹H NMR (5:3 MeOD:Toluene-*d*₈, 400 MHz, 300 K): δ = 7.54 (d, ³*J* = 7.8 Hz, 6H), 6.98 (d, ³*J* = 8.8 Hz, 6H), 2.33 (t, ³*J* = 7.5 Hz, 6H), 1.74 – 1.68 (m, 6H), 1.36 – 1.26 (m, 78H), 0.89 (t, ³*J* = 6.7 Hz, 9H);

¹³C NMR (5:3 MeOD:Toluene-*d*₈, 100 MHz, 301 K): δ = 173.9, 145.0, 134.8, 125.0, 122.2, 37.9, 32.9, 30.7 (m), 30.4 (m), 23.6, 14.6;

ESI-MS: *m/z* calculated for C₆₉H₁₁₄N₄O₃ [M+H]⁺ 1047.89, found 1048.25;

IR: ν = 3291 cm⁻¹ (amide N–H stretch), 1654 cm⁻¹ (amide carbonyl stretch), 1600 cm⁻¹ (amide N–H bending).

Compound 8



Compound **5** (5.0 g, 14.3 mmol) was reduced with tin (II) chloride (32 g, 143 mmol) in a mixture of acetonitrile (300 mL) and ethanol (360 mL) by refluxing overnight under argon. The next day, the reaction was allowed to cool and then it was diluted with ethyl acetate (500 mL) and washed with Na₂CO₃ (2 x 300 mL) and a brine solution (2 x 300 mL) before being dried over Na₂SO₄. The brownish-red tris-amine intermediate was recovered after removal of solvent in vacuum. This intermediate (145 mg, 0.5 mmol) was then dissolved in dichloromethane (30 mL) along with triethylamine (400 μ L, 2.5 mmol) under argon. This mixture was stirred inside of an ice bath and behenic chloride (359.0 mg, 2.0 mmol) was added. The next day, the reaction was diluted with diethylether (300 mL), washed with 1M HCl (2 x 100 mL) and brine (2 x 100 mL), dried over Na₂SO₄ before concentrating under

reduced pressure. The material is then concentrated with celite and loaded on a silica column, which is subsequently washed with cyclohexane and ethyl acetate. The pure product is retrieved from the top of the column, dissolved in methanol:toluene (5:3, 200 mL), filtered, dried under reduced pressure, brought up in ether (500 mL) and washed with water (2 x 100 mL.). The final product is obtained as an off-white powder after concentrating under reduced pressure for an 77% yield (485 mg, 0.386 mmol).

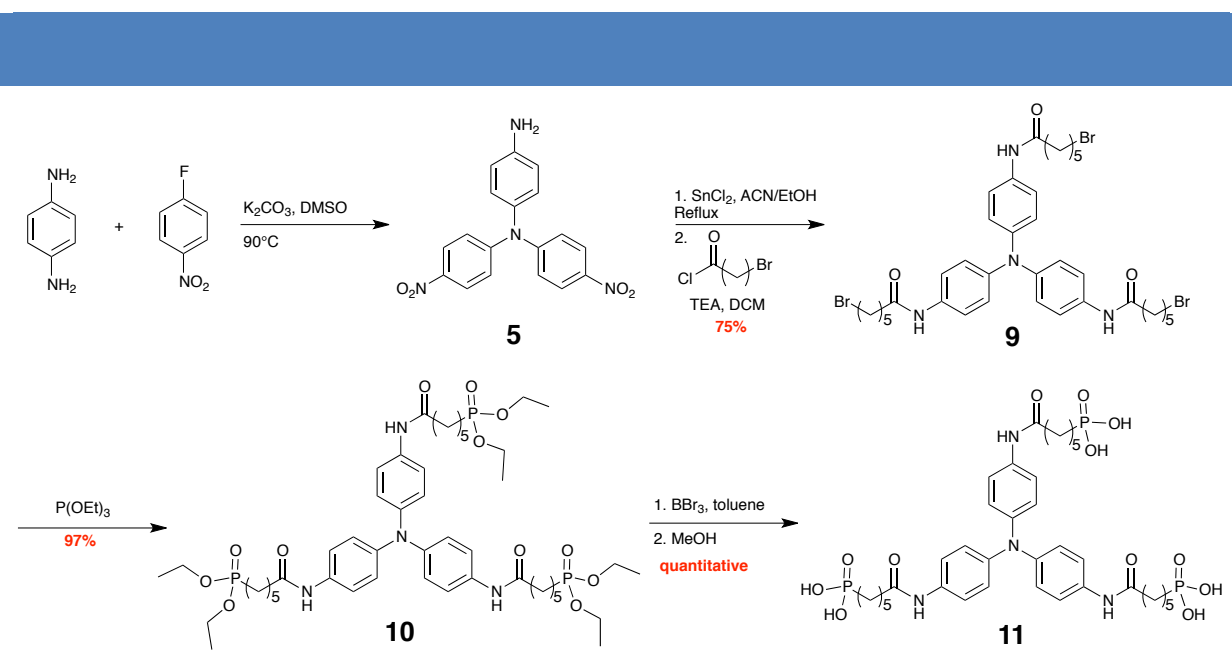
^1H NMR (5:3 MeOD:Toluene- d_8 , 400 MHz, 300 K): δ = 7.55 (d, 3J = 7.6 Hz, 6H), 6.98 (d, 3J = 8.6 Hz, 6H), 2.33 (t, 3J = 7.5 Hz, 6H), 1.76 – 1.70 (m, 6H), 1.36 – 1.26 (m, 108H), 0.88 (t, 3J = 6.75 Hz, 9H);

^{13}C NMR (5:3 MeOD:Toluene- d_8 , 100 MHz, 300 K) δ = 173.7, 145.0, 134.7, 125.0, 122.1, 37.9, 32.9, 30.7 (m), 30.6, 30.4, 30.2, 23.6, 14.6;

ESI-MS: m/z calculated for $\text{C}_{84}\text{H}_{144}\text{N}_4\text{O}_3$ $[\text{M}+\text{H}]^+$ 1258.12, found 1258.41;

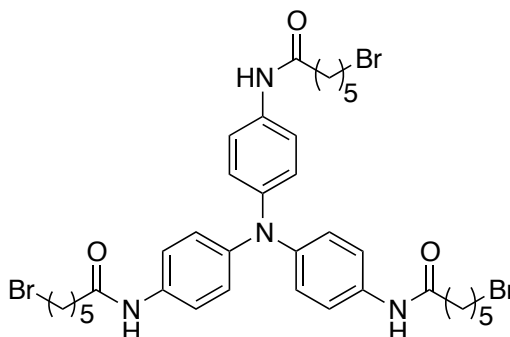
IR: ν = 3291 cm^{-1} (amide N–H stretch), 1654 cm^{-1} (amide carbonyl stretch), 1601 cm^{-1} (amide N–H bending).

c. Phosphonic acid tris-amide triarylamine



Scheme S3 | Synthetic route to the phosphonic acid substituted tris-amide triarylamine.

Compound 9



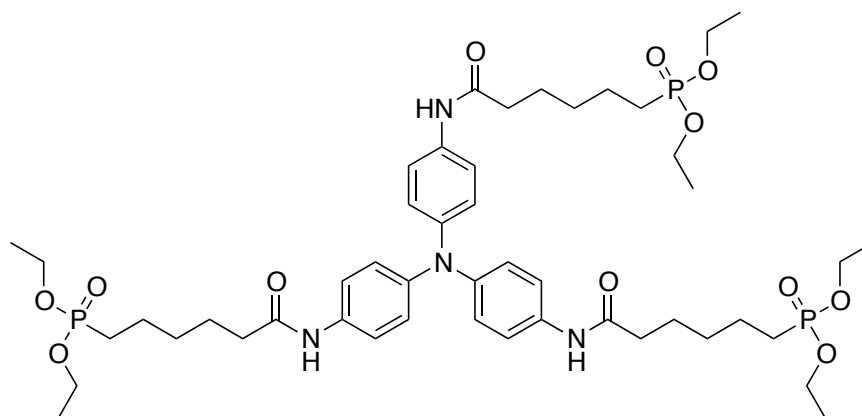
Compound **5** (5.0 g, 14.3 mmol) was reduced with tin (II) chloride (32 g, 143 mmol) in a mixture of acetonitrile (300 mL) and ethanol (360 mL) by refluxing overnight under argon. The next day, the reaction was allowed to cool and then it was diluted with ethyl acetate (500 mL) and washed with Na₂CO₃ (2 x 300 mL) and a brine solution (2 x 300 mL) before being dried over Na₂SO₄. The brownish-red tris-amine intermediate was recovered after removal of solvent in vacuum. This intermediate (400 mg, 1.4 mmol) was dissolved in dichloromethane (60 mL) along with triethylamine (0.763 mL, 5.5 mmol). The solution was placed in an ice bath and 6-bromohexanoyl chloride (0.841 mL, 5.5 mmol) was added dropwise. After the addition, the ice bath was removed and the reaction allowed proceeding overnight at room temperature. The next day, the reaction was diluted with ether (600 mL), washed with 1M HCl (2x 120 mL), brine (2x 120 mL) and then dried down under reduced pressure. The resulting powder was further washed with copious amounts of water to remove residual triethylamine before being dried to give pure compound **9** as an off-white powder (860 mg, 75% yield).

¹H NMR (MeOD, 400 MHz, 300 K): δ = 7.38 (d, ³*J* = 8.9 Hz, 6H), 6.92 (d, ³*J* = 8.9 Hz, 6H), 3.42 (t, ³*J* = 6.8 Hz, 6H), 2.33 (t, ³*J* = 7.5 Hz, 6H), 1.89 - 1.79 (m, 6H), 1.70 - 1.64 (m, 6H), 1.52 - 1.42 (m, 6H);

¹³C NMR (MeOD, 100 MHz, 300 K): δ = 172.7, 144.0, 133.3, 123.7, 121.2, 36.2, 32.6, 32.2, 27.3, 24.6;

ESI-MS: *m/z* calculated for C₃₆H₄₅Br₃N₄O [M]⁺ 820.10; found 820.16

Compound 10



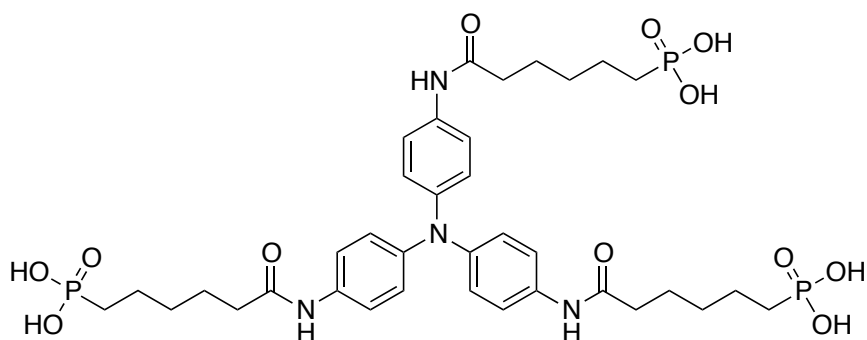
Triarylamine **10** was synthesized under solvent free conditions. Briefly, triarylamine compound **9** (98.4 mg, 0.12 mmol) was placed in a round bottom flask and heated to 100°C. Then, triethyl phosphite (1 mL, 5.8 mmol) was added, and the reaction mixture was heated to reflux (156°C), allowing the removal of ethyl bromide (using a fractionating column attached to a condenser). After 5 hours, the remaining triethyl phosphite was removed by vacuum distillation, and the crude product was transferred onto a celite pad which was washed with cyclohexane (100 mL) and ethyl acetate (100 mL) to remove trace amounts of triethyl phosphite. Finally, the celite pad was washed in methanol, and the resulting solution was filtered and dried down to provide compound **10** (109 mg, 97% yield) as a yellow oil.

¹H NMR (MeOD, 400 MHz, 300 K): δ = 7.38 (d, 3J = 8.9 Hz, 6H), 6.91 (d, 3J = 8.9 Hz, 6H), 4.07 – 4.00 (m, 12H), 2.32 (t, 3J = 7.4 Hz, 6H), 1.88 – 1.84 (m), 1.70 – 1.64 (m), 1.47 – 1.42 (m), 1.26 (t, 3J = 7.0 Hz, 18H);

¹³C NMR (MeOD, 100 MHz, 296 K): δ = 174.2, 145.4, 134.8, 125.1, 122.6, 63.2, 37.5, 30.9, 26.3, 25.0, 23.2, 16.7;

ESI-MS: m/z calculated for C₄₈H₇₅N₄O₁₂P₃ [M+H]⁺ 993.46, found 993.85

Compound 11



Triarylamine **10** (493.2 mg, 0.5 mmol) was dissolved in toluene (100 mL) under argon and the solution was cooled to -30°C . BBr_3 (neat, 381 μL , 4.02 mmol) was dissolved in toluene (5 mL) and the solution was added dropwise to the triarylamine solution at -30°C . After the addition, the mixture was allowed to warm to room temperature and then heated to 70°C for 6 hours. Purification by preparative HPLC afforded pure compound **11** (410 mg, 99% yield) as a colorless oil.

$^1\text{H NMR}$ (D_2O , 400MHz, 300K) $\delta = 7.27$ (bs, 2H), 7.00 (bs, 2H), 1.7 – 1.35 (bs, 10H)

ESI-MS: m/z calculated for $\text{C}_{36}\text{H}_{51}\text{N}_4\text{O}_{12}\text{P}_3$ 825.27, found 825.59

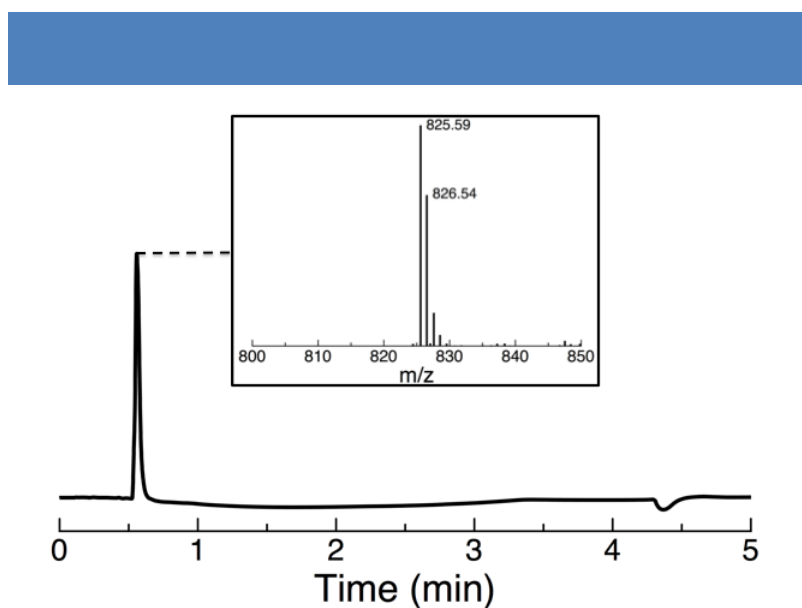
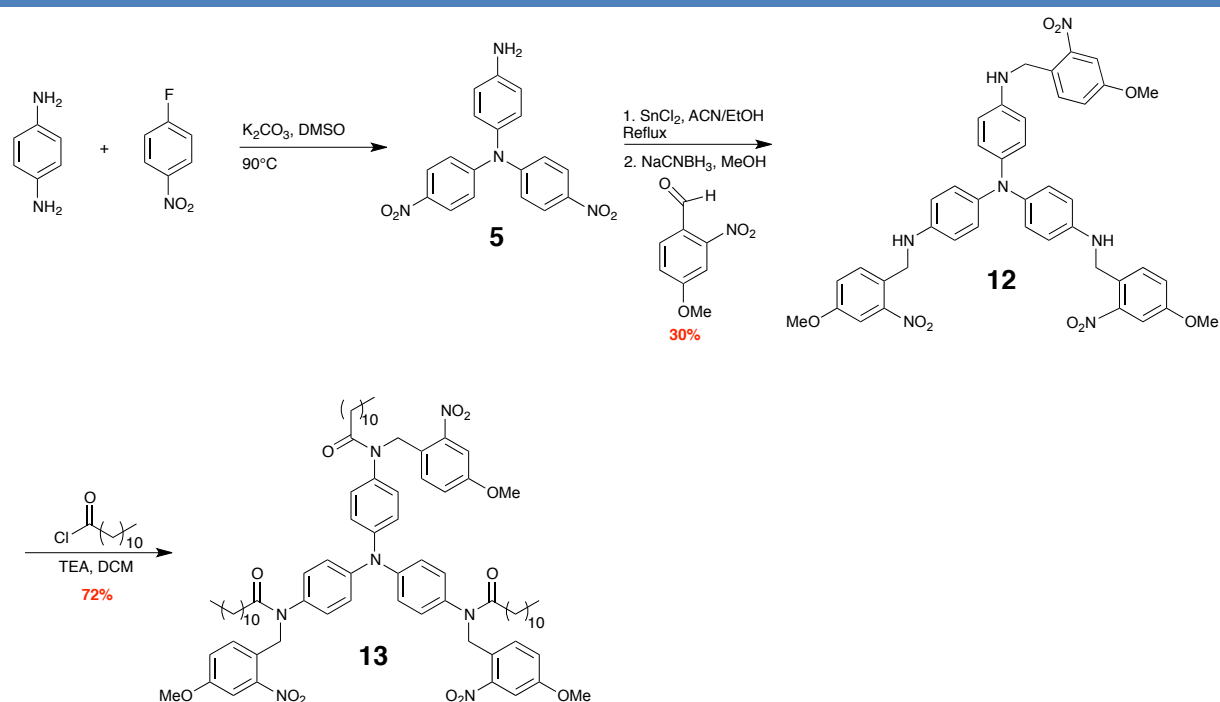


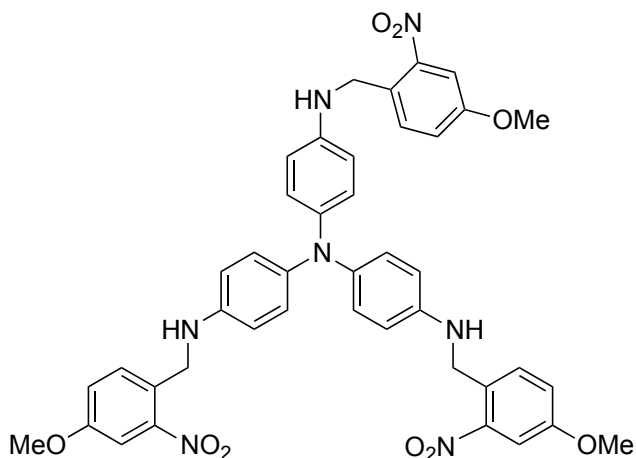
Figure S1 | LC/MS trace after preparative HPLC purification of the product showing the isolation of the pure deprotected product.

d. Protected tris-amide synthesis



Scheme S4 | Synthetic scheme for the synthesis of the protected tris-amide triarylamine.

Compound 12



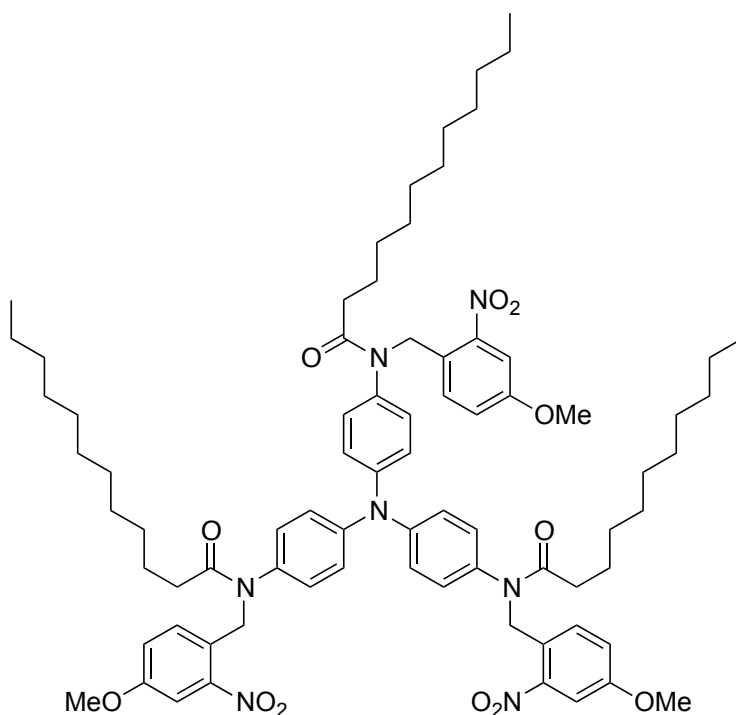
Tris-amine triarylamine precursor **5** (93 mg, 0.32 mmol) was mixed together with 4-methoxy-2-nitro-benzaldehyde (190 mg, 1.05 mmol) in methanol (40 mL) under argon. Sodium cyanoborohydride (103 mg, 1.28 mmol) was added and the solution was stirred overnight at room temperature. Then the solvent was removed under vacuum and the crude product purified by column chromatography (SiO_2 , cyclohexane \rightarrow cyclohexane/ethyl acetate

3:1) provided compound **12** (75.0 mg, 30% yield) as a light gray powder.

¹H NMR (CDCl₃, 400 MHz, 300 K): δ = 7.60 - 7.52 (m, 6H), 7.11 (dd, ³*J* = 8.6 Hz, ⁴*J* = 2.6 Hz, 3H), 6.81 (d, ³*J* = 8.8 Hz, 6H), 6.44 (d, ³*J* = 8.8 Hz, 6H), 4.56 (s, 6H), 3.86 (s, 9H);

ESI-MS: *m/z* calculated for C₄₂H₃₉N₇O₉ [M+H]⁺785.28, found 785.38

Compound 13

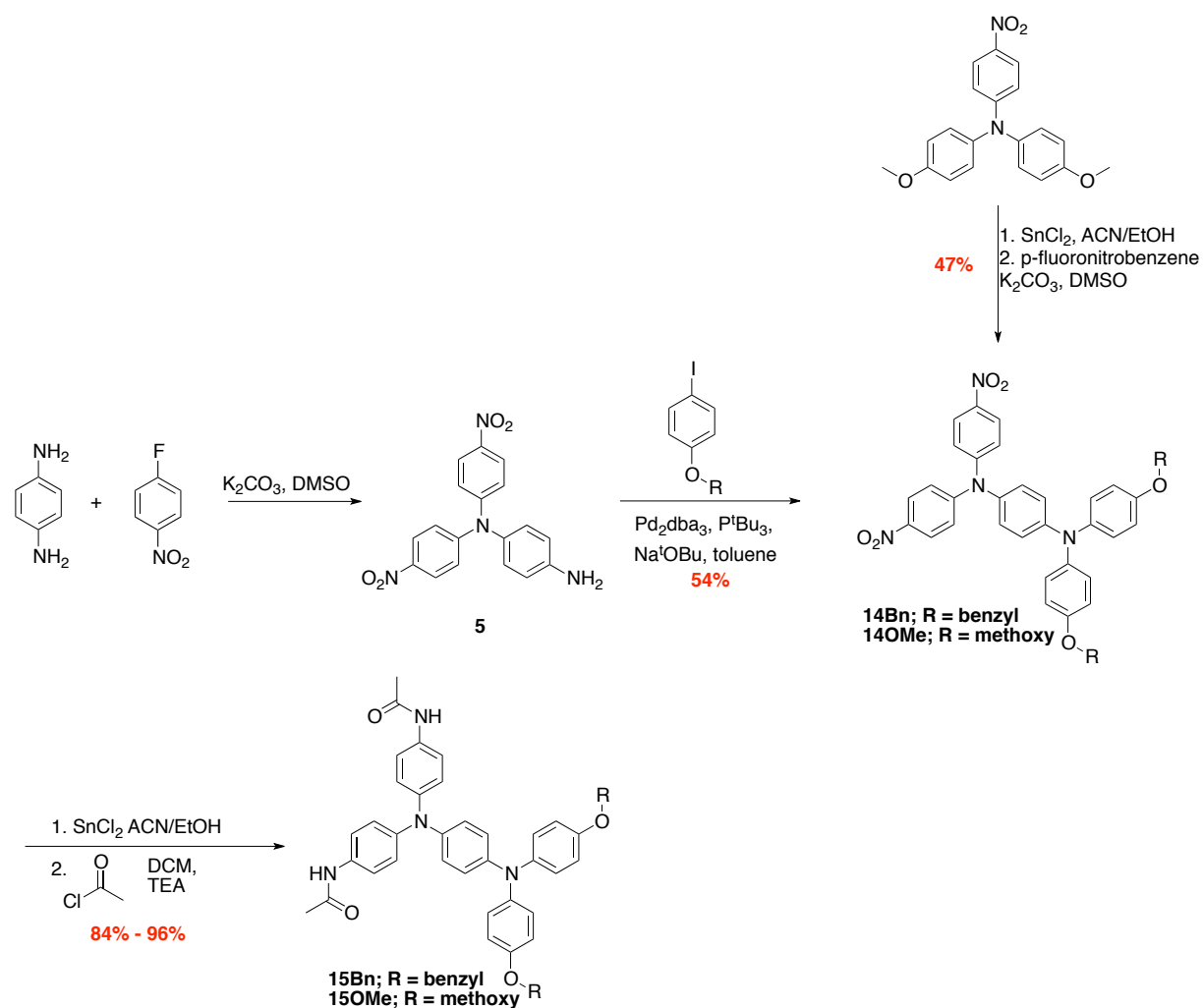


The protected amine precursor **12** (75 mg, 0.095 mmol) and triethylamine (80 μ L, 0.57 mmol) was dissolved in dichloromethane (40 mL) under argon at 0°C. Dodecyl chloride (136 μ L, 0.57 mmol) was added dropwise and the reaction slowly warmed to room temperature. The next day, the reaction mixture was diluted in ethyl acetate and washed twice with water and dried with sodium sulfate. The pure product was separated over a silica column in cyclohexane and ethyl acetate to give a yellow oil in 72% yield.

¹H NMR (CDCl₃, 400 MHz, 300 K): δ = 7.59 (d, ³*J* = 8.8 Hz, 3H), 7.35 (d, ⁴*J* = 2.4 Hz, 3H), 7.13 (dd, ³*J* = 8.9 Hz, ⁴*J* = 2.5 Hz, 3H), 7.01 (d, ³*J* = 8.8 Hz, 6H), 6.86 (d, ³*J* = 8.3 Hz, 6H), 5.20 (s, 6H), 3.84 (s, 9H), 2.15 (t, ³*J* = 7.7 Hz, 6H), 1.62 – 1.57 (m, 6H), 1.36 – 1.22 (m, 42H), 0.87 (t, ³*J* = 7.0 Hz, 9H);

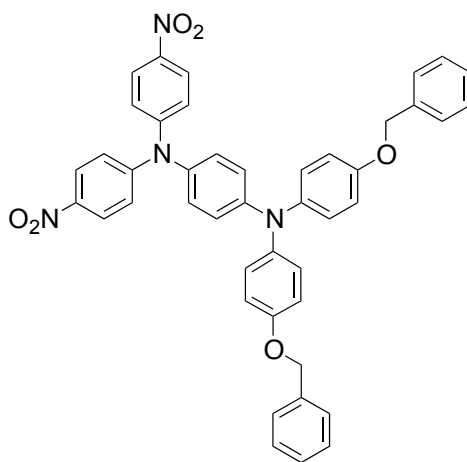
^{13}C NMR (CDCl_3 , 100 MHz, 300 K): $\delta = 173.7, 159.1, 149.7, 146.7, 137.3, 132.2, 129.2, 125.1, 124.8, 120.0, 109.3, 56.0, 49.0, 34.4, 32.0, 29.8, 29.6$ (x 2), 29.5 (x 2), $25.6, 22.8, 14.3$;
ESI-MS: m/z calculated for $\text{C}_{78}\text{H}_{105}\text{N}_7\text{O}_{12}$ $[\text{M}+\text{H}]^+$ 1332.78, found 1332.69

e. Two-center and three-center triarylamine synthesis



Scheme S5 | General synthetic scheme for the two-redox center triarylamine derivative.

Compound 14OBn

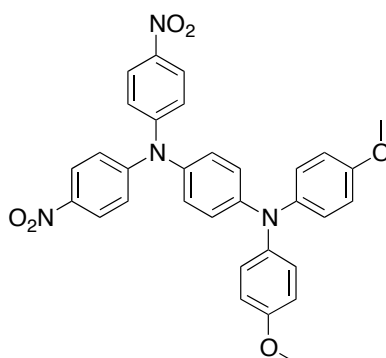


Under argon atmosphere in a schlenk tube, tris(dibenzylideneacetone)dipalladium(0) (0.392 g, 0.428 mmol) was stirred with P(*t*-Bu)₃ (0.428 mL, 0.428 mmol) in 5 mL toluene for 10 minutes. Then, the triarylamine intermediate **5** (1 g, 2.85 mmol) was added, along with 1-(benzyloxy)-4-iodobenzene (5.4 g, 17.4 mmol) and sodium tert-butoxide (1.67 g, 17.4 mmol). The mixture was heated for 24 hours at 100 °C. Toluene was removed under vacuum and the resulting crude was transferred a minimal volume of dichloromethane and was filtered through a pad of silica gel. Further purification by column chromatography (SiO₂, cyclohexane/ethyl acetate) provided compound **14OBn** (165.0 mg, 54% yield) as a yellow oil.

¹H NMR (400 MHz, CDCl₃, 300 K) δ = 8.14 (d, ³J = 9.2, 4H), 7.30 - 7.47 (m, 10H), 7.16 (d, ³J = 9.2, 4H), 7.11 (d, ³J = 9.0, 4H), 6.94 (d, ³J = 9.0, 4H), 6.91 (br.s, 4H), 5.05 (s, 4H)

ESI-MS: m/z calculated for C₄₄H₃₄N₄O₆ [M+H]⁺ 715.25, found 715.34

Compound 14OMe



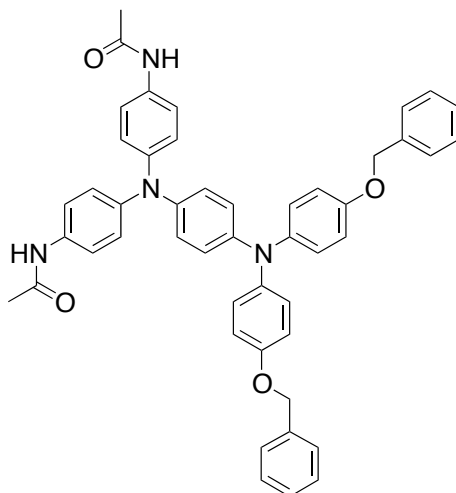
4-methoxy-N-(4-methoxyphenyl)-N-(4-nitrophenyl)aniline was prepared according to our described procedure.¹ This intermediate (1.0 g, 2.85 mmol) was dissolved with tin (II) chloride dihydrate (5.15 g, 22.8 mmol) in mixture of ethanol (75 mL) and acetonitrile (75 mL) and stirred overnight with reflux under argon atmosphere. The next day, the reaction was cooled down to room temperature and diluted with ethyl acetate (250 mL). The organic phase was washed with 1M NaOH (3 x 75 mL), then water (2 x 100mL), brine (1 x 50 mL), and dried over Na₂SO₄ and concentrated under reduced pressure. This was then immediately dissolved with potassium carbonate (1.58 g, 11.4 mmol) in DMSO (10 mL) under argon atmosphere. 1-fluoro-4-nitrobenzene (0.636 mL, 5.99 mmol) was added by syringe and the reaction heated to 90°C for 4 days. After that time, the solution was allowed to cool to room temperature, and upon dilution with water (200mL) a dark red solid precipitated. The product was extracted with dichloromethane (500 mL) and the organic phase washed with water (2 x 200 mL) and dried over Na₂SO₄. After evaporation of solvent, the crude product was purified by column chromatography (SiO₂, cyclohexane/dichloromethane 50:50 → pure dichloromethane) to give **14OMe** (751 mg, 1.34 mmol, 46.8 %) as dark red solid.

¹H NMR (CDCl₃, 400 MHz, 300 K) δ = 8.14 (d, ³J = 9.3, 4H), 7.16 (d, ³J = 9.3, 4H), 7.12 (d, ³J = 9.1, 4H), 6.89 - 6.93 (m, 4H), 6.87 (d, ³J = 9.1, 4H), 3.80 (s, 6H).

¹³C NMR (CDCl₃, 100 MHz, 300 K): δ = 156.7, 152.1, 148.2, 142.5, 140.1, 136.0, 128.3, 127.4, 125.6, 121.8, 120.4, 115.1, 55.7

ESI-MS: m/z calculated for C₃₂H₂₆N₄O₆⁺ [M]⁺, 562.19; found 562.35

Compound 15OBn



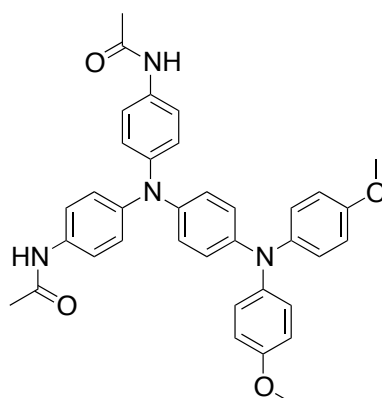
Compound **14OBn** (0.7 g, 1.24 mmol) was dissolved in dry dichloromethane (50 mL). The reaction mixture was cooled down with an ice bath and then triethylamine (879 μ L, 6.32 mmol) and acetyl chloride (447 μ L, 6.27 mmol) were added dropwise. The mixture was then allowed to stir for 30 min at room temperature until a white precipitate appeared. Dichloromethane (600 mL) was then added to the reaction mixture in order to dissolve the precipitate. The organic phase was washed with NaHCO₃ (sat.) (2 x 100 mL), brine (100 mL), and dried over Na₂SO₄. Concentration under vacuum afforded a yellowish solid which was washed with acetone (30 mL), diethyl ether (10 mL) and finally dried under vacuum to provide compound **15OBn** (1.48 g, 96% yield) as a white solid.

¹H NMR (DMSO-*d*₆, 400 MHz, 300 K) δ = 9.84 (s, 2H), 7.49 - 7.42 (m, 8H), 7.39 (dd, ³*J* = 8.0 Hz, ⁴*J* = 2.6 Hz, 4H), 7.32 (dd, ³*J* = 7.8 Hz, ⁴*J* = 2.6 Hz, 2H), 7.00 - 6.93 (m, 8H), 6.90 (d, ³*J* = 8.9 Hz, 4H), 6.83 (d, ³*J* = 9.0 Hz, 2H), 6.77 (d, ³*J* = 9.0 Hz, 2H), 5.04 (s, 4H), 2.01 (s, 6H);

¹³C NMR (DMSO-*d*₆, 100 MHz, 300 K): δ = 167.8, 154.3, 143.1, 142.7, 141.0, 140.8, 137.1, 134.1, 128.4, 127.8, 127.7, 125.5, 124.3, 123.4, 122.2, 120.3, 115.7, 69.5, 23.8;

ESI-MS: *m/z* calculated for C₄₈H₄₂N₄O₄⁺ [M]⁺ 738.32, found 738.44

Compound 15OMe

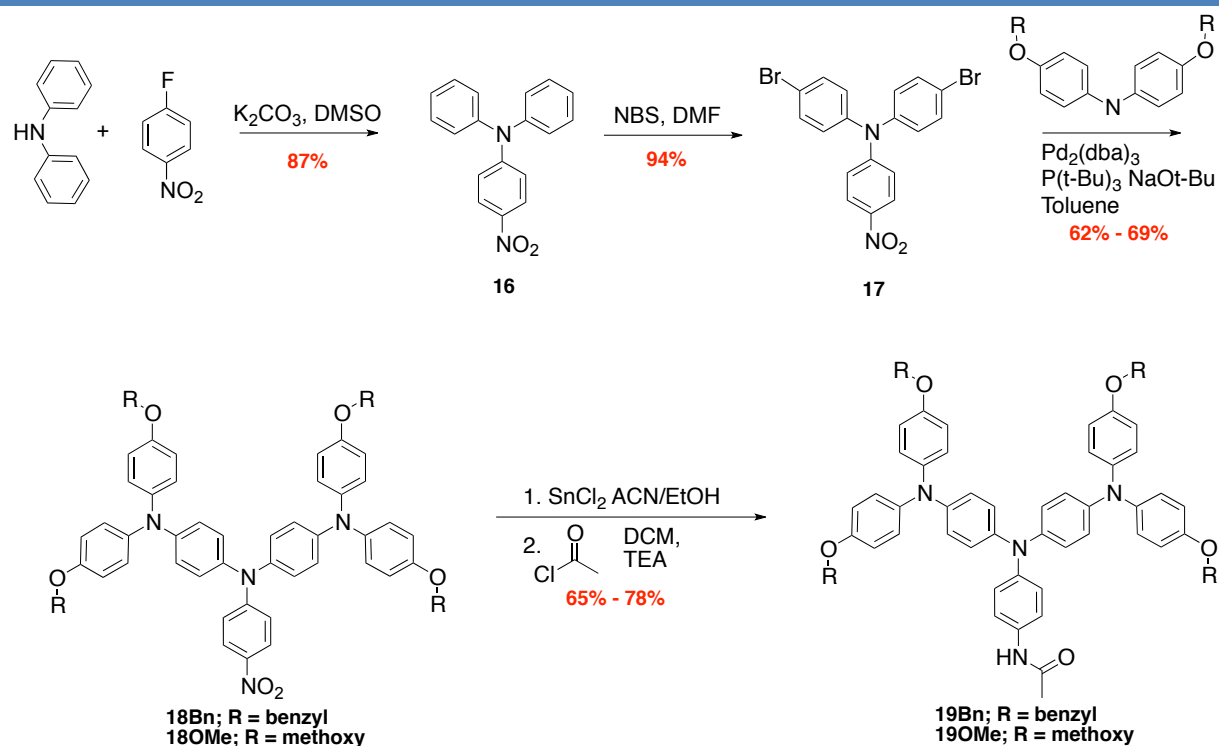


Compound **14OMe** (1.37 g, 2.09 mmol) and tin (II) chloride dihydrate (2.81 g, 12.4 mmol) was dissolved in a mixture of ethanol (50 mL) and acetonitrile (50 mL) and the reaction mixture was stirred overnight at reflux under an argon atmosphere. Afterwards, the solution was cooled down to room temperature and diluted with ethyl acetate (250 mL). The organic phase was washed with 1M NaOH (3 x 50mL), water (100 mL) and brine (100 mL), dried over Na₂SO₄ and concentrated under reduced pressure. The residue was then dissolved in dry dichloromethane (50 mL) and the reaction mixture cooled down with an ice bath. First triethylamine (519 μ L, 3.73 mmol) and acetyl chloride (266 μ L, 3.73 mmol) were added dropwise. The mixture was then allowed to stir for 30 min at room temperature until a white precipitate appeared. Dichloromethane (200 mL) was added and the organic phase was washed with NaHCO₃ (sat.) (2 x 100 mL), brine (100 mL), and dried over Na₂SO₄. Concentration under vacuum afforded a yellowish solid which was washed with acetone (30 mL), diethyl ether (10 mL) and finally dried under vacuum to provide compound **15OMe** (613 mg, 84% yield) as a white solid.

¹H NMR (DMSO-d₆, 400 MHz, 300 K) : δ = 9.83 (s, 2H), 7.45 (d, J = 8.9, 4H), 6.97 (d, J = 9.0, 4H), 6.85 - 6.93 (m, 8H), 6.83 (d, J = 8.9, 2H), 6.75 (d, J = 9.0, 2H), 3.72 (s, 6H), 2.00 (s, 6H)

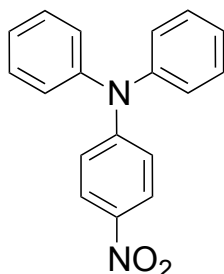
¹³C NMR (DMSO-d₆, 100 MHz, 300 K): δ = 167.8, 155.2, 143.3, 142.7, 140.8, 140.6, 134.1, 125.7, 124.5, 123.4, 121.9, 120.3, 114.8, 55.2, 23.8

ESI-MS: m/z calculated for C₃₆H₃₄N₄O₄⁺⁺ [M]⁺⁺, 586.26; found 586.42



Scheme S6 | General synthetic scheme for the three-redox centered triarylamine derivative.

Compound 16



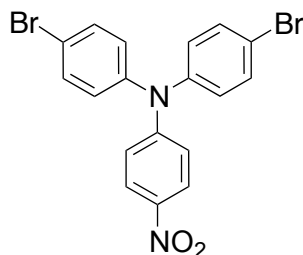
To a solution of diphenylamine (10.0 g, 59.1 mmol) in dry DMF (250 mL), sodium hydride (2.85 g, 71.3 mmol) was added portionwise under argon atmosphere. Then 1-fluoro-4-nitrobenzene (6.9 mL, 65.0 mmol) was added dropwise over 30 min. The reaction mixture was then stirred at room temperature overnight. After that time, cooled water (600 mL) was added to the reaction mixture leading to the formation of a yellow precipitate. This solid was filtrated and recrystallized from toluene giving compound **16** (15 g, 87% yield) as orange crystals.

$^1\text{H NMR}$ (400 MHz, CDCl_3 , 300K) δ = 8.04 (d, $^3J = 9.4$, 2H), 7.37 (m, 4H), 7.14 - 7.25 (m,

6H), 6.92 (d, $^3J = 9.4$, 2H).

ESI-MS: m/z calculated for $C_{18}H_{14}N_2O_2$ $[M]^+$ 290.11, found 290.27

Compound 17

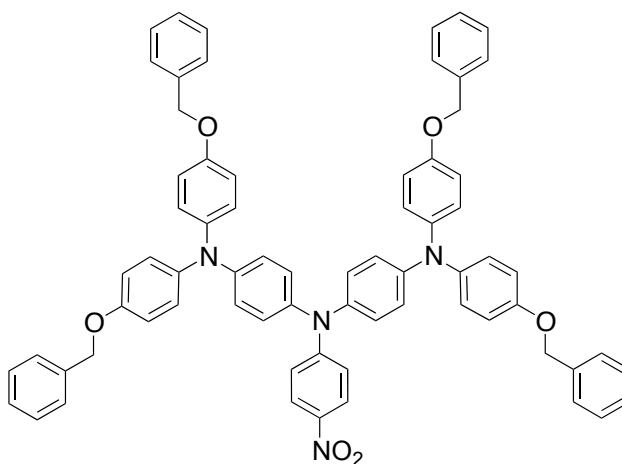


Triarylamine precursor **16** (3.0 g, 10.3 mmol) was dissolved in DMF (20 mL) under an argon atmosphere. Then a solution of N-bromosuccinimide (4.27 g, 24.0 mmol) in DMF (15 mL) was added dropwise at room temperature. After 12 hours, an orange precipitate appeared. The reaction mixture was stirred for two additional days. Afterwards, the reaction mixture was diluted with water (200 mL). The orange precipitate was filtered under reduced pressure and dried at 95 °C. This orange solid was then dissolved in a minimal volume of dichloromethane (50 mL) and cold methanol (150 mL) was added slowly until precipitation occurred, providing compound **17** (4.35 g, 94% yield) as yellow crystals.

1H NMR (CDCl₃, 400 MHz, 300 K): $\delta = 8.06$ (d, $^3J = 9.2$ Hz, 2H), 7.48 (d, $^3J = 8.8$ Hz, 4H), 7.03 (d, $^3J = 8.8$ Hz, 4H), 6.96 (d, $^3J = 9.2$ Hz, 2H).

ESI-MS: m/z calculated for $C_{18}H_{12}Br_2N_2O_2$ $[M]^+$ 447.92, found 448.04

Compound 18Bn



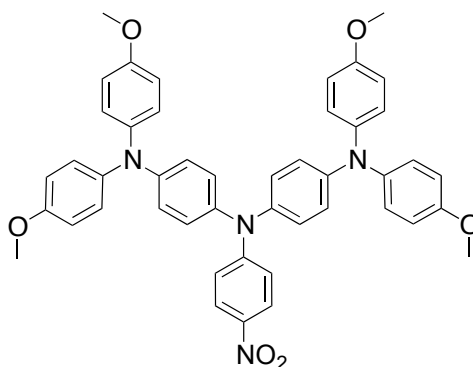
Brominated triarylamine precursor **17** (747 mg, 1.67 mmol), bis(4-(benzyloxy)phenyl)amine (1.4 g, 3.67 mmol), sodium tert-butoxide (480 mg, 5.00 mmol), P(*t*-Bu)₃ (250 μ L, 0.25 mmol) and tris(dibenzylideneacetone)dipalladium(0) (229 mg, 0.25 mmol) were mixed in dry toluene (32 mL) under an argon atmosphere in a schlenk tube. The reaction mixture was stirred at 90 °C for 3 days. Further purification by column chromatography (SiO₂, dichloromethane) afforded pure compound **18** (1.2 g, 69% yield) as a dark red solid.

¹H NMR (CDCl₃, 400 MHz, 300 K): δ = 8.02 (d, ³*J* = 9.4 Hz, 2H), 7.48 - 7.31 (m, 20H), 7.09 (d, ³*J* = 8.8 Hz, 8H), 7.00 (d, ³*J* = 8.8 Hz, 4H), 6.95 - 6.90 (m, 12H), 6.84 (d, ³*J* = 9.4 Hz, 2H), 5.05 (s, 8H);

¹³C NMR (CDCl₃, 100 MHz, 300 K): δ = 155.4, 154.2, 146.8, 140.9, 139.0, 137.6, 137.1, 128.7, 128.1, 127.6, 126.8, 125.7, 121.3, 119.6, 116.0, 115.9, 70.5;

ESI-MS: *m/z* calculated for C₇₀H₅₆N₄O₆ [M]⁺ 1048.42, found 1048.51

Compound 180Me



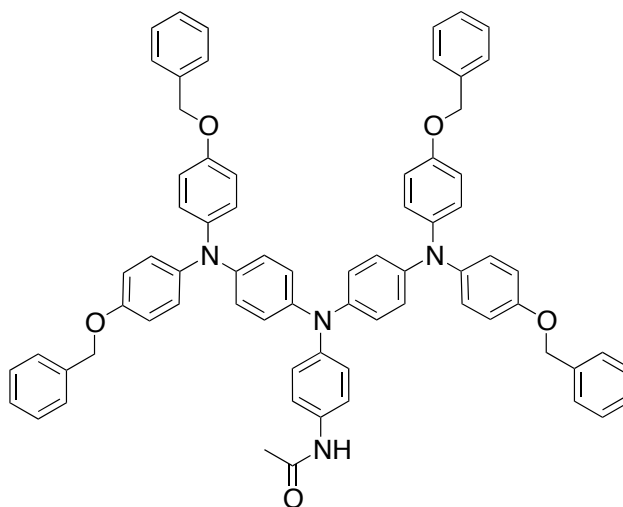
Brominated triarylamine precursor **17** (444 mg, 0.991 mmol), 4,4'-dimethoxydiphenylamine (500 mg, 2.18 mmol), sodium tert-butoxide (285 mg, 2.97 mmol), P(*t*-Bu)₃ (149 μ L, 0.149 mmol) and tris(dibenzylideneacetone)dipalladium(0) (136 mg, 0.149 mmol) were mixed in dry toluene (19 mL) under an argon atmosphere in a schlenk tube. The reaction mixture was stirred at 90 °C for 3 days. After which the reaction was cooled down, solvent evaporated under vacuum, and the product purified by column chromatography (SiO₂, dichloromethane) (457 mg, 62% yield) as a dark red solid.

¹H NMR (CDCl₃, 400 MHz, 300 K): δ = 8.00 (d, ³*J* = 9.0 Hz, 1H), 7.08 (d, ³*J* = 8.9 Hz, 8H), 6.96 (br s, 16H), 6.91 (d, ³*J* = 9.0 Hz, 2H), 6.85 (d, ³*J* = 8.9 Hz, 4H), 6.77 (d, ³*J* = 8.9 Hz, 4H), 3.71 (s, 12H),

¹³C NMR (CDCl₃, 100 MHz, 300 K): δ = 156.3, 154.2, 146.9, 140.7, 139.0, 137.5, 127.5, 126.9, 125.7, 121.0, 116.1, 115.0, 55.6

ESI-MS: *m/z* calculated for C₄₆H₄₀N₄O₆⁺ [M]⁺, 744.29; found 744.39

Compound 19Bn



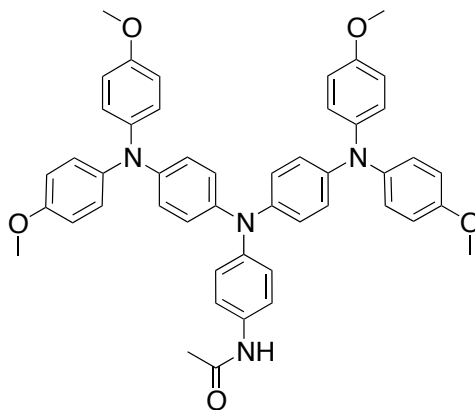
A solution of precursor **18** (1.2 mg, 1.14 mmol) and tin (II) chloride dihydrate (2.58 g, 11.4 mmol) was dissolved in a mixture of ethanol (20 mL) and acetonitrile (10 mL) and the reaction mixture was stirred overnight at reflux under an argon atmosphere. Afterwards, the solution was cooled down to room temperature and diluted with ethyl acetate (250 mL). The organic phase was washed with 1M NaOH (3 x 50mL), water (100 mL) and brine (100 mL), dried over Na₂SO₄ and concentrated under reduced pressure. The next reaction was setup directly by dissolving the crude amine product with triethylamine (247 μ L, 1.78 mmol) in dry dichloromethane (25 mL) and cooling down the reaction mixture to 0 °C with an ice bath. Acetyl chloride (125 μ L, 1.76 mmol) was added dropwise and the solution was left to warm up to room temperature and react for 3 hours. The reaction mixture was diluted with dichloromethane (300 mL), and the organic layer was washed with NaHCO₃ (sat.) (50 mL), brine (30 mL), and dried over Na₂SO₄. Concentration under reduced pressure afforded a reddish solid which was washed with acetone (30 mL), diethyl ether (10 mL) and dried under vacuum to give compound **19** (787 mg, 65% yield) as a grayish solid.

¹H NMR (DMSO-*d*₆, 400 MHz, 300 K): δ = 9.82 (s, 1H), 7.50 - 7.30 (m, 22H), 7.00 – 6.90 (m, 16H), 6.91 (d, ³*J* = 9.0 Hz, 2H), 6.85 (d, ³*J* = 8.9 Hz, 4H), 6.77 (d, ³*J* = 8.9 Hz, 4H), 5.04 (s, 8H), 2.00 (s, 3H);

¹³C NMR (DMSO-*d*₆, 100 MHz, 300 K): δ = 167.8, 154.3, 143.0, 142.8, 141.0, 140.8, 137.1, 133.9, 128.4, 127.8, 127.6, 125.5, 124.3, 123.2, 122.2, 120.3, 115.7, 69.5, 23.8;

ESI-MS: m/z calculated for C₇₂H₆₀N₄O₅ [M]⁺ 1060.46, found 1060.57.

Compound 190Me



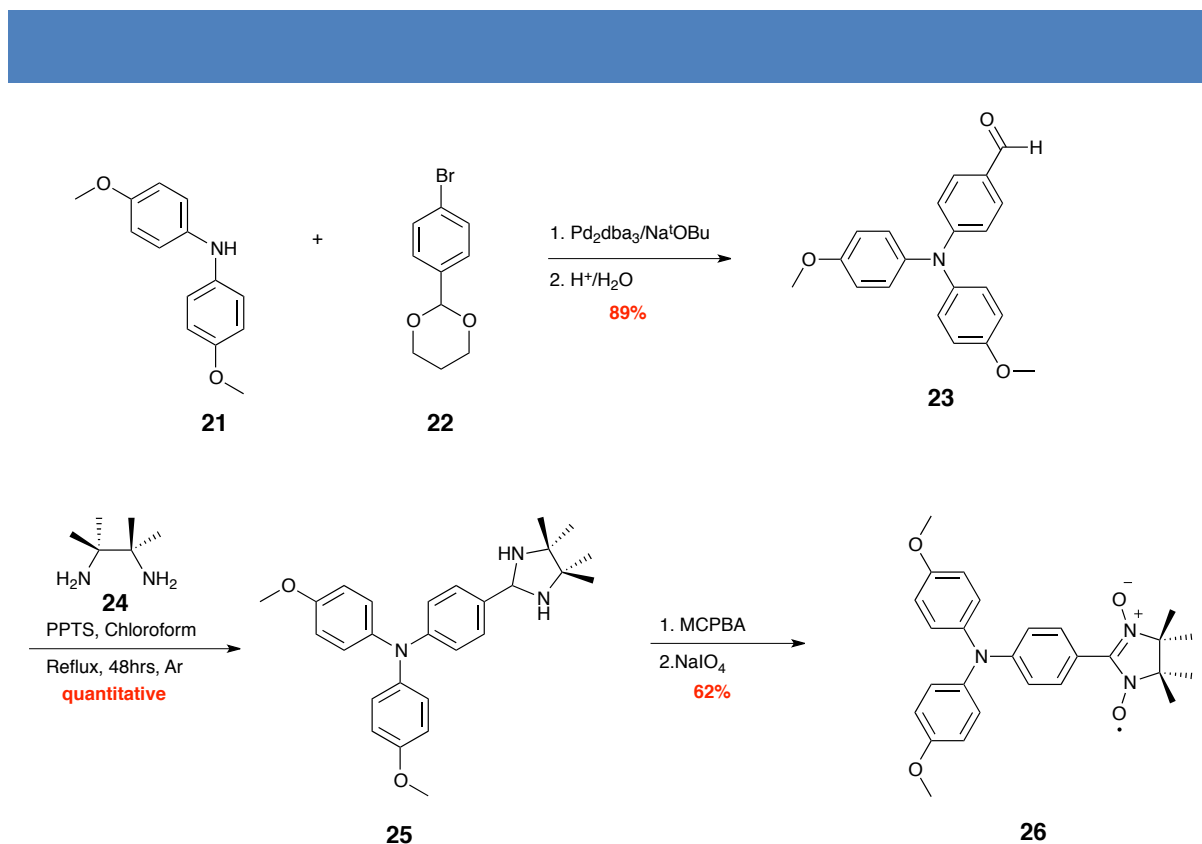
A solution of **18OMe** (290 mg, 0.406 mmol) and triethylamine (0.0846 mL, 0.609 mmol) in dry dichloromethane (10 mL) was cooled to 0°C with an ice bath and stirred for 5 minutes. Acetyl chloride (0.0434 mL, 0.609 mmol) was then added dropwise, and the mixture was allowed to stir overnight under argon atmosphere at room temperature. After that time the reaction mixture was diluted with DCM (100 mL), washed with NaHCO₃ (sat.) (2 x 25 mL), brine (2 x 25 mL), dried over Na₂SO₄ and the solvent removed under vacuum. The pure product **19OMe** was obtained after purification by column chromatography (SiO₂, cyclohexane/ethylacetate 9:1 → pure ethyl acetate) as a yellowish solid in 78% yield (239 mg, 0.316 mmol).

¹H NMR (DMSO-*d*₆, 400 MHz, 300 K): δ = 9.81 (s, 1H), 7.44 (d, ³*J* = 8.9, 2H), 6.96 (d, ³*J* = 9.0, 8H), 6.80-6.93 (m, 14H), 6.75 (d, ³*J* = 9.0, 4H), 3.71 (s, 12H), 2.00 (s, 3H).

¹³C NMR (DMSO-*d*₆, 100 MHz, 300 K): δ = 167.8, 155.2, 143.2, 142.8, 140.9, 140.6, 133.9, 125.6, 124.4, 123.0, 121.9, 120.3, 114.8, 55.2, 23.8.

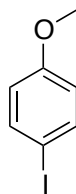
ESI-MS: m/z calculated for C₄₈H₄₄N₄O₅⁺ [M]⁺, 756.33; found 756.50

f. Triarylamine nitronyl nitroxide synthesis



Scheme S7 | Synthetic route to the methoxy substituted triarylamine-nitronyl nitroxide compound.

Compound 20

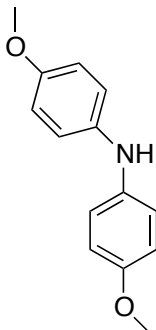


A solution of 4-iodophenol (5.64 g, 25.6 mmol), methyl iodide (3.04 g, 21.4 mmol) and K_2CO_3 (17.7 g, 128.4 mmol) in acetone (120 mL) was heated to reflux for 8 hours. Then, the reaction mixture was diluted in diethylether (200 mL) and the organic phase was washed with 1M KOH (2 x 200 mL), followed by a brine wash (200 mL), and finally concentrated under reduced pressure to afford compound **20** (4.84 g, 99% yield) as white crystals .

$^1\text{H NMR}$ (CDCl_3 , 400MHz, 300K) δ = 7.56 (d, $^3J = 9.0$ Hz, 2H), 6.68 (d, $^3J = 9.0$ Hz, 2H), 3.78 (s, 3H)

ESI-MS: m/z calculated for C₇H₇BrO [M]⁺ 185.97, found 186.13

Compound 21



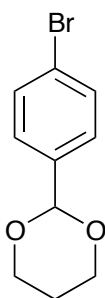
4-aminoanisole (687.4 mg, 5.45 mmol) and 4-iodoanisole (1.92 g, 8.18 mmol) were dissolved in DMSO (25 mL) in a Shlenk tube. Copper iodide (215 mg, 1.09 mmol), L-proline (250 mg, 2.18 mmol), and K₂CO₃ (2.28 g, 16.4 mmol) were then added under Argon. The reaction mixture was heated to 90°C for 2 days, after which the reaction mixture was poured over a pad of silica gel and then purified by column chromatography (SiO₂, cyclohexane → cyclohexane/ethyl acetate 3:1) to give compound **21** (1.12 g, 87% yield) as a white powder .

¹H NMR (CDCl₃, 400 MHz, 300 K): δ = 6.93 (d, ³J = 9.0 Hz, 4H), 6.82 (d, ³J = 8.9 Hz, 4H), 3.79 (s, 6H);

¹³C NMR (CDCl₃, 100 MHz, 300 K): δ = 154.4, 138.1, 119.7, 114.9, 55.8;

ESI-MS: m/z calculated for C₁₄H₁₅NO₂ [M]⁺ 229.11 , found 229.29

Compound 22



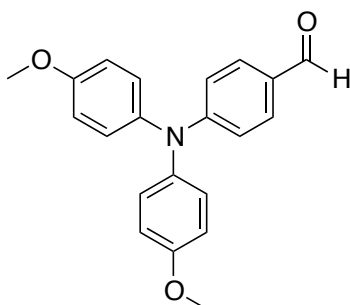
The reaction carried out with a Dean-Stark apparatus. Briefly, 4-bromobenzaldehyde (2.06 g, 11.1 mmol) was dissolved in toluene (100 mL) and then 1,3-propanediol (2.41 mL, 33.4 mmol) and *p*-toluenesulfonic acid (103 mg, 0.54 mmol) were added sequentially. The reaction mixture was then stirred at reflux for 24 h. After cooling to room temperature, the reaction mixture was washed using 1M NaOH (2x 300 mL) and the organic phase was dried over Na₂SO₄. Concentration in vacuo provided compound **22** (2.61 g, 97% yield) as a white powder.

¹H NMR (CDCl₃, 400 MHz, 300 K): δ = 7.49 (d, ³J = 8.5 Hz, 2H), 7.36 (d, ³J = 8.5 Hz, 2H), 5.46 (s, 1H), 4.28 – 4.24 (m, 2H), 4.01 – 3.94 (m, 2H), 2.27 – 2.15 (m, 2H);

¹³C NMR (CDCl₃, 400 MHz, 300 K): δ = 137.8, 131.3, 127.8, 122.8, 100.8, 67.3, 25.7;

ESI-MS: m/z calculated for C₁₀H₁₁BrO₂ [M+H]⁺ 242.99, found 243.21

Compound 23



Under argon, Pd₂dba₃ (201 mg 0.22 mmol) and tert-butyl phosphine (0.22 mL, 0.22 mmol) were dissolved and stirred in toluene (5 mL) for 10 min. bis-methoxydiarylamine **21** (1.0 g,

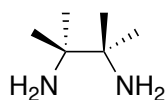
4.36 mmol), protected 4-bromobenzaldehyde **22** (3.08 g, 10.9 mmol) and sodium tert-butoxide (4.19 g, 43.6 mmol) were then added to the reaction mixture which was stirred at 100°C for 24 h. After cooling to room temperature, the reaction mixture was run through a silica plug (100% ethyl acetate). The eluted product was then stirred with 1M HCl (100 mL) for 5 min and then extracted with ethyl acetate (200 mL). After concentration under vacuo, the resulting crude product was purified by column chromatography (SiO₂, 10:1 cyclohexane:ethyl acetate) to provide compound **23** (1.29 g, 89% yield) as an oil.

¹H NMR (CDCl₃, 400 MHz, 300 K): δ = 9.76 (s, 1H), 7.63 (d, ³J = 8.6 Hz, 2H), 7.13 (d, ³J = 8.9 Hz, 2H), 6.89 (d, ³J = 8.9 Hz, 2H), 6.85 (d, ³J = 8.8 Hz, 2H), 3.82 (s, 6H);

¹³C NMR (CDCl₃, 100MHz, 300K) δ = 190.3, 157.4, 154.1, 138.8, 131.1, 128.0, 126.7, 116.7, 115.0, 55.5

ESI-MS: m/z calculated for C₂₁H₁₉NO₃ [M+H]⁺ 334.14, found 334.17

Compound 24

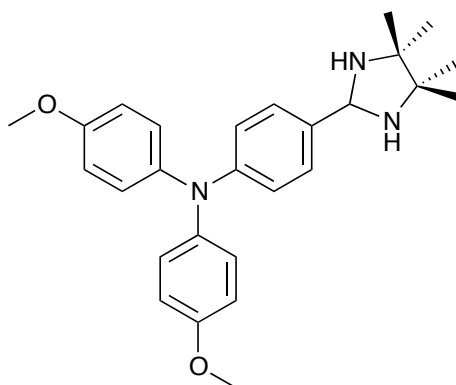


A solution of 2,3-dinitro-dimethyl butane (507 mg, 2.9 mmol) in concentrated HCl (10 mL) was heated to 50°C under argon. Then, tin powder (2.8 g, 23.6 mmol) was added gradually and the mixture heated to reflux over 2 hours. Afterwards, the reaction was cooled to room temperature and solid NaOH (5 g) was added until the solution became strongly basic. Water (50 mL) was then added to the reaction flask and the product steam distilled (product boiling point = 157°C). Further coevaporation with pentane afforded pure compound **24** (313 mg, 93% yield) as a white powder which was readily identifiable by ¹³C NMR.

¹H NMR (CDCl₃, 400 MHz, 300 K): δ = 1.07 (s, CH₃), 1.26 (brs, NH₂)

¹³C NMR (CDCl₃, 100MHz, 300K) δ = 54.8, 26.4

Compound 25

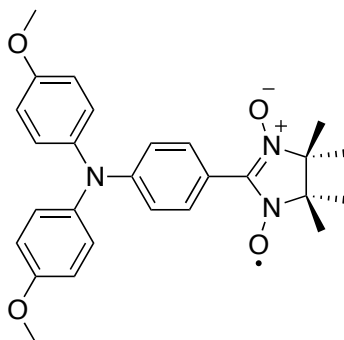


A solution of triarylamine-aldehyde precursor **23** (140 mg, 0.42 mmol), pyridinium p-toluenesulfonate (11 mg, 0.042 mmol) and 2,3-diamino-dimethyl butane (146 mg, 1.26 mmol) in chloroform (40 mL) was stirred under argon at 60°C for two days. The reaction mixture was then dried down under vacuo and the crude product was purified by column chromatography (SiO₂ basified with triethylamine, cyclohexane/ethyl acetate 4:1) to yield compound **25** as a sticky yellow solid which was taken directly into the oxidation reaction.

¹H NMR: (CDCl₃, 400 MHz, 300 K): δ = 7.34 (d, ³J = 8.3 Hz, 2H), 7.02 (d, ³J = 8.9 Hz, 4H), 6.90 (d, ³J = 8.6 Hz, 2H), 6.81 (d, ³J = 9.0 Hz, 4H), 5.11 (s, 1H), 3.79 (s, 6H), 1.25 – 1.15 (m, 12H)

ESI-MS: m/z calculated for C₂₇H₃₃N₃O₂ [M+H]⁺ 432.26, found 432.37

Compound 26



A biphasic mixture of the cyclic aminal **25** (0.42 mmol) in CH₂Cl₂ (15 mL) and a saturated solution of NaHCO₃ (15 mL) was cooled down to 0°C, and further treated with a solution of

MCPBA (282 mg, 1.26 mmol) in dichloromethane (30 mL). After one hour, an aqueous solution of NaIO₄ (1.8 mmol in 3 mL H₂O) was added and the reaction allowed to stir for 2 more hours. Afterwards, the reaction mixture was extracted with dichloromethane (100 mL), the resulting organic phase was washed with H₂O (2 x 100 mL) and concentrated under vacuum. Further purification by column chromatography (SiO₂ basified with triethylamine, cyclohexane → cyclohexane/ethyl acetate 3:1) followed by crystallization from acetonitrile to provide compound **26** (99 mg, 61% yield over 2 steps) as purple needles.

MS (ESI): M+2H⁺ calculated: 462.2, found 462.38

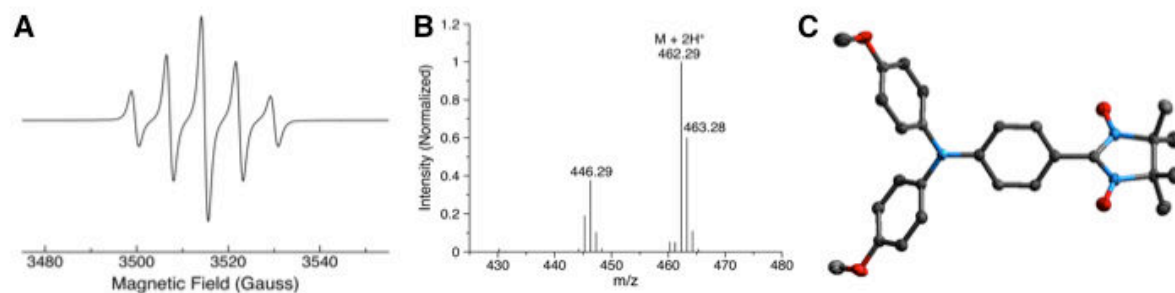
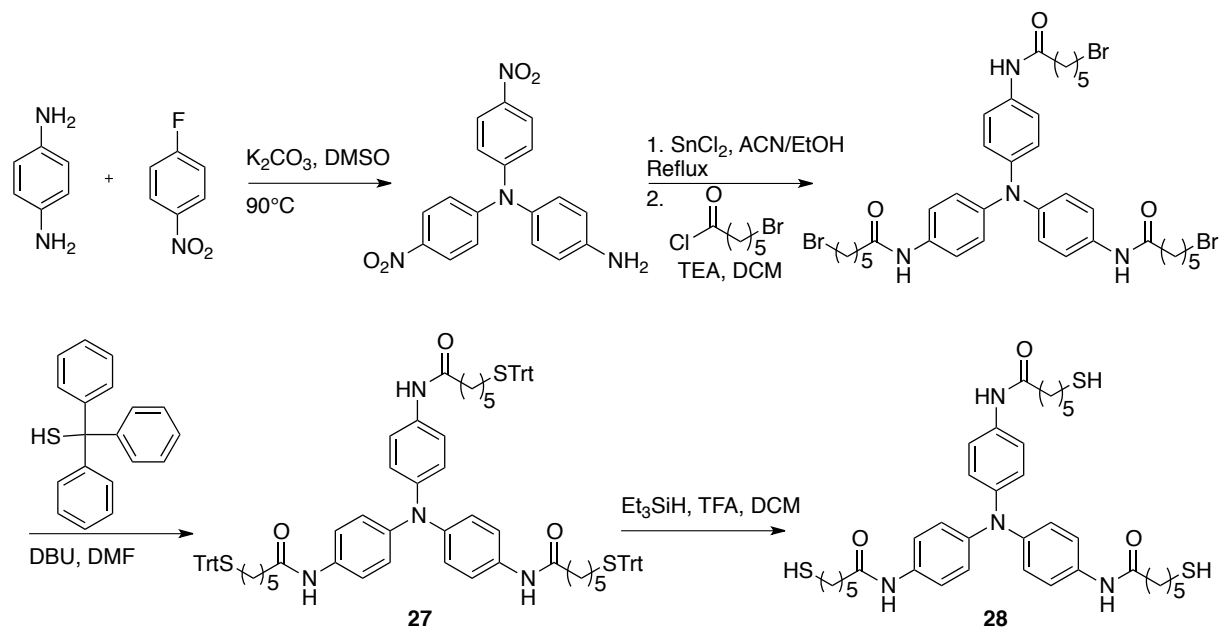


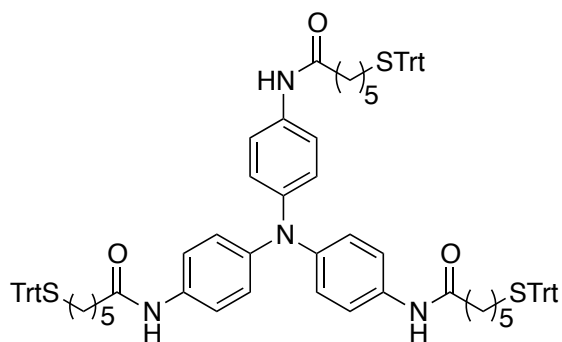
Figure S2 | EPR signal with the typical five-line pattern of nitronyl nitroxides (a). Mass spectrometry trace showing the M+2H⁺ peak and the oxygen fragmentation peak (b). Crystal structure of the TAA-NN molecule (c).

g. Thiolated tris-amide triarylamine synthesis



Scheme S9 | Synthetic route to tris-amide thiol triarylamine (TATASH).

Compound 27



Triarylamine intermediate **10** (500 mg, 0.61 mmol) and DBU (0.359 mL, 2.4 mmol) were dissolved in DMF (40 mL). Triphenylmethanethiol (672 mg, 2.4 mmol) was then added and the reaction mixture was heated to 35°C and allowed to react overnight. The next day, the reaction mixture was dissolved in ethyl acetate (400 mL), and the organic layer was washed with water (3 x 120 mL), with brine (1 x 120 mL), dried over sodium sulfate and further concentrated under vacuum. The crude product was loaded on a silica column and washed

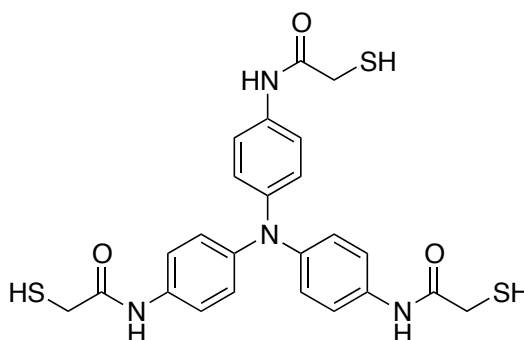
with cyclohexane and ethyl acetate. The product was retrieved from the top of the column, dissolved in a mixture of methanol and toluene and the solution filtered, providing compound **5** (731 mg, 86% yield) as a white powder.

¹H NMR (5:3 MeOD:Toluene, 400MHz, 300K) δ = 7.59 (d, ³J = 8.7 Hz, 6H), 7.51 (d, ³J = 7.5 Hz, 18H), 7.16-7.06 (m, overlap with toluene), 7.04 (d, ³J = 8.9 Hz, 6H), 2.27-2.20 (m, 12H), 1.57-1.48 (m, 6H), 1.46-1.38 (m, 6H), 1.36-1.30 (m, 6H)

¹³C NMR (5:3 MeOD:Toluene, 100MHz, 300K) δ = 173.5, 146.3, 145.1, 134.7, 130.6, 128.6, 127.4, 125.0, 122.2, 67.5, 37.6, 32.7, 29.5 (m), 26.3

ESI-MS: m/z calculated for C₉₃H₉₀N₄O₃S₃ [M+H]⁺ 1408.62, found 1408.47

Compound 28



Deprotection of trityl intermediate **5** was performed on a small scale the same day as monolayer formation in order to avoid unwanted oxidation of the thiol groups. It is critical to perform the purification under an inert atmosphere to avoid oxidation of the free thiols. First, compound **3** (5 to 20 mg) was placed inside a round bottom flask under Argon in dichloromethane (5 mL, filtered over basic alumina) along with triethylsilane (0.5 mL) and trifluoroacetic acid (1 mL). The solution was stirred for 1 hr. at room temperature, and the contents protected from light. The solvent was then removed under vacuum and the flask backfilled with argon. The contents were then dissolved in a 3:1 mixture of cyclohexane:ethyl acetate (5 mL) and the solution loaded on top of a silica column. After washing the column with at least 2 column volumes (min. 10 mL), the product was retrieved from the top of the column and dried. It was then dissolved in methanol (5 mL) and run

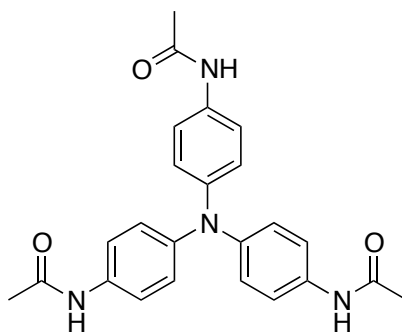
through a column filled with neutral alumina. For each deprotection, the purity of the product was checked by LC/MS and ^1H NMR. A molar absorptivity coefficient of $1940\text{ M}^{-1}\text{ cm}^{-1}$ was determined for the absorption maximum at 322nm and was used to adjust the concentrations for the subsequent monolayer deposition procedure (chapter 7).

^1H NMR (MeOD, 400MHz, 300K) δ = 7.42 (d, ^3J = 8.9 Hz, 6H), 6.96 (d, ^3J = 8.9 Hz, 6H), 2.52 (t, ^3J = 7.2 Hz, 6H), 2.37 (t, ^3J = 7.1Hz, 6H), 1.68-1.62 (m, 12H), 1.52-1.42 (m, 6H)

ESI-MS: m/z calculated for $\text{C}_{36}\text{H}_{48}\text{N}_4\text{O}_3\text{S}_3$ $[\text{M}]^+$ 680.29, found 680.49

h. TSOF Synthesis

Compound 29



Compound **5** (5.0 g, 14.3 mmol) was reduced with tin (II) chloride (32 g, 143 mmol) in a mixture of 300 mL acetonitrile and 360 mL ethanol by refluxing overnight under argon. The next day, the reaction was allowed to cool and then it was diluted with ethyl acetate (500 mL) and washed with Na_2CO_3 (2 x 300 mL) and a brine solution (2 x 300 mL) before being dried over Na_2SO_4 . The brownish-red tris-amine intermediate was recovered after removal of solvent in vacuum. 1.0 g (3.44 mmol) of this intermediate was then dissolved in 100 mL of dichloromethane along with 1.98 mL (14.2 mmol) of triethylamine under argon. This mixture was stirred inside of an ice bath and acetyl chloride (1.01 mL, 14.2 mmol) was added dropwise. The next day, the reaction was diluted with diethylether (500 mL), washed with 1M HCl (2 x 200 mL) and brine (2 x 200 mL), dried over Na_2SO_4 before concentrating under reduced pressure. The material is then concentrated with celite and loaded on a silica column, which is subsequently washed with cyclohexane and ethyl acetate. The pure product is

retrieved from the top of the column, dissolved in methanol:toluene (5:3, 200 mL), filtered, dried under reduced pressure, brought up in ether (300 mL) and washed with water (2 x 200 mL.). The final product is obtained as an off-white powder after concentrating under reduced pressure for an 87% yield (1.03 g, 1.24 mmol). Crystallization was performed by first dissolving 75 mg in 10.5 mL of methanol and 3.4 mL of toluene and then letting the solution slowly evaporate at room temperature over a week to afford colorless rod-shaped crystals.

^1H (DMSO, 400MHz, 293K) δ = 9.95(s, 3H), 7.46 (d, $^3J=8.9\text{Hz}$, 6H), 6.87 (d, $^3J=8.8\text{Hz}$, 6H), 2.01 (s, 9H)

^{13}C NMR (DMSO, 100MHz, 295K) δ = 167.8, 142.7, 134.2, 123.5, 120.3, 23.8

MS (ESI) calculated for $\text{C}_{24}\text{H}_{24}\text{N}_4\text{O}_3$: 416.18 (M^+); found: 416.38

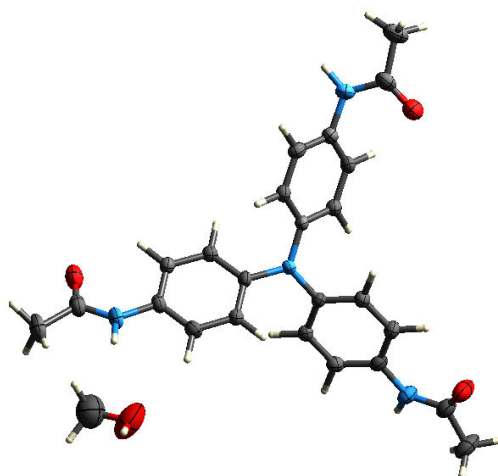


Figure S3 | Crystal structure of 29.

3. Procedures specific to chapter 2

EPR studies

For compound **4**⁺, a band with an interline distance of $A_h = 8.1$ Gauss, a width of 40 Gauss and a g factor of 2.0037 (3520 Gauss). The number of spins was determined by comparing with a TEMPO standard as a reference, where an intensity of 1.22×10^{14} for a concentration of 1 mM was determined. The standard EPR protocol involved first taking an EPR of the non-irradiated solution to insure that there was no radical present. Then each solution was irradiated using a 20W halogen lamp (intensity = 0.06 W/cm^2) for a specified period of time as described in the text and an EPR spectrum recorded (1-2 min in the dark). All of the irradiation time periods were added in order to determine the total time. After irradiation for the maximum amount of time ($t = 3765$ s), each solution was stored in the dark and an EPR spectrum recorded periodically in order to follow the radical decay kinetics.

NMR studies

Kinetics studies by NMR were performed by adding a certain mol % of oxidant or seeds, (or irradiating with a pulse of light) to an NMR tube containing neutral **4** at a concentration of 10mM, and then placing the NMR tube in the NMR and taking periodic NMR scans (4 scans at a time, with $t = 0$ corresponding to the time of oxidant addition).

UV/VIS/NIR studies

Solutions of the non self-assembled triarylamine in four different chlorinated solvents (chloroform, dichloromethane, tetrachloroethane, and carbon tetrachloride) were prepared at 1 mM. A scan was recorded before irradiation to insure the absence of oxidation. Each solution was then irradiated for set time intervals using the standard 20 W halogen lamp. After $t = 3765$ s, each solution was stored in the dark and a spectrum recorded every 30 min over several days.

AFM studies

Samples were prepared by irradiating a solution of **4** and then removing the solvent under rotary evaporation at 40°C.

XRD studies

X-ray diffraction patterns were recorded on different lines with the same samples contained in a 1 mm thick Lindemann capillary or in a sealed cell of 1 mm thickness with mica windows. The scattering window from 300 Å to 3 Å was investigated with the combination of 3 lines using a linear focalized monochromatic Cu-K_{α1} beam obtained from a sealed-tube generator (600 W) equipped with a bent quartz monochromator: the patterns were recorded with an Inel CPS120 detector and with phosphor imaging screens. Imaging plates were scanned with a Storm 820 scanner and profiles were generated with ImageJ.

Samples were prepared from 10 mM solution of freshly purified **4** in chloroform which had been irradiated for 1 hr which were then analyzed by powder X-ray diffraction. Attempts to grow single crystals were unsuccessful.

Sonication studies

A solution of the non self-assembled triarylamine at 0.1 mM was prepared and irradiated with a 20 W halogen lamp for 1 hr. The initial UV/Vis spectrum was recorded and the sample was further sonicated in the absence of light in intervals over a sonication stage of 3600 s.

Seeding studies

A solution of non self-assembled triarylamine at 1mM was prepared and irradiated with a 20 W halogen lamp for 4065 s. At the end of the irradiation time, a defined quantity of the irradiated solution was added to the non self-assembled sample and NMR spectra were recorded until the aromatic signals became completely flat.

Modelling

Computational modeling was performed using HyperChem 7.5. First, the geometry was optimized using either the semi-empirical PM3 algorithm or with *ab initio methods*

(STO-3G). Ensembles of molecules were then optimized using the Amber96 molecular mechanics algorithm with a dielectric constant of 2.2 chosen for the medium.

4. Procedures specific to chapter 6

Organogelation

Tube inversion experiments were carried out inside a screw cap vial with 1 mL of solvent. The reported values are an average from three separate trials. Differential Scanning Calorimetry (DSC) was carried out using a Setaram micro DSC III inside a sealed sample capsule. The scan rate was 1.0 °C/min between 0 °C and 55 °C. The reported data comes from the second scan cycle.

X-ray scattering

Thin films of TATA **1** were prepared from chloroform solutions (4 mg/mL) drop cast onto a mica surface. In the case of the irradiated thin-film, irradiation was performed in solution for 15 minutes prior to drop casting. Measurements were performed in a Bruker Nanostar.

5. Gold Nanoparticle Synthesis and Functionalization Procedures

13 nm Gold Nanoparticle Synthesis

Gold nanoparticles were prepared according to the standard procedure of Turkevich and Frens.¹⁶³ Before starting all glassware was cleaned with aqua regia and rinsed thoroughly with milli-q water. Then, 39.4mg of HAuCl₄ (trihydrate form, 3H₂O) was dissolved in 90mL of milli-q water and brought to a rolling boil. Under vigorous stirring, a solution of trisodium citrate (dihydrate, 102.9mg in 10mL of milli-q water) was added all at once. The mixture was further heated for 10 minutes, before allowing the suspension to cool to room temperature. The solution volume was adjusted to 100mL with milli-q water and the final suspension stored in a clean glass bottle. TEM characterization revealed an average size of 12.83 nm ± 1.27 nm.

¹⁶³ Turkevich, J.; Stevenson, P. C.; Hillier, J.,. *Discussions of the Faraday Society* 1951, 11 (0), 55-75.

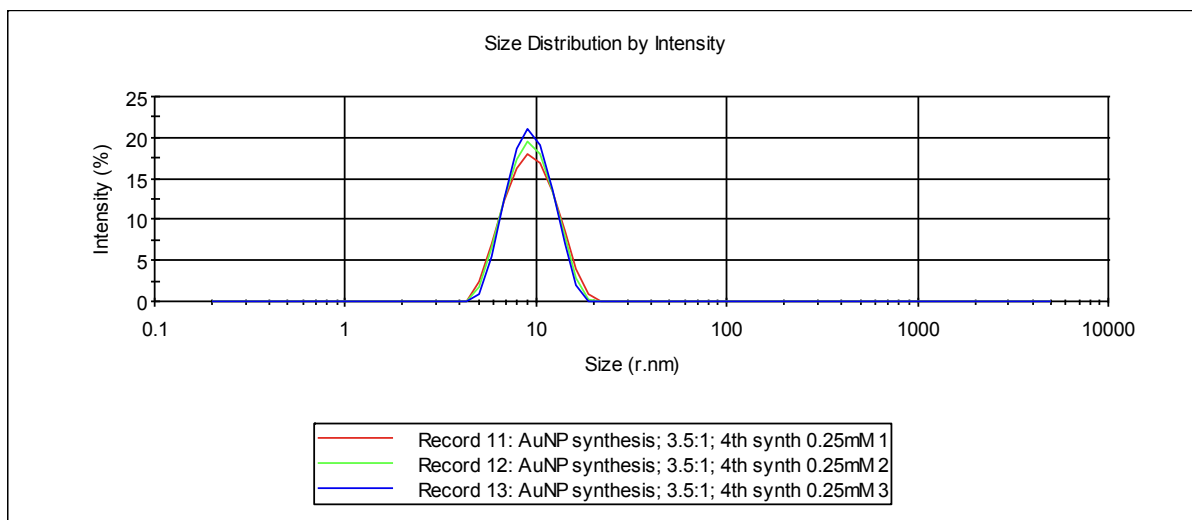


Figure 117 | Particle size of synthesized gold nanoparticles taken by dynamic light scattering (zetasizer nano). Average radius = 8.95 nm, PDI = 0.05.

Preparation of plasmonic substrates

50 μL of polystyrene-poly-2-vinylpyridine (PS-P2VP; 5 mg/mL in *o*-xylene) was spin-coated onto either glass or silicon substrates at 4000 RPM. The substrates were then placed inside a closed 500 mL container suspended above 10 mL of *o*-xylene for 24 hours, with the temperature maintained at 23°C. Next, the substrates were incubated in a solution of 13 nm gold nanoparticles (synthesized from a 1 mM HAuCl_4 solution) for 2.5 hours. The substrates were then rinsed twice with milli-Q water (5 minute incubations). This was followed by oxygen plasma treatment for 20 minutes. The cleaned substrates were then incubated in a 10 μM MeOH solution of **2** for 1 hour under argon. Afterwards, the solution was removed and the substrates rinsed with methanol twice (5 minutes incubations) before being dried under a stream of argon. The connected nanoclusters were prepared by incubating the substrates for 24 hours in a 1 mM chloroform solution of **1** under argon. Doped fibers of **1** were prepared by irradiating the chloroform solution for 10 minutes with a 20 W halogen lamp placed 5 cm from the sample vial. Undoped substrates were protected from light throughout the incubation process. The solution was removed by tilting the glass vial containing the substrates at a 30° angle and pipetting off the chloroform. Washing was performed by incubating the substrates for 5 minutes in fresh chloroform solution.

Preparation of ordered plasmonic assemblies at a liquid-liquid interface

The biphasic system is setup in a cylindrical screw-cap vial with a diameter of 1.2cm. 1mL of aqueous nanoparticle solution and 1 mL of TATA chloroform solution (pre-irradiated for 1 hr. with a 20W halogen lamp placed 5 cm from the sample) is then added to the vial. The interface forms at a height of 0.8 cm above the bottom of the vial. The sample is then centrifuged in a swinging bucket rotor for 1hr. The rotation speed is adjusted for the appropriate RCF according to the following formula:

$$RCF = 11.18 * r * \left(\frac{Q}{1000}\right)^2$$

where RCF is the relative centrifugal force in units of 'g' (gravitational acceleration), r is the radius from the center of the centrifuge to the interface, and Q is the speed of rotation in RPM. The samples are then transferred to a TEM grid by gently placing the grid on top of the interface and lifting up. Passing through the interface and then removal will result in multiple layers.

6. Density Functional Theory Calculations

a. DFT calculations from chapter 5

Geometry optimizations were carried out using spin-polarized unrestricted density functional theory (UB3LYP) with the 6-311G(d,p) basis set on the uncharged and charged triplet states. Frequency calculations, stability checks, as well as population analysis were performed using these geometries. Single-point energy calculations were performed with the larger 6-311++G(d,p) basis set for the purposes of calculating the coupling constants. The singlet state energies were found using the broken symmetry approach described in chapter 5, where the “stable=opt” and “guess=mix” keywords were invoked.

b. DFT calculations from chapter 6

All calculations were performed with the M062X functional using the 6-31G(d) basis set and carried out with Gaussian 09.² The M062X functional is a hybrid DFT functional that has

been shown to effectively model non-covalent interactions.³ Geometry optimizations were performed on the single molecule (neutral and radical cation), the stacked dimer (neutral and radical cation), and a stacked trimer (radical cation). The alkyl chains were omitted during calculations.

The *reorganization energy* (λ) was calculated using the energy of the monomers:⁴

$$\lambda = E^{+n} - E^{++} + E^{n+} - E^{nn}$$

where E^{+n} is the energy of the cation in the geometry of the optimized neutral species, E^{++} is the energy of the cation in its optimized geometry, E^{n+} is the energy of the neutral species in the geometry of the optimized cation, and E^{nn} is the energy of the neutral monomer in its optimized geometry.

The *electronic coupling* (V) was calculated using the energy splitting-in-dimer method, involving the energies of the HOMO and HOMO-1 orbitals of the neutral dimer:⁵

$$V = 1/2(E_{\text{HOMO}} - E_{\text{HOMO-1}})$$

The *interaction energy* for the dimer species was performed using the counterpoise correction to correct for the basis set superposition error commonly found in DFT calculations of molecular ensembles. Single-point interaction energies were computed for the optimized radical cation dimer while varying the stacking distance and the dihedral angle between the two molecules. For the dimer, the binding energy was found by:

$$\Delta E_{\text{D}} = E_{\text{D_BSSE}} - 2 * E_{\text{monomer}}$$

Calculations gave the following energies:

$$E_{\text{D_BSSE}} = -2746.389364305202 \text{ hartrees}$$

$$E_{\text{monomer}} = -1373.1775961 \text{ hartrees}$$

$$\Delta E_{\text{D}} = \mathbf{-89.72 \text{ KJ/mol}}$$

The binding energy of the radical cation dimer was calculated by:

$$\Delta E_{\text{D_cation}} = E_{\text{D_cation_BSSE}} - (E_{\text{monomer}} + E_{\text{monomer_cation}})$$

Calculations gave the following energies:

$$E_{\text{D_cation_BSSE}} = -2746.191729235972 \text{ hartrees}$$

$$E_{\text{monomer}} = -1373.1775961 \text{ hartrees}$$

$$E_{\text{monomer_cation}} = -1372.9553626 \text{ hartrees}$$

$$\Delta E_{\text{D_cation}} = \mathbf{-154.30 \text{ KJ/mol}}$$

The *frontier orbitals* were calculated as follows: the HOMO was taken from the neutral

monomer calculation, and the band gap was taken from the first excitation energy from time-dependent DFT calculations.⁶

c. TATA optimized geometry coordinates

Neutral Monomer - M062X/6-31G(d)

```
1\1\GINC-HPC-N261\FOpt\RM062X\6-31G(d)\C24H24N4O3\ARMAO\26-Sep2013\0\#nM
062X/631G(d)Optintegral=ultrafineguess=readgeom=checkpoint\C10TTAA_monomer_M06
2X_631GdOptUF\0,1\H,4.0796923428,7.6764717737,0.0715183067\H,2.5762696341,7.940
2892495,0.9618199927\C,3.0223455178,7.413795548,-0.1127586285\H,2.5277795699,7.746
0245863,0.8034101399\C,2.9132875461,5.9181044526,-0.3489866453\O,3.7058828919,5.32
17268147,-1.0523182477\H,1.2533034423,5.9315102362,0.8291629136\N,1.8389363972,5.3
282683606,0.2690485499\H,2.9514093746,3.2643053006,-1.1250135154\C,1.4279413812,3.
9815092132,0.2132389647\C,2.0818103592,3.0007967405,-0.5406699145\C,0.2993107992,3
.6220351353,0.9577607825\H,-0.2152142261,4.3735749471,1.5525346628\C,1.5947999636,
1.6992635654,-0.5464170624\H,2.0980360103,0.9466105462,-1.1455144295\C,0.166954377
9,2.3171875641,0.9652581733\C,0.4741297968,1.3331581062,0.2048170633\H,2.296078895
8,-0.1313808059,1.560828743\H,3.8923436358,2.0035754686,1.5556607955\C,2.088469227
,-1.015910088,0.9671643129\H,1.0383410686,2.0550512391,1.5567801974\C,2.9851344358
,-2.0722603895,0.9593660527\N,-0.0000365657,0.0000353901,0.1995143782\C,0.91693543
59,-1.0776244085,0.2046983724\H,5.5945136925,-6.1933104589,-0.9616480042\H,-1.86656
01844,1.3366821117,-1.1554683057\O,2.7604102643,-5.8668745827,-1.0621685702\C,2.733
2834344,-3.2278813411,0.2121131806\C,3.6705047997,-5.4804562542,-0.3544195369\N,3.6
943318884,-4.256929258,0.2673109946\C,49112279021,-6.3224505672,-0.1169467278\C,-2.
2679067723,0.5277252519,-0.5527631558\C,0.6743742365,-2.2299267276,-0.5486745143\C
,-1.39178666 57,-0.2559172476,0.203850746\C,1.5580830424,-3.3024665487,-0.543705400
4\H,4.5070890541,-4.0533377391,0.8316755333\H,5.4410069435,-6.0650014459,0.8035940
083\H,4.6112483709,-7.3700846242,-0.0835629784\H,-0.22819336,-2.2881214952,-1.14921
92966\C,-3.6385126456,0.2985195149,-0.5479235807\H,-4.300823762,0.9164217099,-1.136
6430262\H,1.3525595502,-4.186085796,-1.1303742795\C,-1.9242440897,-1.2991341509,0.9
691380459\H,-1.2620535825,-1.9192161675,1.5649689556\C,-4.1618385172,-0.7540857184
,0.2110407544\C,-3.2873640144,-1.5477848837,0.9612480231\N,-5.5335883909,-1.0717623
88,0.266139555\H,-3.6818311293,-2.3657613834,1.5601190088\O,-6.4600961436,0.541872
2302,-1.0640633446\H,-5.7640500432,-1.8765306835,0.8316344795\C,-6.5809830064,-0.43
92692747,-0.3560318149\H,-7.9716712427,-1.6851726265,0.798681669\C,-7.9313031267,-1
.0907953147,-0.1174822462\H,-8.6863365376,-0.3053623489,-0.0753699986\H,-8.16630788
81,-1.7397349165,-0.9663875897\Version=AM64L-G09RevB.01\State=1-A\HF=-1373.1775
961\RMSD=5.635e-09\RMSF=2.672e-05\Dipole=-0.0071403,0.0014371,2.2170849\Quadrup
ole=6.5250483,6.5151101,-13.0401584,-0.0380487,-0.0385127,-0.059168\PG=C01
[X(C24H24N4O3)]\@
```

Radical Cation Monomer – M062X/6-31G(d)

```
1\1\GINC-HPC-N294\FOpt\UM062X\6-31G(d)\C24H24N4O3(1+,2)\ARMAO\2
```

5-Sep-2013\0\#n M062X/6-31G(d) Opt integral=ultrafine guess=read
geom=checkpoint\C10-TTAA_monomer_cation_M062X_6-31GdOptUF\1,2\H,-7.12275065
97,-4.9430079369,-0.5909998016\H,-5.6415482219,-5.9287369656,-0.5193294956\C,-6.1531
513718,-5.0529614445,-0.1083432014\H,-6.2974899572,-5.2115409149,0.96472107\C,-5.34
98616147,-3.7990179681,-0.3634122589\O,-5.7458164961,-2.8641057046,-1.0193165489\H,
-3.8598348975,-4.6464402611,0.769991606\N,-4.0866964515,-3.8171634303,0.2351611674\
H,-4.1302740093,-1.4601805297,-1.1152735642\C,-3.1083363126,-2.8387184886,0.1963610
507\C,-3.237250358,-1.6403395282,-0.5355328744\C,-1.9253050262,-3.0700177546,0.9283
19941\H,-1.8235106644,-3.9830551141,1.5079920309\C,-2.2118782058,-0.7155432961,-0.5
202880763\H,-2.3029401059,0.1921164528,-1.1081888148\C,-0.9027204122,-2.1474326566
,0.9370173456\C,-1.0347200398,-0.9499820533,0.2108169593\H,-2.0099643653,1.17145027
72,1.5275903 13\H,-2.5359883752,3.5703040402,1.512747062\C,-1.4071047563,1.8554827
602,0.9395647832\H,-0.0086934573,-2.3286578469,1.5243752814\C,-1.6951
845966,3.2023062999,0.9316813447\N,0.0004652014,0.0000853294,0.2142734678\C,-0.305
049842,1.3716757984,0.2115843897\H,-2.3166219431,7.8501237735,-0.5117516949\H,0.98
6518997,-2.0908966732,-1.1075183102\O,0.3894505805,6.4091860545,-1.0183893644\C,-0.
9047654147,4.1115492653,0.1986686873\C,-0.6171115059,6.5332175994,-0.3607361842\N,
-1.2632377969,5.4479893573,0.2383823137\C,-1.3011560489,7.8556327067,-0.1037917824\
C,1.7267458143,-1.5580419511,-0.5193855428\C,0.4851218844,2.2741883211,
-0.5206097535\C,1.3408153329,-0.4210987815,0.211142995\C,0.1964257605
,3.6245200527,-0.5351724112\H,-2.093948495,5.6658149193,0.7747360672\
H,-1.3632028678,8.0598856226,0.9694721975\H,-0.7228296725,8.64056783
87,-0.5881268288\H,1.3158773554,1.8995168979,-1.1098862106\C,3.040292
0576,-1.9837290597,-0.5337248057\H,3.3311016736,-2.8475017146,-1.11285
24762\H,0.7977241485,4.3081297163,-1.115822847\C,2.3115517849,0.29237
90128,0.9373371101\H,2.0212091616,1.1575024156,1.5241590555\C,4.0132686981,-1.2726
901018,0.1984928014\C,3.6217757548,-0.1320299005,0.9295
803231\N,5.3497124153,-1.6309539666,0.2383372393\H,4.3613257706,0.41
28477287,1.5093994104\O,5.3539683065,-3.5459384592,-1.0136419619\H,5.
9542949898,-1.0194706331,0.7729209581\C,5.9655896323,-2.7348736412,-0.
3585507714\H,7.6621056384,-2.8480669688,0.9704090729\C,7.453054024,-2.8035601608,-
0.1027941238\H,7.8427037838,-3.6988489971,-0.5842477885\H,7.9560044639,-1.92315156
17,-0.5145667245\Version=AM64L-G09RevB.01\State=2-A\HF=-1372.9552568\S2=0.7686
62\S2-1=0.\S2A=0.750303\RMSD=8.956e-09\RMSF=1.588e-05\Dipole=0.0026602,-0.00225
68,2.283082\Quadrupole=20.7691003,20.7258331,-41.4949334,0.0092091,0.0023061,0.0453
951\PG=C01 [X(C24H24N4O3)]\@

Neutral Dimer – M062X/6-31G(d)

1\1\GINC-HPC-N104\FOpt\RM062X\6-31G(d)\C48H48N8O6\ROOT\22-Sep-20 13\0\#n
M062X/6-31G(d) Opt integral=ultrafine guess=read geom=checkpoint
t\C10-TTAA_dimer_M062X_6-31GdOpt2ultra.com\0,1\H,4.0347956292,-1.78
21450203,1.195330166\H,8.1522568214,0.0964811914,3.044579087\H,1.5784516499,-1.670
707722,1.115590581\C,3.5123075766,-1.0438590483,1.78925
14641\H,0.6595149636,2.2006271062,1.0908342772\H,6.0248953426,0.3703191877,3.4419

465519\H,-0.4689181061,4.3860839255,1.1738389574\C,2.124
9831146,-0.978377811,1.7487523325\H,-2.2337191981,-0.514146265,1.1208
754085\C,-0.2035772744,2.3332606843,1.7361767307\N,5.6406826849,-0.12
41496987,2.6490594904\C,7.9910742435,-0.4171296436,2.0946163511\C,-0.
8388830276,3.5683250734,1.77824719\O,-4.0992348911,-4.7792991732,0.72
3349242\H,-3.5607008412,-2.5841815462,1.2129595404\C,4.2277316012,-0.
1230636392,2.5586667144\C,-1.9083338357,-1.3304345271,1.758583618\C,-2.6598935696,-
2.4980926401,1.8061631348\C,6.5318243415,-0.5996281683
,1.7348646941\H,-3.2908374233,5.0510002431,3.4609545878\C,1.42201603
28,-0.0305974612,2.4985811854\H,-2.9840354552,8.0349983593,2.14939892
61\C,-3.7880728876,-5.333721838,1.7681141963\N,0.0081533456,0.0105256
608,2.4667727288\C,-0.662645695,1.2560724383,2.4999607132\C,-0.735314
4594,-1.1925331988,2.5066918197\C,-1.9822487092,3.7332041994,2.563902
909\N,-2.6847743539,4.9588825648,2.6578469672\H,8.4750223465,0.14548
23037,1.293126091\C,3.5307529911,0.8334866812,3.3018545019\H,-4.13196
26393,7.0230574223,3.0573824535\C,-2.2206885786,-3.5741548194,2.58136
21959\C,2.1453124759,0.872301453,3.286783636\C,-3.6095055556,7.140106
2258,2.1057652661\O,6.2031786263,-1.1474290969,0.6919955686\N,-2.9291
100664,-4.7961828422,2.6787134988\C,-2.7325312171,5.9622128475,1.7374
949092\C,-0.3157825747,-2.2661020552,3.30107537\C,-1.7943407797,1.4365
952189,3.3037042066\C,-2.4523051179,2.6564362895,3.3207566256\C,-1.04
33151335,-3.4456674415,3.3232690696\H,4.0796266283,1.5535535969,3.904
1198998\H,-2.6927644961,-5.372350 284,3.4743178619\H,1.6157643785,1.6
135537337,3.8765293924\H,0.5913626384,-2.1757023297,3.889792308\O,-2.
1123857739,5.9429126769,0.6836380189\H,-0.6946877983,-4.2778953865,3
.9301913786\H,-2.1631568226,0.6110998644,3.9039554723\H,-3.341281187
6,2.7765092013,3.9353780624\C,-4.359717717,-6.6869693926,2.1342023139
\H,-4.1131955131,-7.391448857,1.3366403704\H,-5.4481963148,-6.60147180
18,2.1743340524\H,-3.9965576622,-7.0783984447,3.0866328874\H,8.461149
6266,-1.402520181,2.1366714162\H,0.5740422899,8.4988184489,-1.4518082
747\H,-0.8468492541,8.491138679,-2.4961455934\C,-0.3204600505,7.93209
97682,-1.7174223342\H,-0.9700596095,7.8326569411,-0.844563186\C,0.113
8355085,6.5940237701,-2.2912969659\O,0.9903896221,6.5137092295,-3.134
466943\H,-1.2570126963,5.7271883406,-1.0592856355\N,-0.5771931217,5.5
284868771,-1.785738489\H,1.2230794425,4.3353289766,-3.4701620736\C,-0.4174476646,4.
164370494,-2.0883082645\C,0.5581949529,3.6559534211,-2.
9558210955\C,-1.2869814163,3.2732976226,-1.4513305254\H,-2.046411795
9,3.6635876636,-0.7786237369\C,0.654527591,2.2835053665,-3.1507489358
\H,1.4114726347,1.8896737909,-3.8226352247\C,-1.1623352762,1.90361571
39,-1.6264368807\C,-0.182823017,1.3864259924,-2.4790071624\H,1.980138
9566,0.9533115517,-1.1015200781\H,4.1959844388,-0.0736879896,-0.77703
53346\C,2.2297315532,0.0358545096,-1.625129755\H,-1.8285832399,1.2297
900382,-1.0969749064\C,3.4779100964,-0.5405132311,-1.4463501779\N,-0.0
065939932,-0.0119120915,-2.6456924519\C,1.2918021073,-0.5586171735,-2

.474139548\H,7.7758791952,-3.543567163,-2.475856283\H,-2.3605522544,0.2540938863,-3.8278779881\O,5.1463446979,-4.1421271168,-3.C,7.0291613663,-3.7084856303,-1.6940904808\C,-2.3242431528,-0.5920916123,-3.1480179795\C,1.6491140032,-1.7373701221,-3.1375257824\C,-1.1296335072,-0.8625182646,-2.4723037673\C,2.8854676222,-2.3395642608,-2.9385035119\H,5.5876055162,-1.7924111951,-1.0461044229\H,7.2704681247,-3.0867404598,-0.8286687688\H,7.07042683,-4.7633972748,-1.4159471047\H,0.9292725223,-2.2000917142,-3.8062833843\C,-3.4648332115,-1.3601453473,-2.9476202558\H,-4.385024369,-1.1289154073,-3.4652669845\H,3.1407150965,-3.2586843019,-3.4465707426\C,-1.0888112623,-1.9608369069,-1.6087052273\H,-0.1730256328,-2.1952520817,-1.0750929987\C,-3.418091067,-2.4513115399,-2.07000401\C,-2.2126535105,-2.7522678971,-1.427899799\N,-4.5194411972,-3.2697898111,-1.761933711\H,-2.1719145981,-3.5987112664,-0.7471812432\O,-6.1548430668,-2.4185708577,-3.121356822\H,-4.3525700744,-3.9503352076,-1.0281940675\C,-5.7870570415,-3.2091900049,-2.2696628923\H,-6.3168935817,-4.7570672768,-0.8116500435\C,-6.729534469,-4.2481736792,-1.6860179326\H,-7.6650053341,-3.7525053022,-1.4193359784\H,-6.9560322688,-4.9872025393,-2.4596232618\H,-4.3405205612,7.2869515837,1.3076702324\\Version=AM64L-G09RevB.01\State=1-A\HF=-2746.4037963\RMSD=6.826e-09\RMSF=1.214e-05\Dipole=0.0143901,0.0403901,7.8531163\Quadrupole=10.3032153,10.5235544,-20.8267697,0.1438414,-0.1277225,-0.0011252\PG=C01[X(C48H48N8O6)]\@

Radical Cation Dimer – M062X/6-31G(d)

1\1\GINC-HPC-N189\FOpt\UM062X\6-31G(d)\C48H48N8O6(1+,2)\ROOT\22-Mar-2013\0\#n M062X/6-31G(d) FOpt=Z-matrix guess=read geom=checkpoint\nf\C10-TTAA_dimer_cation_M062X_6-31GdOpt.com\1,2\H,2.2199135154,3.8198573263,1.2200086559\H,1.0906617058,8.0756254114,3.0866295212\H,1.8589407367,1.382593813,1.1237902113\C,1.4177419562,3.3700172555,1.7915204386\H,-2.1498819404,0.9168849605,1.1215690298\H,0.391495391,6.01126185,3.4886110948\H,-4.4387507891,0.0098035798,1.2085421659\C,1.2077321375,1.9982923362,1.737823378\H,0.269963171,-2.3081649518,1.100283134\C,-2.3574310613,0.0422719592,1.7316808453\N,0.735333894,5.5769146953,2.6481652342\C,1.2211024648,7.8765630405,2.0211647196\C,-3.649430732,-0.4649711688,1.7779219819\O,4.4153144508,-4.3845477359,0.5729517252\H,2.1956881172,-3.8416569048,1.1959227128\C,0.5674484479,4.1737985958,2.553766657\C,1.1239912393,-2.0577282926,1.7229795478\C,2.2068002086,-2.9263957877,1.7742603855\C,1.2121352721,6.4050700481,1.677920814\H,-5.4144917142,-2.7063629328,3.4513708542\C,0.1782820543,1.3938502256,2.4669443353\H,-8.2931866664,-2.3199635771,1.627022334\C,4.949861107,-4.2583084733,1.6687486673\N,-0.0113846535,-0.0085132679,2.4136313466\C,-1.3200541046,-0.5486392247,2.4601219861\C,1.109657776,-0.8727380019,2.4649157889\C,-3.9202965182,-1.6105584156,2.5287048666\N,-5.2181073559,-2.1710056398,2.6164277795\H,0.4185470837,8.3709667694,1

.4661771365\C,-0.4653575767,3.577474327,3.2812115182\H,-7.5647925093,
-3.1053286821,3.0503285383\C,3.323931902,-2.5985272968,2.5456798145\C
, -0.6507867476,2.2031388746,3.2526469238\C,-7.4468448183,-2.9098210101
,1.9827171392\O,1.5944985538,5.9983343852,0.5864151162\N,4.4574106892,-3.441867898
8,2.6410786387\C,-6.1717672452,-2.1726686001,1.643976800
5\C,2.2202517393,-0.5668773432,3.2605917592\C,-1.6063800763,-1.6791286
423,3.2346817241\C,-2.8875001566,-2.2102363713,3.253036645\C,3.318576
6965,-1.4137014911,3.2849229581\H,-1.1273296204,4.1951338211,3.882716
2156\H,5.0082793739,-3.3492072291,3.4838781778\H,-1.4497006694,1.7520
937976,3.8324296085\H,2.2257368832,0.3430432698,3.8519961834\O,-6.01
25308575,-1.6330940209,0.555109048\H,4.1810102289,-1.1539727535,3.893
3679599\H,-0.8178238248,-2.1491114922,3.8136861135\H,-3.0903434142,-3.
0993635129,3.8449325248\C,6.2249353228,-4.9904432611,2.0166386194\H,
7.0525568879,-4.530207951,1.4693715413\H,6.1360257321,-6.0236239213,1
.6770262977\H,6.4556073375,-4.9795184004,3.0836734165\H,2.1678878252
,8.3038990234,1.6864708813\H,-8.5631819002,1.3065608057,-1.9733070931
\H,-8.2945369408,-0.4104705774,-2.3497061712\C,-7.9103821739,0.4528319
007,-1.7970487622\H,-7.8993716774,0.1951633377,-0.734166333\C,-6.52170
28999,0.792278445,-2.2904116751\O,-6.2773629936,1.7299433487,-3.01854
71537\H,-5.8646544522,-0.7990885691,-1.1684429555\N,-5.5548254027,-0.0
955435264,-1.8363345298\H,-4.1409220534,1.6455746257,-3.3924473963\C,
-4.1916553749,-0.0559749627,-2.0621205202\C,-3.5505304104,0.909346701
4,-2.8665525254\C,-3.4132060338,-1.0408798778,-1.4201466686\H,-3.90819
08546,-1.7696463393,-0.7854580578\C,-2.1729633692,0.9053345842,-2.9704
505505\H,-1.6792394283,1.6445418655,-3.5936828717\C,-2.041239344,-1.04
0320062,-1.5277227495\C,-1.3977791077,-0.0517661733,-2.2936417403\H,-0
.799055956,2.1441306343,-0.9619622079\H,0.4232651732,4.2741057363,-0.7
618899927\C,0.1225521502,2.2963140251,-1.5140933405\H,-1.4540778864,-1.7701376061,
-0.97988612\C,0.8046163532,3.4863197872,-1.4042210665\N,
0.0047834024,0.0070862873,-2.3407244139\C,0.6552500086,1.2513177093,-2.2896357584\
H,3.7868016788,7.4071655746,-2.3371708604\H,-0.55905368
25,-2.2686233806,-3.6055893565\O,4.6400184884,4.5898394553,-2.9891826
838\C,2.0429398052,3.6740834091,-2.0519736102\C,3.9424315561,5.270400
3916,-2.2685021377\N,2.6868996565,4.8758783306,-1.8252014981\C,4.3348
120796,6.6447241626,-1.7741196777\C,0.3255932697,-2.3253560195,-2.9
792816208\C,1.868602648,1.4499115469,-2.9712413996\C,0.7584426615,-1.1770246646,-2.
2940713083\C,2.5577698511,2.6424796489,-2.864452612
8\H,2.2298777334,5.4932816788,-1.157123378\H,4.0914554701,6.7678549
426,-0.7147585669\H,5.4027256014,6.7833693849,-1.9367791528\H,2.26134
18086,0.6565375195,-3.5996494611\C,1.0166399935,-3.5173389495,-2.87804
74607\H,0.6825093263,-4.3963889747,-3.4095230261\H,3.4886261373,2.791
4930436,-3.3919285635\C,1.9314494424,-1.238387362,-1.5206303015\H,2.2
609973346,-0.3654818282,-0.9668548211\C,2.1692314756,-3.5877838281,-2.0675203695\C,
2.623360618,-2.422993993,-1.4152981884\N,2.8898853134,

-4.745863433,-1.8432686473\H,3.4980350041,-2.4862862262,-0.7753595097
\O,1.6720374602,-6.2896709065,-3.0195886698\H,3.6508956121,-4.6601868
08,-1.1727331086\C,2.6079639935,-6.0282238259,-2.2949407417\H,3.88435
53271,-6.8775763856,-0.7650361603\C,3.6022201149,-7.0578075,-1.8060358 877\H,3.16
06212724,-8.0475612559,-1.9148377578\H,4.5087568684,-7.0068
543448,-2.4178728827\H,-7.4547052124,-3.8618118774,1.4438601379\\Vers
ion=AM64L-G09RevB.01\State=2-A\HF=-2746.2049318\S2=0.768604\S2-1=0.
\S2A=0.7503\RMSD=5.559e-09\RMSF=9.779e-05\Dipole=-0.0028964,0.0 0644
26,4.5843782\Quadrupole=18.6543243,18.8406138,-37.4949381,0.129722,0 .0
919572,0.0510183\PG=C01 [X(C48H48N8O6)]\@